Examination of Property-Reactivity Relationships of Early Transition Metal
Carbides and Nitrides as Catalysts and Catalytic Supports

by

Brian M. Wyvratt

A dissertation submitted in partial fulfillment
of the requirements for the degree of
Doctor of Philosophy
(Chemical Engineering)
in the University of Michigan
2016

Doctoral Committee:

     Professor Levi T. Thompson, Jr., Chair
     Professor Mark A. Barteau
     Associate Professor Bart M. Bartlett
     Professor Emeritus Phillip E. Savage

To my loving mother and father,
who instilled in me all the qualities to make this possible,
and to my brother, who kept me sane while they did so.

ACKNOWLEDGEMENTS

The work presented in this dissertation would not be possible without the help and support from a number of talented and caring researchers, friends, and family. First, I would like to thank my advisor, Professor Levi Thompson for his support, guidance, and time throughout the highs and lows during the last five years of research. His criticism and encouragement have molded me into the person I am today. I am forever grateful for the freedom he granted me during my graduate studies to explore different topics and reactions in the field of catalysis.

I would also like to extend my appreciation to my dissertation committee. I was privileged to have been surrounded by experts in the field of catalysis, reaction engineering, and materials chemistry. Interactions in both research discussions and classes have broadened and advanced my knowledge in many areas related to these subjects and I do not believe I'd be the same researcher and scholar without their guidance. I'd first like to thank Professor Barteau, whose knowledge of catalysis and surface science is unbounded. His questions and comments were thought-provoking and constantly improved my experimental technique and thought process. I'd also like to acknowledge Professor Savage, who taught me extensively about reaction engineering and catalysis in the graduate reaction engineering course and about statistical analysis associated with my research. I am similarly grateful towards Professor Bartlett for providing his insight into materials chemistry through both the chemistry course in the fall of 2014 and our casual conversations in the time since then. Interactions with

committee members have always been friendly and insightful and I appreciate all of their time and dedication to my development.

It is also necessary to acknowledge other people at Michigan that contributed to my professional growth. I've had the privilege to work alongside a great number of individuals over the last 5 years in the Thompson Research group, each of whom have helped me in one form or another to develop as a researcher as well as a human being. I am grateful for my interactions with Dr. Saemin Choi, Dr. Paul Rasumussen, Dr. Alice Sleightholme, Dr. Galen Fisher, Dr. Aaron Shinkle, Dr. Kana Okada, Dr. Richard Ezike, Dr. Priyanka Pande, Dr. Gaowei Wang, Dr. Yuan Chen, Dr. Amin Bazyari, Dr. Iljeong Heo, Dr. Jason Gaudet, Dr. Tapiwa Mushove, Dr. Krista Hawthorne, Dr. Tanya Breault, Dr. Wes Brogden, Dr. Shawn Eady, Dr. Abdoulaye Djire, Allison Franck, Ryan Franck, Jonathan Kucharyson, Siu on Tung, Sydney Laramie, Wei-Chung Wen, Jennifer Jocz, Sarah Paleg, Scott Johnson, Sarah Carl, Anisha Rehlan, Olabode Ajenifujah, Digna Vora, and Nishanth Bharadwaj. I have learned a great deal from them and would not have completed what I have on this research project without everyone's help and support. I would like to thank both Jacqueline Close and Nishanth Bharadwaj for their help with experiments and data analysis during their time working with me.

There are a few individuals I would like to specifically thank from this group. First, Dr. Saemin Choi has been my mentor and friend for the better part of the five years I've spent at the University of Michigan. He was always willing to give his time to help and sat through a great number of venting sessions detailing my frustrations over the years. Saemin was constantly encouraging and positive about research even when I was having trouble. His advice and support will remain with me in my time after Michigan. I

must also thank Dr. Gaowei Wang, who taught me nearly everything I know about catalysis and materials characterization in the Thompson group. He was a great friend and a helpful mentor lending me his time during my first year and a half in the group. His support will not be forgotten. I'm also very grateful to Ryan Franck, whose friendship and help over the last five years has had a great impact on my work and time in Michigan. I'd also like to thank Dr. Jason Gaudet, who I spent a great deal of time discussing research and experimental design with, ranging from X-ray absorption spectroscopy experiments (x2) to temperature-programmed desorption experiments. Jason provided a great deal of guidance and help, time that resulted in our co-authoring two journal articles together. I'd also like to acknowledge Dr. Yuan Chen, who I've spent countless long nights working beside in lab and who has always been there to talk, be it research related or otherwise. She will continue to be a good friend beyond my time at Michigan. Lastly, I must thank Dr. Josh Schaidle and Dr. Neil Schweitzer, two previous Thompson group graduate students whose projects inspired my own. Josh and Neil were always receptive to conversations and questions regarding the techniques and general path of the research project. Their time and help could not be more appreciated.

I'd lastly like to take this time to say thank you and I love you to my family. Without them, truly none of this would've been possible. My brother, Kevin, has always

been supportive and caring throughout my graduate studies. We've grown a great deal since our fighting days 10-15 years ago. I've always looked up to him and have appreciated his guidance whenever he'd provide it. He is one of my closest friends and I'm eager to spend time with him in the upcoming years back in New Jersey.

My parents have played an immeasurable, indescribable role in my life to date. I cannot convey the appreciation that I have for their time, their sacrifice, and their love throughout my life, but especially in these last five years. Growing up in a house of organic chemists was not easy, but I could not have two better role models to be around and learn from. The road to here has not always been smooth, but my parents have always been there to provide advice, both on research and on life. My father is one of the brightest organic chemists I know. He has devoted many hours towards discussing reaction pathways and useful analyses. His support extends beyond the laboratory and classroom as he has exposed me to a variety of extracurricular activities that have shaped me into a well-rounded individual. I am ready to take his money on the golf course every weekend for the foreseeable future. My mother and I are far more similar than I care to admit. All of the traits in my mother that I've complained about for the last 27 years, I see in myself as I reflect on the last five years of work. However, these traits have made me the researcher, scholar, and person that I am today, and for that I am forever grateful. She has been my greatest supporter throughout my graduate studies. Her dedication and devotion of countless hours of her time to discussing and reviewing my research will always be appreciated and never be forgotten. I love you both.

TABLE OF CONTENTS

LIST OF FIGURES

xiii

xv

LIST OF TABLES

CHAPTER 1

Introduction

1.1.   Motivation

Both the world's population and energy demands have trended upward for the last 15 years and current projections indicate that these trends will continue through 2040 [1]. Global energy demand is expected to rise by ~40% by 2040, an increase of ~200 quadrillion BTU, due to population growth, improved lifestyles, and emerging third-world countries. Transportation fuel is a major contributor to current energy demands (~20%, equivalent to 100 quadrillion BTU), and demands due to transportation are also expected to rise by 40% by 2040 [1]. Most of this energy (70-80%) will be from gasoline, diesel, and jet fuels, generally obtained through the refinement of crude oil (Figure 1.1).

Transportation fuel mix
Millions of oil-equivalent barrels per day

Asia Pacific

Other
Natural gas
Fuel oil
Jet fuel
Biodiesel
Diesel
Ethanol
Gasoline

North America

Europe
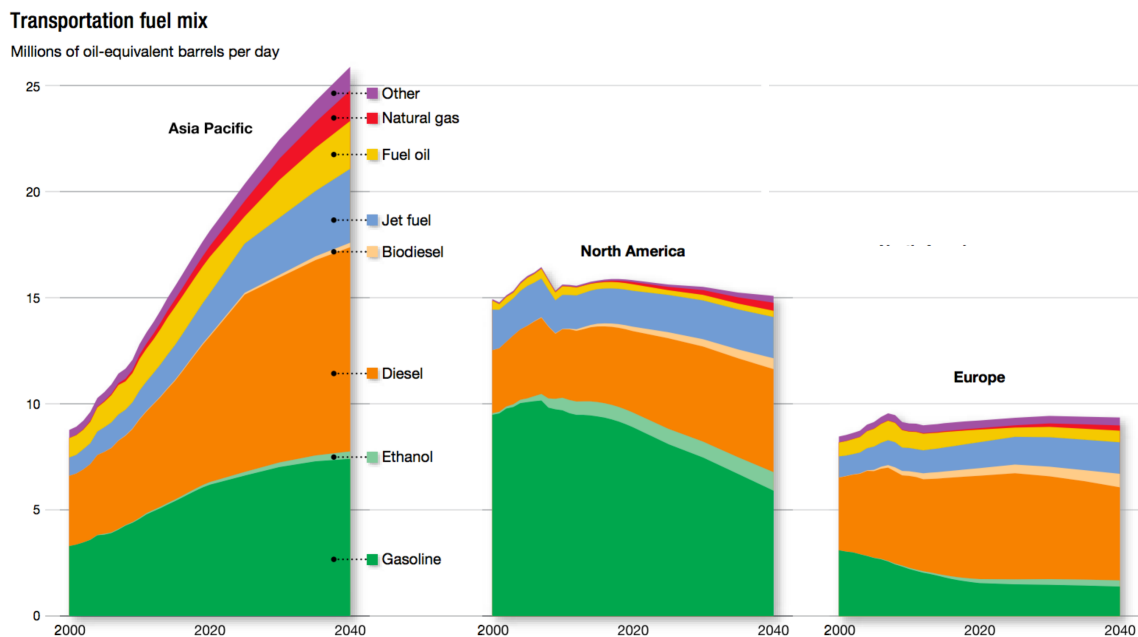
Figure 1.1. Global transportation energy demands by region. Adapted from [1].

Crude oil, a non-renewable fossil fuel, is a problematic energy feedstock for a variety of reasons. First, current (2015) estimates by a major oil company (BP, formerly British Petroleum) conservatively estimate enough crude oil reserves to last only 52.5 years assuming current extraction and refinement technological practices as well as current energy consumption projections [2]. While 50 years appears to be a low estimate as technological advances in both locating and accessing oil reserves will likely extend this timeframe, there is still a finite amount of crude oil in the world. Second, the price of crude oil is highly volatile with futures prices (Nymex) ranging from ~$30 to $140 per barrel, which translates into variable prices downstream in goods and services [3]. Third, the use of crude oil-derived fuels has deleterious effects on the environment given the evolution of CO_2 during combustion and the impact of this CO_2 on global climate change. Use of crude oil currently accounts for ~75% of global CO_2 emissions [4]. Lastly, the United States has become dependent on imported crude oil since a significant amount of the world's crude oil production (~85%) comes from outside the US [5]. This dependence on imports results in higher prices and some vulnerability for the US.

As a result, the development and use of alternative sources for transportation fuels have become areas of interest. While crude oil production is projected to increase as much as 60% from 2010 to 2040, the production of liquid fuels from natural gas and biomass is also expected to increase dramatically (~40 and ~100%, respectively) (Figure 1.2). A number of solutions for the transportation sector have been proposed, tested, and at times implemented, such as vehicles propelled by compressed or liquefied natural gas (CNG/LNG), electricity, hydrogen, methanol, and dimethyl ether [6,7].
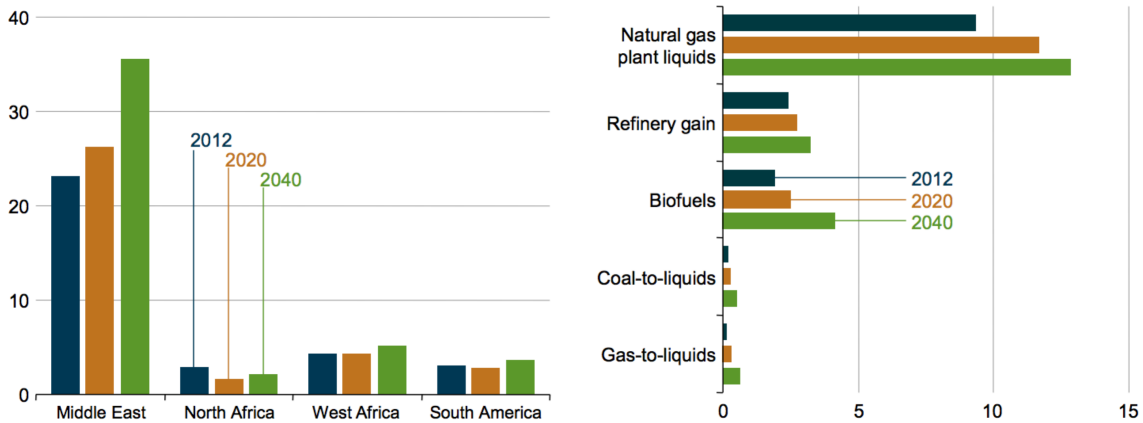
Figure 1.2. (left) OPEC crude and lease condensate (light liquid hydrocarbons) production and (right) world totals for other liquid production fuels and their sources. Axes listed in million oil-equivalent barrels per day. Adapted from [5].

While a number of potential replacement fuels have been explored, few have gained widespread deployment given the infrastructure challenges associated with the use of unconventional fuels for transportation and electricity generation. However, the U.S. government took steps towards energy independence with the Energy Policy Act of 2005 and the Energy Independence and Security Act of 2007. The Renewable Fuel Standard, established by these Acts, requires that all transportation fuels sold within the US are blended to a minimum volume percent (expected to be ~14.5% for 2017 [8]) of renewable fuels. The total volume required to be blended in to gasoline increases each year, and will reach 36 billion gallons by 2022 [9]. In order to meet these mandates, significant research funds have been and are continually being allocated towards finding new, cheaper sources and methods for producing biofuels from biomass. Tax breaks have been added as well as other monetary incentives to farmers and industries producing crops and/or biofuels [9]. Likely due to these combined factors, the global production of biofuel increased by a factor of five between 2000 and 2010 alone [10].

There are a number of different biofuel production processes being developed (Figure 1.3) [10]. Biomass can be converted biochemically through anaerobic digestion,

fermentation, and enzymatic reactions to form products known as biogas or ethanol [11,12]. In addition, biomass can be converted via transesterification of oils from oil-based plants to yield a biodiesel [13]. Thermochemically, biomass can be combusted to form hydrogen, gasified to form syngas, or pyrolyzed to form bio-oil [11,12].

	Advanced biofuels			Conventional biofuels
	Basic and applied R&D	Demonstration	Early commercial	Commercial
Bioethanol		Cellulosic ethanol		Ethanol from sugar and starch crops
Diesel-type biofuels	Biodiesel from microalgae; Sugar-based hydrocarbons	BtL[1]-diesel (from gasification + FT[2])	Hydrotreated vegetable oil	Biodiesel (by transesterification)
Other fuels and additives	Novel fuels (e.g. furanics)	Biobutanol; DME[3]; Pyrolysis-based fuels	Methanol	
Biomethane		Bio-SG[4]		Biogas (anaerobic digestion)
Hydrogen	All other novel routes	Gasification with reforming	Biogas reforming	

■ Liquid biofuel   ■ Gaseous biofuel

Figure 1.3. Commercialized and conceptual biofuels based on type and source in 2011. Adapted from [10].

The current commercial processes (1st generation biofuels) are mostly biochemical conversion to form ethanol and bio-diesel (alkyl esters). Of the biomass sub-categories (starch/sugar, aquatic, oil seed, woods, grasses), starch/sugar crops and oil seed plants were first used for the production of biofuels [11,12]. Starch/sugar crops are converted to ethanol via fermentation. First, enzymes are used to hydrolyze a mash of the starch crops, releasing the sugars from the cells. These sugars are then used to produce ethanol via fermentation using microorganisms such as yeast. Lastly, the ethanol can be refined further via downstream distillation and filtration processes [11,12,14,15]. Utilizing crops as an energy feedstock, especially crops that could help mitigate worldwide food shortages, is an unattractive notion.

Alternatively, another pathway involves transesterification of vegetable oils, typically in the form of triglycerides. The oils are reacted with an alcohol (e.g., methanol, ethanol) in the presence of a catalyst (typically sodium hydroxide, potassium hydroxide) (Figure 1.4) to form fatty acid esters and glycerol [13,16]. Following reaction, the fatty acids and glycerol can be easily separated due to the immiscible layers. The overall cost of this process to produce bio-oil as well as the large amounts of glycerol by-products produced have delayed its widespread adoption [17]. New catalysts are being developed in an attempt to reduce costs [18] and researchers have also been exploring potential uses for glycerol [19,20].
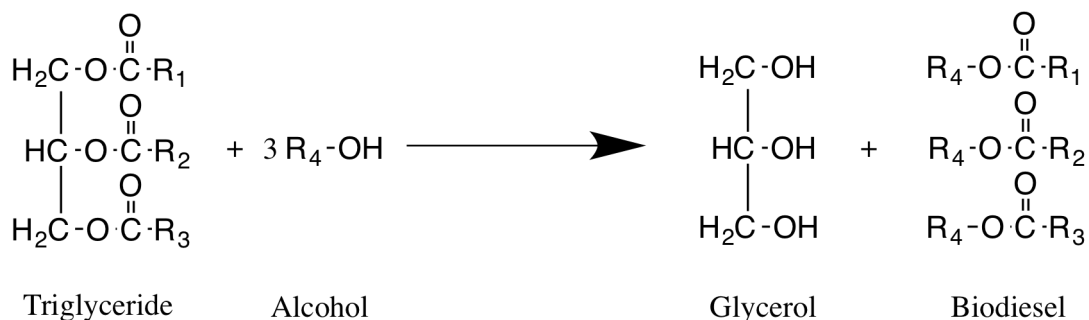
Figure 1.4. Simplified chemical reaction for the transesterification of triglycerides to form fatty acid esters (biodiesel).

Research on thermochemical methods for biomass conversion to biofuels has primarily focused on two methods: (1) biomass pyrolysis to produce bio-oil, a complex mixture of oxygenated compounds [21,22,23], which can be refined to generate diesel and jet fuels and (2) biomass gasification to produce syngas, a mixture of carbon monoxide and hydrogen, followed by its conversion to waxes, diesel, and gasoline via the Fischer-Tropsch synthesis (FTS) process [24,25]. These processes are different than the biochemical processes as they generate biofuels compatible with current infrastructure and transportation engines (typically referred to as "drop-in fuels") [26,27,28].

Biofuels from the pyrolysis and gasification routes represent promising 2nd generation biofuel technologies for a variety of reasons: (1) advanced state of the technologies, (2) ability to use as drop-in fuels with the current transportation fuel infrastructure, and (3) ease of widespread implementation and production. FTS and fast pyrolysis-based synthetic gasoline and diesel can be immediately used in current vehicles and infrastructure, whereas alcohol-based fuels (e.g., methanol, ethanol) would likely require modifications to the current vehicle fleet. Furthermore, FTS has the potential to generate very "clean" fuels (low sulfur and nitrogen content) given that the synthesis gas can be cleaned and refined prior to hydrocarbon synthesis. Lastly, these processes can be readily scaled to meet demand, while fermentation processes are inherently batch reactor-based with lower throughput.

It is of major importance to note that biomass transformations do not proceed readily. Instead, the reactions that govern this conversion must be facilitated by catalysts. The research described in this dissertation focuses on the catalytic materials, in particular early transition-metal carbides and nitrides, for these biomass conversion processes. The next two sections will describe two thermochemical methods for converting biomass to biofuels. After these 2 sections, early transition-metal carbide and nitrides, a class of catalytic materials, will be discussed.

1.2.   Conversion of Biomass to Chemicals and Fuels via Fast Pyrolysis

One route for the conversion of biomass into fuels is through pyrolysis of biomass followed by condensation of volatilized compounds to afford a "pyrolysis oil", which is subsequently upgraded. Initially, biomass pyrolysis involves the thermal decomposition of biomass in the absence of oxygen to produce a pyrolysis oil and char/solid residue

6

[29,30]. This oil typically (depends on biomass) has a specific energy that is lower than that of conventional fuel oil [30], likely due to the large amount of oxygen typically observed in the oil (Table 1.1) [31]. For applications in energy sectors such as transportation, the bio-oil must be upgraded into a cleaner burning, low viscosity, and more chemically stable fuel of higher gross energy [32]. Pyrolysis oil consists of a number of different compounds with various chemical functionalities, including carboxylic acids, alcohols, aldehydes, alkenes, aromatics, furans, ketones, esters, phenols, and sugars [33,34,35]. Hydrogenation, deoxygenation, and C-C coupling reactions are all relevant for converting/upgrading pyrolysis oil towards liquid fuels [36]. Hydrogenation reactions are required in order to bring the H/C molar ratio from typical pyrolysis oil ranges (0.9-1.5) to those similar to gasoline and diesel (1.9-2.2). Deoxygenation reactions are aimed at removing oxygen, to produce a fuel of higher gross energy. Lastly, C-C coupling may be required in order to generate a longer hydrocarbon, more consistent with those found in gasoline (C_4-C_{12}), diesel (C_{10}-C_{15}) and jet fuel (C_{11}-C_{20}).
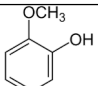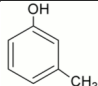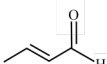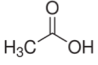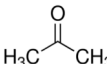
Table 1.1. Elemental compositions of petroleum crude oil and pyrolysis bio-oil by weight

	Petroleum crude oil (wt%)	Pyrolysis bio-oil (wt%)
C	83–86	55–65
H	11–14	5–7
O	<1	30–50
N	<4	<0.1
S	<1	<0.05
Water	0.1	20–30

One of the primary issues with this process is the complexity involved in upgrading the resulting pyrolysis oil. Since numerous functional groups (~300-400 different chemical compounds) and competing reactions are involved in the conversion of

pyrolysis oil, catalytic materials must be robust enough to convert all of the compounds to useful products in a cost efficient manner [36]. Fundamental catalytic research is typically conducted on a model compound, consisting of one or more chemical functionalities found in pyrolysis oil. Key model compounds studied in the literature are shown in Table 1.2 [37,38,39,40,41]. A few reports from the National Renewable Energy Laboratory summarize the state-of-the-art catalytic research and ultimately explore the feasibility of such a process with current catalytic systems [36,74]. According to this report, the primary focus of current catalysis research should be on maintaining high carbon efficiencies during reactions while catalyst cost and lifetime are currently of secondary importance [74]. Current catalysts are not yet sufficient for the desired application and new catalysts need to be discovered to accelerate this technology.

Table 1.2. Common model compounds used as probe molecules for biomass-derived catalytic conversion.

Probe Molecules		Functionalities
Guaiacol	OCH₃, OH	Phenol, ether
Cresol	OH, CH₃	Phenol
Crotonaldehyde		Alkene, aldehyde
Acetic Acid	H₃C, OH	Carboxylic acid
Acetone	H₃C, CH₃	Ketone

1.3.   Conversion of Biomass to Chemicals and Fuels via Gasification

Biomass gasification also presents an attractive pathway towards the production of liquid fuels for use in the transportation sector, primarily due to the pre-existing

knowledge surrounding this technology due to already commercial production of liquid fuels via gasification and upgrading of coal and natural gas. The production of liquid fuels via coal or natural gas gasification and upgrading has origins back during World War II. While widespread adoption has not been realized, numerous companies are currently attempting to commercialize the generation of liquid fuels through gasification and Fischer-Tropsch synthesis processes. An example process converting natural gas to liquid fuels is shown in Figure 1.5 for one such company [42]. However, natural gas is still a fossil fuel in finite supply. Gasification of biomass to generate syngas for Fischer-Tropsch upgrading is similar to the conversion of natural gas, although the feedstock is a solid instead of a gas. The general process for biofuel production via gasification involves
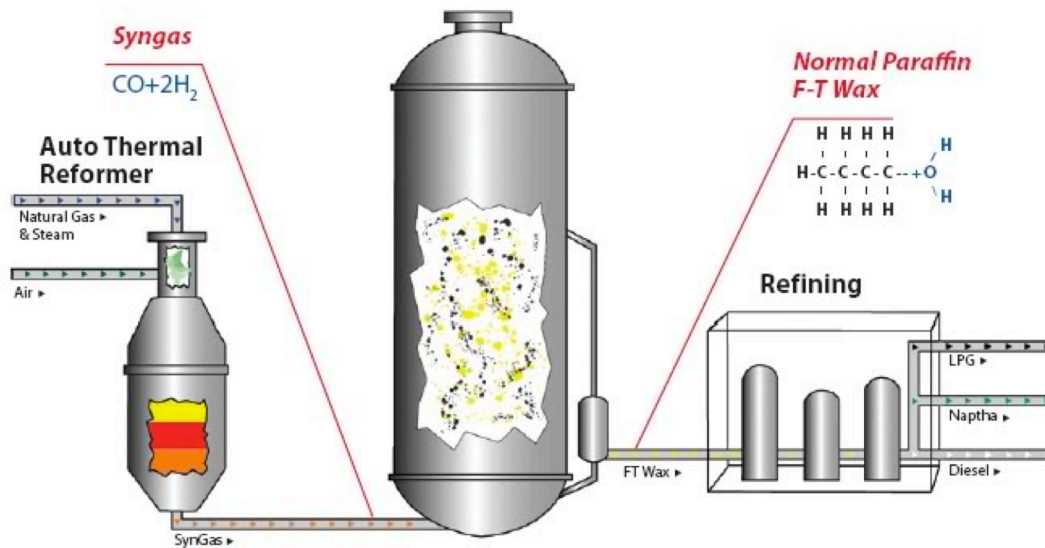
Figure 1.5. Process schematic detailing the conversion of natural gas into LPG, Naptha, and diesel fuels via gasification, Fischer-Tropsch synthesis, and downstream refining. Taken from [42].

four steps: gasification of solid biomass to generate syngas, water-gas shift to optimize the H_2/CO feed ratio, Fischer-Tropsch synthesis, and downstream refining. Syngas is typically reformed via water-gas shift chemistry to improve the H_2/CO ratio to optimal levels ($H_2/CO \sim 2$) before feeding into Fischer-Tropsch synthesis reactors downstream to

generate long chain hydrocarbons. Catalysts are required for the water-gas shift reaction and Fischer-Tropsch synthesis steps. The following two sections will discuss these two reactions.

1.3.1. Water-Gas Shift Reaction

The water-gas shift reaction (WGS) generates H_2 from a mixture of CO and H_2O, and producing CO_2 as a by-product:

$$CO + H_2O \leftrightarrow CO_2 + H_2 \tag{1.1}$$

This reaction plays an important role in industrial hydrogen (H_2) generation as WGS is used to convert CO generated via reforming of hydrocarbons to produce H_2. Reforming of hydrocarbons typically produces streams with H_2/CO ratios ranging between 1-3 depending on the hydrocarbon source [43]. Gasification of biomass has been reported to yield H_2/CO ratios between ~0.3 and 1.2 [44]. The WGS reaction is often used to generate more H_2 or adjust the H_2/CO ratio for use in downstream processes, such as alcohol synthesis (e.g., methanol) [45] or Fischer-Tropsch synthesis [46]. These operate at an optimal H_2/CO ratio close to ~2 [45,46].

The WGS reaction is exothermic (ΔH_{rxn} = -41 kJ/mol) [47]. As a result, WGS is performed in two different temperature regimes as a trade-off between kinetic and thermodynamic barriers. In typical industrial settings, WGS is first conducted at high temperatures (350-450°C) in the presence of a chromium-promoted iron oxide catalyst (Fe_2O_3-Cr_2O_3). At these high temperatures (commonly referred to as "HTS"), WGS rates are high, but high CO conversions are unachievable due to the thermodynamic limitations. Therefore, after passing through the HTS reactor, the effluent stream is cooled and fed into a second reactor operating between 200 and 250°C using a Cu-ZnO-

Al_2O_3 catalyst to achieve higher conversions [47]. While used commercially, these catalysts have specific limitations, specifically the LTS catalysts. Cu is prone to sintering if process temperatures get too high and Cu-ZnO-Al_2O_3 is deactivated in the presence of chlorine and sulfur in the feed.

1.3.2. Fischer-Tropsch Synthesis

The Fischer-Tropsch synthesis reactions involve the conversion of synthesis gas (CO and H_2) into useful fuels and chemicals, specifically long-chain hydrocarbons and alcohols.

Paraffin Production:
$$nCO + (2n + 1)H_2 \rightarrow C_nH_{2n+2} + nH_2O \qquad (1.2)$$

Olefin Production:
$$nCO + (2n)H_2 \rightarrow C_nH_{2n} + nH_2O \qquad (1.3)$$

Alcohol Production:
$$nCO + (2n)H_2 \rightarrow C_nH_{n+2}O + (n-1)H_2O \qquad (1.4)$$
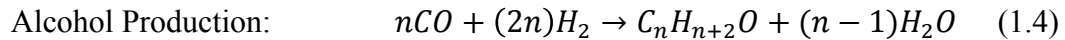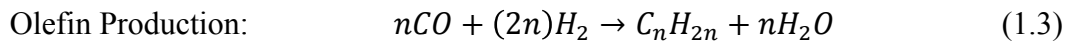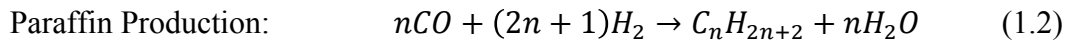
The WGS reaction (Equation 1.1) is an undesired reaction between CO and water produced by the Fischer-Tropsch reaction.

Fischer-Tropsch synthesis (FTS) was first studied in ~1925 by Franz Fischer and Hans Tropsch [48] and gained traction during World War II as a way to produce motor fuels in order to gain energy independence [49]. This process was first fully commercialized by Sasol in South Africa in the 1950s to convert coal-based syngas into a variety of products, ranging from C_3-C_4 hydrocarbons to heavy oils and hard waxes (C_{23}+). In this plant and others, Sasol claims to have produced nearly 1.5 billion barrels of synthetic fuel as of 2015 [50]. Shell also constructed a Fischer-Tropsch plant in Malaysia utilizing natural gas-based feedstock that came online in 1993 (14,700 barrels per day) [51].

However, widespread adoption of Fischer-Tropsch has been limited due to high costs, low efficiencies, and variable interest in alternative sources of transportation fuels, typically due to changing crude oil prices. Increased environmental awareness and the shale gas boom that began in the mid-to-late 2000s [52] have led to renewed interest in FTS. A number of companies are investing in plants aimed at converting natural gas into liquid fuels using FTS, and smaller companies are looking to develop mobile reactor units equipped with reformers and Fischer-Tropsch reactors for site-specific conversion of natural gas. A prime application of this process is to convert the natural gas flared from oil and natural gas well-sites into transportation fuels. Despite this, it should be noted that natural gas is fuel of finite amount. Biomass-to-liquids facilities have the potential to replace natural gas-to-liquids processes given similarities in the reactions and process design.

One route to increasing the viability of this process is improving the catalysts used. Given the competing reactions and variety of products formed in FTS, both activity and selectivity are important for a catalyst to be considered commercially viable. For FTS, the desired products are higher hydrocarbons, such as C_{8+} molecules, while CH_4 and CO_2 are undesired products. Olefins and alcohols are also desired products as they are precursors to a variety of chemicals.

Higher hydrocarbons are formed through carbon chain elongation on the catalyst surface by coupling of -CH_2- fragments, either through initial CO dissociation, surface oxygenate formation, or CO addition to a surface-H bond [53,54]. This chain elongation or polymerization has been extensively studied, and follows a chain polymerization model mathematically constructed by G. Schulz [55] and P. Flory [56], and ultimately

applied by R. Andersen [57]. This model (Andersen-Schulz-Flory model, ASF) computes the distribution of hydrocarbons based on a single parameter, α, termed the C-C chain growth probability:

$$W_n = (1 - \alpha)^2 n\alpha^{n-1} \tag{1.5}$$

where W_n is the weight fraction of the products containing n carbons and α is the C-C chain growth probability (a ratio detailing the relative rates of chain elongation versus termination of the polymerization process) [57].

The hydrocarbon distributions obtained during FTS are primarily influenced by the process conditions and catalysts. Low temperatures, high pressures, and low H_2/CO feed ratios generate longer hydrocarbons [58]. Despite the dependence on process conditions, the hydrocarbon distribution tends to be more dependent on the catalyst used. There is a large body of work that has explored the different active metal phases, catalyst syntheses and catalyst formulations. From previous research, it is widely accepted that Fe, Co, and Ru are the best catalytic metals for Fischer-Tropsch synthesis [59]. Ruthenium is an expensive metal of limited supply. Therefore, Fe and Co are the most commonly employed active phases for FTS, and the catalysts often include promoters such as K, Mn, Re, and Pt to aid in reduction, dispersion, and C_5+ selectivity [59]. However, these catalysts still suffer from low activities, catalyst deactivation, and, in the case of Co, high costs, prompting research to develop new FTS catalyst formulations.

1.4. Early Transition Metal Carbide and Nitride catalysts and catalytic supports

Wide-spread adoption of alternative fuels faces a number of hurdles, in particular the need for high efficiency, low cost catalytic materials to perform the required chemical transformations from biomass to syngas or pyrolysis oil and then, ultimately, into

transportation fuels [60,61]. Catalytic materials for the conversion of syngas to hydrocarbons via Fischer-Tropsch synthesis have been the subject of research for nearly 100 years and, while commercial catalysts are available (Fe/SiO$_2$, Co/Al$_2$O$_3$), these catalysts suffer from high costs, low activities, or poor robustness. Recently, the conversion of oxygenated complexes into useful chemicals and/or precursors to transportation fuels has been investigated for the upgrading of pyrolysis bio-oil [62,63]. These reviews note that hydrodeoxygenation currently represents the best route for upgrading bio-oil to more resemble the specifications of crude oil, noting, however, that current catalysts are inadequate due to high costs and extensive deactivation from carbon deposition. This dissertation explores the use of early transition-metal carbides (TMC) and nitrides (TMN) as catalysts and catalyst supports for reactions relevant to biomass conversion applications, in particular WGS, FTS, and selective hydrogenations for pyrolysis oil upgrading. The research described in this dissertation examines trends between properties of these materials and their catalytic reactivity.

1.4.1. Chemical and Physical Properties of Early TMC and TMN

Early transition-metal carbides and nitrides are a class of materials formed by inserting carbon or nitrogen into vacant interstitial sites of the crystal lattice of an early transition metal (e.g., Ti, V, Nb, Mo, W) [64]. The resulting crystal structure of the carbide or nitride is governed by geometric and electronic factors [64,65], namely the Hägg rule and the Engel-Brewer theory of metals. The Hägg rule indicates that if the ratio of radii between the non-metal (e.g., C, N) to metal (e.g., Ti, V, Mo) is less than 0.59 (assuming hard-ball atoms), the two atoms can produce a stable interstitial compound [65]. Radii greater than 0.59 generate less typical crystal lattices [66]. The Engel-Brewer

theory states that the crystal structure adopted depends on the s-p electron count of the final compound with increasing counts shifting the structure from body centered cubic (bcc) to hexagonal close packed (hcp) to face centered cubic (fcc) [67]. Carbides and nitrides have been synthesized in a variety of crystal structures, ranging from hexagonal (e.g., WC) to hcp (e.g., Mo_2C, W_2C) to fcc (e.g., Mo_2N, W_2N, VN, NbC) [64]. Crystal structures of two Mo carbide phases are shown in Figure 1.6. Metal-nonmetal stoichiometry and synthesis conditions also have the potential to dictate crystal structure. For example, Mo nitride has been reported in numerous Mo:N stoichiometries and crystal structures: Mo_2N [68,91], MoN [69], and MoN_2 [70].

α-MoC₁₋ₓ - fcc

β-Mo₂C - orthorhombic
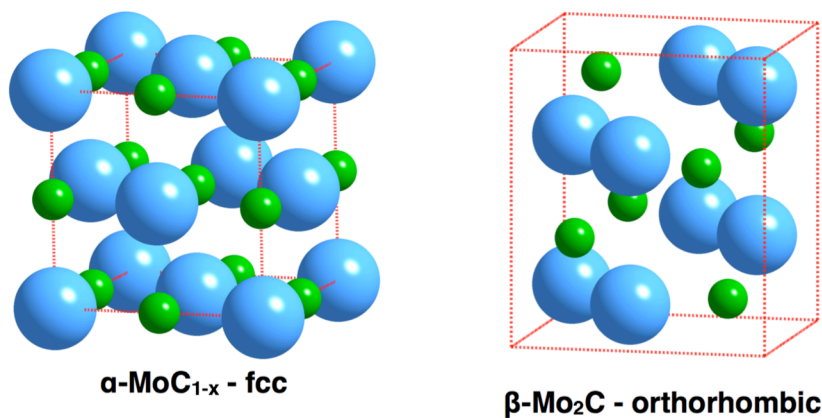
Figure 1.6. Crystal structures of (left) α-MoC_{1-x} and (right) β-Mo_2C. Note: β-Mo_2C is technically orthorhombic, but closely resembles an hcp structure. Blue and green balls represent Mo and C, respectively.

These materials have gained widespread interest in the field of heterogeneous catalysts due to the pioneering work by Levy and Boudart in 1973 [71]. In this work, Levy and Boudart reported the "platinum-like" catalytic behavior of WC. In particular, WC was capable of catalytically oxidizing H_2 to evolve water as well as isomerizing 2,2-dimethylpropane to 2-methylbutane, two reactions previously thought to be uniquely catalyzed by a select group of precious metals (Pt, Au, and Ir). In contrast, metallic W was inactive for these reactions [71]. The authors suggested that the observed catalytic

activity arose from changes in the electronic structure due to the addition of C to the W lattice. Subsequent research investigated the effect of C or N addition on the physical and electronic properties of carbides and nitrides, together with their relationship to catalytic reactivity [72,73]. Colton et al. observed changes in the X-ray photoelectron valence band spectra for W versus WC, noting that WC has an occupied electronic density of states similar to that of Pt [72], as was initially suggested by Levy and Boudart [71]. It is now well accepted that the insertion of carbon or nitrogen expands the metal lattice leading to changes in bonding, electronic structure, and material properties. These changes are generally described as (1) a "ligand effect" and/or (2) an "ensemble effect" [74,75]. The ligand effect describes the changes in electronic structure, which result from charge transfer (typically from the metal to the nonmetal atom), metal d-orbital mixing with nonmetal s-p states, and increased distance between metal atoms [74]. The ensemble effect involves a change in the number of metal atoms at the surface, as carbides, for example, can be Mo- and C-terminated, which will likely change the catalyst interaction with adsorbates.

The electronic effects result in differences in the d-band density of states for carbides or nitrides when compared to the parent metal, an example of which is shown for Mo and Mo_2C in Figure 1.7 [76]. Under the d-band model, developed by Hammer and Nørskov [77,78,79], materials characterized by a d-band center closer to the Fermi energy (E_f) will be more reactive towards adsorbates than materials with the d-band center further from E_f; typically, there is a linear correlation between adsorbate binding energy and d-band center. Compared to Mo(110), the d-band for Mo_2C is broadened (especially for the carbon-terminated Mo_2C) which shifts the d-band center to a value

further below E_f when compared to Mo(110). Therefore, Mo_2C is expected to be less reactive to adsorbates than Mo(110), a phenomenon that has been confirmed experimentally [80].
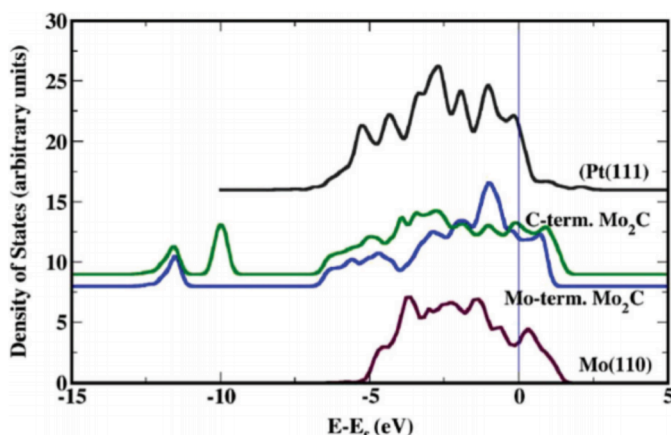
Figure 1.7. d-band density of states for Pt(111), Mo(110), and C and Mo-terminated Mo_2C. Adapted from [76].

Carbides and nitrides have been the focus of numerous studies investigating their applicability as catalysts for a variety of reactions. They have been reported active for thermocatalytic reactions, such as, but not limited to, CO hydrogenation (FTS) [81,82,83], ammonia synthesis [84,85], hydrogenolysis [71,86], hydrodeoxygenation [87], hydrogenation of alkenes and aromatics [88,89], and dehydrogenation [90,91]. In summary, these catalysts exhibited high FTS rates, but poor selectivity; in addition, carbides and nitrides were excellent hydrogenation and dehydrogenation catalysts, exhibiting comparable or higher activity to those of Pt group metal catalysts. These catalysts are also highly active for hydrodeoxygenation, and exhibit reactivity highly dependent on the surface chemistry of the catalyst (e.g., carbide versus oxycarbide surface). Given their high conductivities [64], they have also been employed in electrochemical applications catalyzing reactions such as the hydrogen evolution reaction [92] and methanol oxidation [93,94]. Despite nearly four decades of literature reports

17

detailing the chemistry and catalytic performance of early transition-metal carbides and nitrides, new reports continue to provide valuable information, which is required to further accelerate these catalysts to commercial use.

1.4.2. Early Transition Metal Carbides and Nitrides as Supports for Metals

In addition to their interesting properties and catalytically active phases, early transition metal carbides and nitrides have been reported to be excellent support materials for active metals. Catalytic supports play a critical role with regard to the performance of heterogeneous catalysts. The most important function of the support is typically to facilitate dispersion of the active phase, and high surface areas are beneficial for this purpose. In 1988, Oyama et al. described temperature-programmed reaction syntheses for carbides and nitrides of metals belonging to group IVB-VIB (e.g., Ti, V, Cr, Mo, W), which utilized metal oxides as precursors rather than metals [64,95]. This approach produced materials with surface areas as high as ~190 m^2/g [95]. While both metallic (e.g., Mo) and oxide precursors (e.g., MoO_3) typically begin with very low surface areas (<1 m^2/g), the synthesis procedure results in very different porosities and surface morphologies of the final compound depending on which precursor is used. When using a metallic precursor such as Mo, carbon or nitrogen must penetrate into the metal and expand the lattice; material sintering commonly occurs in this process limiting the material surface area. In contrast, when employing an oxide precursor, carbon or nitrogen essentially replaces the oxygen in the lattice with minimal disruption of the placement of Mo atoms (topotactic exchange). Due to the differences in density between oxides (e.g., MoO_3) and the corresponding carbides or nitrides (e.g., Mo_2C, Mo_2N), a large porous

network is generated since the compound maintains the original external size and shape of the oxide precursor [65,95].

Nitride- and carbide-supported metals have been reported to be active as catalysts for chemical reactions, including, but not limited to, hydrodenitrogenation (HDN) and hydrodesulfurization (HDS) [96,97], selective hydrogenations [98,99], FTS [100,101], methanol steam reforming [102,103], and water–gas shift [104,105], as well as electrochemical reactions such as hydrogen evolution [106,107] and hydrogen oxidation reactions [108]. For most of these studies, the performance of the carbide- or nitride-supported metal catalyst far exceeded the performance of the bare carbide or nitride. One common explanation for the enhanced performance of carbide- and nitride-supported metal catalysts is a strong metal-support interaction leading to synergy between the two constituents, perhaps accompanied by significant electronic changes to the metal and/or support. For example, Rodriguez et al. reported thiophene HDS activities for Au/TiC(001) approximately 40% higher than a conventional Ni/MoS_x catalyst, noting that both bare TiC(001) and Au(111) alone exhibited negligible HDS activity [96]. The enhanced activity was hypothesized to result from cooperative catalysis in the bonding of thiophene as well as dissociation of H_2 to produce the hydrogen required for hydrogenolysis of the C-S bond. In another example, Perret and coworkers observed enhanced hydrogenation rates of p-chloronitrobenzene and m-dinitrobenzene using Au on Mo_2C or Mo_2C/Al_2O_3 when compared to the bare Mo_2C catalysts or Au/Al_2O_3 at equivalent Au loadings [98]. Griboval-Constant, et al. observed drastic differences in FTS rate (~10 times higher) and selectivity (>70% C_5+ versus <15% for WC) by promoting WC with Ru (Ru/WC) [101]. For the electrocatalytic hydrogen evolution

reaction, Esposito et al. noted activities of Pt/WC and Pt/W$_2$C that resembled those of metallic platinum foil, while WC and W$_2$C exhibited significantly lower reaction rates [106,109]. This performance is hypothesized to result from similarities between Pt/WC and bulk Pt.

The Thompson group has also conducted numerous studies utilizing carbides and nitrides as catalytic supports, also observing synergy and strong metal-support interactions. Patt explored the promotion of Mo$_2$C with a variety of metals for the water-gas shift reaction (Figure 1.8) [110]. The Mo$_2$C- and Mo$_2$N-supported Pt catalysts far exceeded the performance of bulk Mo$_2$C as well as the Cu-Zn-Al commercial catalyst. After Patt's initial studies, numerous catalyst formulations were explored utilizing various carbides and nitrides as supports for both water-gas shift [111] and methanol steam reforming [112]. Differences in selectivity and activity, both promotional and deleterious, were observed for the carbide- and nitride-supported metal catalysts studied.
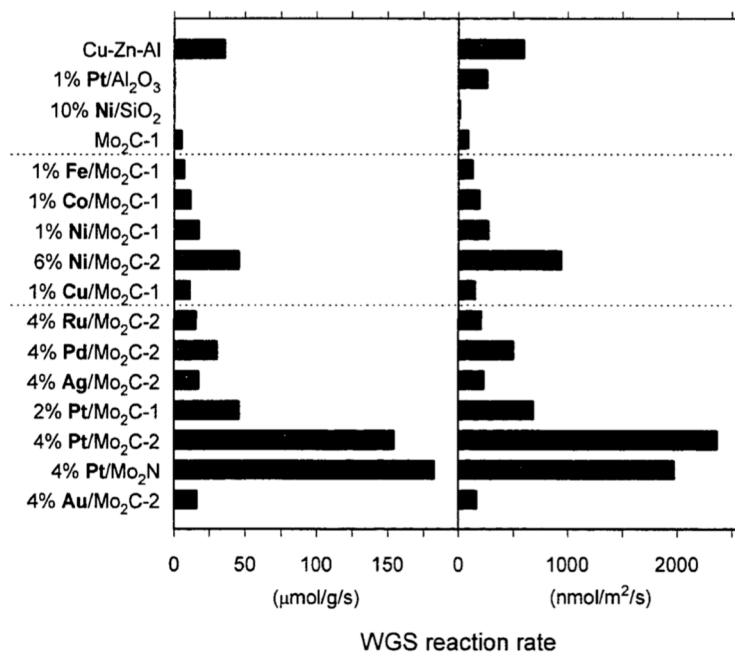
Figure 1.8. Gravimetric (left) and areal (right) water-gas shift rates for the carbide and nitride–supported metal catalysts, pretreated in 15% CH$_4$/H$_4$ at 590°C. Taken from [110].

20

4% Pt/Mo$_2$C exhibited ~10-15 times higher WGS activity relative to bare Mo$_2$C [110]. As a result, Schweitzer et al. studied the effect of Pt-Mo$_2$C metal-support interactions on the water-gas shift performance [105]. Using density functional theory and X-ray absorption spectroscopy, Schweitzer et al. determined that Pt exhibits a strong interaction with Mo$_2$C and forms raft-like (two-dimensional) particles, even at high Pt loadings. This interaction and the resulting excellent Pt dispersion were rationalized by the difference in bond energy between the Pt-Mo$_2$C and Pt-Pt bonds (Pt-Mo$_2$C was ~0.9eV more favorable). Ultimately, the results suggested that the active sites for the WGS reaction were located at the perimeter of the Pt particles (the interface between Pt and Mo$_2$C), perhaps via a bifunctional mechanism. It is possible that Pt domains adsorbed CO, while Mo$_2$C performed water activation, with the reaction to evolve CO$_2$ and H$_2$ occurring at the interface between the two domains [105]. In another study of metal-support interactions in Mo$_2$C systems, Schaidle et al. observed an interesting phenomenon during wet impregnation of metal salts onto Mo$_2$C [113]. Wet impregnation is the synthesis method commonly used by the Thompson group to deposit metals onto carbides and nitrides.   Upon interaction with Mo$_2$C, H$_2$PtCl$_6$, (NH$_3$)$_4$Pd(NO$_3$)$_2$, and Cu(NO$_3$)$_2$ all were spontaneously reduced to their metallic states, while Co(NO$_3$)$_2$ and Fe(NO$_3$)$_3$ remained in their oxidized states. These results indicate strong metal-support interactions occurring not only during catalytic reactions, but also during synthesis. These collective reports detail the impressive performance and unique properties of early transition-metal carbides and nitrides as catalytic supports.

Despite the wealth of knowledge available regarding the fundamental catalytic properties of carbides and nitrides, both as catalysts and catalyst supports, further studies are necessary to advance the use of these materials as catalysts in a commercial setting. In particular, little is known about the active sites of these catalytic materials as well as the cause of synergy from metal-support interactions. Elucidating trends between material properties and reactivity will help develop understanding around these topics, knowledge that can be used to inform the desired catalyst structure for end applications.

1.5.   Organization of the Dissertation and Research Goals

The overall goal of the research presented in this dissertation was to elucidate material property-reactivity relationships for early transition-metal carbides and nitrides with an emphasis on reactions relevant to biomass conversion to transportation fuels. Three main objectives were formulated:

1. Establish relationships between the hydrogen binding sites in early transition-metal carbides and nitrides with regard to the location of hydrogen and the reactivity of hydrogen for hydrogenation reaction.

2. Determine the effect of passivation (controlled oxidation) of Mo_2C prior to the catalyst synthesis for Pt/Mo_2C water-gas shift catalysts. The presence (or absence) of surface redox chemistry between Mo_2C and depositing Pt is expected to play a role in the structure, composition, and reactivity of these materials.

3. Evaluate Mo_2C-supported metal catalysts for Fischer-Tropsch synthesis using high metal loadings of common Fischer-Tropsch and alcohol synthesis active metals (Ru, Co, Fe, Ni, K, Cu).

The dissertation is divided into five chapters as outlined below.

Chapter 1: Introduction

This chapter explores the high level motivation for the catalytic studies presented in this dissertation as they relate to the production of alternative energy fuels. Details regarding the reactions studied (selective hydrogenation of oxygenates, water-gas shift, and Fischer-Tropsch) are presented.

Chapter 2: Reactivity of Hydrogen in Early Transition Metal Carbides and Nitrides

This chapter explores the presence of hydrogen in interstitial (subsurface) sites in early transition-metal carbides and nitrides and then correlates relative interstitial site population (compared to surface sites) to hydrogenation product selectivity. Thermal desorption spectra and density functional theory calculations were employed to determine the location of hydrogen in these materials, while reaction rates and selectivities are reported for materials with different hydrogen populations. Trends were observed between the relative density of interstitial hydrogen and the selectivity towards C=O bond hydrogenation in crotonaldehyde. Extended studies were performed to investigate the population of carbides and nitrides with hydrogen via dehydrogenation reactions.

Chapter 3: Pt-Mo₂C Redox Chemistry and Water-Gas Shift Performance

This chapter describes the presence of surface redox chemistry between Pt and Mo₂C during wet impregnation synthesis, and explores the implications of redox chemistry on catalyst structure and reactivity for the water-gas shift reaction. Results from X-ray photoelectron spectroscopy, X-ray absorption spectroscopy, adsorption studies, scanning electron microscopy, and the water-gas shift reaction collectively

showed the deleterious effects of the passivation layer (absence of redox chemistry) on Pt dispersion and, ultimately, water-gas shift activity.

Chapter 4: Fischer-Tropsch Synthesis over Metal/Mo₂C Catalysts

The research described in this chapter explores the use of Mo_2C-supported metal catalysts with high metal loadings for the Fischer-Tropsch synthesis reaction. Physical and catalytic properties are reported, including surface areas, CO uptakes, and FTS reaction rates and selectivities. Co and Ru, two well-known FTS catalysts, were surprisingly inactive when supported on Mo_2C.

Chapter 5: Understanding the Activity of Mo₂C-supported Ru or Co Catalysts for Fischer-Tropsch Synthesis

Work performed in this chapter investigates the causes of poor performance of Co and Ru metals when deposited on Mo_2C for FTS. The effect of particle size, metal precursor, and reduction conditions are explored as they relate to FTS performance. In addition, characterization of the catalyst surface is performed on Mo_2C- and SiO_2-supported materials for comparison of Mo_2C to a typical FTS catalyst support.

Chapter 6: Summary and Future Outlook

This chapter summarizes key findings from the research and relates these results back to the bigger picture of technologies and catalysts for the production of renewable transportation fuels. Based on the findings reported in this dissertation, extensions of the current research and new research thrusts are proposed.

1.6.   References

[1]   The Outlook for Energy: A View to 2040, ExxonMobil 2013.
[2]   BP Statisical Review of World Energy, BP, June 2015.
[3]   New York Stock Exchange, www.nyse.com. Accessed August 2016

[4]   S.A. Molina-Murillo, C. Rojas. *The Paradigm of Forests and the survival of the Fittest*, CRC Press, Boca Raton, FL, 2015.

[5]   EIA Energy Outlook, 2014.

[6]   A. Demirbas, Energy Sources, Part A, 30 (2008) 1473-1483.

[7]   J. Romm, Energy Policy 34 (2006) 2609-2614.

[8]   "Proposed Renewable Fuel Standards for 2017, and the Biomass-based diesel Volume for 2018." EPA. https://www.epa.gov/renewable-fuel-standard-program/proposed-renewable-fuel-standards-2017-and-biomass-based-diesel. Accessed August 2016.

[9]   Renewable Fuel Standard, U.S. Environmental Protection Agency.

[10]   *Technology Roadmap: Biofuels for Transport*, International Energy Agency, http://www.iea.org/publications/freepublications/publication/biofuels_roadmap_web.pdf, Accessed August 2016.

[11]   S.N. Naik, V.V. Goud, P.K. Rout, A.K. Dalai, Renewable and Sustainable Energy Reviews 14 (2010) 578-597.

[12]   P.S. Nigam, A. Singh, Progress in Energy and Combustion Science 37 (2011) 52-68.

[13]   D.Y.C. Leung, X. Wu, M.K.H. Leung, Appl. Energy 87 (2010) 1083-1095.

[14]   L.R. Lynd, J.H. Cushman, R.J. Nichols, C.E. Wyman, Science 251 (1991) 1318-1323.

[15]   Y. Lin, S. Tanaka, Appl. Microbiology and Biotechnology 69 (2006) 627-742.

[16]   A. Demirbas. Energy Conversion and Management 49 (2008) 125-130.

[17]   R. Sims, M. Taylor, *From 1st- to 2nd-Generation Biofuel Technologies*. International Energy Agency, https://www.iea.org/publications/freepublications/publication/2nd_Biofuel_Gen.pdf, Accessed August 2016.

[18]   M.E. Borges, L. Díaz, Renewable and Sustainable Energy Reviews, 16 (2012) 2839-2849.

[19]   K. Pathak, M.K. Reddy, N.N. Bakhshi, A.K. Dalai, Appl. Cat. A: General 372 (2010) 224-238.

[20]   Z.Y. Zakaria, N.A.S. Amin, J. Linnekoski, Biomass and Bioenergy 55 (2013) 370-385.

[21]   C.A. Mullen, A.A. Boateng, Energy & Fuels 22 (2008) 2104-2109.

[22]   J.H. Marsman, J. Wildschut, F. Mahfud, H.J. Heeres, J. Chromatography A. 1150 (2007) 21

[23]   C.A. Mullen, G.D. Strahan, A.A. Boateng, Energy Fuels, 23 (2009) 2707-2718.

[24]   S. Dasappa, *Transformation of Biomass: Theory to Practice*, First Edition. Ed. Andreas Hornung, John Wiley & Sons, Ltd., 2014.

[25]   H.B. Goyal, D. Seal, R.C. Saxena, Renewable and Sustainable Energy Reviews 12 (2008) 504-517.

[26]   A.V. Bridgewater, Chem. Eng. Journal, 91 (2003) 87-102.

[27]   A.V. Bridgewater, Biomass and Bioenergy 38 (2012) 68-94.

[28]   D.A. Ruddy, J.A. Schaidle, J.R. Ferrell III, J. Wang, L. Moens, J.E. Hensley, Green Chem. 16 (2014) 454-490.

[29]   D. Meier, O. Faix, Bioresource Technology 68 (1999) 71-77.
[30]   A.V. Bridgwater, G.V.C. Peacocke, Renewable and Sustainable Energy Review 4 (2000) 1-73.
[31]   D.A. Ruddy, J.A. Schaidle, J.R. Ferrell III, J. Wang, L. Moens, J.E. Hensley, Green Chem. 16 (2014) 454-490.
[32]   S. Czernik and A. V. Bridgwater, Energy Fuels, 18 (2004) 590.
[33]   C.A. Mullen, A.A. Boateng, Enegy & Fuels, 22 (2008) 2104-2109.
[34]   C. Branca, P. Giudicianni, C. Di Blasi, Ind. Eng. Chem. Res. 42 (2003) 3190-3202.
[35]   C.A. Mullen, G.D. Strahan, A.A. Boateng, Energy & Fuels 23 (2009) 2707-2718.
[36]   A. Dutta, J.A. Schaidle, D. Humbird, F.G. Baddour, A. Sahir, Top. Catal. 59 (2016) 2-18.
[37]   R. Ma, K. Cui, L. Yang, X. Ma, Y. Li, Chem. Commun. 51 (2015) 10299-10301.
[38]   C.J. Chen, W.S. Lee, A. Bhan, Appl. Cat. A: General, 510 (2016) 42-48
[39]   M. Tamura, K. Tokonami, Y. Nakagawa, K. Tomishige, ACS Catal. 6 (2016) 3600-3609.
[40]   J.A. Schaidle, J. Blackburn, C.A. Farberow, C. Nash, K.X. Steirer, J. Clark, D.J. Robichaud, D.A. Ruddy, ACS Catal. 6 (2016) 1181-1197.
[41]   H. Ren, W. Yu, M. Salciccioli, Y. Chen, Y. Huang, K. Xiong, D.G. Vlachos, J.G. Chen, ChemSusChem 6 (2013) 798-801.
[42]   "Syntroleum to deliver bio-based synthetic jet fuel to U.S. Department of Defense." *Biopact*. http://global.mongabay.com/news/bioenergy/2007/07/syntroleum-to-deliver-bio-based.html. Accessed August 2016.
[43]   R. Kothari, D. Buddhi, R.L. Sawhney, Renewable and Sustainable Energy Reviews 12 (2008) 553-563.
[44]   A.K. Rajvanshi, "Biomass Gasification," *Alternative Energy in Agriculture*, Vol. 2, Ed. D. Yogi Goswami, CRC Press, 1986, 83-102.
[45]   J.-P. Lange, Catal. Today. 64 (2001) 3-8.
[46]   M.E. Dry, Catal. Today 71 (2002) 227-241.
[47]   C. Ratnasamy, J.P. Wagner, Catalysis Reviews 51 (2009) 325-440.
[48]   H. Schulz. Appl. Catal. A: General 186 (1999) 3-12.
[49]   D. Leckel, Energy & Fuels, 23 (2009) 2342-2358.
[50]   Sasol, "Sasol Produces 1.5 Billion Barrels of Synthetic Fuel from Coal in Fifty Years," http://www.sasol.com/media-centre/media-releases/sasol-produces-15-billion-barrels-synthetic-fuel-coal-fifty-years, Accessed August 2016.
[51]   S. T. Sie, M. M. G. Senden, H. M. H. Van Wechem, *Catalysis Today* 8 (1991) 371-394.
[52]   Shale Gas Production, *U.S. Energy Information Administration,* https://www.eia.gov/dnav/ng/ng_prod_shalegas_s1_a.htm, Accessed August 2016.
[53]   Davis, B., *Fuel Processing Technology* 71 (2001) 157-166.
[54]   M. Roper, in Catalysis in C1 Chemistry (W. Keim, ed.), Reidel, Dordrecht. 1983, 41-88.

[55]   G.V. Schulz, J. Phys. Chem. 32 (1936) 27.

[56]   P.J. Flory, J. Am. Chem. Soc. 58 (1936) 1877.

[57]   Anderson, R. B. Catalysts for the Fischer-Tropsch Synthesis, Van Nostrand Reinhold, New York, 1956. Vol. 4.

[58]   G. P. Van Der Laan, A. A. C. M. Beenackers, Kinetics and Selectivity of the Fischer-Tropsch Synthesis: A Literature Review, *Catalysis Reviews: Science and Engineering* 41 (1999) 255-318.

[59]   H. Jahangiri, J. Bennett, P. Mahjoubi, K. Wilson, S. Gu, Catal. Sci. Technol. 4 (2014) 2210-2229.

[60]   D.M. Alonso, J.Q. Bond, J.A. Dumesic, Green Chem. 12 (2010) 1493-1513.

[61]   S.K. Hoekman, Renewable Energy 34 (2009) 14-22.

[62]   P.M. Mortensen, J.-D. Grunwaldt, P.A. Jensen, K.G. Knudsen, A.D. Jensen. Appl. Catal. A: General 407 (2011) 1-19.

[63]   D.A. Bulushev, J.R.H. Ross, Catal. Today 171 (2011) 1-13

[64]   Oyama, S. T. Introduction to the chemistry of transition metal carbides and nitrides. In The Chemistry of Transition Metal Carbides and Nitrides; Oyama, S. T., Ed.; Blackie Academic & Professional: London, U.K., 1996.

[65]   S.T. Oyama, Catal. Today 15 (1992) 179-200.

[66]   S. Carenco, D. Portehault, C. Boissière, N. Mézailles, C. Sanchez. Chem. Rev. 113 (2013) 7981-8065.

[67]   L. Brewer, Science, 161(1968) 115

[68]   J.-G. Choi, J.R. Brenner, C.W. Colling, B.G. Demczyk, J.L. Dunning, L.T. Thompson, Catal. Today 15 (1992) 201-222.

[69]   X. Zhao, K.-J. Range, J. Alloys and Compounds 296 (2000) 72-74.

[70]   Wang, S.; Ge, H.; Sun, S.; Zhang, J.; Liu, F.; Wen, X.; Yu, X.; Wang, L.; Zhang, Y.; Xu, H.; Neuefeind, J. C.; Qin, Z.; Chen, C.; Jim, C.; Li, Y.; He, D.; Zhao, Y. J. Am. Chem. Soc. 2015, 137, 4815−4822.

[71]   Levy, R. B.; Boudart, M. Science 1973, 181, 547−549.

[72]   R.J. Colton, J.-T.J. Huang, J.W. Rabalais, Chem. Phys. Letters, 34 (1975) 337-339.

[73]   N.I. Ilchenko, N.P. Chebotareva, N.V. Shvidak. React. Kinet. Catal. Letters 4 (1976) 343-349.

[74]   D.A. Ruddy, J.A. Schaidle, J.R. Ferrell III, J. Wang, L. Moens, J.E. Hensley, Green Chem. 16 (2014) 454-490.

[75]   P. Liu, J.A. Rodriguez, Catal. Letters 91 (2003) 247-252.

[76]   J.R. Kitchin, J.K. Nørskov, M.A. Barteau, J.G. Chen, Catal. Today 150 (2005) 66-73.

[77]   B. Hammer, J.K. Nørskov, Nature, 376 (1995), 238-240

[78]   B. Hammer, J.K. Nørskov, Surface Science, 1995. 343: 211-220

[79]   B. Hammer, Y. Morikawa, J.K. Nørskov, Physical Review Letters, 76 (1996) 2141-2144

[80]   J.G. Chen, Chem. Rev. 96 (1996) 1477-1498.

[81]   I. Kojima, E. Miyazaki, J. Catalysis 89 (1984) 168-171.

[82]   P.M. Patterson, T.K. Das, B.H. Davis, Appl. Cat. A: General 251 (2003) 449-455.

[83]   J.A. Schaidle, L.T. Thompson, J. Catalysis 329 (2015) 325-334.

[84]   R. Kojima, K.-I. Aika, Appl. Cat. A: General 219 (2001) 141-147.

[85]   D.A. King and F. Sebba, J. Catalysis 4 (1965) 430–439.

[86]   G.S. Ranhotra, A.T. Bell, J.A. Reimer, J. Catalysis 108 (1987) 40-49.

[87]   M.M. Sullivan, C.-J. Chen, A. Bhan, Catal. Sci. Tehcnol. 6 (2016) 602.

[88]   J. S. Lee, M. H. Yeom, K. Y. Y. Park, I.-S. Nam, J. S. Chung, Y. G. Kim, S. H. Moon, J. Catalysis, 128 (1991) 126–136.

[89]   M.-L. Frauwallner, F. López-Linares, J. Lara-Romero, C. E. Scott, V. Ali, E. Hernández and P. Pereira-Almao, Appl. Cat. A: General 394 (2011) 62–70.

[90]   M.K. Neylon, S. Choi, H. Kwon, K.E. Curry, L.T. Thompson. Appl. Cat. A: General 183 (1999) 253-265.

[91]   H. Abe, A.T. Bell, J. Catalysis 142 (1993) 430-436.

[92]   H. Vrubel, X. Hu, Angew. Chem. 124 (2012) 12875-12878.

[93]   E.C. Weigert, M.B. Zellner, A.L. Stottlemyer, J.G. Chen, Top. Catal. 46 (2007) 349-357.

[94]   A.L. STottlemyer, E.C. Weigert, J.G. Chen, Ind. Eng. Chem. Res. 50 (2011) 16-22.

[95]   S.T. Oyama, J.C. Schlatter, J.E. Metcalfe, III, J.M. Lambert, Jr. Ind. Eng. Chem. Res. 27 (1988) 1639-1648.

[96]   J.A. Rodriguez, P. Liu, Y. Takahashi, K. Nakamura, F. Viñes, F. Illas, J. Am. Chem. Soc. 131 (2009) 8595–8602.

[97]   M. Lewandowski, A. Szymanska-Kolasa, P. Da Costa, C. Sayag, Catal. Today 119 (2007) 31–34.

[98]   N. Perret, X. Wang, L. Delannoy, C. Potvin, C. Louis, M.A. Keane, J. Catal. 286 (2012) 172–183.

[99]   M. Xiang, D. Li, H. Xiao, J. Zhang, W. Li, B. Zhong, Y. Sun, Catal. Today 131 (2008) 489–495.

[100] A. Griboval-Constant, J. Giraudon, G. Leclercq, L. Leclercq, Appl. Catal., A: General 260 (2004) 35–45.

[101] Griboval-Constant, J. Giraudon, I. Twagishema, G. Leclercq, M.E. Rivas, J. Alvarez, M.J. Pérez-Zurita, M.R. Goldwasser, J. Mol. Catal. A: Chem. 259 (2006) 187–196.

[102] W. Setthapun, S.K. Bej, L.T. Thompson, Top. Catal. 49 (2008) 73–80.

[103] A.C. Lausche, J.A. Schaidle, L.T. Thompson, Appl. Catal., A: General 401 (2011) 29–36.

[104] J.A. Schaidle, A.C. Lausche, L.T. Thompson, J. Catal. 272 (2010) 235–245.

[105] N.M. Schweitzer, J.A. Schaidle, O.K. Ezekoye, X. Pan, S. Linic, L.T. Thompson, J. Am. Chem. Soc. 133 (2011) 2378–2381.

[106] D.V. Esposito, S.T. Hunt, Y.C. Kimmel, J.G. Chen, J. Am. Chem. Soc. 134 (2012) 3025–3033.

[107] I.J. Hsu, Y.C. Kimmel, X. Jiang, B.G. Willis, J.G. Chen, Chem. Commun. 48 (2012) 1063–1065.

[108] R. Venkataraman, H.R. Kunz, J.M. Fenton, J. Electrochem. Soc. 150 (2003) A278–A284.

[109] D.V. Esposito, S.T. Hunt, A.L. Stottlemyer, K.D. Dobson, B.E. McCandless, R.W. Birkmire, J.G. Chen, Angew. Chem. Int. Ed. 49 (2010) 9859-9862.

[110] J.J. Patt, PhD Dissertation, University of Michigan, 2003.

[111] T.E. King, PhD Dissertation, University of Michigan, 2007.

[112] W. Setthapun, S.K. Bej, L.T. Thompson, Top. Catal. 49 (2008) 73-80.

[113] J.A. Schaidle, N.M. Schweitzer, O.T. Ajenifujah, L.T. Thompson. *J. Catalysis* 289 (2012) 210-217.

CHAPTER 2

Reactivity of Hydrogen in Early Transition Metal Carbides and Nitrides

2.1. Introduction

Hydrogenation reactions are of major industrial relevance, particularly in the production of commodity chemicals and fuels. This chapter describes the hydrogen adsorbing sites observed by thermal desorption spectroscopy for various early transition metal carbides and nitrides, the location and nature of these hydrogen sites, and the reactivity of the hydrogen for hydrogenation reactions. As described previously in Chapter 1, early transition-metal carbides and nitrides are formed by inserting carbon or nitrogen into interstitial sites of the metal lattice [1]. These interstitial sites can also be populated by other small atoms like hydrogen (see Figure 2.1 for an example).
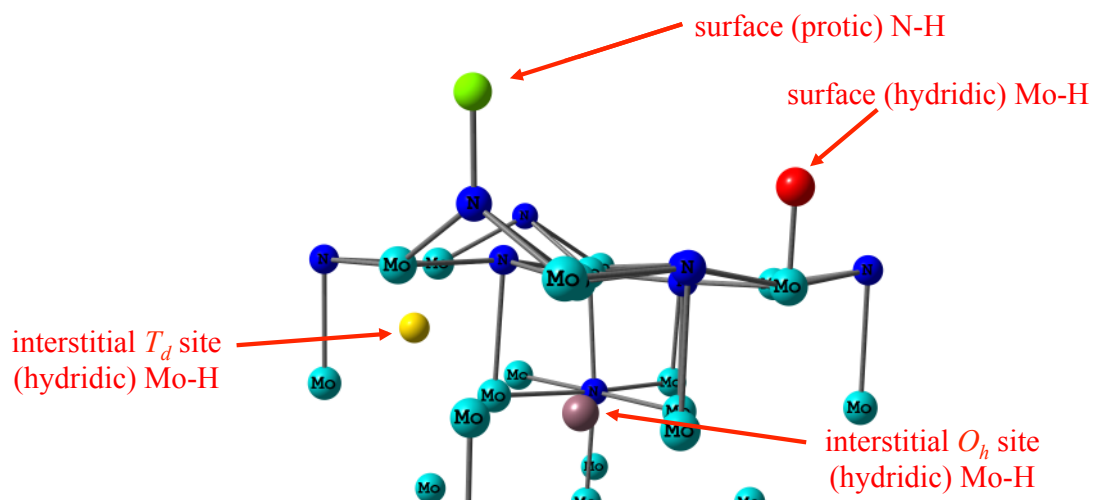
Figure 2.1. Schematic of an Mo_2N unit lattice indicating potential binding sites for hydrogen both on and in the material.

There are many well known examples of hydrogen populating interstitial sites in transition metal lattices, most notably in Pd and Ni [2,3,4,5]. Similarly, in the context of carbides and nitrides, Choi et al. [6] and Zhang et al. [7] reported evidence of subsurface hydrogen in molybdenum nitride (γ-Mo$_2$N) based on results from thermal desorption experiments. More recently, Pande et al. characterized hydrogen in γ-Mo$_2$N, concluding that hydrogen can be inserted into and extracted from interstitial sites in the lattice as the materials were electrochemically cycled [8]. This observation was based on the reduced intensity of the Mo-Mo multiple scattering peaks at certain potentials using in situ X-ray absorption spectroscopy (Figure 2.2). This decrease in intensity was hypothesized to result from hydrogen insertion into interstitial octahedral sites. Very little is known about the reactivity of the different hydrogen species associated with carbides and nitrides. This chapter describes the hydrogen adsorbing sites observed by thermal desorption spectroscopy for early transition metal carbides and nitrides, the location and nature of these hydrogen sites, and the reactivity of the hydrogen for hydrogenation reactions.
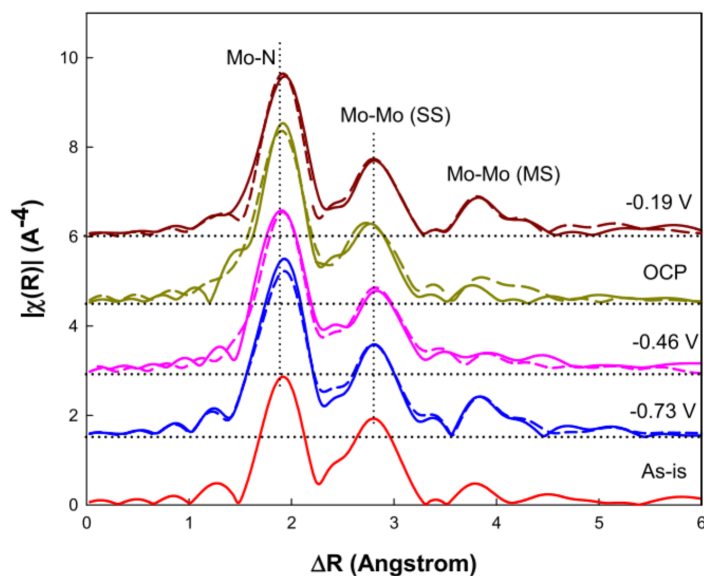
Figure 2.2. Fourier transforms of the EXAFS spectra (Mo K) for Mo$_2$N as-synthesized and at specified potentials simulating electrochemical cycling. Taken from [8].

These interstitial or subsurface hydrogen could indirectly and/or directly affect the catalytic properties of nitrides and carbides, perhaps via a hydrogen-based version of the Mars-van Krevelen-type mechanism [9,10]. For example, reports by Daley et al. showed that subsurface hydrogen hydrogenated ethylene on a Ni surface while surface hydrogen was inactive for this reaction [11]. The reaction barrier for subsurface hydrogen was lower than that for hydrogen on the surface due to the adsorption geometry of ethylene. Palladium is also known to absorb significant quantities of hydrogen [12]. Shirai et al. compared the reactivity of hydrogen diffusing through a palladium membrane (surface and subsurface) and hydrogen was predominantly on the surface for thiophene hydrodesulfurization (HDS) [13]. The surface and subsurface materials possessed higher activities than the materials with hydrogen present solely on the surface. Oliveira et al. recently implicated subsurface hydrogen as contributing to the delayed deactivation of Mo_2C during benzene hydrogenation [14]. In this work, theoretical calculations indicated that hydrogen intercalation into Mo_2C is thermodynamically feasible, but only when accompanied by hydrogen adsorption on the surface. They hypothesized that subsurface hydrogen diffused to the surface after hydrogen on the surface was depleted. That being said, the authors did not postulate a possible location of hydrogen in the Mo_2C unit lattice. While there is definitive experimental and computational evidence for the presence of subsurface hydrogen in early transition metal nitrides and carbides, very little is known about the behavior of this type of hydrogen in catalytic reactions [10-14].

In this work, the hydrogen sites associated with a variety of carbides and nitrides (Mo, W, V, Nb, and Ti-based) were initially screened using thermal desorption spectroscopy. Based on our results as well as literature reports detailing hydrogen

desorption from Mo_2N [6,7] and the potential for subsurface hydrogen [6,8], initial work explored the location and reactivity of hydrogen sites on or in Mo_2N. The binding of hydrogen was first probed for Mo_2N using thermal desorption spectroscopy to characterize both the number and character of hydrogen sites. Density functional theory calculations and inelastic neutron scattering were used to determine the most likely location of hydrogen associated with Mo_2N. In addition, the reactivity of the hydrogen associated with these materials was probed using 2-buten-1-al (also known as crotonaldehyde), a highly reactive α,β-unsaturated aldehyde. The selective hydrogenation of α,β-unsaturated aldehydes like crotonaldehyde (CA) is of great interest, particularly for the conversion of biomass to chemicals and fuels [15]. Key correlations were drawn between product selectivity and the relative population of H-binding sites. Work was conducted to elucidate the reaction pathway for crotonaldehyde hydrogenation over hydrogenated Mo_2N catalysts.

With initial studies detailing trends in the reactivity of hydrogen in Mo_2N as a foundation, this study was extended in 2 ways: (1) exploring the reactivity of hydrogen in other interesting nitrides (W_2N, VN) and (2) investigating the use of other hydrogen sources to populate the hydrogen sites, such as hydrocarbons or ammonia. W_2N and VN demonstrated multiple desorption peaks suggesting the presence of more than one hydrogen adsorption site. These adsorption sites could also lend to differences in reactivity towards crotonaldehyde. Another study investigated the possibility of using alternative hydrogen sources, such as hydrocarbons, to populate the hydrogen sites in these materials through substrate dehydrogenation. After use in dehydrogenation of

model substrates at elevated temperatures, the resulting catalysts were analyzed by thermal desorption spectroscopy to measure the extent of hydrogen site population.

2.2 Experimental Methods

2.2.1. Catalyst Synthesis

The early transition metal (Mo, W, V, Nb) carbides and nitrides studied were synthesized via temperature-programmed reaction methods previously reported (methods shown in Table 2.1) [16,17]. TiC and TiN catalysts were synthesized using yet unpublished methods [18]. TiC was synthesized using the maximum temperature possible for the current equipment set up (1100°C), and was not optimized. All precursors (ammonium paramolybdate (AM); tungsten trioxide (WO_3); vanadium pentoxide (V_2O_5); niobium pentoxide (Nb_2O_5); titanium dioxide (TiO_2)) were first crushed and sieved to a particle size range of 125 – 250 μm. The precursor was loaded into a quartz flow-through reactor, supported by a bed of quartz wool, and secured in a vertical tube furnace. The precursor was heated from room temperature to the first temperature (T_1), at a ramp rate of β_1 under flow of either H_2, 15% CH_4/H_2 or NH_3. The temperature was then held for a specified soak time or increased further at a different ramp rate (β_2 and β_3). For example, to synthesize β-Mo_2C, ~1.3 g of AM was heated in 15% CH_4/H_2 first from room temperature to 200°C in 17 minutes. After reaching 200°C, the material was heated to 590°C in 6.5 hours and held at 590°C for 2 hours. It should be noted that for α,β-Mo_2C the gas was changed from H_2 to 15% CH_4/H_2 when the reactor began heating from 350°C to 590°C.

Following reaction, the material was cooled to room temperature by removal of the reactor from the furnace. When the reactor cooled to below 30 °C, the material was

34

exposed to 1 % O_2/He at 20 mL min^{-1} for at least five hours to passivate the surface and prevent bulk oxidation upon exposure to air. All of the resulting materials were stored under vacuum or in an argon-filled glove box to limit additional exposure to oxygen.

Table 2.1. Protocols used to synthesize the investigated carbides and nitrides

Parent Metal	Material	Precursor	Precursor Weight (g)	Synthesis Gas	Flow rate (mL/min)	T_1 (°C)	$t_{1,ramp}$ (min)	β_1 (K/min)	$t_{1,soak}$ (min)	T_2	$t_{2,ramp}$ (min)	β_2 (K/min)	$t_{2,soak}$ (min)	T_3	$t_{3,ramp}$ (min)	β_3 (K/min)	$t_{3,soak}$ (min)
Mo	β-Mo$_2$C	AM	1.3	15% CH$_4$/H$_2$	250	200	17	10.29	0.00	590	390	1.00	120	-	-	-	-
	α,β-Mo$_2$C	AM	1.3	H$_2$ then 15% CH$_4$/H$_2$	400	350	70	4.64	720	590	90	2.67	120	-	-	-	-
	γ-Mo$_2$N	AM	1.5	NH$_3$	400	350	33	9.85	0	450	150	0.67	0	700	150	1.67	60
W	β-W$_2$C	WO$_3$	1.1	15% CH$_4$/H$_2$	250	200	17	13.24	0	650	450	1.00	300	-	-	-	-
	W$_2$N	WO$_3$	1.3	NH$_3$	360	270	20	12.25	0	600	660	0.50	180	-	-	-	-
	WC	WO$_3$	1.0	15% CH$_4$/H$_2$	400	200	17	10.29	0	850	650	1.00	60	-	-	-	-
	WC$_{1-x}$	WO$_3$	1.0	15% CH$_4$/H$_2$	250	200	17	10.29	0	750	550	1.00	60	-	-	-	-
V	VC	V$_2$O$_5$	0.4	15% CH$_4$/H$_2$	800	900	88	9.94	120	-	-	-	-	-	-	-	-
	VN	V$_2$O$_5$	0.5	NH$_3$	1100	750	157	4.62	60	-	-	-	-	-	-	-	-
Nb	NbC	Nb$_2$O$_5$	0.4	15% CH$_4$/H$_2$	800	900	88	9.94	120	-	-	-	-	-	-	-	-
	NbN	Nb$_2$O$_5$	0.5	NH$_3$	600	800	775	1.00	300	-	-	-	-	-	-	-	-
Ti	TiC	TiO$_2$	0.5	15% CH$_4$/H$_2$	400	1100	1075	1.00	60	-	-	-	-	-	-	-	-
	TiN	TiO$_2$	0.5	NH$_3$	450	300	30	9.17	0	1000	750	0.93	60	-	-	-	-

2.2.2. Catalyst Characterization

2.2.2.1. X-ray Powder Diffraction

The crystal structure of the synthesized catalysts was determined via X-ray powder diffraction. Diffraction patterns were collected on a Rigaku Miniflex X-ray diffractometer employing a Cu Kα X-ray source and a Ni filter. Patterns were obtained in a 2θ range of 10° to 90° at a scan rate of 5°/min and a 0.01° step size unless otherwise specified. Patterns were analyzed using JADE software and compared to standards from the International Centre for Diffraction Data (ICDD) database.

2.2.2.2. N$_2$ Physisorption Measurements

Material surface areas were calculated using the Brunauer-Emmett-Teller (BET) method applied to a N$_2$ physisorption isotherm. A brief description of the experiment follows. First, the empty tube weight was measured and recorded. The material in the tube was then degassed by first heating the material to 350°C under vacuum (<5 mm Hg)

for 4 hr. The tube was measured post-degas, catalyst included. The tube was then transferred to the analysis port and exposed to discrete nitrogen partial pressures relative to the saturation pressure. Surface areas were calculated by applying the BET method [19]. Pore size distributions were calculated from the nitrogen isotherm by applying the Barrett-Joyner-Halenda (BJH) method for mesopores [20] and the Horvath-Kawazoe (HK) method for micropores [21].

2.2.2.3. H_2 Temperature-Programmed Reduction

Hydrogen temperature-programmed reductions (H_2-TPRs) were conducted on a Micromeritics Autochem 2920, equipped with a thermal conductivity detector (TCD) and a Pfeiffer Vacuum Quadstar GSD-301 Mass Spectrometer (MS). Approximately 0.1g was supported on a quartz wool plug in the quartz U-tube reactor in each H_2-TPR experiment. Prior to reduction, the material surface was purge by flowing He (70 mL/min) over the surface at 200°C for 2 hours. The reactor was then cooled to room temperature and the gas was subsequently switched to 10% H_2/Ar flow (70 mL/min). The reactor temperature was then heated at a constant rate (20°C/min) from ~30°C to 800°C while recording the spectra with both the TCD and MS. The spectra were correlated to the heat rate to obtain intensity vs. temperature plots. A salt-ice bath was used as a downstream condenser before the detectors to remove the water produced during reduction for more accurate analysis.

2.2.2.4. H_2 Temperature-Programmed Desorption

Thermal desorption experiments were conducted using a Micromeritics Autochem 2920 equipped with a thermal conductivity detector and a Pfeiffer Vacuum Quadstar GSD-301 Mass Spectrometer. To obtain the thermal desorption spectra in a typical run,

approximately 0.1g of the passivated catalyst was loaded into a U-shaped quartz tube reactor, supported on a bed of quartz wool. The catalyst was heated in 10 % H_2/Ar (70 mL min^{-1}) to 500°C at 15°C min^{-1} and held at this temperature for 0.5 hours. The material was then cooled to 35°C (15°C min^{-1}) and held at 35 °C in flowing 10 % H_2/Ar (70 mL min^{-1}) for 1 hour. The gas was switched to He (70 mL min^{-1}) and the material was allowed to equilibrate for 0.5 hours. The material was then heated to 500°C at 15°C min^{-1} to desorb the hydrogen. The final desorption temperature was limited based on the observed decomposition during reduction as illustrated by N_2 (m/z = 28) or CH_4 (m/z = 15, to avoid interference from water fragments) release. Upon reaching 500°C, the material was cooled to room temperature in He. This initial reduction/desorption procedure, which is designed to remove the passivation layer, was performed prior to all subsequent treatments including hydrogen population.

To populate the material with hydrogen, the material was heated in 10% H_2/Ar (70 mL min^{-1}) to the desired temperature (35-500 °C) at 15°C min^{-1}, held at this temperature for 0.5 hours then quickly cooled to room temperature. Materials populated with hydrogen will be referred to as TMN-H_x (e.g., Mo_2N-H_x). The quantity and character of hydrogen was determined by heating the material in He (70 mL min^{-1}) to 800°C at 15°C min^{-1} while recording ion currents at m/z values of 2 (H_2), 17 (NH_3), 18 (H_2O), 28 (N_2), and 32 (O_2). The H_2 signal was calibrated before each experiment to adjust for changes in the mass spectrometer vacuum pressure. The method described by Falconer and Madix [22] was used to determine the desorption energies of the hydrogen sites. Heating rates (β) during desorption were varied between 3 and 90°C min^{-1}. The densities of hydrogen in the various sites were determined by deconvoluting the TPD

spectra into, for simplicity, a series of Gaussian peaks and integrating the areas. The optimal heat treatment conditions varied from material to material based on the reduction temperature observed in the H_2-TPR for removal of the passivation layer and the observed decomposition at higher temperatures. Variation in conditions will be expressed in the results section for each material. For the initial screening of H_2 desorption sites for all of the materials, the materials were reduced at 500°C for 0.5 h followed by the TPD in He.

2.2.2.5. Scanning Electron Microscopy

Scanning electron micrographs of the catalysts were obtained using FEI Nova Nanolab Dualbeam (FIB/SEM) located in the Michigan Center for Materials Characterization at the University of Michigan. The materials were supported on sample holders using copper tape and were gold sputter coated to improve conductivity. Elemental analyses of specific micrographs were obtained using Energy Dispersive X-ray Spectroscopy (EDX).

2.2.2.6. Crotonaldehyde Hydrogenation

The materials (in this case, Mo_2N, W_2N, VN, and MoC_{1-x}) were pretreated and populated with hydrogen using the same preparation procedures to those used for the H_2-Temperature Programmed Desorption experiments (Section 2.2.2.4 above). The only differences in the process were the batch size (900-1100 mg vs. 100 mg catalyst) and the apparatus used for the pretreatment/H_2 population protocol. A larger initial batch size was used in order to allow for (1) multiple reaction times or temperatures, (2) replicates of the batch reactions for error analysis, and (3) temperature desorption spectra for determination of the relative site density of the hydrogen sites. At 900-1100 mg, the flow

rate of 10% H_2/Ar and He were adjusted in order to maintain a gas hourly space velocity (GHSV, hr^{-1}) consistent with the experiments conducted on the AutoChem 2920. The apparatus used was a miniaturized version of the synthesis reactor used to synthesize the catalysts, described in Section 2.2.1. The apparatus utilizes an 8-inch OD, 8-inch long clam-shell furnace obtained from Applied Test Systems with a maximum temperature rating of 900°C. A 16 inch quartz tube reactor with a frit for supporting quartz wool and the catalyst bed was used. The tube was secured in place using Swagelok ultra-torr fittings and o-rings. Swagelok ball valves were attached to the ends of the ultra-torr fittings in order to prevent the catalyst from air exposure during transfer steps.

Following pretreatment and H_2 population of the materials (different conditions for each material and desired site population), the materials in the reactor were transferred into an argon glove box without exposure to air. Approximately 8 x 100 mg of the γ-Mo_2N-H_x material (~30-40 μmol H_2 per 100 mg) were weighed out and placed into vials. Approximately 100 mg was loaded into the 2920 AutoChem quartz U-tube reactor for TPD analysis and determination of relative site density. To verify that the catalyst was not reoxidized (not exposed to oxygen during this process), approximately 1 mg of material was removed from the glove box. A properly handled material remained highly pyrophoric when exposed to air. The 8 sealed vials of catalyst were transferred to an oxygen-free, water-tolerant N_2 flow through glove box. In this glove box, 100 mg was transferred from the vials into 1.4 mL Swagelok batch reactors. Each reactor was then charged with 1.25 mL of a stock solution containing 30.6 mL ethanol, 0.02 mL crotonaldehyde (~10 μmol per 1.25 mL) and 0.05 mL decane (internal standard, ~10 μmol per 1.25 mL). Ethanol was chosen as the solvent given the literature showing high

activity in alcohol solvents (ethanol, isopropanol) [23,24]. For the experiments aimed at elucidating the reaction pathway, crotonaldehyde was replaced with crotyl alcohol or butyraldehyde at 10 μmol per 1.25 mL. The batch reactors were sealed in the glove box. The headspace contained N_2 at 1 atm (at room temperature). The reactors were placed in a 40-70°C sandbath (Techne Calibration) for 1-3 hr. Subsequently the reactors were removed from the sand bath and the liquid products were removed and the contents were filtered (Fisher, Sterile Nylon filters, 0.2 μm pore size) for analysis. Product analysis was done by gas chromatography (GC). GC analysis was performed on a Varian GC-450 equipped with an flame ionization detector (FID) and autosampler. Product separation was performed using either a Porabond Q or DB-WAX column.

Some reactions were run with a H_2 atmosphere (at 10 atm) as opposed to 1 atm N_2 in order to compare the reactivity of Mo_2N-H_x systems where the material was prepopulated with hydrogen or where the hydrogen dissolves into the solvent from the gaseous headspace and then reacts over the catalyst. The CA/decane/ethanol reaction mixture was added to the batch reactor and the reactor was sealed in the N_2 glove box. Instead of a Swagelok cap, however, a fitting equipped with a tube and high-pressure valve was used. The headspace was evacuated and filled with hydrogen at 10 atmospheres five times to displace the nitrogen headspace. The reaction was then conducted as usual for 1 hr at 70°C. The reaction work-up was repeated based on the description immediately above. Typical liquid-phase reactions are conducted with a hydrogen headspace and an unpopulated catalyst [23,24].

Reactant conversions were calculated based on the disappearance of crotonaldehyde relative to the initial concentration; these values are based on the GC

peak areas obtained. Mass balance closure was monitored by comparing the moles of products (both hydrogenation products and acetals) formed to the moles of crotonaldehyde consumed. Product selectivities were calculated by dividing the moles of a particular product by the moles of all products generated.

2.2.2.7. Dehydrogenation Reactions

2.2.2.7.1. Temperature-Programmed Reactions (TPRxn)

The dehydrogenation of *N*-methylpyrrolidine to *N*-methylpyrrole was performed via TPRxn on the Micromeritics Autochem 2920 instrument previously discussed. Pyrroles have relevance in pharmaceutical, agrochemical, and electronic applications and one synthesis route is through the dehydrogenation of pyrrolidines [25]. Approximately 0.1g of the passivated catalyst was loaded into a U-shaped quartz tube reactor, supported on a bed of quartz wool. The material was pretreated using the same preparation procedures to those used for the thermal desorption spectroscopy experiments (Section 2.2.2.4 above). The materials used in the TPRxn were purged of bound hydrogen unless otherwise stated. Following pretreatment and purging of the surface, the material was exposed to a mixture of *N*-methylpyrrolidine in He at 50 mL/min. The *N*-methylpyrrolidine/He mixture was generated using a bubble saturator at -20°C. After allowing the system to equilibrate, as indicated by a stable TCD signal, the catalyst bed was heated from 30°C to 500°C at 15 K/min. Throughout the heating, the following mass-to-charge values were recorded by the mass spectrometer: 2 (H_2), 14 (N), 16 (NH_2, O), 17 (NH_3, OH), 18 (H_2O), 28 (CO, N_2), 57 (*N*-methylpyrrolidine), 78 (*N*-methylpyrrole), 81 (*N*-methylpyrrole), and 85 (*N*-methylpyrrolidine). Upon reaching 500°C, the material was cooled to RT; the gas was switched to He at 70 mL/min after

reaching RT. The material was heated in He at 15 K/min to 800°C while monitoring the same fragmentation specifications in the mass spectrometer to afford a thermal desorption spectrum. These H_2-TPD spectra were compared to those for materials treated using gaseous H_2 or purged.

2.2.2.7.2.   Batch Reactions

For batch dehydrogenation reactions, the apparatus and experimental procedure were identical to those used in the crotonaldehyde hydrogenation experiments (Section 2.2.2.6) with the only difference being that a purged surface was used for reaction in this case as opposed to a hydrogenated surface. Different substrate/solvent combinations were used for the reactions, including 1-butanol, 1-phenylethanol, and 9,10-dihydroanthracene, as well as ethanol, hexanes, and toluene solvents. Product analysis was again performed on a Varian GC-450 equipped with an FID, autosampler, and 1177 injector. Product separation was performed using a DB-WAX column.

2.2.2.8.   Inelastic Neutron Scattering and Density Functional Theory
Calculations

This work was performed in collaboration with Professor James Mayer and Dr. Elizabeth Mader from the Chemistry Department at Yale University as well as Professor Thomas Cundari and Dr. Daniel Pardue from the Chemistry department at the University of North Texas through the NSF phase II center, Center for Enabling New Technologies Through Catalysis. Density functional theory (DFT) calculations performed at the University of North Texas and Inelastic Neutron Scattering (INS) results obtained at the TOSCA beamline at Rutherford Appleton National Laboratory will be discussed in the results and discussion sections to provide a greater understanding of the location of the

hydrogen in these materials as well as the energetics for hydrogen adsorption and reaction. These results were obtained and analyzed by Dr. Daniel Pardue (DFT) and Dr. Elizabeth Mader (INS), and discussed together in an effort to greater understand the catalyst systems.

2.2.2.8.1.   Inelastic Neutron Scattering (INS)

Two Mo_2N samples were prepared and stored in Ar for analysis at the Rutherford Appleton Laboratory's ISIS synchroton source. Samples of γ-Mo_2N and γ-Mo_2N-H_X (2.7 g each) were characterized, the latter containing approximately equal population of surface and subsurface hydrogen sites (*vide infra*). The INS data was obtained at the TOSCA beamline [26]. Each sample was loaded into an aluminum foil sachet inside a glovebox and smoothed to an even layer. The sachet was placed between two aluminum plates, one with a small inset (4 cm x 4.5 cm x 1 mm), sealed with In wire (dia. = 1 mm) to prevent exposure to air, and screwed together. The sample was then removed from the glovebox, mounted on a centering stick and lowered into the cryostat. Spectra were collected at 10 K for 24 hours. The data was statistically averaged in Mantid [27] and normalized by total area. A binomial smoothing algorithm with a smoothing factor of 5 was applied using Igor Pro [28]. Simulation of the INS spectra was accomplished using A-Climax [29] from the VASP calculations detailed below; no scaling factor was applied to the frequencies.

2.2.2.8.2.   Computational Simulations

The geometric and electronic structures of the various hydrogen species bound on and in γ-Mo_2N coordination were calculated using the Vienna ab Initio Simulation Package (VASP) code [30,31,32]. Periodic boundary conditions along with the repeated

slab method were employed. A seven-layer slab model (with the atoms in the sixth and seventh layers frozen) was used. Ultrasoft pseudopotentials with the applied projector-augmented wave (PAW) [33] method as provided by VASP were used to describe the inner core of all atoms. The PBE exchange-correlation GGA functional was employed [34]. A kinetic energy cutoff 400 eV and a 1 x 3 x 3 Monkhorst-Pack [35] k-point mesh was used for the super cell after tests of several cutoffs and mesh sizes. All reported energies are internal energies (ΔE) at 0 K.

2.3. Results

2.3.1. Materials Screening and Hydrogen Sites

One of the goals of this work was to screen various early transition metal carbides and nitrides for two key characteristics: (1) number and type of hydrogen desorption sites and (2) hydrogen desorption temperature, which can be correlated to hydrogen binding strength. By evaluating these two characteristics, the location of hydrogen sites on or in the catalyst could be initially hypothesized and a small group of materials would then be selected for further investigation.

X-ray diffraction (XRD) patterns for the various molybdenum, tungsten, vanadium, niobium, and titanium-based catalysts can be found in Figure 2.3. The XRD patterns for the Mo, W, V, and Nb materials all match the expected diffraction patterns for the desired crystal structures. Under the synthesis conditions used, the resulting TiC was a mixed phase, containing ~87% Ti_2O_3 and ~13% TiC based on weighted whole pattern fitting using the JADE software. Given equipment constraints, the synthesis temperature was not increased above 1100°C for the synthesis of TiC and thus, pure phase TiC was not synthesized. Apparent from the diffraction patterns, many of these

metal carbides are isostructural with their metal nitrides, with face centered cubic (FCC) being the most common crystal structure. The only pure-phase materials studied here that deviated from the FCC crystal structure were Mo_2C and W_2C, which exhibited a distorted orthorhombic structure, very close to hexagonal close-packed (HCP).
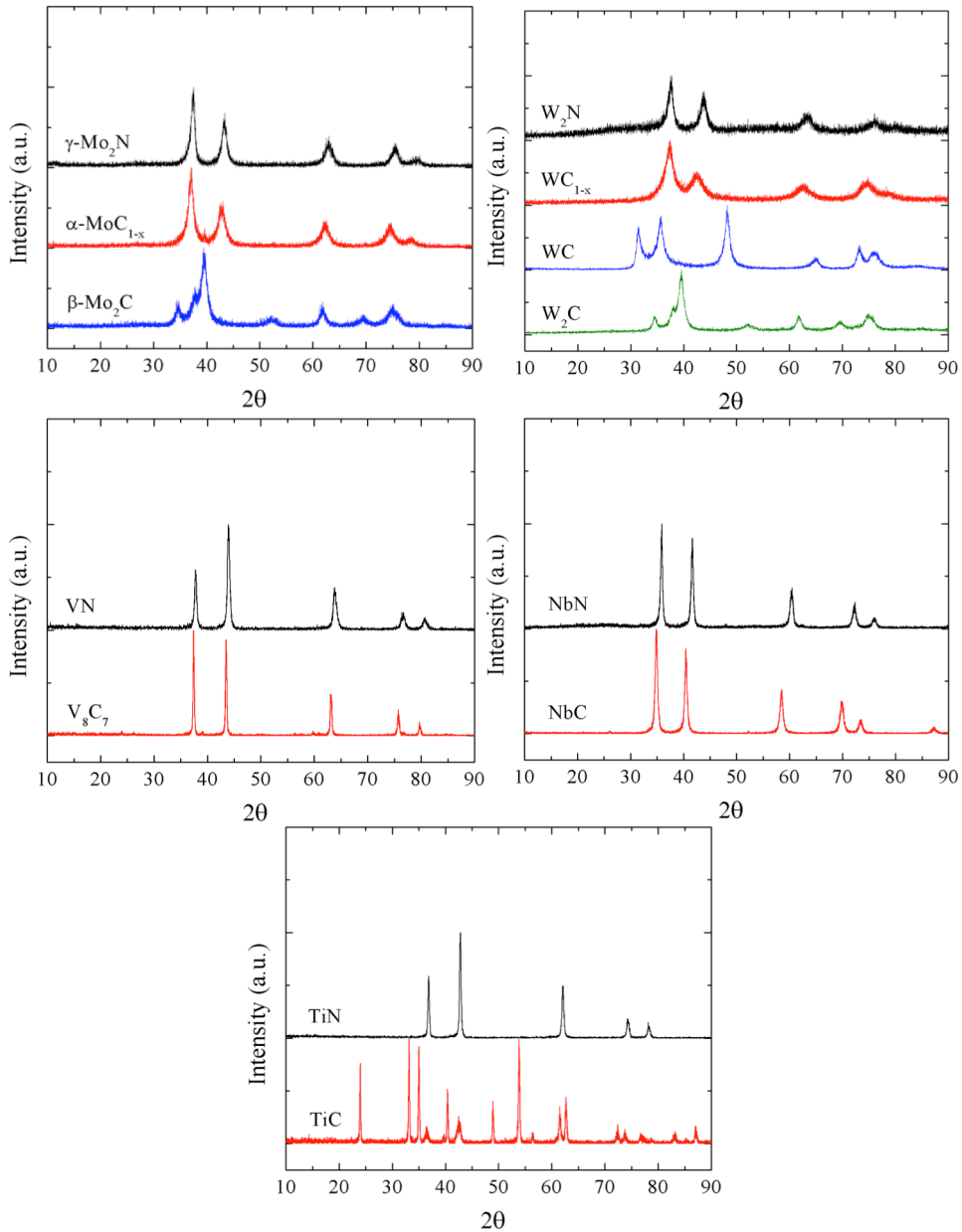
Figure 2.3. X-ray diffraction patterns for the Mo, W, V, Nb, and Ti-based materials studied. Scan rate was set to 5°C min^{-1} with a step size of 0.02° over a 2θ range of 10 to

90°. All diffraction patterns were normalized to the intensity of the largest peak for plotting purposes.

The number and type of hydrogen binding sites were initially screened using H_2 temperature-programmed desorption (recorded by monitoring the m/z = 2 signal) following reduction in 10% H_2/Ar at 500°C for 0.5 h. A summary of the hydrogen uptake and hydrogen stoichiometry can be found in Table 2.2. The thermal desorption spectra for all the materials studied are shown in Figure 2.4 as weight-normalized spectra. Significant hydrogen uptake and desorption were observed for both the nitrides and carbides of Mo, W, and V, while NbC was the only material that adsorbed substantial hydrogen out of the Nb and Ti-based materials.

While the desorption spectra differed for every material analyzed, some trends could be drawn across carbides vs. nitrides and metal:nonmetal stoichiometry. One dominant low-temperature desorption peak was commonly observed for carbides, likely corresponding to a weakly bound surface hydrogen. Though carbides exhibited one main desorption peak, the desorption temperatures and minor desorption peaks differed for each material.

For example, comparing the FCC tungsten and molybdenum carbides to their HCP structural counterpart, hydrogen was found to desorb at higher temperatures (350-500°C) with quite a few desorption shoulders at higher temperatures. Also, comparing the spectra for W_2C and WC, two tungsten carbides differing only in the metal:nonmetal stoichiometry, two low temperature (96 and 192°C) desorption peaks were observed for W_2C and only one higher temperature (334°C) desorption peak for WC, indicating that the higher concentration of carbon in the lattice affects the hydrogen adsorption. This

result can be explained by either changes in the electronic structure of the material or consumption of hydrogen binding sites by the increased molar concentration of carbon in the lattice.

Of greater interest, the nitrides were found to uptake a substantial amount of hydrogen, and Mo_2N, W_2N, and VN all showed two very distinct desorption peaks. These two desorption peaks can likely be as associated with two distinct hydrogen binding sites. As these materials have two distinct sites, Mo_2N, W_2N, and VN were selected for further analysis aimed at understanding the location and chemistry of the two observed sites as well as the effect of these sites on hydrogenation reactions. Building on available literature on hydrogen desorption from Mo_2N [6,7] and the potential for subsurface hydrogen [6,8], initial work explored the hydrogen sites for Mo_2N.

Table 2.2. Crystal structure, BET surface area, and hydrogen uptake capacity of the Mo, W, V, Nb, and Ti-based materials studied.

Parent Metal	Catalyst	Surface Area $(m^2/g)^a$	Hydrogen Uptake $(umol/g)^{b,c}$	Areal Hydrogen Uptake $(umol/m^2)^b$	Stoichiometry (Catalyst)-H_x
Mo	Mo_2C	71	162	2.28	$Mo_2C-H_{0.033}$
	Mo_2N	93	310	3.33	$Mo_2N-H_{0.064}$
	MoC_{1-x}	108	256	2.37	$MoC_{1-x}-H_{0.052}$
W	W_2C	21	47	2.24	$W_2C-H_{0.013}$
	W_2N	88	528	6.00	$W_2N-H_{0.202}$
	WC	22	65	2.95	$WC-H_{0.018}$
	WC_{1-x}	100	108	1.08	$WC_{1-x}-H_{0.041}$
V	V_8C_7	12	3	0.25	$V_8C_7-H_{0.000}$
	VN	43	83	1.93	$VN-H_{0.005}$
Nb	NbC	27	5	0.20	$NbC-H_{0.001}$
	NbN	17	0	0	$NbN-H_{0.000}$
Ti	TiC	<1	0	0	$TiC-H_{0.000}$
	TiN	24	0	0	$TiN-H_{0.000}$

[a] Surface area was calculated by applying the BET method to a N_2 physisorption isotherm
[b] Hydrogen uptake capacities were obtained by integrating the area under the thermal desorption spectra and using a mass spectrometer response factor for H_2 obtained at the beginning and end of each TPD experiment to convert the area to moles. The moles were normalized to catalyst weight or surface area.
[c] The error associated with the gravimetric hydrogen uptake is ±10% based on experimental repeats.
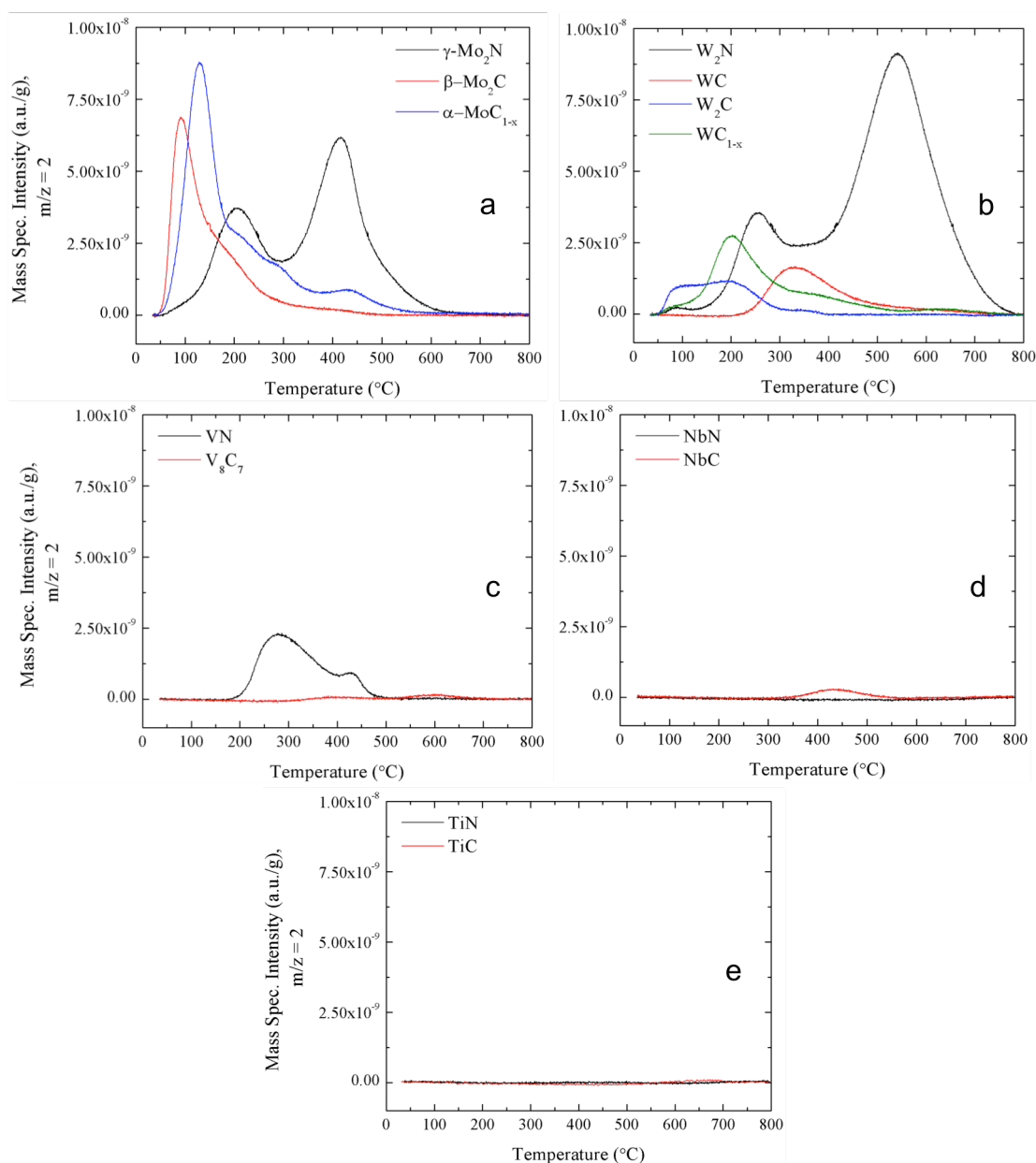
Figure 2.4. Weight-normalized H_2-TPD spectra for the (a) Mo, (b) W, (c) V, (d) Nb, and (e) Ti-based catalysts following reduction in 10% H_2/Ar at 500°C for 0.5 h. Spectra were taken by recording the *m/z* 2 (H_2) signal while heating the sample to 800°C at 15°C/min.

2.3.2. Hydrogen Adsorption on Molybdenum Nitride

Hydrogen temperature-programmed reductions (TPR) were used to determine the conditions for both removal of the passivation layer from Mo_2N and then adsorption of hydrogen on the unpassivated catalyst. The TPR results used to determine the

temperature at which the passivation layer can be removed, as well as to determine the stability of Mo_2N in hydrogen at high temperatures is shown in Figure 2.5. A large reduction peak is observed at ~400°C with a shoulder at ~500°C. The peak observed at 400°C is likely due to the formation of water as a result of the reduction of the passivation layer, while the 500°C peak can be attributed to formation of NH_3, perhaps by removal of surface nitrogen through hydrogenation. At temperatures above 600°C, the material is likely decomposing, as indicated by the formation of nitrogen (m/z = 28). As indicated, the reduction temperature of 500°C is sufficient for reduction of the passivation layer without causing bulk decomposition of the nitride to form N_2. As a result, in all steps, temperatures were restricted to 500°C or below regardless of the gas. The passivation layer on Mo_2N is removed by reduction with hydrogen at 500°C for 0.5 h and then the catalyst surface is purged of any residual hydrogen by heating the material in He to 500°C with no soak time. The resulting "native" Mo_2N was reduced (with hydrogen adsorption) by treatment in 10% H_2/Ar at 500 °C for 30 min to produce Mo_2N-H_X. *Note that in all of the following studies, Mo_2N is referred to as the material after passivation layer removal and surface purge steps.*
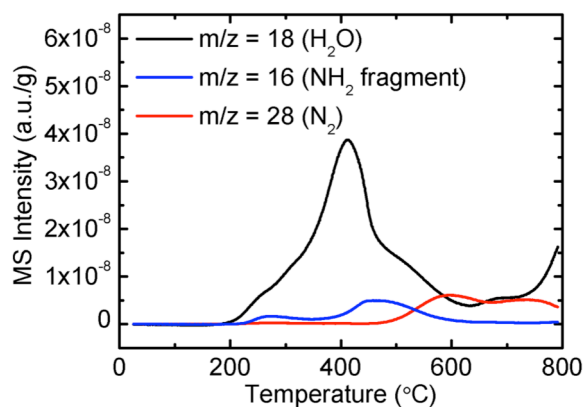
Figure 2.5. Temperature-programmed reduction spectra for reduction of passivated Mo_2N. The heating rate was 15 K min^{-1}.

2.3.3. Materials Characterization and Location of Hydrogen Sites in Mo_2N

The X-ray diffraction patterns for the as-synthesized materials (Figure 2.6) before and after hydrogen treatment are consistent with γ-Mo_2N [36]. No peaks were observed for oxide phases, indicating complete nitridation of the oxide reactant during the preparation of Mo_2N. Passivation of the material likely produced a thin amorphous oxygen-rich layer that protected the underlying nitride from oxidation when exposed to air, although the layer is too thin to see via XRD. The average γ-Mo_2N crystallite size is 7.9 ± 1.0 nm based on line broadening analysis. The crystallite size for γ-Mo_2N-H_x is similar, indicating that treatment with hydrogen does not significantly affect the structure. Surface areas for the γ-Mo_2N and γ-Mo_2N-H_x materials were 103.6 ± 0.4 and 143.7 ± 0.3 m^2/g, respectively. This increase in surface area following hydrogen treatment is likely due to the uncovering of micropores previously blocked during the passivation step, as illustrated in our previous work [37].
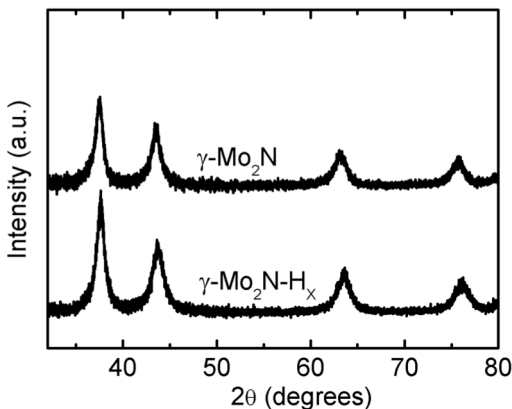
Figure 2.6. X-ray diffraction pattern for γ-Mo_2N prior to hydrogen treatment and after hydrogen treatment (γ-Mo_2N-H_x).

Temperature programmed desorption (TPD) of hydrogen from γ-Mo_2N-H_x following 500°C resulted in two desorption peaks (Figure 2.7), consistent with reports by Li et al. [38]. In some samples, two small shoulders at ~100 and 500°C were also present.
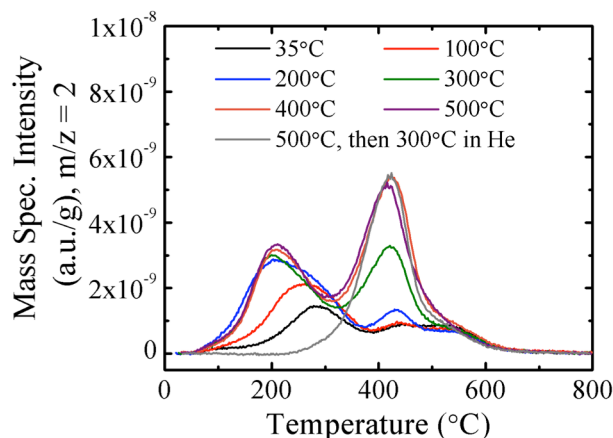
Figure 2.7. Thermal desorption spectra for Mo_2N-H_x following reduction in 10% H_2/Ar at varying temperatures after an initial reduction and purge step. The gray line also represents a surface reduced at 500°C followed by desorption of the low temperature site by heating the reduced material to 300°C in He.

The growth of the two desorption peaks was studied by varying the reduction temperature. However, the passivation layer had to be removed prior to this analysis to ensure that the surface prior to the experiment was identical in all cases. To produce more controlled experimental conditions, a method was developed to first remove the passivation layer by reducing at 500°C for 0.5 h and then purge the surface of any residual hydrogen by heating the material in He to 500°C with no soak time. The material was then exposed to different reduction temperatures. Thermal desorption spectra for the materials prepared at varying reduction temperatures are shown in Figure 2.7. The low temperature desorption peak (referred to as "Peak A") is observed to have a second-order dependence on reduction temperature based on the shift in peak desorption temperature observed with increasing hydrogen desorption intensity, likely due to increasing surface coverage of hydrogen at higher temperatures [39]. A second-order dependence is consistent with a recombinative desorption process. The low temperature site becomes saturated at roughly 200°C reduction temperature. With higher temperatures (above 200°C), the high-temperature desorption peak (referred to as "Peak B") begins to

populate until reaching saturation at around 400°C. The growth of the high-temperature

desorption peak appears first order given the constant desorption temperature despite

changing surface coverage. Further, as indicated by the gray spectrum shown in Figure

2.7, the high temperature desorption site can be completely isolated by desorbing the low

temperature site at 300°C. It should be noted that the high temperature desorption peak is

present in all of the spectra to some degree, indicating that the purge step does not desorb

all of the hydrogen.

Given the relatively high desorption temperature for one of the desorption peaks

and considering results in the literature [6-8,14], it is possible that the high temperature

desorption peak is due to the presence of subsurface hydrogen. To test this hypothesis,

thermal desorption spectroscopy, inelastic neutron scattering, and density functional

theory were employed. Leary et al. [40,41] studied the effect of heat rate on the

distribution of surface and subsurface sites in hydrogen thermal desorption spectra. This

analysis has been applied to Pd [41] and Mo_2N [6]. As a result, for systems where the

activation energy for diffusion is much less than that for desorption, the relative peak

intensities of surface-to-subsurface hydrogen should increase with increasing heating rate

(β). It is important to note that hydrogen is observed to diffuse with relative ease through

the bulk of a variety of metals (low activation energy for diffusion) [42]. For two surface

bound species that do not interact, the relative peak intensities should remain constant at

different heating rates. The TPD spectra obtained at different heating rates (Figure 2.8)

show that the relative intensity of the low-temperature peak increases relative to the

intensity of the high-temperature peak with increasing heating rate. These results are

consistent with the presence of surface and subsurface hydrogen species. In addition, the
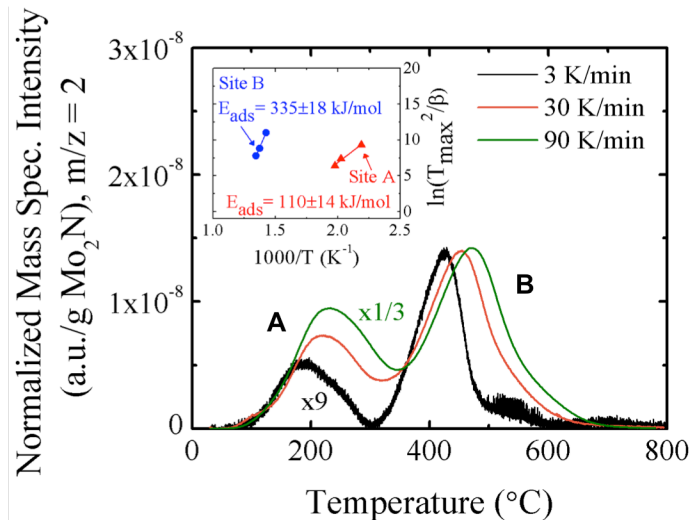
Figure 2.8. Thermal desorption spectra for Mo_2N-H_x as a function of heating rate ($\beta = 3$, 30, 90 K min^{-1}). The spectra were normalized to allow for plotting on the same scale. The inset represents the desorption activation energies of the two peaks calculated using the Falconer-Madix method [22].

calculated activation energy for desorption, calculated using the Falconer-Madix method, from Peak B is greater than the activation energy for desorption from Peak A. The calculated desorption energies using the Falconer-Madix method were found to be 110 ± 14 kJ mol^{-1} and 335 ± 18 kJ mol^{-1} for the surface and subsurface desorption peaks, respectively. These values are consistent with those reported previously for molybdenum nitride thin films (96 and 222 kJ mol^{-1}) [43]. The lower desorption energy is similar to that for many metals; for example, Ertl and coworkers reported heats of desorption from Pd of 105 kJ mol^{-1} at nearly all surface coverages [44]. The high desorption energy peak (Peak B) for $\gamma-Mo_2N-H_x$ is likely due to the presence of subsurface hydrogen, which would desorb after diffusion to the surface region; this will be discussed further in the Discussion section (Section 2.4).

Density functional theory (DFT) calculations (conducted by the Cundari group at the University of North Texas) were performed in order to determine the most

energetically favorable two-hydrogen configuration in a Mo_2N slab. The most favorable two-hydrogen system was found to contain a surface bound monodentate κ^1-N-H bond and a subsurface μ^6-Mo-H bond in an octahedral site as seen in Figure 2.9 (Model #6). The κ^1-N-H + μ^6-Mo-H configuration was ~4 kcal mol^{-1} more favorable than a system with two surface bound κ^1-N-H species (Model #7) and ~12 kcal mol^{-1} more favorable than a system containing a κ^1-N-H and κ^1-Mo-H surface species (Model #5) (see Table 2.3). Occupation of the tetrahedral μ^4-Mo-H was energetically uphill. The results are consistent with the surface-subsurface system suggested by thermal desorption spectroscopy experiments. For further confirmation, the most favorable system from DFT was used to calculate IR active vibrational modes for the two-hydrogen species and inelastic neutron scattering (INS) was performed to observe these vibrational modes. This work was performed by Dr. Elizabeth Mader of the Mayer group (Yale University) at the Rutherford Appleton Laboratory in the United Kingdom. As seen in Figure 2.10, while the results are very noisy, the difference spectra appear to show the anticipated features for the two types of hydrogen, though the N-H features are far more intense. More details regarding the computational and neutron scattering results are available in the collaborative manuscript on this work [45].
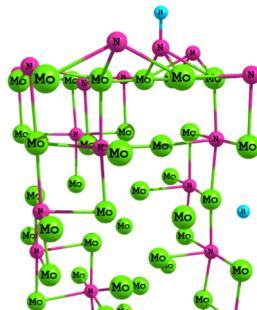
Figure 2.9. The most favorable two-hydrogen configuration for a Mo_2N-H$_x$ system calculated using density functional theory and VASP code. *Computations performed by Daniel Pardue in Professor Thomas Cundari's group at University of North Texas.*

Table 2.3. Energies of hydrogen addition to γ-Mo$_2$N. Energies are relative to the energy-minimized structure of γ-Mo$_2$N and the appropriate equivalents of H$_2$.

Model #	Structure	Stoichiometry	ΔE (H• addn) kcal mol^{-1}
1	γ-Mo$_2$N		0
2	κ^1-NH$_{surf}$	γ-Mo$_2$NH$_{0.3}$	-6.6
3	μ^6-MoH$_{sub}$	γ-Mo$_2$NH$_{0.3}$	-6.4
4	κ^1-MoH$_{surf}$	γ-Mo$_2$NH$_{0.3}$	+6.3
5	κ^1-MoH$_{surf}$ + κ^1-NH$_{surf}$	γ-Mo$_2$NH$_{0.7}$	-1.4
6	μ^6-Mo$_6$H$_{sub}$+ κ^1-NH$_{surf}$	γ-Mo$_2$NH$_{0.7}$	-13.3
7	$(\kappa^1$-NH$_{surf})_2$	γ-Mo$_2$NH$_{0.7}$	-9.1
8	μ^2-NH$_{2\text{-}surf}$	γ-Mo$_2$NH$_{0.7}$	+0.5

Figure 2.10. Normalized Inelastic Neutron Scattering (INS) spectra for (--, red) γ-Mo$_2$N and (--, blue) γ-Mo$_2$N-H$_x$ samples and their difference spectrum (--, black, γ-Mo$_2$N-H$_x$ – γ-Mo$_2$N, offset from zero for clarity). Also shown is the simulated INS spectra (summed over 0-4 quantum transitions). Areas in the difference spectrum showing loss upon the addition of hydrogen are well represented with the k^1-NH$_{surf}$ model (--, green). Areas showing growth upon the addition of hydrogen are consistent with a m^6-Mo$_6$H$_{sub}$ model (--, pink). *Performed by Elizabeth Mader in Prof. Mayer's group at Yale University.*

Given these results, it is hypothesized that the low temperature hydrogen desorption peak arises from heterolytic recombination of a surface N-H and a subsurface Mo-H, while the high temperature hydrogen desorption peak results from homolytic recombination of two subsurface Mo-H. The former case represents a recombination of a

protic and hydridic hydrogen, while the latter involves a recombination between two hydridic hydrogen.

2.3.4. Mo₂N-Hₓ with Different Hydrogen Site Populations

Having elucidated the location and nature of the two hydrogen sites associated with Mo_2N, subsequent experiments were carried out to determine the reactivity of these individual hydrogen sites. Ideally, the reactivity of these sites would be analyzed using a flow reactor for hydrogen adsorption on a bed of Mo_2N followed by introduction of reactant. Since subsurface sites were found to be populated only after surface site saturation at temperatures between 200 and 300°C, it would be difficult to know which hydrogen sites are actually populated in the course of a packed bed reaction. Furthermore, subsurface hydrogen may be an inactive bystander in reactions. Therefore, the intrinsic activity of each site was probed by preferential hydrogen site population and use of the resulting Mo_2N-H_x in stoichiometric batch reactions.

In order to obtain different relative site densities for reaction analysis, procedures were developed for population of the different hydrogen sites. Information from previous TPD experiments (Figure 2.7) was used to determine thermal treatments for optimizing different site populations. To obtain a mixture of the two sites ($\%H_{subsurface}$ = ~65-70%), Mo_2N was reduced in 10% H_2/Ar at 500°C for 0.5 h. To obtain predominantly subsurface sites ($\% H_{subsurface}$ = ~95%), Mo_2N was first reduced in 10% H_2/Ar at 500°C for 0.5 h after the initial reduction and surface purge, then cooled to room temperature, followed by heating to 300°C in inert He to desorb the surface sites. It was difficult to optimize population of the surface sites given the mechanism for hydrogen population and the fact that not all hydrogen could be removed during the purge step following removal of the

passivation layer. However, we were able to obtain an optimal surface site density (% $H_{subsurface}$ = ~45-50%) by reducing the Mo_2N in 10% H_2/Ar at 200°C for 0.5 h. Thermal desorption spectra for the optimal conditions can be found in Figure 2.11.

The timescale for exchange between the surface and subsurface sites was determined by "aging' the materials in He (70 mL min^{-1}) at 35°C for varying amounts of time. Figure 2.12 shows TPD spectra for the γ-Mo_2N-H_x following this "aging" step. The results indicate that there was minimal migration of hydrogen from Peak A (surface) to Peak B (subsurface) (Figure 2.12a). The peak area associated with site A decreases with time, likely due to slow desorption of H_2 into the gas phase, while the site B peak
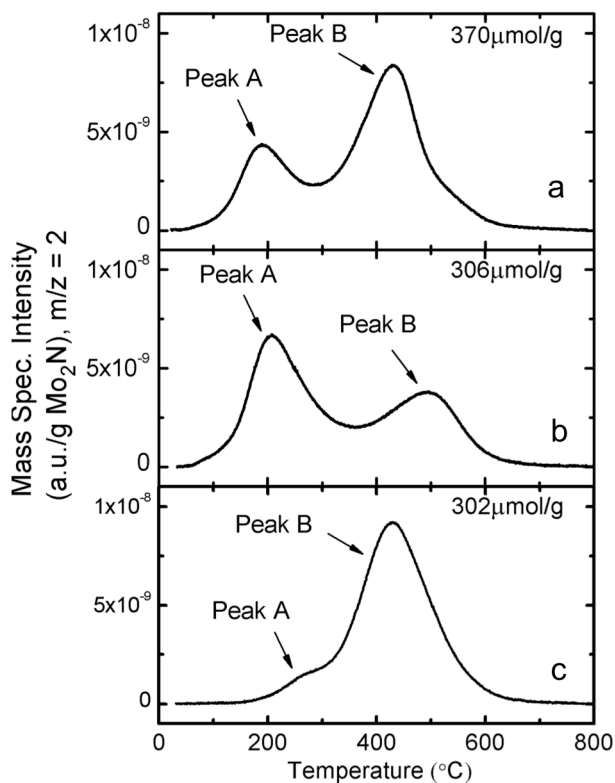
Figure 2.11. Thermal desorption spectra for the optimal hydrogen population conditions. The spectra correspond to (a) a material reduced in 10% H_2/Ar at 500°C for 0.5 h (non-selective population), (b) a material reduced in 10% H_2/Ar at 200°C for 0.5 h (Peak A-selective population), and (c) a material reduced in 10% H_2/Ar at 500°C for 0.5 h followed by hydrogen desorption to 300°C in He (Peak B-selective population).

does not significantly increase. Conversely, there was slow hydrogen migration from site B to site A during the 8 hour aging period (Figure 2.12b). These results suggest that the hydrogen site populations did not change significantly for up to 120 min after treatment, which is the average time frame between catalyst pretreatment and the start of the batch reactions (due to transfer into and between glove boxes).
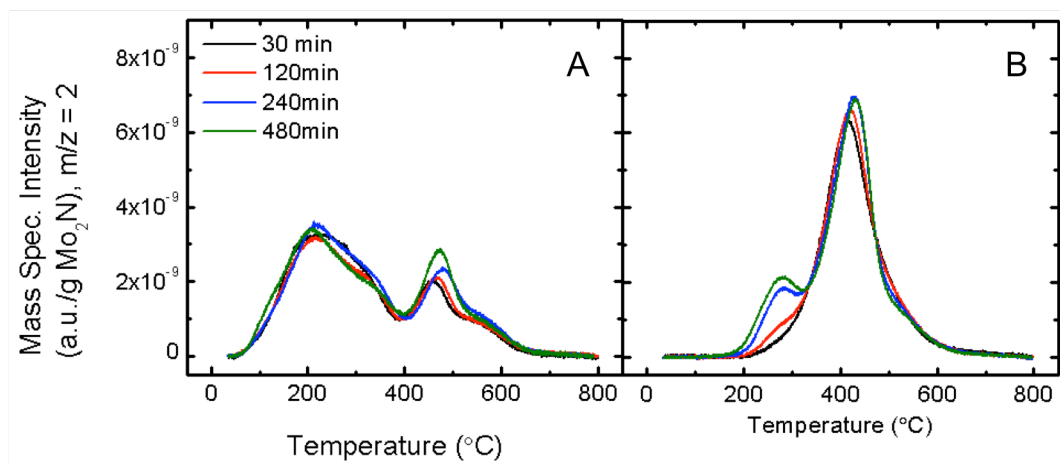
Figure 2.12. Thermal desorption spectra of hydrogen from γ-Mo$_2$N following hydrogen treatment at (a) 200 °C for 0.5 hr (site A) and (b) 500 °C for 0.5 hr, followed by desorption in He at 300°C for 0.5 hr (site B) aimed at monitoring diffusion between sites. The spectra represent the following "aging" times in He (70 mL min^{-1}) at 35 °C: 0.5, 2, 4, 8 hr. Heating rate of 15 °C min^{-1}.

2.3.5. Reactivity and Selectivity of Surface versus Subsurface Hydrogen Sites for

Crotonaldehyde Hydrogenation

With these selective methods for hydrogen site population and awareness of the diffusion between sites, the hydrogenation reactivity of the individual sites can be evaluated. To probe the reactivity, γ-Mo$_2$N-H$_x$ populated via the three methods discussed above was placed in a reactor (0.1g γ-Mo$_2$N-H$_x$ containing ~30-40 µmol H$_2$) and exposed to solutions containing 10 µmol crotonaldehyde (CA) in ethanol solvent (1.25 mL) with decane (10 µmol) as an internal standard under a nitrogen atmosphere. After 1 hr at 70 ° C, 63±7% of the CA had reacted, independent of the initial hydrogen site population,

although the measured products only accounted for approximately 2/3 of the converted CA (Figure 2.13a). In addition to the expected hydrogenation products, acetals were formed via reactions of the aldehydes with ethanol (i.e., 1,1-ethoxybutane or 1,1-ethoxybutene derived from butyraldehyde or crotonaldehyde, respectively). These side reactions have been observed previously and are likely due to acidic sites on the nitrides [46]. Improved mass balance closure (within error, ±10%) was detected using another GC and column, with (hemi)acetals accounting for the majority of the previous 35% gap (Figure 2.13b). Reports in literature commonly use the DB-WAX column for analyses involving crotonaldehyde hydrogenation in alcohol solvents [23,24]. Measured hydrogenation conversions (and selectivities) were comparable between gas chromatographs. The hydrogenation products, butyraldehyde ($CH_3CH_2CH_2CHO$), crotyl alcohol ($CH_3CH=CHCH_2OH$) and butanol ($CH_3CH_2CH_2CH_2OH$), accounted for ~6-15% (~2-6 μmol) of the total hydrogen associated with the γ-Mo_2N-H_x.
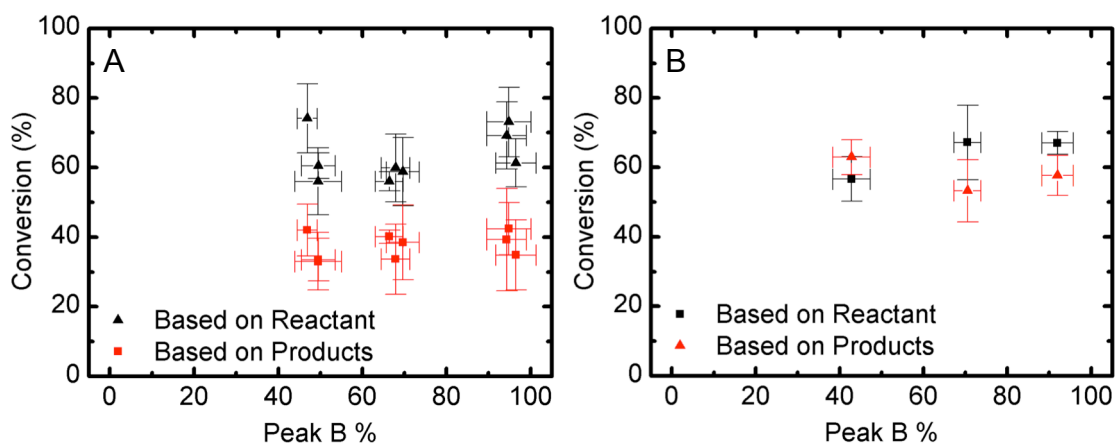
Figure 2.13. Crotonaldehyde conversions based on reactant (i.e., crotonaldehyde) and measured products (hydrogenated products and (hemi)acetals) analyzed on two different GC columns: (A) Porabond Q and (B) DB-WAX.

Crotonaldehyde hydrogenation selectivities for formation of crotyl alcohol (CrOH), butyraldehyde (BuAL), and butanol (BuOH) are plotted as a function of the

relative percentage of hydrogen associated with Peak B (Figure 2.14). As the percentage

of hydrogen associated with these sites increases, the CrOH selectivity increased linearly

while the BuAL and BuOH selectivities decreased linearly. These trends were consistent

for experiments carried out for 1, 2 and 3 hr age times at 70 °C. Extrapolation suggests

that a catalyst populated solely with "Peak B" hydrogen would have nearly 100 %

selectivity for hydrogenation of the C=O double bond to produce CrOH. While catalyst

containing high densities of hydrogen associated with Peak A could not be prepared,

extrapolation from the available data predicts a catalyst with solely Peak A hydrogen

would produce approximately 60% crotyl alcohol, 20% butyraldehyde, and 20% butanol.

The amount of by-products (hemiacetals and acetals, between 7-21% total selectivity)

observed due to reaction of the CA with the ethanol solvent appeared to correlate

inversely with the total amount of hydrogen, but did not depend on which hydrogen site

was populated. The formation of acetals, which does not require hydrogen, should be

unaffected by the nature of the hydrogen on the surface or in the subsurface. Hydrogen-

deficient surfaces would be expected to facilitate the formation of (hemi)acetals while

hydrogen rich surfaces should produce hydrogenation products. In this work, saturated

(hemi)acetals were more prominent with a higher percent of hydrogen associated with

Peak A, while unsaturated (hemi)acetals were more prominent with lower Peak A

percentages.
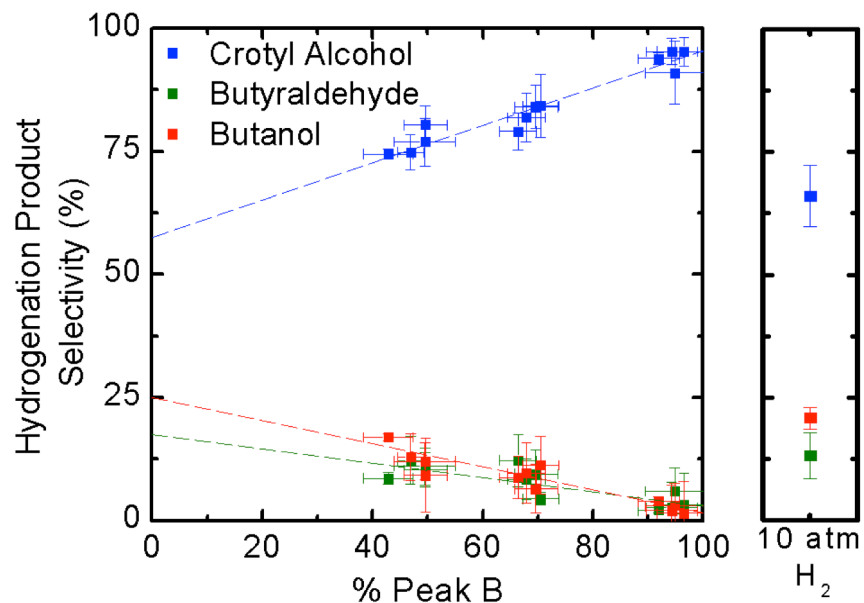
Figure 2.14. Hydrogenation product selectivity after 1 hr reaction. (Left) As a function of the relative density of the high-temperature hydrogen desorption site (peak B) in pre-formed γ-Mo_2N-H_x. (Right) By generating γ-Mo_2N-H_x *in situ* from γ-Mo_2N and 10 atm H_2(g) headspace in the presence of crotonaldehyde.

For comparison, a typical batch-type hydrogenation reaction was conducted using a pressurized hydrogen headspace as the hydrogen source with Mo_2N in the CA/decane/ethanol reaction mixture. The selectivity results are shown on the right side of Figure 2.14. Selectivity to form crotyl alcohol is lower than for reactions utilizing pre-hydrogenated Mo_2N. Based on the linear extrapolation through the selectivity data for reactions using pre-hydrogenated Mo_2N, the approximate percent of Peak B hydrogen *in situ* is roughly 22 ± 3 %, indicating a catalyst dominated by surface hydrogen. Previous results (Figure 2.7) showed that hydrogen fails to significantly penetrate into Peak B sites below 200 °C. To obtain a rough estimate of the Peak A and Peak B site populations *in situ*, Mo_2N alone was subjected to similar conditions (sans solvent and high pressure). The thermal desorption results in Figure 2.15 were compared to the typical Mo_2N-H_x TPD following hydrogen population at 500 °C. At 70 °C, the material is predominantly

populated with Peak A plus ~18% Peak B, which is within experimental error of the anticipated Peak B% (22 ± 3 %) based on selectivity results. While this is an indirect comparison due to system differences (absence of ethanol and high pressures), these results indicate that the linear correlation drawn from the selectivity data in Figure 2.14 can also be applied to low Peak B%.
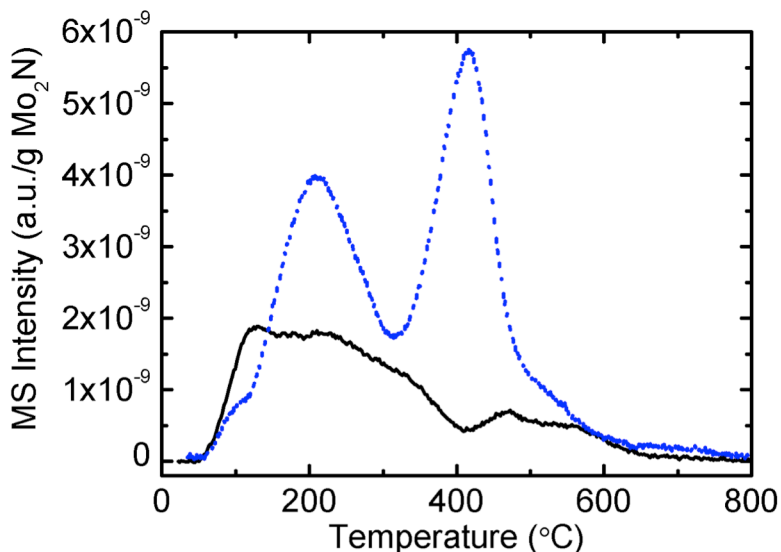
Figure 2.15. Thermal desorption spectra for Mo_2N-H_x prepared by H_2 population at 500 °C (- -) and 70°C (–).

For comparison, this experiment was also performed on a 2.3wt% Pt/Al_2O_3 catalyst synthesized via dry impregnation, and reduced at 250°C. Under identical reaction conditions (70°C, 10μmol CA in ethanol, 10 atm H_2), the Pt catalyst exhibited selectivities of 28 ± 5%, 8 ± 2%, and 64 ± 7 % for butyraldehyde, crotyl alcohol, and butanol, respectively. The selectivities are drastically different from those observed for Mo_2N, although typical selectivities for Pt-group metals are quite variable. Ir/TiO_2 exhibited crotyl alcohol selectivities close to 70% [47], while Pt/CeO_2 and Pt/ZrO_2 exhibited 30-50% selectivity towards crotyl alcohol [48]. Carbon-supported Pd, Pt, Ru, and Au demonstrated crotyl alcohol selectivities of 0, 10, 17, and 37%, respectively [49].

While the selectivities of the pre-populated molybdenum nitride catalysts studied here appear to be attractive for commercial use, the reaction conditions are quite different from those for typical crotonaldehyde hydrogenation experiments in flow or high-pressure batch systems.

The temperature dependence of the hydrogenation reactions (and side reactions) was investigated by varying the temperature of the 1 hr batch reactions between 40 and 70°C. The hydrogenation product yields and the product selectivities as a function of temperature and Peak B % are shown in Figure 2.16(a) and Figure 2.16(b-d), respectively. Arrhenius plots of conversion rates for the three different hydrogen site populations studied (Figure 2.17) show the slope of the best-fit line increases with increasing Peak B %. Temperature appears to have a greater effect on hydrogenation rate in the case subsurface hydrogen and less of an effect for surface hydrogen. It should be noted that the use of batch reactions together with high conversions of the reactants results in reaction rates which are inherently limited, both by mixing and concentration of reactants. Therefore, no activation energies can be reported for these reactions with sufficient accuracy.

Hydrogenation product selectivities were also influenced by reaction temperature (Figure 2.16b-d), with the extent of impact depending on the Peak B %. At high percentages, selectivities were relatively unaffected by the reaction temperature, likely given that one key reaction pathway/mechanism predominates for this case. For lower Peak B %, the crotyl alcohol selectivity increases slightly with higher reaction temperatures, perhaps indicating the presence of competing reaction pathways with different intrinsic activation energies. The most profound temperature effect is observed

for the butyraldehyde formation in which the selectivity for the 50% Peak B case decreases from ~20 to ~5% as the temperature increases from 40 to 70 °C. It appears that higher reaction temperatures facilitate the conversion of butyraldehyde to either crotyl alcohol via isomerization or butanol via further hydrogenation.
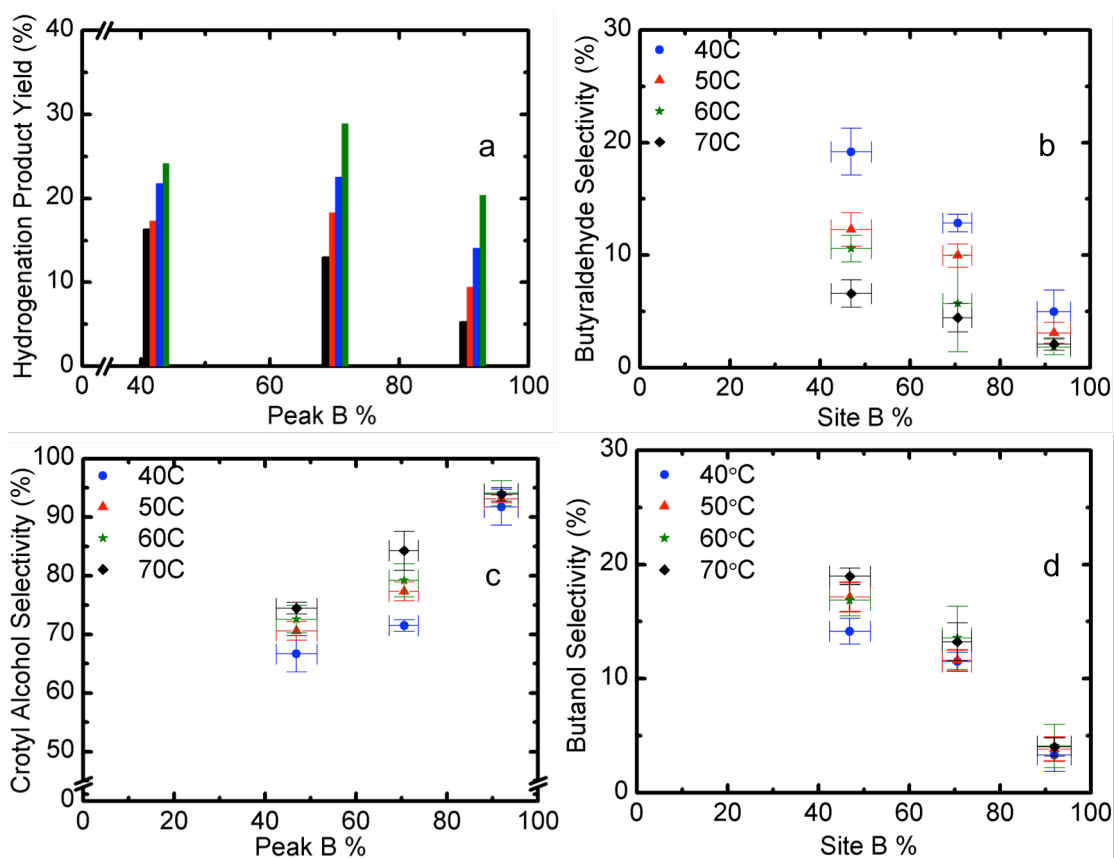
Figure 2.16. Hydrogenation product yield (top left) and selectivity for formation of butyraldehyde (top right), crotyl alcohol (bottom left), and butanol (bottom right) as a function of Peak B % and varying temperature (40-70°C).

To assess this possibility, γ-Mo$_2$N-H$_x$ materials with varying Peak B% were reacted with butyraldehyde or crotyl alcohol under the same reaction conditions for 1 hr. The butyraldehyde and crotyl alcohol conversions are compared to those for crotonaldehyde in Table 2.4. Butyraldehyde reacted readily to form butanol and by-products such as 1-ethoxybutanol and 1,1-diethoxybutane while crotyl alcohol did not

react further. These results indicate that butanol was formed directly from butyraldehyde while crotyl alcohol, once formed, was unreactive in the presence of γ-Mo$_2$N-H$_x$.
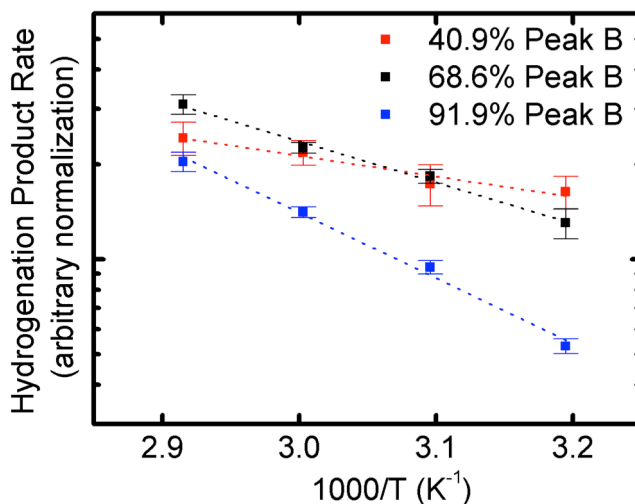
Figure 2.17. Arrhenius plots detailing conversion to hydrogenation products as a function of 1000/T for the 3 site distributions studied.

Table 2.4. Conversions to hydrogenation products after 1 hr reaction for the various H$_2$ populated Mo$_2$N with crotonaldehyde, butyraldehyde or crotyl alcohol as the starting reactant.

| Reactant[a] | % Peak B | Conversion to Products (%) | | | | |
		BuAL	CrOH	BuOH	Total Hydrogenation	(hemi) acetals
CA	49	4 ± 1	26 ± 7	4 ± 2	34 ± 7	5.3
	70	3 ± 1	24 ± 1	2 ± 1	28 ± 9	4.4
	94	2 ± 1	25 ± 1	1 ± 1	27 ± 3	9.9
BuAL	49	-	0	31 ± 6	31 ± 6	8.9
	70	-	0	26 ± 6	26 ± 6	13.0
	94	-	0	29 ± 8	29 ± 8	8.8
CrOH	49	0	-	0	0	0
	70	0	-	0	0	0
	94	0	-	0	0	0

[a]Abbreviations: CA = Crotonaldehyde, BuAL = Butyraldehyde, CrOH = Crotyl Alcohol, BuOH = 1-Butanol

65

Importantly, for the material with 94% Peak B, the hydrogenation products account for more than twice the amount of hydrogen associated with Peak A. This supports the direct participation of the hydrogen associated with Peak B, either via diffusion to a surface site or from a different active site. However, the experimental error associated with this hydrogen balance is magnified by the low hydrogen conversion at the H_2:reactant ratios used. Therefore, the γ-Mo_2N-H_x catalyst was reacted with excess CA (10:3.5 CA:H_2 ratio) in ethanol at 70 °C for 12 hours in an attempt to react all of the hydrogen in/on the Mo_2N-H_x. The reaction time was varied with experiments running between 1 and 12 hours in separate batch reactors to determine the progression of reaction with time. In this particular experiment, after 12 hr of reaction, all of the hydrogen was removed based on the product yields (Figure 2.18). Interestingly, hydrogen migration between different sites appears to be slow in the absence of CA and solvent, but the presence of CA and/or solvent appear to facilitate diffusion of hydrogen from the subsurface to the surface. The enhanced selectivity for C=O bond hydrogenation
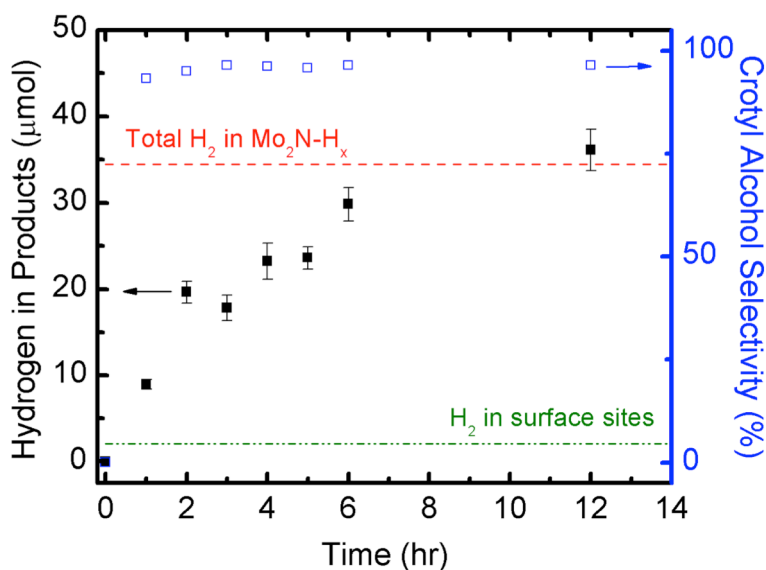
Figure 2.18. Hydrogen consumption as a function of reaction time for γ-Mo_2N-H_x (~35 μmol H_2, 92% peak B) with excess CA (100 μmol) in EtOH at 70 °C.

was retained throughout the reaction, achieving an overall crotyl alcohol selectivity of 97% after 12 hr.

2.3.6. Crotonaldehyde Hydrogenation over Other Carbides/Nitrides

Following the promising results and interesting trends found for crotonaldehyde hydrogenation over hydrogenated Mo_2N, a similar evaluation was conducted for W_2N-H_x and $VN-H_x$. First, however, the thermal desorption heating rate was varied for these two material systems in order to probe the location of hydrogen as previously reported by Leary et al. [40,41]. Results from these experiments are shown in Figure 2.19 for W_2N and VN. Similar to Mo_2N, results for both W_2N and VN are consistent with the presence of surface and subsurface hydrogen in these materials as indicated by changes in relative peak height with changing heating rate. It is likely that these materials may exhibit similar selectivity trends as Mo_2N based on the presence of subsurface hydrogen.
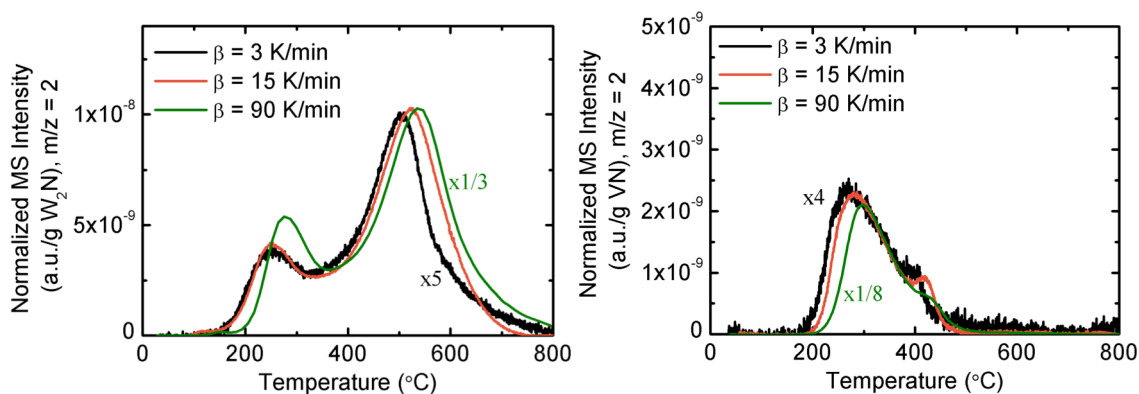
Figure 2.19. H_2 thermal desorption spectra for W_2N-H_x (left) and $VN-H_x$ (right) following pretreatment at 500°C in 10% H_2/Ar for 0.5 hr. The desorption spectra were obtained at different heating rates ($\beta = 3, 15, 90$ K/min).

Temperature programmed desorptions were performed on these materials to determine conditions for populating the different hydrogen sites as previously shown for the Mo_2N system (Figure 2.11). The thermal desorption spectra for W_2N-H_x and $VN-H_x$ (Figure 2.20) indicate that temperatures should be limited to ~500°C and 600°C for W_2N
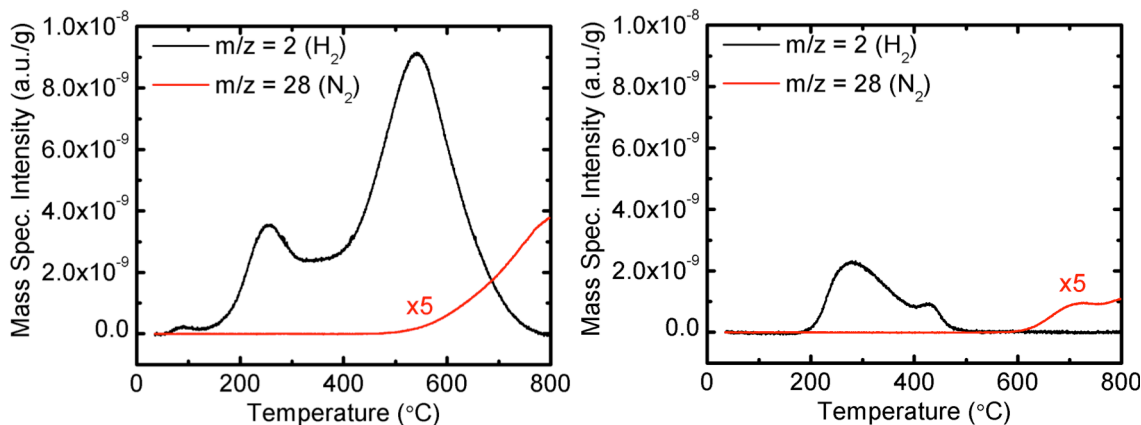
Figure 2.20. H$_2$ thermal desorption spectra for W$_2$N-H$_x$ (left) and VN-H$_x$ (right) following pretreatment at 500°C in 10% H$_2$/Ar for 0.5 hr. Mass spectrometer signals for m/z values of 2 and 28 are shown, corresponding to H$_2$ and N$_2$, respectively.

and VN, respectively, to avoid decomposition accompanied by N$_2$ evolution. This upper temperature limit will not be a factor for VN-H$_x$ as H$_2$ completely desorbs from the two sites by 500°C, allowing for the surface to be "purged" after heating with H$_2$ to remove the passivation layer followed by heating in inert He (both performed at 500°C) to remove any adsorbed hydrogen prior to final hydrogen population for this analysis. However, an upper limit of 500°C for W$_2$N-H$_x$ will not allow for complete desorption of the high temperature peak centered at ~560°C and, thus, complete evacuation of hydrogen from the material could not be achieved as was the case for Mo$_2$N-H$_x$.

Methods for preferential site population were developed for W$_2$N-H$_x$ and VN-H$_x$. Due to the temperature limitations of W$_2$N and the inability to completely "purge" the material, only two conditions were developed for reactivity analysis: (1) containing both peaks and (2) containing only the peak above 400°C. In order to obtain spectra containing both peaks, W$_2$N was pretreated at 500°C in 10% H$_2$/Ar for 0.5 hr. To obtain spectra with only the high temperature peak, the material was first pretreated at 500°C in 10% H$_2$/Ar for 0.5 hr, then cooled to room temperature, and then heated to 400°C in He to desorb the

low temperature peak. Spectra for the two conditions are shown in Figure 2.21. The conditions used allow for complete selectivity of the high temperature desorption peak in W_2N for analysis. It should be noted that work was conducted in an effort to develop methods for populating only the low temperature sites. Higher relative site densities of the low temperature desorption peak can be obtained using lower reduction temperatures (not shown). However, due to the inability to completely purge the surface because of temperature limitations and the need for high temperatures to remove the passivation layer, the low temperature reduction treatments were not used.
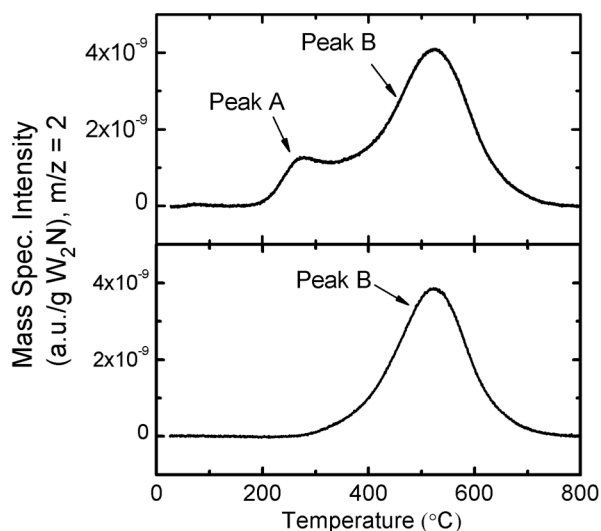
Figure 2.21. H_2 temperature programmed desorption spectra for the two site population conditions used for the W_2N-H_x reactivity experiments. The top and bottom spectra represent condition (1) and (2), respectively.

For the VN-H_x system, the relative peak densities were varied by changing the temperature of desorption in inert He with the following final temperatures used: (1) 25°C, (2) 400°C, (3) 410°C, and (4) 420°C. The resulting spectra (Figure 2.22) show shifts in the relative peak densities with increasing desorption temperature from predominantly Peak A (~25% Peak B) to a mixture of Peak A and B (~60% Peak B),

with cases (B) and (C) providing densities in between. The relative densities were again calculated by fitting the spectra to a series of Gaussian peaks.
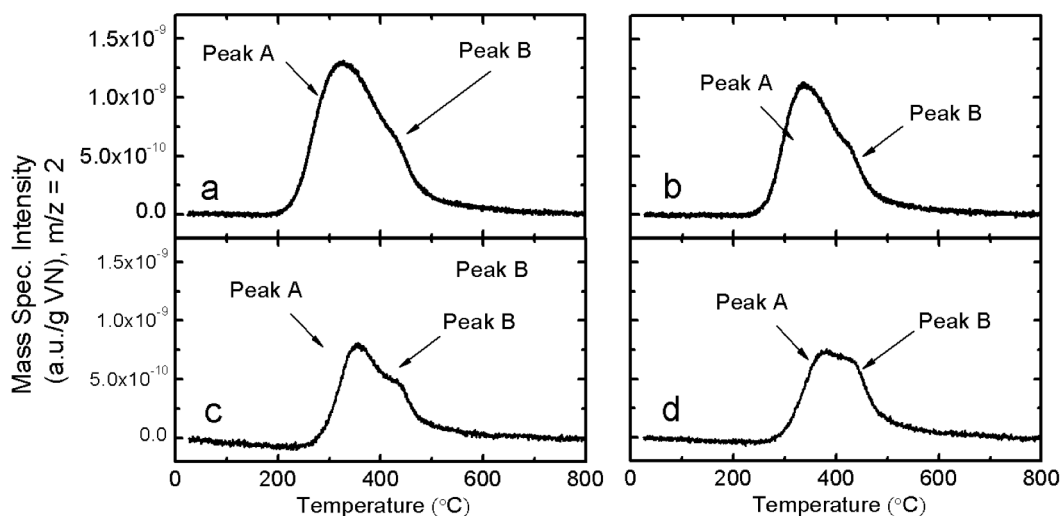
Figure 2.22. H_2 TPD spectra for VN-H_x following different treatment conditions. All catalysts were pretreated at 500°C in 10% H_2/Ar for 0.5 hr and then heated in He to (A) 25°C, (B) 400°C, (C) 410°C, and (D) 420°C to desorb the low temperature peak.

The materials with different hydrogen site populations were exposed to the reaction conditions for crotonaldehyde hydrogenation, which is explained in detail in Section 2.2.2.6 and the corresponding results are summarized in Table 2.5. W_2N-H_x was found to be relatively inactive for hydrogenation under both conditions tested, with conversions less than 1%. Instead, extensive formation of (hemi)acetal by-products was observed with ~80% conversion after the 1 hour reaction. Conversely, VN-H_x was moderately active for crotonaldehyde hydrogenation and nearly 100% selective towards C=O bond hydrogenation to form crotyl alcohol with low conversion to (hemi)acetals. Of note, the reactivity performance of neither W_2N-H_x nor VN-H_x showed much dependence on the hydrogen distribution. These results are in stark contrast to those found for Mo_2N-H_x. These differences will be addressed in the discussion section.

It is worth commenting on the observed differences in selectivity towards formation of (hemi)acetal by-products among the catalysts studied (Mo_2N-H_x, W_2N-H_x, VN-H_x). Literature suggests that this reaction is catalyzed by acidic solutions [50].

Table 2.5. Performance of W_2N-H_x and VN-H_x catalysts for crotonaldehyde hydrogenation in ethanol at 70°C for 1 hour.

Catalyst	% Peak B	Conversion to Products (%)				
		BuAL	CrOH	BuOH	Total Hydrogenation[b]	(hemi) acetals
W_2N-H_x	79±6	0	0.4 ± 0.1	0.3 ± 0.1	0.7 ± 0.1	80.3
	97±4	0	0.4 ± 0.1	0.2 ± 0.1	0.6 ± 0.1	73.3
VN-H_x	27±6	0.1 ± 0.1	0	8.2 ± 0.5	8.3 ± 0.5	3.6
	28±7	0.1 ± 0.1	0.1 ± 0.1	6.1 ± 0.1	6.3 ± 0.2	2.6
	38±9	0.1 ± 0.1	0.1 ± 0.1	11.0 ± 0.1	11.2 ± 0.2	3.0
	59±6	0.1 ± 0.1	0.2 ± 0.1	13.7 ± 0.3	13.9 ± 0.3	11.1

[a] Abbreviations: BuAL = Butyraldehyde, CrOH = Crotyl Alcohol, BuOH = 1-Butanol
[b] Total conversion to hydrogenated products

Recent reports have shown that acidic sites on solid, heterogeneous catalysts can also catalyze this reaction between alcohols and an aldehyde [51,52,53]. Therefore, it has become common to characterize the acid sites on heterogeneous catalysts for studies involving aldehyde hydrogenation in alcohol solvents [54]. Typically, acid sites are characterized via titration with a basic compound. Mo_2N, W_2N, and VN were therefore characterized by NH_3 TPD (Figure 2.23) to obtain an acid site density for the catalysts. All three catalysts exhibit ammonia desorption peaks at ~110°C and shoulders at ~250-300°C, although in different relative amounts. For VN, there is another shoulder at ~500°C. NH_3 uptake capacities were calculated by integrating the area under the curve and converting this area to a mole amount by using a calibration response factor determined during each experiment. The number of acid sites per gram decreases in the

following order: W_2N (365 μmol/g) > Mo_2N (272 μmol/g) > VN (167 μmol/g). These results are consistent with the trend in (hemi)acetal formation of these catalysts during crotonaldehyde hydrogenation (Table 2.4 and Table 2.5). As 100mg of catalyst was used per reactor, the W_2N, Mo_2N, and VN catalyst reactions would have ~37, 27, and 17 μmol of acid sites hydrogenation reaction, respectively. This trend correlates well with acetal formation, with W_2N exhibiting the highest conversion towards acetals while VN had the lowest acetal production rate. It is possible that the activity and/or number of acid sites for W_2N predominates over the hydrogenation activity leading to the relative inactivity of W_2N towards hydrogenation of crotonaldehyde.
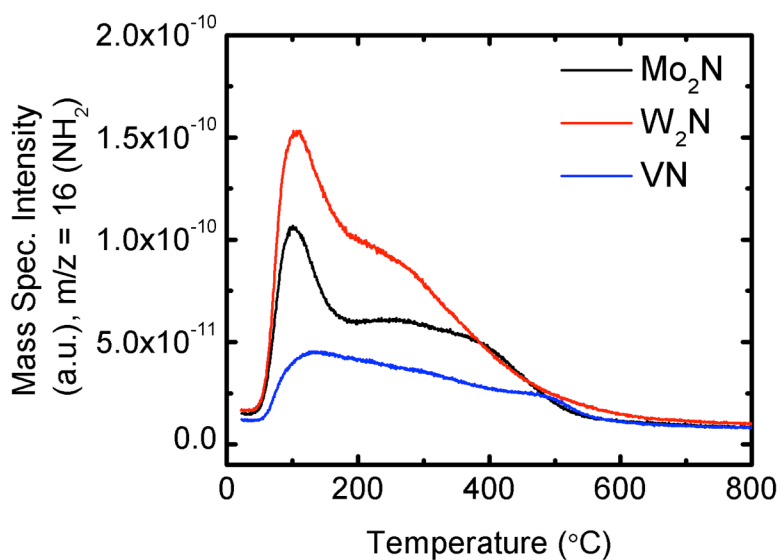
Figure 2.23. NH_3 temperature-programmed desorption spectra for Mo_2N, W_2N, and VN following NH_3 adsorption at room temperature for 0.5 hr. The heating rate was 15 K/min.

2.3.7. Population of Hydrogen Binding Sites using Alternative Hydrogen Sources

In addition to gaseous H_2, there are many other potential sources of hydrogen to use in populating these materials with hydrogen. Of major interest are NH_3 and/or CH_4, which are used during the synthesis of these materials, as well as dehydrogenation of hydrocarbons and alcohols. Carbide and nitrides appear to have a high affinity for and are

capable of adsorbing a substantial amount of hydrogen. NH_3 and CH_4 are commonly used as pretreatment gases prior to catalytic flow reactions for these materials, mainly due to their ability to recarburize or renitridize the catalyst surfaces, resulting in enhanced reactivity. Furthermore, dehydrogenation reactions to generate olefins, ketones, or aldehydes are important reactions in chemical synthesis and petroleum conversion [55].

2.3.7.1.   Hydrogen Population via NH_3 Reduction

In this chapter, the γ-Mo_2N catalysts used have been primarily subjected to gaseous hydrogen for both pretreatment/reduction following passivation (see Section 2.3.1.) and subsequent hydrogen population. However, after initial synthesis of Mo_2N using gaseous NH_3 and subsequent passivation, pretreatment has sometimes utilized NH_3 instead of H_2 as the reductant [16]. Pretreatment in NH_3 may have the added effect of re-populating the Mo_2N surface with nitrogen, which had been displaced by oxygen during the previous passivation step. To test the effect of NH_3 on hydrogen population, thermal desorption spectra were recorded of Mo_2N-H_x following reduction at 500 °C and 700 °C in NH_3 (Figure 2.24, top image). Results show that NH_3 pretreatment produces a new H_2 desorption peak at ~525°C, while the previously observed desorption peaks (at ~200°C and 425°C) following population in H_2 at 500°C are absent from the spectra. There are no differences between spectra of Mo_2N-H_x following NH_3 exposure at 500°C versus 700°C. It might be expected that exposure of Mo_2N to NH_3 at high temperature followed by H_2 at 500°C would yield Mo_2N-H_x with 3 characteristic desorption peaks. Interestingly, the thermal desorption spectrum after NH_3 pretreatment at 700°C followed by exposure to H_2 at 500°C strongly resembles the spectrum after only H_2 treatment at 500°C. The H_2 desorption peak at 525°C may either be metastable or evolve from

73

decomposition of NH_3 on the Mo_2N at high temperatures. The NH_3 desorption spectra

(Figure 2.24, bottom image) show one main desorption peak at low temperature (~150-
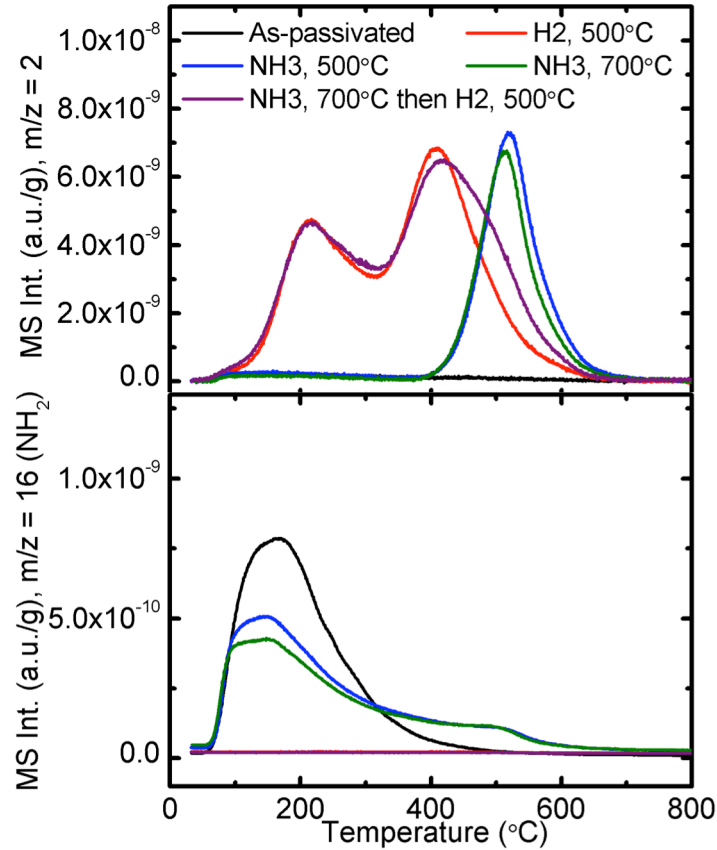
Figure 2.24. Thermal desorption spectra of Mo_2N-H_x for m/z = 2 (top) and m/z = 16 (bottom) following 5 different pretreatments: passivated (no hydrogen added), H_2 reduction at 500°C, NH_3 reduction at 500°C, NH_3 reduction at 700°C, and NH_3 reduction at 700°C followed by H_2 reduction at 500°C. m/z values of 2 and 16 correspond to H_2 and NH_2 (fragment of NH_3), respectively.

200°C) for the passivated and NH_3-pretreated cases. In the spectra following exposure to

NH_3 at high temperatures, there is a small shoulder at ~500°C, which is consistent with

the H_2 desorption temperature. Likely, the hydrogen desorption results from the

decomposition of NH_3 to form N_2 and H_2 at high temperatures based on the similar

desorption temperatures of H_2 ($m/z = 2$) and NH_2 ($m/z = 16$). NH_3 is known to decompose

above 600°C in the absence of catalytic materials [56] and early transition-metal carbides

and nitrides have been reported to be active for NH_3 decomposition [57].

Mo$_2$N materials exposed to NH$_3$ pretreatments were used for crotonaldehyde hydrogenation under typical batch reaction conditions to check for any hydrogenation activity. After NH$_3$ pretreatment at 700 °C for 0.5 hr, the catalyst was relatively inactive for hydrogenation. While all of the crotonaldehyde was "consumed" after 1 hr reaction, the products detected only accounted for ~3.9 ± 0.3 % conversion (yields of 2.6% and 1.3% for (hemi)acetal side products and crotyl alcohol, respectively). This is not unexpected if the surface is saturated with adsorbed NH$_3$, and not atomic hydrogen, as the TPD suggests. NH$_3$ would bind to acidic sites, the type of site known to be active for acetal formation, and would thereby hinder this reaction from occurring. Further, without atomic or molecular hydrogen available, no hydrogenation would occur. The small degree of reaction observed could have been produced via acidic sites that have lost the adsorbed NH$_3$ (i.e., weak acid sites), as well as some residual hydrogen formed by NH$_3$ decomposition at high temperatures. The complete disappearance of CA may result from adsorption of CA onto the catalyst surface as the Mo$_2$N has a higher CA uptake (~19 μmol/100 mg) based on pulse chemisorption than the total CA charged into the reactor (10 μmol/100 mg). Conversely, CA polymerization may also occur on the NH$_3$ pretreated surface, not present in the H$_2$-pretreated case [58].

2.3.7.2. Hydrogen Population via Dehydrogenation Reactions

Carbides and nitrides have the potential to aid in the catalysis of dehydrogenation reactions by extracting hydrogen from model substrates into the hydrogen binding sites of these materials. Dehydrogenation reactions are exceedingly important commercial reactions for the production of precursors to plastics and rubbers, among many others. Carbides and nitrides have previously been reported active for dehydrogenation of

substrates such as, but not limited to, cyclohexane [59], butylamine [60], n-butane [61], and benzyl alcohol [62]. The possibility of using dehydrogenations as an alternative source of hydrogen to populate sites on/in these materials will be explored in this section.

Initially, the performance of the carbides and nitrides of W and Mo was explored for the dehydrogenation of *N*-methylpyrrolidine to *N*-methylpyrrole (Figure 2.25). These catalysts were screened using a temperature-programmed reaction (TPRxn) technique, which constantly monitored the reaction performance while flowing reactant over the catalyst surface and heating the catalyst bed at a constant heat rate. Hydrogen TPD was performed on the catalyst following the TPRxn to probe the hydrogen sites populated during reaction.

N-methylpyrrolidine   *N*-methylpyrrole
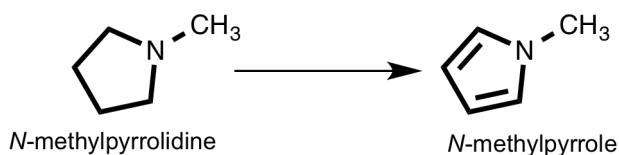
Figure 2.25. Reaction for the dehydrogenation of *N*-methylpyrrolidine to *N*-methylpyrrole.

The dehydrogenation TPRxn spectra for the catalysts studied are shown in Figure 2.26. All four catalysts converted *N*-methylpyrrolidine to hydrogen and *N*-methylpyrrole. Carbon balance closure was ~80-100% for the series of catalysts and activity for the catalysts was as follows: MoC_{1-x} > WC_{1-x} > Mo_2N > W_2N. These results indicate that carbides are more active than nitrides for dehydrogenation, and that the parent metal in the compound has an influence on activity. Since these four catalysts are isostructural, the differences in performance are not due to crystal structure and must be inherent to the metal and nonmetal atom combinations of these materials. Interestingly, previous reports in the literature indicated that Mo and W nitrides were more active for dehydrogenation of n-butane than the corresponding carbides [63]. The observed differences may be due to

76
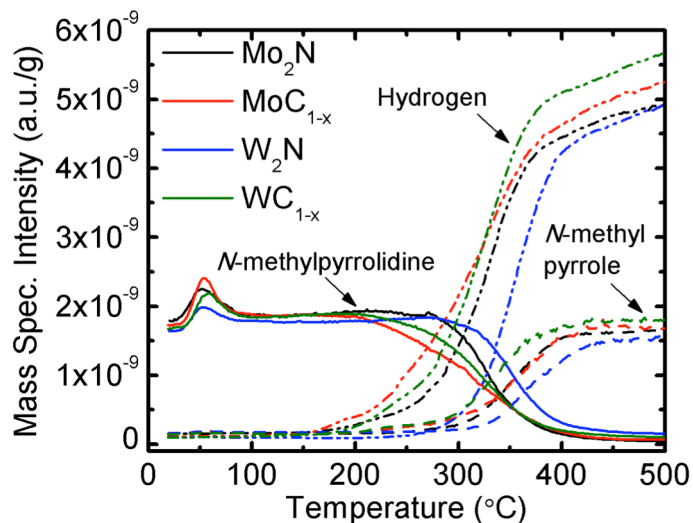
Figure 2.26. *N*-methylpyrrolidine dehydrogenation over Mo_2N, MoC_{1-x}, W_2N, and WC_{1-x} catalysts. Reactant (0.07% *N*-methylpyrrolidine in He) flow rate was set to 50 mL/min. Heating rate, b, was set to 15 °C /min. Catalysts were heated to 500°C in 10% H_2/Ar for 0.5 hr, followed by heating the catalysts in He to 500°C (purge step) to remove most of the H_2 from the material prior to use. No other species were observed.

different interactions occurring between the carbide and nitride catalysts and nitrogen-containing compounds relative to alkanes, and will be explored more in the discussion section.

Following the temperature-programmed reaction to 500°C, the materials were cooled to room temperature in the *N*-methylpyrrolidine/He mixture. The catalysts were then heated to 600°C in He to desorb any species, affording thermal desorption spectra. Hydrogen TPD spectra for the four catalysts following dehydrogenation reaction (Figure 2.27) are compared to the spectra obtained from a purged material and a material populated via gaseous H_2. The TPD spectra following H_2 pretreatment are consistent with the results previously observed (Figure 2.7), although the high temperature desorption peaks are more pronounced for WC_{1-x}. Further, with the exception of a small peak in WC_{1-x} at ~550°C, no H_2 desorption is observed for the "Purged Surface" case indicating that any hydrogen adsorbed during the initial H_2 pretreatment can be removed during the
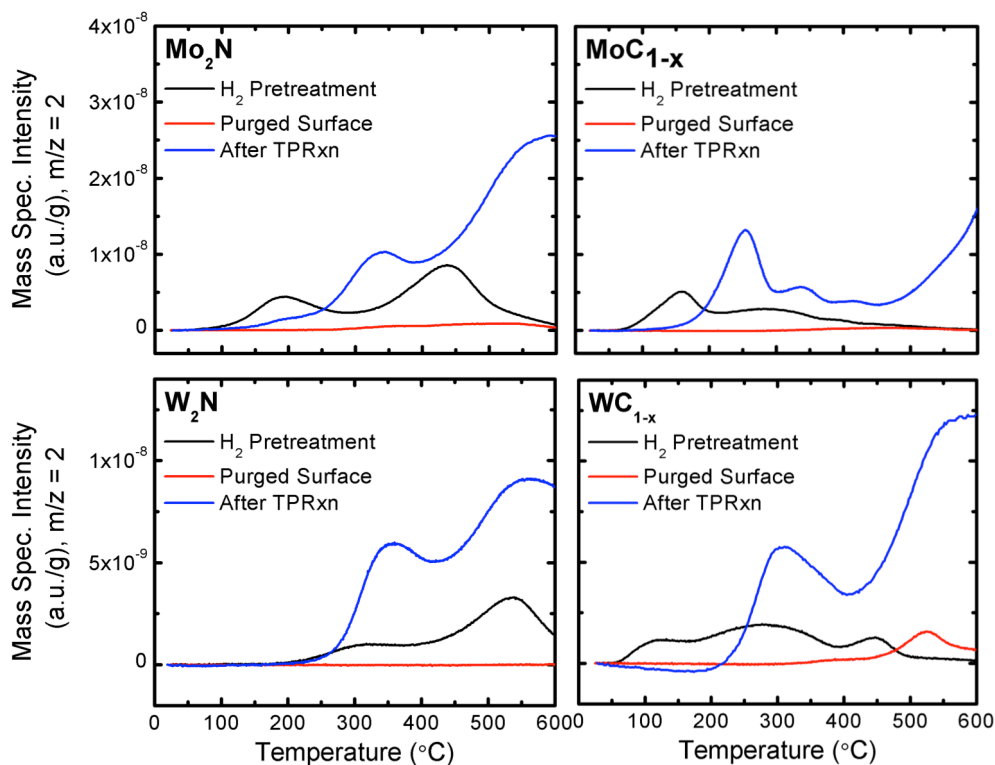
Figure 2.27. Hydrogen TPD for Mo_2N, MoC_{1-x}, W_2N, and WC_{1-x} following three different conditions: (1) 500°C in 10% H_2/Ar for 0.5h ("H_2 Pretreatment"), (2) 500°C in 10% H_2/Ar for 0.5h followed by heating in He to 500°C ("Purged Surface"), and (3) 500°C in 10% H_2/Ar for 0.5h, heating in He to 500°C, and heating to 500°C in a mixture of 0.07% *N*-methylpyrrolidine/He ("After TPRxn"). Heating rates were set to 15°C /min.

purge step. Hydrogen desorption peaks are observed for the four materials following TPRxn as well. The characteristic shape of the spectra seems consistent with that of the H_2 pretreated catalysts, however, the desorption peak centers are shifted to higher temperatures. This shift likely results from changes to the catalyst surface as a result of the dehydrogenation reaction and interactions between the surface and the nitrogen-containing heterocycle. The shift in desorption temperature is most pronounced for Mo_2N. Interestingly, the spectrum for WC_{1-x} resembles that of W_2N post-reaction, potentially indicating that the carbide surface is being nitridized during reaction. Since the carbide is synthesized through a topotactic exchange of C into the W_2N lattice, it is

78

possible that under a nitrogen-rich atmosphere the opposite reaction could occur. Nonetheless, hydrogen desorption is observed following TPRxn indicating that these materials are populated with hydrogen either directly or indirectly during reaction with *N*-methylpyrrolidine.

Direct hydrogen population would involve the transfer of hydrogen from *N*-methylpyrrolidine to the material surface/subsurface, while indirect hydrogen population may proceed through the formation of gaseous H_2 via dehydrogenation, which has already been used to populate these materials. In the case of direct population, hydrogen adsorption sites would help facilitate the transfer of hydrogen from the model substrate to the catalyst surface. For that scenario, dehydrogenation activity of these materials should be influenced by the occupancy of these sites prior to reaction (H-free Mo_2N should be more active than Mo_2N-H_x). *N*-methylpyrrolidine TPRxns were performed over a purged ("Mo_2N") and hydrogenated ("Mo_2N-H_x") Mo nitride material to test this hypothesis (Figure 2.28). The differences in activity were negligible for the two conditions studied.
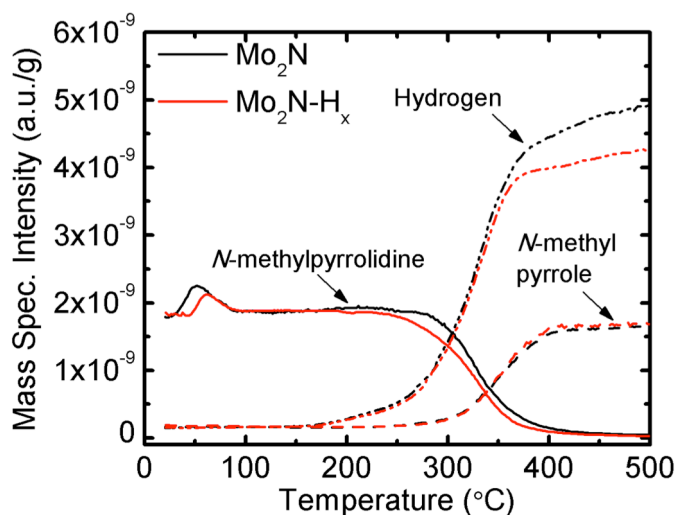
Figure 2.28. *N*-methylpyrrolidine TPRxn over purged and hydrogenated Mo_2N. Heating rates were set to 15 K/min and the reactant feed (50 mL/min) was 0.07% *N*-methylpyrrolidine/He.

While the onset for conversion of *N*-methylpyrrolidine occurred at slightly lower temperatures for Mo_2N-H_x than for Mo_2N, the formation of hydrogen and *N*-methylpyrrole were nearly identical. Based on these results, it appears that the hydrogen binding sites do not play an active role in dehydrogenation catalysis over these materials. Instead, it is more likely that the catalysts are populated with hydrogen indirectly, using the gaseous hydrogen produced during the reaction.

Since carbides and nitrides can be populated with hydrogen via dehydrogenation reactions, additional model substrates, 9,10-dihydroanthracene, 1-phenylethanol, and 1-butanol, were evaluated. 9,10-Dihydroanthracene and 1-phenylethanol represent model compounds containing relatively weak C-H bonds. The C-H bond dissociation energies for 9,10-dihydroanthracene and 1-phenylethanol are 78 and 88 kcal/mol, respectively, compared to 101 kcal/mol for both ethane and ethanol [64,65]. Further, 1-phenylethanol represents a substrate presenting two potential reaction pathways: dehydrogenation to acetophenone or dehydration to styrene, allowing comparison between the preferred pathway over carbides and nitrides. 1-butanol was also selected to represent a saturated version of crotonaldehyde. These three (dehydrogenation of 9,10-dihydroanthracene, 1-phenylethanol, and 1-butanol) reactions (shown in Figure 2.29) were run in the liquid phase given the high boiling points and low vapor pressures of the reactants.

First, dehydrogenation of 9,10-dihydroanthracene (50 μmol) was conducted at 100°C in toluene solvent and under a N_2 headspace over 100 mg of Mo_2N and MoC_{1-x}. Following 4 and 8 hour reaction times, the yield of anthracene, the dehydrogenation product, was quite low for both catalysts studied (Table 2.6). However, MoC_{1-x} was more active than Mo_2N, consistent with the *N*-methylpyrrolidine dehydrogenation TPRxn

results. The cause of the low activity is not yet known; however, it is feasible that reactant adsorption may be irreversibly poisoning the catalyst surface as has been observed during benzene hydrogenation over Mo_2C [66]. Higher reaction temperatures were not explored to improve catalyst performance due to the limitations of the toluene solvent (B.P. 110.6°C). These conditions were, however, suitable to obtain >85% yield (500 μmol) for homogeneous catalysts used previously [67].
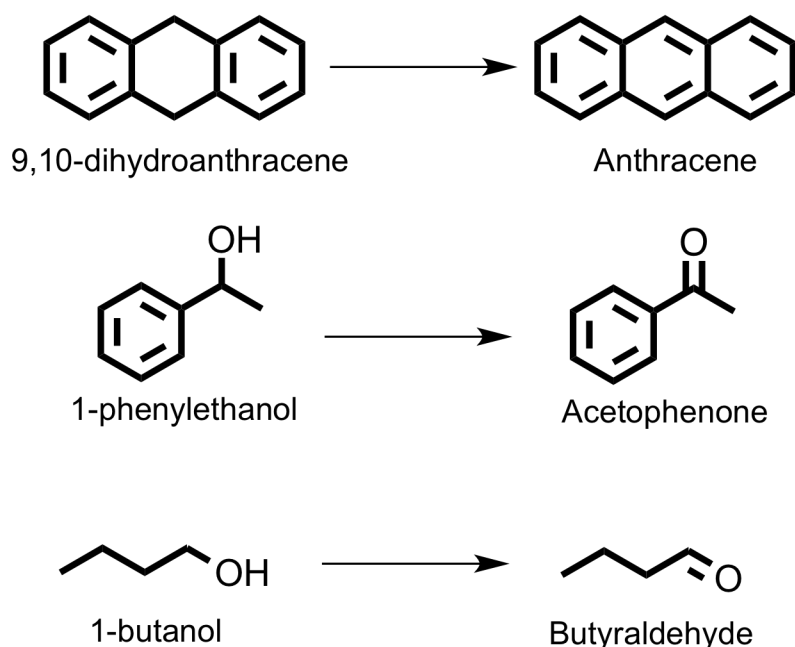
Figure 2.29. Reaction schemes for the dehydrogenation model substrates used: 9,10-dihydroanthracene, 1-phenylethanol, and 1-butanol.

Table 2.6. Anthracene Yields for Dehydrogenation of 10 μmol of 9,10-dihydroanthracene with 100 mg of Mo_2N or MoC_{1-x}. Reaction was conducted at 100°C in toluene solvent with a N_2 headspace for 4 or 8 hours and the anthracene yield was measured via GC.

Catalyst	Time (hr)	Anthracene Yield (%)
Mo_2N	4	1.8 ± 0.1
	8	2.5 ± 0.4
MoC_{1-x}	4	4.5 ± 0.3
	8	6.5 ± 0.9

Given the poor performance of these catalysts with hydrocarbons and aromatics such as 9,10-dihydroanthracene, focus was then shifted towards substrates containing oxygen, as carbides and nitrides are known to be very reactive towards oxygenates [1,68,69,70]. Mo_2N was tested for the dehydrogenation of 1-phenylethanol (10 μmol) to acetophenone at 100°C in toluene and its performance compared to that of 5wt% Pt/C (Sigma Aldrich). The conversion of 1-phenylethanol to acetophenone over Pt/C was 73.4% and the carbon balance was in good agreement (~87% carbon recovery). However, no acetophenone was detected following reaction over Mo_2N despite quantitative conversion of 1-phenylethanol. Instead, multiple unknown GC peaks were observed at longer retention times (Figure 2.30). Gas chromatography-mass spectrometry (GC-MS) was performed in an attempt to identify the unknown peaks. The higher retention time unknown peaks appear to be diphenyl ethyl and diphenyl methyl derivatives, which can result from coupling reaction between two toluene molecules or styrene and toluene [71]. It should be noted that these structures represent the best fits when compared to known MS fragmentation patterns. However, it is definitive that these peaks represent a coupling reaction with multiple phenyl groups. Ethylbenzene was also an observed product in the
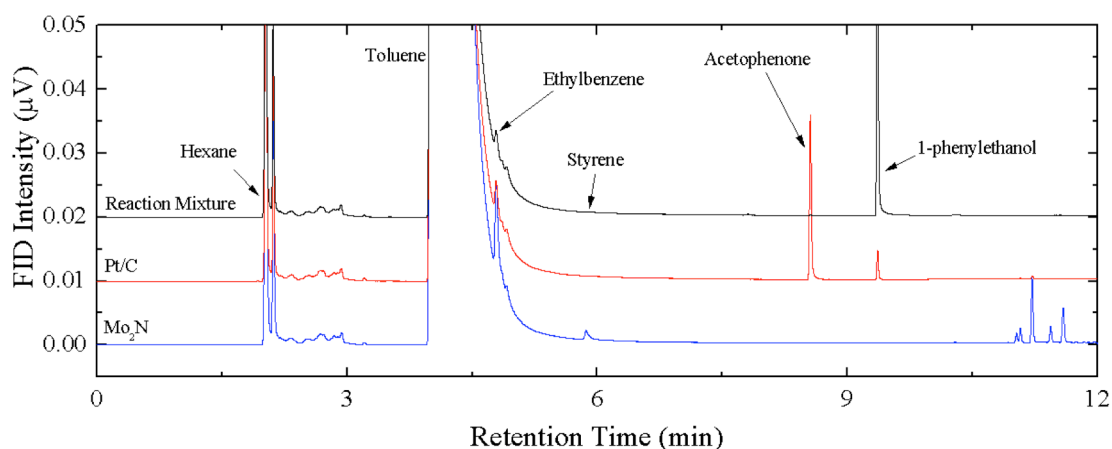
Figure 2.30. GC chromatograms of the reaction mixture for 1-phenylethanol in toluene and after 4 hour reaction over Pt/C or Mo_2N catalysts.

82

GC-MS chromatogram. These results point towards the dehydration of 1-phenylethanol over Mo$_2$N to form styrene, which can be either hydrogenated to form ethylbenzene or coupled with toluene to form the diphenyl ethyl derivatives. It is also possible that partial styrene oligomerization is occurring over Mo$_2$N and the products observed are decomposition products of this oligomer. Based on these results, Mo$_2$N catalysts are more active for dehydration of 1-phenylethanol than dehydrogenation to acetophenone.

To help elucidate the reaction pathway, Mo$_2$N was exposed to reactant mixtures of 1-phenylethanol in toluene, acetophenone in toluene, and styrene in toluene (reactant and possible intermediates). Each reactant (10 μmol) was charged into a separate reactor and allowed to react for 4 hours at 100°C then analyzed by GC (Figure 2.31). Reaction of 1-phenylethanol over Mo$_2$N produced results consistent with previous experiments. Acetophenone was relatively unreactive in the presence of Mo$_2$N. There is measurable conversion (~44%), but this may be due to irreversible chemisorption as aldehydes were shown to chemisorb onto Mo$_2$N based on our work with crotonaldehyde (see Section 3.7; paper reference if appropriate). As expected, the reaction of styrene over Mo$_2$N produced the same GC spectrum as for reaction of 1-phenylethanol, indicating that the reactions of
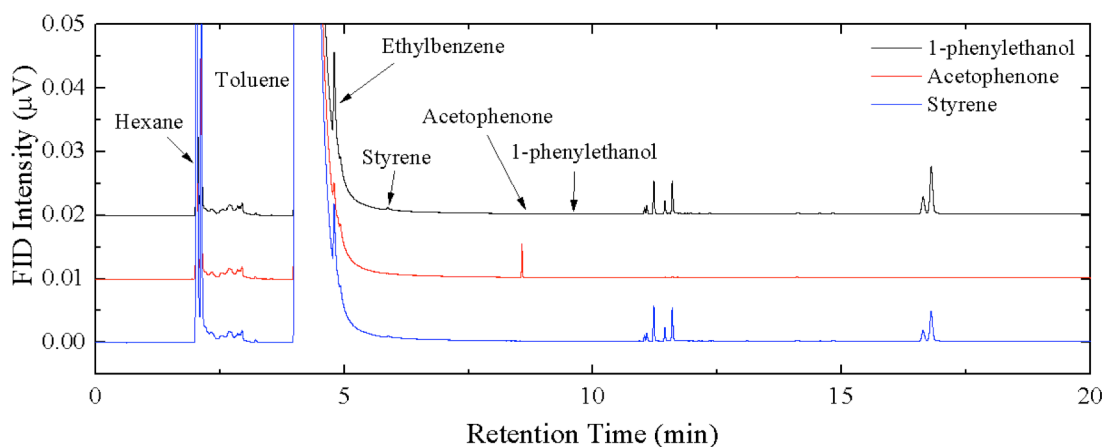
Figure 2.31. Gas chromatograms for the solutions following reaction of Mo$_2$N with 1-phenylethanol (black), acetophenone (red), and styrene (blue) in toluene.

these two compounds proceed via similar pathways. Likely, 1-phenylethanol is dehydrated over Mo_2N to afford water and styrene, which reacts to generate the diphenyl species. These possibilities are summarized in the reaction schematic shown Figure 2.32.
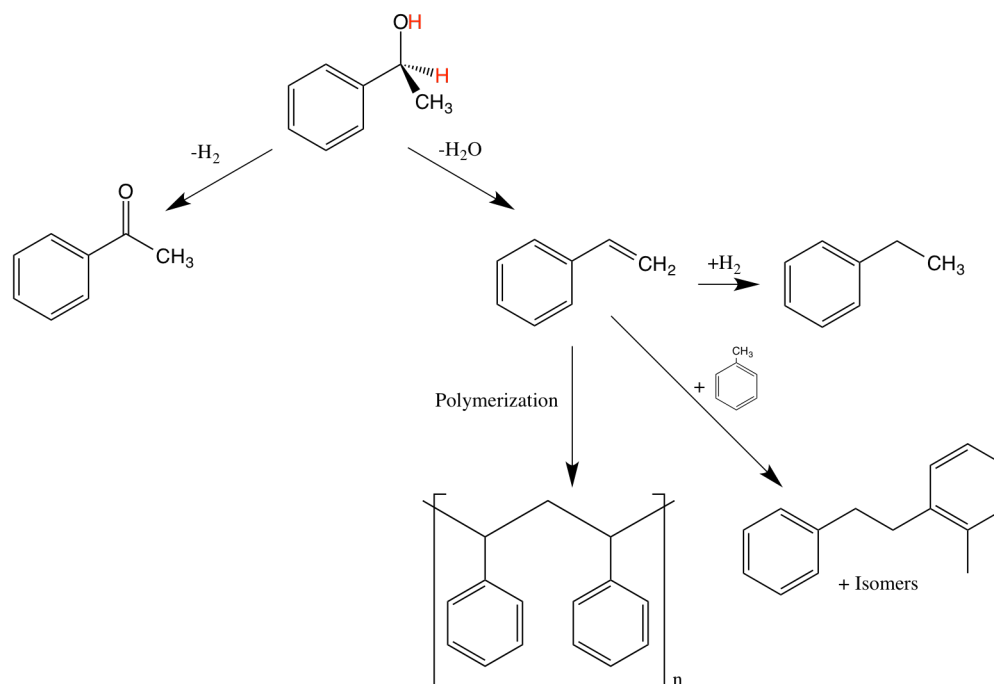
Figure 2.32. Possible reaction pathways for 1-phenylethanol

Mo_2N and MoC_{1-x} were also explored as catalysts for 1-butanol dehydrogenation at higher temperatures (200°C) than those used in the 1-phenylethanol and 9,10-dihydroanthracene experiments. These reactions were run in pure 1-butanol with 100 mg of catalyst. Given its boiling point of 118°C and Antoine equation parameters [72], 1-butanol can be kept in the liquid phase by applying headspace pressures in excess of 9.2 bar. In order to ensure liquid phase reaction, the Swagelok batch reactors were pressurized to 12 bar with a He headspace. GC-FID product analysis was conducted for both the gas and liquid phase products. The pressurized gas headspace was vented into a

line connected to a Valco 10-port valve, which injected some of the gas stream onto the GC column. Liquid analysis was conducted via typical injection through a septum into the 1177 injector. Results for the 3 hour reactions at 150°C and 200°C over the catalysts studied are shown in Table 2.7. Dehydrogenation products such as 1-butyraldehyde, crotyl alcohol, and crotonaldehyde were observed in the liquid phase, while 1-butene and n-butane were observed in the pressurized gaseous headspace. MoC_{1-x} was found to be more active than Mo_2N for both dehydrogenation and dehydration reactions. The dehydrogenation rates were ~2.5 times higher than the dehydration rates for Mo_2N, while they were only ~1.5 higher for MoC_{1-x}. Interestingly, crotyl alcohol was the dominant dehydrogenation product, the reason for which is not yet well understood. Butane formation may be due to the hydrogenation of 1-butene with hydrogen formed via dehydrogenation. It should be noted that X-ray diffraction patterns of the spent catalysts (not shown) showed no changes to the bulk structure indicating the dehydration reactions were proceeding catalytically and not through hydrolysis of the catalyst.

Table 2.7. Dehydrogenation and dehydration product yields from the reaction of 1-butanol over 200 mg Mo_2N and MoC_{1-x}. Reactions were conducted at 200°C in 1-butanol for 4 hours. 12 bar of He was used in the gaseous headspace to keep 1-butanol in the gas phase.

Conditions	Temperature	Dehydrogenation Products (mmol)	Dehydration Products (mmol)
Mo_2N	200°C	163 ± 14	68 ± 16
MoC_{1-x}		464 ± 26	312 ± 33

These results suggest that, while early transition-metal carbides and nitrides can be populated with hydrogen via dehydrogenation of model substrates, these materials are relatively poor catalysts for dehydrogenation reactions. Furthermore, the hydrogen sites did not appear to directly participate in the dehydrogenation reaction mechanism; instead,

the materials are likely populated by reaction with the gaseous hydrogen formed as a result of dehydrogenation. In the case of alcohols, such as 1-butanol and 1-phenylethanol, dehydration to form olefins was a more prevalent reaction pathway than dehydrogenation.

2.4. Discussion

2.4.1. The Chemical Nature of Hydrogen on and in γ-Mo$_2$N-H$_x$

The principal goal of this research was to investigate the population and reactivity of surface and interstitial or subsurface hydrogen associated with early transition-metal carbides and nitrides. After treatment of carbides and nitrides of Mo, W, V, Ti, and Nb with gaseous hydrogen, the hydrogen binding sites were initially screened using H$_2$ temperature-programmed desorption. Based on the observation of two distinct desorption peaks in their spectra, the nitrides were investigated further to determine the physical location of hydrogen in/on the materials, develop methods to preferentially populate the desorption peaks (or sites), and evaluate their reactivity in the hydrogenation of an α,β-unsaturated aldehyde (i.e., crotonaldehyde). Trends were developed between hydrogen desorption peak density and hydrogenation product selectivity. Lastly, materials were populated with hydrogen via alternative hydrogen sources, in particular reduction in NH$_3$ and dehydrogenation of model substrates.

Following high temperature reduction in H$_2$/Ar, all carbides and nitrides studied exhibited distinct H$_2$ desorption spectra. In general, carbides exhibited one dominant peak while the nitrides displayed multiple large desorption peaks (Figure 2.4). Carbides and nitrides of Mo, W, and V showed the most hydrogen profound uptakes (Figure 2.4a-c), while the Nb and Ti-based materials exhibited low or negligible uptakes (Figure

2.4d,e). For the carbides, the gravimetric hydrogen uptakes decreased in the following order: $MoC_{1-x} > Mo_2C > WC_{1-x} > WC > W_2C > VC$. On an areal basis, the trend is slightly different: $WC > W_2C \sim MoC_{1-x} \sim Mo_2C > WC_{1-x} >> VC$. For the nitrides, the gravimetric and areal uptakes both follow the same trend: $W_2N > Mo_2N > VN$. These results indicate that the Mo and W carbide-based materials exhibit similar intrinsic areal uptakes, while VC uptake is lower. This is not a surprising result as comparisons are commonly drawn between the semi-carbide analogs of W and Mo [16,73,74].

Both metal:nonmetal stoichiometry and crystal structure in carbides appear to effect the total site densities, number of sites, and strength of the adsorption bond. The crystal structure of Mo carbides has been reported to drastically impact the catalytic performance of these materials [75]. Focusing on the W results (Figure 2.4b), the peak desorption temperature (indicative of binding strength) decreased in the following order: $WC > WC_{1-x} \sim W_2C$. Thus, it appears that the electronic or ensemble effects resulting from a carbon-rich surface (WC) may result in a stronger surface-hydrogen bond than a carbon-deficient surface (WC_{1-x}, W_2C). Further, as WC, WC_{1-x}, and W_2C represent different crystallographic structures (simple hexagonal, hexagonal close packed [hcp], and face centered cubic [fcc]), one explanation for the difference in binding strength may be the structure of nearest neighbors. It is well-known that adsorbates can bind to multiple sites, such as terraces, step edge defects, and grain boundary defects [76,77]. The crystal structure could possibly affect the energetics of these binding sites. Also of note, comparisons of the effect of crystal structure in the absence of other differences can be made between MoC_{1-x} (fcc) and Mo_2C (hcp) as well as WC_{1-x} (fcc) and W_2C (hcp). The crystal structure of Mo carbides has been reported to drastically affect the catalytic

performance of these materials [78]. Both the fcc and hcp materials represent Mo or W semicarbides, with metal:nonmetal stoichiometries close to 0.5. MoC_{1-x} and Mo_2C exhibit similar desorption profiles dominated by a peak around 100°C (blue and red spectra in Figure 2.4a). However, MoC_{1-x} has 3 shoulders at ~200°C, ~290°C, and ~440°C that are not observed for Mo_2C. Similar observations are made for the W semicarbides, as WC_{1-x} and W_2C materials appear to have comparable desorption peaks (~90°C, 200°C, and 350°C), but they appear in different relative percentages (Figure 2.4b). These desorption peak shoulders may result from binding sites that are inaccessible or of differing extents of exposure in the hcp crystal structure.

Recent literature based on density functional theory (DFT) proposes multiple possible adsorption sites for hydrogen, both dissociative and molecular, in hexagonal Mo_2C (see Figure 2.33) [79,80,81]. These reports suggest the possibility of different H adsorption behavior on the various surface facets. For example, the (001) plane will only adsorb H_2 in a dissociative manner, while the (100), (101), and (201) will adsorb H_2 molecularly, although there is a low barrier towards H_2 dissociation [80]. Furthermore, at high surface coverages, different surfaces were found to exhibit multiple favorable hydrogen adsorption configurations. For example, the (001) surface can yield 4 configurations (one bridge, three hollow), the (100) surface has 3 possible configurations (one top, two hollow), and the (101) surface has 3 possible configurations (one bridge, two top). This suggests that the exposed crystal facet can have a strong impact on the hydrogen adsorption. Changes to the bulk crystal structure may generate new hydrogen adsorption sites by either exposing new facets or changing the relative density of exposed facets. Furthermore, desorption peaks are observed at higher temperatures for MoC_{1-x}

more consistent with those attributed to subsurface hydrogen as observed for Mo_2N. It is plausible that the fcc crystal structure (i.e., MoC_{1-x}) is more conducive towards hydrogen dissolution than hcp (i.e., Mo_2C) due to different diffusion paths into the subsurface vacancies. Transition-state calculations using density functional theory would help analyze this effect.
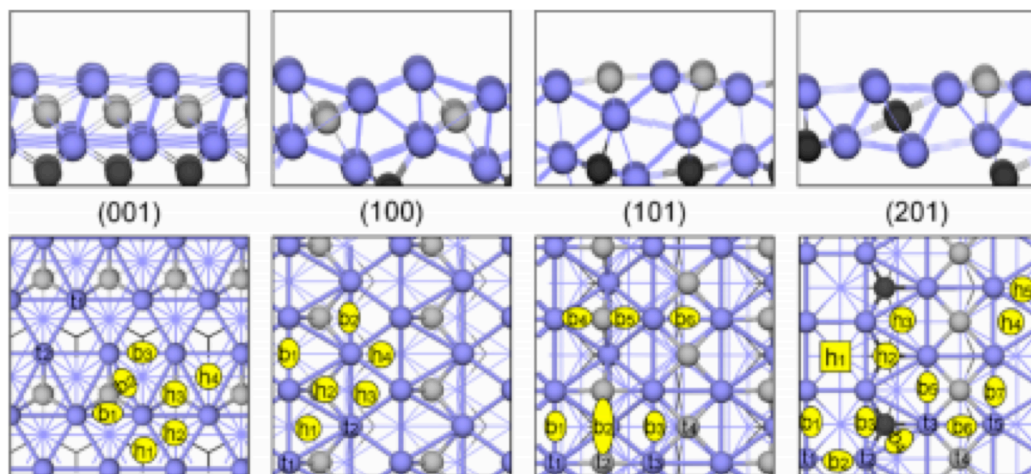
Figure 2.33. Surface crystallographic structure and potential adsorption sites for hydrogen on the different crystal facets for hexagonal Mo_2C. Adapted from [80].

In contrast to the carbide materials, the nitrides exhibited two large desorption peaks. W_2N exhibited the most pronounced high-temperature peak while VN exhibited the smallest. As DFT results indicate that H prefers to sit on the surface ($\varkappa^1$-N-H) and in octahedral holes (μ^6-Mo-H) for Mo_2N-H_x, it is not surprising that VN exhibits the smallest subsurface hydrogen peak since all of the octahedral holes are occupied by nitrogen atoms in this compound. In Mo_2N and W_2N only half of the octahedral sites are occupied. These results provide a great deal of information about the behavior and adsorption of hydrogen on/in these materials, however, additional studies should be performed to deconvolute the role of parent metal, crystal structure, and stoichiometry in these systems.

The multiple, distinct, hydrogen desorption peaks observed in the spectra of Mo, W, and V nitrides prompted further study of the intrinsic reactivity of individual hydrogen sites in these materials. A major goal of the research conducted in this chapter was to develop relationships between hydrogen sites and hydrogenation performance. Methods were developed to prepare γ-Mo$_2$N-H$_x$ materials with varying distributions of hydrogen sites, the nature of the hydrogen at different sites was characterized using experimental and computational methods, and crotonaldehyde (CA) hydrogenation selectivities were evaluated for materials with different hydrogen distributions.

Based on the TPD results, at least two types of sites are occupied by hydrogen in γ-Mo$_2$N. The two peaks observed during the TPD experiments yield very different desorption energies, of 110 (Peak A) and 335 (Peak B) kJ mol^{-1}, respectively. The increase in the height of Peak A relative to that for Peak B with increasing heating rate is evidence of migration of hydrogen from Peak B to Peak A at elevated temperatures. This implies that the inter-site diffusion activation energy is less than the activation energy for the direct desorption of H$_2$ under Peak B. While activation energies for the diffusion of hydrogen in γ-Mo$_2$N are not available, activation energies for hydrogen diffusion between subsurface sites in Mo and Pd are small, on the order of 5-15 kcal mol^{-1} [82]. Consequently, the high desorption energy for Peak B may result from a high energetic barrier for recombination of two H atoms.

The TPD experiments, DFT calculations and INS spectra are consistent with the presence of protic, surface κ^1-NH$_{surf}$ and hydridic, interstitial μ^6-MoH$_{sub}$. However, the simple assignment of Peak A as κ^1-NH$_{surf}$ and Peak B as μ^6-MoH$_{sub}$ is insufficient to explain the observed exchange of hydrogen between sites and the dependence of CA

selectivity on site population. Exchange between the sites producing the peaks was slow under our hydrogenation conditions (70°C). Therefore, for γ-Mo$_2$N-H$_x$ with 92% Peak B, a simple two site model would require the chemically unlikely step of direct chemical reaction of a μ^6-MoH$_{sub}$ with a surface-bound CA.

We suggest that the mechanism for the adsorption and desorption of H$_2$ is a heterolytic process and that Peaks A and B each represent *pairs* of reaction sites. In particular, it is proposed that H$_2$ is added across a Mo–N bond to produce κ^1-NH$_{surf}$ and κ^1-MoH$_{surf}$. The κ^1-MoH$_{surf}$ site is energetically unfavorable relative to the subsurface sites according to density functional theory calculations (-6.4 and +6.3 kcal mol^{-1} for μ^6-Mo-H$_{sub}$ and κ^1-MoH$_{surf}$, respectively); therefore, this hydrogen migrates into the lattice producing μ^6-Mo-H$_{sub}$. Desorption of H$_2$ producing Peak A would then occur by migration of interstitial hydrogen back to the surface where heterolytic recombination of a κ^1-NH$_{surf}$ and κ^1-MoH$_{surf}$ pair could occur. In molecular chemistry, H$_2$ addition across polar metal–halide bonds is common and often facile [83]. The heterolytic cleavage of H$_2$ into a single γ-Mo$_2$N unit cell forming N-H$_{surf}$ + Mo-H$_{subsurf}$, is calculated to be favored by -1.1 kcal mol^{-1} over the formation N-H$_{surf}$ + Mo-H$_{subsurf}$ where there is no interaction between the hydrogens. The parallel calculation for homolytic cleavage of H$_2$ into two κ^1-NH$_{surf}$, is unfavorable by 4.1 kcal mol^{-1}. Both calculations support the assertion of heterolytic cleavage in this system specifically.

Additionally, in such a case, an equilibrium would exist between surface κ^1-Mo-H$_{surf}$ and interstitial μ^6-Mo-H$_{sub}$, such that as surface Mo-H is consumed, diffusion from interstitial sites repopulates the surface. As the NH$_{surf}$ species are depleted, Mo-H$_{surf}$ would dominate. Peak B then results from evolution of H$_2$ via recombination of two Mo-

H$_{surf}$ (see proposed model in Figure 2.34). This recombination seems likely to have a Coulombic penalty because the Mo-H$_{surf}$ are hydridic, which may explain the large desorption energy observed. However, the DFT calculations indicate that surface Mo-H species are thermodynamically unfavorable by at least 6 kcal mol^{-1}. Thus, the high desorption energy may also stem from the inherent difficulty involved in the diffusion and recombination of two interstitial Mo-H species. Consequently high temperatures must be applied to facilitate recombination through the unfavorable Mo-H surface sites.
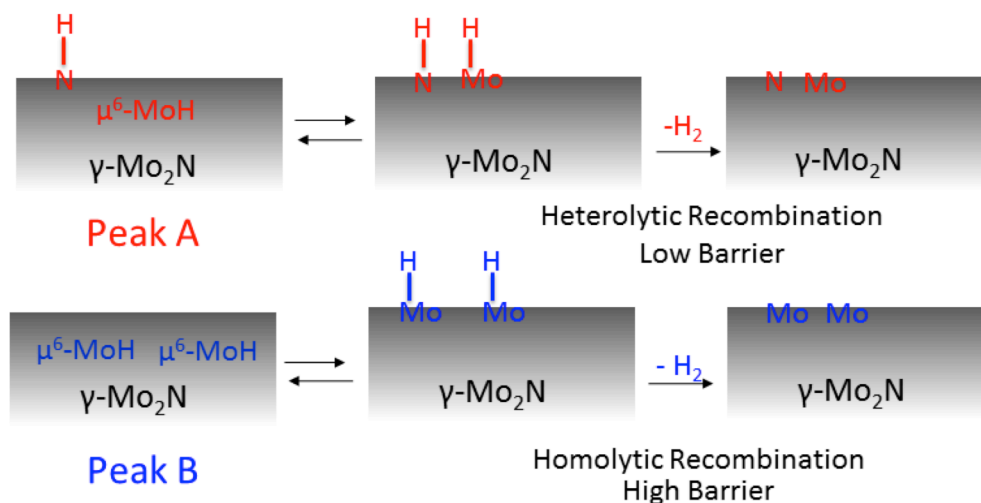
Figure 2.34. Proposed chemical structures and pathways for TPD Peaks A and B.

2.4.2. Hydrogen Site Population and Crotonaldehyde Hydrogenation

The reactions of γ-Mo$_2$N-H$_x$ with excess crotonaldehyde (CA) showed that essentially all of its adsorbed hydrogen can be transferred to CA, including both the surface and subsurface H. This transfer occurred under the relatively mild conditions used for the chemical reactions (1 h at 70°C), despite the slow exchange between sites and loss of the subsurface hydrogen as H$_2$ only above 300°C in the TPD experiments.

Computational analysis shows that CA binds to the surface through the carbonyl oxygen (κ^1-Mo-O bond, -11 kcal/mol). Control experiments with butyraldehyde and

crotyl alcohol show that 1-butanol is only formed through butyraldehyde as an intermediate. Therefore, it is the initial hydrogen transfer that determines the final product selectivity. This is not surprising, as the first hydrogen transfer is also commonly considered the rate-limiting step for CA hydrogenation over metallic catalysts [84,85].

The reactivity results indicate that subsurface hydrogen is preferentially involved in the hydrogenation of CA to crotyl alcohol. The reaction pathway likely involves migration of the subsurface H to surface Mo–H sites, which are indicated to be accessible via DFT calculations, although higher in energy than the ground state κ^1-NH$_{surf}$/μ^6-Mo-H$_{sub}$ arrangement. Based on the hydrogen desorption model described earlier, Peak A in the TPD spectrum is for H$_2$ derived from κ^1-NH$_{surf}$ and κ^1-MoH$_{surf}$. Reasonable transition states for H transfer to either the C=O or C=C bond in CA can be drawn for κ^1-MoH$_{surf}$ (Figure 2.35, right) and κ^1-NH$_{surf}$, respectively (Figure 2.35, left). Therefore, the resulting product distribution would be non-selective as observed. When the hydrogen population is biased towards that of Peak B, the material preferentially contains κ^1-MoH$_{surf}$ and μ^6-MoH$_{sub}$ sites. The κ^1-MoH$_{surf}$ sites favor C=O hydrogenation over C=C as observed is favored both by the 6-membered ring geometry (Figure 2.35, right) and by the preference of the hydridic H for reacting with the electrophilic carbon.

It is interesting that the hydrogenation of CA by γ-Mo$_2$N-H$_x$, containing both Peak A and Peak B hydrogen, is not very selective. The model in Figure 2.34 implies a substantial surface coverage of N-H groups, but only low concentrations of surface Mo-H formed by the unfavorable diffusion of subsurface hydrogen. The low-concentration of κ^1-MoH$_{surf}$ must therefore be more reactive toward C=O hydrogenation than the κ^1-NH$_{surf}$ species are toward C=C hydrogenation.
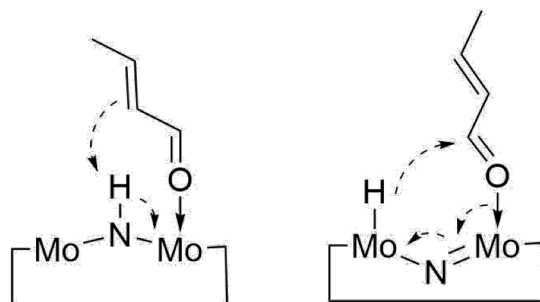
Figure 2.35. Proposed intermediates for CA reduction. The schematics hypothesize the interaction of CA with (left) κ^1-NH_{surf} species and (right) κ^1-MoH_{surf} species over Mo_2N.

It is worth noting the very different selectivities between the use of Mo_2N-H_x versus a headspace of 10 atm H_2 with either Mo_2N-H_0 or Pt/Al_2O_3. Crotyl alcohol selectivities between ~72 and 96% were achieved for the pre-hydrogenated Mo_2N-H_x material while Mo_2N and Pt/Al_2O_3 under a H_2 headspace produced lower selectivities (~65 and 8%, respectively). These results illustrate the selectivity benefits of employing a hydrogenated Mo_2N.

The reactivity trends observed for Mo_2N-H_x were not universal to other early transition metal carbides and nitrides. W_2N was inactive for hydrogenation under the conditions used, perhaps for two possible reasons: (1) the formation of acetals occurred at a faster rate than the hydrogenation of crotonaldehyde and/or (2) hydrogen associated with these materials were bound too strongly to W_2N to allow for hydrogen addition to proceed. Conversely, VN was active for crotonaldehyde hydrogenation and exhibited near 100% selectivities to crotyl alcohol for all hydrogen populations tested at the temperature used. These results potentially indicate that one of the hydrogen sites is not active for hydrogenation or that the hydrogens associated with the two observed desorption peaks behave similarly in the presence of crotonaldehyde.

2.4.3. Alternative Hydrogen Sources and Dehydrogenation Performance

Other potential hydrogen sources, NH_3 and dehydrogenation model substrates, were evaluated for populating the carbide and nitride materials with hydrogen. Reduction of carbides and nitrides in NH_3 was found to generate a different H_2 desorption peak, though further analysis indicated that this hydrogen was not reactive and could be attributed to the decomposition of NH_3 given a similar desorption shoulder for NH_3 at the same temperature. The carbide and nitride materials were capable of site population via interaction with the hydrogen gas formed as a result of the dehydrogenation of model compounds, such as N-methylpyrrolidine, at high temperatures (~250-300°C). However, the carbides and nitrides were not very active catalysts for dehydrogenation at lower temperatures (~100°C) in the liquid phase. While complete 1-phenylethanol conversion was observed in our system, no acetophenone was produced. Instead, styrene was formed via dehydration and reacted further to form diphenyl compounds. For comparison, Chakraborty et al. observed complete conversion and nearly 90% yield of acetophenone from 500 μmol of 1-phenylethanol following reaction with a homogeneous Ni catalyst under similar conditions for 24 hours [67]. While complete 1-phenylethanol conversion was observed in our system, no acetophenone was produced. Instead, styrene was formed via dehydration and reacted further to form diphenyl complexes. While poor dehydrogenation was observed over carbides and nitrides studied, there are literature reports detailing dehydrogenation activity for other substrate/solvent combinations. In one example, Li et al. recently reported on the dehydrogenation of benzyl alcohol at 120°C in dimethyl sulfoxide (DMSO) over MoC_{1-x} and Mo_2C, noting that Mo_2C was more active than MoC_{1-x} [62]. However, chemically, dehydration reactions are not a

feasible pathway for benzyl alcohol. Therefore, Li et al. only observed dehydrogenation to benzaldehyde. Comparison of the relative reaction rates for dehydrogenation and dehydration of 1-phenylethanol in our work indicated that dehydration is favored. It may prove worthwhile to investigate dehydrogenation of benzyl alcohol over MoC_{1-x} and Mo_2N using the same experimental conditions to test the intrinsic dehydrogenation activity in the absence of a dehydration pathway.

2.5. Summary

The formation, location, nature and reactivity of hydrogen species in/on early transition-metal carbides and nitride have been investigated. H_2-treatment of these materials affords a hydrogen-containing material (i.e., γ-Mo_2N-H_x). Carbides exhibited primarily one dominant desorption peak, while spectra for nitrides contained two peaks. Mo_2N-H_x, a common catalyst from the carbide and nitride family, was the focus of the work for much of the chapter. A combination of experimental (TPD, INS) and theoretical (DFT) approaches indicated the presence of multiple hydrogen sites on/in Mo_2N: surface nitrogen-bound (κ^1-NH_{surf}); surface Mo-bound (κ^1-MoH_{surf}); and subsurface Mo-bound (μ^6-Mo_6H_{sub}). The reactivity of the hydrogen in γ-Mo_2N-H_x was probed using liquid-phase crotonaldehyde (CA) hydrogenation, a model for assessing product selectivity between C=O and C=C hydrogenation paths. γ-Mo_2N-H_x prepared with preferential population of the hydrogen associated with high temperature desorption (TPD Peak B) gave high chemoselectivity to C=O hydrogenation. On the other hand, extrapolation to material with only low temperature desorption (TPD Peak A) hydrogen sites indicated roughly equal selectivity for C=O and C=C hydrogenation.

Based on the characterization and reactivity results, a model for hydrogen adsorption was proposed in which H_2 initially adds to γ-Mo_2N via a heterolytic mechanism, forming surface NH (κ^1-NH_{surf}) and MoH (κ^1-MoH_{surf}) groups. The κ^1-MoH_{surf} site was found to be less energetically favorable than the subsurface interstitial hydrogen site (μ^6-MoH_{sub}); therefore hydrogen likely migrates into the lattice particularly at higher temperatures. It is hypothesized that H_2 desorption Peak A stems from the heterolytic recombination of surface κ^1-NH_{surf} and μ^6-MoH_{sub}, while Peak B results from the more energy intensive recombination of two subsurface μ^6-MoH_{sub} species. What is critical, however, is that both κ^1-NH_{surf} and κ^1-MoH_{surf} sites are apparently kinetically accessible under the catalytic conditions for CA hydrogenation. Our results suggest that the κ^1-MoH_{surf}/μ^6-MoH_{sub} sites preferentially hydrogenate the C=O bond in CA while the κ^1-NH_{surf} sites appear to hydrogenate the C=C bond.

Lastly, alternative hydrogen sources, such as NH_3 and dehydrogenation substrates, were also explored for hydrogen population of Mo and W carbides and nitrides. Dehydrogenation reactions resulted in hydrogen population of the materials, but only indirectly through the formation of hydrogen gas followed by reaction with the material surface.

Overall, the results detailed in this chapter indicate that carbides and nitrides can exhibit multiple active sites for catalytic hydrogenations, and that these sites can have different intrinsic reactivity towards model compounds. Our findings may help rationalize the hydrogenation reactivity of this class of catalytic materials, and provide valuable insight into possible methods for tuning or optimizing their performance. In addition, these findings could generate research thrusts in new areas, such as materials for

hydrogen storage and membranes for hydrogen separation via dissociation and recombination.

2.6.   References

[1]   S.T. Oyama (Ed.). (1996). *The Chemistry of Transition Metal Carbides and Nitrides*. London, UK: Blackie Academic & Professional.
[2]   F.A. Lewis, *Platinum Metal Reviews*. 4 (1960) 132-137.
[3]   B. Bhatia, D.S. Sholl, J. Chem. Phys. 122 (2005) 204707.
[4]   R. Löber, D. Hennig, Phys. Rev. B. 55 (1997) 4761
[5]   J. Greeley, M. Mavrikakis, J. Phys. Chem. B. 109 (2005) 3460-3471.
[6]   J.G. Choi, J.R. Brenner, C.W. Colling, B.G. Demczyk, J.L. Dunning, L.T. Thompson. Catalysis Today. 15 (1992) 201-222
[7]   Y. Zhang, Y. Li, C. Li, Q. Xin. Studies in Surface Science and Catalysis. 112 (1997) 457-464
[8]   P. Pande, A. Deb, A.E.S. Sleigtholme, A. Djire, P.G. Rasmussen, J. Penner-Hahn, L.T. Thompson. Journal of Power Sources, 289 (2015) 154-159.
[9]   Y. Madier, C. Descorme, A.M. Le Govic, D. Duprez. J. Phys. Chem. B. 103 (1999) 10999–11006
[10]   S.O. Choi, M. Penninger, C.H. Kim, W.F. Schneider, L.T. Thompson. ACS Catal. 3 (2013) 2719−2728
[11]   S.P. Daley, A.L. Utz, T.R. Trautman, S.T. Ceyer. J. Am. Chem. Soc. 116 (1994) 6001-6002
[12]   F.A. Lewis. Platinum Metals Rev. 1982, 26, 20-27
[13]   M. Shirai, Y. Pu, M. Arai, Y. Nishiyama. Appl. Surf. Sci. 126 (1998) 99-106
[14]   R.R. Oliveira Jr., A.S. Rocha, V.T. da Silva, A.B. Rocha. Appl. Cat. A: General. 469 (2014) 139–145
[15]   D.M. Alonso, J.Q. Bond, J.A. Dumesic. Green Chem., 12 (2010) 1493–1513
[16]   Schaidle, J.A. *PhD Dissertation,* University of Michigan, 2011.
[17]   P. Pande, P.G. Rasmussen, L.T. Thompson. J. Power Sources. 207 (2012) 212-215.
[18]   A. Djire, PhD. Dissertation, University of Michigan, 2016.
[19]   S. Brunauer, P.H. Emmett, E. Teller. J. Am. Chem. Soc. 60 (1938) 309-319.
[20]   E.P. Barret, L.G. Joyner, P.P. Halenda. J. Am. Chem. Soc., 73 (1951) 373-380.
[21]   G. Horváth, K. Kawazoe. J. Chem. Eng. Japan 16 (1983) 70-475.
[22]   J.L. Falconer, R.J. Madix, Surf. Sci. 48 (1975) 393.
[23]   B.C. Campo, M.A. Volpe, C.E. Gigola. *Ind. Eng. Chem. Res.,* 48 (2009) 10234-10239
[24]   B. Campo, G. Santori, C. Petit, M. Volpe. *Appl. Cat. A: General.* 359 (2009) 79-83
[25]   Y. Higashio, T. Shoji. Appl. Cat. A: General 260 (2004) 251-259.
[26]   TOSCA neutron spectrometer: The final configuration. Colognesi, D.; Celli, M.; Cilloco, F.; Newport, R. J.; Parker, S. R.; Rossi-Albertini, V.; Sacchetti, F.; Tomkinson, J.; Zoppi, M., *Applied Physics a-Materials Science & Processing* 2002, *74*, S64-S66.

[27]   a) *Mantid: Manipulation and Analysis Toolkit for Instrument Data*, version 3.3.0; Mantid Project, 2015, http://dx.doi.org/10.5286/Software/Mantid3.3 b) Arnold, O.; Bilheux, J. C.; Borreguero, J. M.; Buts, A.; Campbell, S. I.; Chapon, L.; Doucet, M.; Draper, N.; Ferraz Leal, R.; Gigg, M. A.; Lynch, V. E.; Markvardsen, A.; Mikkelson, D. J.; Mikkelson, R. L.; Miller, R.; Palmen, K.; Parker, P.; Passos, G.; Perring, T. G.; Peterson, P. F.; Ren, S.; Reuter, M. A.; Savici, A. T.; Taylor, J. W.; Taylor, R. J.; Tolchenov, R.; Zhou, W.; Zikovsky, J. Nuclear Instruments and Methods in Physics Research Section A: Accelerators, Spectrometers, Detectors and Associated Equipment 2014, 764, 156–166.

[28]   *Igor Pro*, version 6.3.6.4; Wavemetrics Inc.: Lake Oswego, Oregon, 1988-2014.

[29]   A. J. Ramirez-Cuesta, *Comp. Phys. Commun.* 157 (2004) 226-238.

[30]   G. Kresse, J. Hafner, Phys. Rev. B 47 (1993) 558-561

[31]   G. Kresse, J. Furthmuller, Comput. Mater. Sci. 6 (1996) 15-50

[32]   G. Kresse, J. Furthmuller, Phys. Rev. B 54 (1996) 11169-11186

[33]   G. Kresse, J. Furthmuller, J. Phys. Rev. B 59 (1999) 1758-1775

[34]   H.J. Monkhorst, J.D. Pack, Phys. Rev. B 13 (1976) 5188-5192.

[35]   J.P. Perdew, K. Burke, M. Ernzerhof. Phys. Rev. Lett. 77 (1996) 3865-3868.

[36]   ICDD PDF# 00-025-1366

[37]   B.M. Wyvratt, J.R. Gaudet, L.T. Thompson, *J. Catalysis* 330 (2015) 280-287.

[38]   X.S. Li, Y.X. Chen, Y.J. Zhang, C.X. Ji, Q. Xin, React. Kinet.Catal. Lett. 58 (1996) 391-396

[39]   Hydrogen Effects in Catalysis: Fundamentals and Practical Applications; Paal, Z., Menon, P. G., Eds.; Marcel Decker: New York, 1988.

[40]   K.J. Leary, J.N. Michaels, A.M. Stacy. *AIChE Journal.* 34 (1988) 263-271.

[41]   K.J. Leary, J.N. Michaels, A.M. Stacy. *Langmuir.* 4 (1988) 1251-1257.

[42]   *Hydrogen and Helium Recycling at Plasma Facing Materials.* Ed. Ahmed Hassanein, Kluwer Academic Publishers, Dordrecht, Netherlands, 2001.

[43]   J.G. Choi, H.J. Lee, L.T. Thompson. Applied Surface Science 78 (1994) 299-307.

[44]   R.J. Behm, K. Christmann, G. Ertl. Surface Science 99 (1980) 320-340

[45]   B.M. Wyvratt, J.R. Gaudet, D.B. Pardue, A. Marton, S. Rudic, E.A. Mader, T.R. Cundari, J.M. Mayer, L.T. Thompson, *ACS Catalysis*, 6 (2016) 5797-5806.

[46]   M. del C. Aguirre, P.O. Reyes, M. Oportus, I. Melián-Cabrera, J.L.G. Fierro, Appl. Cat. A: General 233 (2002) 183-196.

[47]   P. Chen, J. Lu, G. Xie, L. Zhu. React. Kinet. Mech. And Catal. 106 (2012) 419-434

[48]   L. Zhu, J.-Q. Lu, P. Chen, X. Hong, G.-Q. Xie, G.-S. Ho M.-F. Luo, J. Molec. Catal. A: Chem. 361 (2012) 52-57

[49]   M.S. Ide, B. Hao, M. Neurock, R.J. Davis, ACS Catal. 2 (2012) 671-683

[50]   F.A.J. Meskens, *Synthesis* 7 (1981) 501-522.

[51]   C. Ando, H. Kurokawa, H. Miura, Appl. Cat. A: General 185 (1999) L181-L183.

[52]   S. Galvagno, G. Capannelli, G. Neri, A. Donato, R. Pietropaolo, J. Mol. Catal. 64 (1991) 237

[53]   B. Coq, P.S. Kumbar, C. Moreau, P. Moreau, M.G. Warawdekar, J. Mol. Catal. 85 (1993) 215.

[54] C. Milone, C. Crisafulli, R. Ingoglia, L. Schipilliti, S. Galvagno. Catal. Today 122 (2007) 341-351.

[55] B.V. Vora, Topic in Catalysis, 55 (2012) 1297-1308.

[56] A.H. White, Wm. Melville, *J.* Am. Chem. Soc., 27 (1905) 373-386.

[57] W. Zheng, T.P. Cotter, P. Kaghazchi, J. Timo, B. Frank, K. Schlichte, W. Zhang, D.S. Su, F. Schüth, R. Schlögl, J. Am. Chem. Soc., 135 (2013) 3458-3464.

[58] J.N. Koral, J. Polymer Science, 61 (1962) S37-S38.

[59] J. Du, J. Wu, T. Guo, R. Zhao, J. Li. RSC Advances, 96 (2014) 53950-53953.

[60] H. Abe, A.T. Bell, J. Catalysis 142 (1993) 430-436.

[61] H. Kwon, L.T. Thompson, J. Eng Jr., J.G. Chen. J. Catalysis 190 (2000) 60-68.

[62] Z. Li, C. Chen, E. Zhan, N. Ta, Y. Li, W. Shen. Chem. Commun. 50 (2014) 4469-4471.

[63] M.K. Neylon, S. Choi, H. Kwon, K.E. Curry, L.T. Thompson. Appl. Cat. A: General 183 (1999) 253-263.

[64] F.G. Bordwell, J.-P. Cheng, A.V. Satish, C.L. Twyman. J. Org. Chem. 57 (1992) 6542-6546.

[65] Y.-R. Luo *Handbook of Bond Dissociation Energies in Organic Compounds*. CRC Press, Boca Raton, Florida, 2003.

[66] A.S. Rocha, A.B. Rocha, V. Teixeira da Silva, Appl. Cat. A: General 379 (2010) 54-60

[67] S. Chakraborty, P.E. Piszel, W.W. Brennessel, W.D. Jones. Organometallics 34 (2015) 5203-5206.

[68] J.A. Schaidle, J. Blackburn, C.A. Farberow, C. Nash, K.X. Steirer, J. Clark, D.J. Robichaud, D.A. Ruddy. *ACS Catal.* 6 (2016) 1181-1197.

[69] H. Ren, W. Yu, M. Salciccioli, Y. Chen, Y. Huang, K. Xiong, D.G. Vlachos, J.G. Chen. ChemSusChem. 6 (2013) 798-801.

[70] J.G. Chen, Chem. Rev. 96 (1996) 1477-1498.

[71] I. Moritani, Y. Fujiwara, Tetrahedron Letters 12 (1967) 1119-1122.

[72] D. Ambrose, R. Townsend, J. Chemical Society. (1963) 3614-3625.

[73] M.R. Toosi, M.H Peyrovi, R. Mondgarian. React. Kinet. Catal. Lett. 98 (2009) 133-138.

[74] M.C. Weidman, D.V. Esposito, Y.-C. Hsu, J.G. Chen. J. Power Sources 202 (2012) 11-17.

[75] S. Li, J.S. Lee, T. Hyeon, K.S. Suslick. Appl. Cat. A: General 184 (1999) 1-9.

[76] S. Vollmer, G. Witte, C. Wöll. Catal. Letters 77 (2001) 97- 101.

[77] B. Hammer, I.H. Nielsen, J.K. Norskov. Catal. Letters 46 (1997) 31-35.

[78] S. Li, J.S. Lee, T. Hyeon, K.S. Suslick. Appl. Cat. A: General. 184 (1999) 1-9.

[79] J. Ren, C-F. Huo, J. Wang, Z. Cao, Y-W. Li, H. Jiao. Surf. Sci. 600 (2006) 2329-2337.

[80] T. Wang, Y.-W. Li, J. Wang, M. Beller, H. Jiao. J. Phys. Chem. C. 118 (2014) 8079-8089.

[81] T. Wang, X. Tian, Y. Yang, Y.-W. Li, J. Wang, M. Beller, H. Jiao. Surf. Sci. 651 (2016) 195-202.

[82] *Hydrogen and Helium Recycling at Plasma Facing Materials*. Ed. Ahmed Hassanein, Kluwer Academic Publishers, Dordrecht, Netherlands, 2001.

[83]   J.R. Webb, S.A. Burgess, T.R. Cundari, T.B. Gunnoe. *Dalton Transactions* 42 (2013) 16646-16665.

[84]   M. Tamura, K. Tokonami, Y. Nakagawa, K. Tomishige, ACS Catal. 6 (2016) 3600−3609.

[85]   W. Shi, L. Zhang, Z. Ni, X. Xiao, S. Xia. RSC Adv. 4 (2014) 27003-27012.

CHAPTER 3

Metal-Mo₂C Redox & Water-gas Shift Performance

3.1. Introduction

Catalyst supports play a critical role in the performance of heterogeneous catalysts. The most important function of the support is typically to facilitate dispersion of the active phase, although the support can also participate in the reaction [1,2] and/or alter the electronic structure of the active phase [3,4]. A variety of supports have been investigated for catalytic applications (e.g., Al_2O_3, SiO_2, C and zeolites) [5-8]. Early transition metal carbides and nitrides offer unique properties as supports for both electrochemical [9] and chemical catalysts [10-12]. These materials can be synthesized with high surface areas (>100m^2/g) [13] and can have catalytic properties that resemble those of platinum group metals (e.g., Pd, Ru, Pt) [14]. Nitride- and carbide-supported metal catalysts have been reported to be active for chemical reactions including, but not limited to, hydrodenitrogenation and hydrodesulfurization of carbazole, thiophene, and 4,6-dimethyldibenzothiophene [10,15], selective hydrogenations of p-chloronitrobenzene and crotonaldehyde [12, 16], CO hydrogenation and Fischer-Tropsch Synthesis [17,18,19,20], methanol steam reforming [21,22], and water-gas shift [11,23], as well as electrochemical reactions, such as hydrogen evolution [9,24] and hydrogen oxidation reactions [25].

Early transition metal carbides and nitrides, like other highly reduced materials, are subject to oxidation on exposure to air. Prior to exposure to air, these materials are

typically treated to form a passivation layer that prohibits bulk oxidation. As a result, most carbide- or nitride-supported metal catalysts reported in the literature have been prepared by deposition or impregnation of the metal onto the passivated carbide or nitride surface [12,15-20,24]. Since the passivation layer is oxygen rich and metal at the surface of the carbide or nitride is oxidized [23], interactions between the passivated material and the deposited metal could be quite different from those for the unpassivated ("native") carbide or nitride. To date, there have been few reports of metal deposition onto unpassivated carbide or nitride supports [11,21,26]. Most indicate that the properties of metals supported on native carbides and nitrides are significantly different from those for metals on the passivated carbides and nitrides. Schweitzer et al. observed the formation of "raft-like" Pt particles on a Mo_2C support with the resulting catalyst exhibiting water-gas shift activities that were superior to those for Pt supported on oxides, which are among the most active known catalysts [11]. Schaidle et al. investigated the deposition of a variety of late transition metals onto unpassivated Mo_2C [26]. They reported that some metal precursors (e.g., Pt^{4+}, Pd^{2+}, Cu^{2+}) were spontaneously reduced during deposition/interaction with the native Mo_2C surface, suggesting the presence of surface redox chemistry (likely through oxidation of Mo). The possibility of redox chemistry is not surprising given that the carbides and nitrides are in a highly reduced state. However, the presence of a passivation layer would likely inhibit this redox chemistry. Shou et al. reported effects of the passivation layer on Rb-promoted Mo_2C-based CO hydrogenation catalysts [27]. The authors focused on defining effects of the presence of the passivation layer during hydrogenation reactions as opposed to during catalyst synthesis, noting that the unpassivated $Rb/Mo_2C/Al_2O_3$ performed similarly to its passivated counterpart.

However, Rb^+ is very difficult to reduce ($E° = -2.93V$) and would likely not be spontaneously reduced upon interaction with Mo_2C as observed with Pt^{4+}, Pd^{2+}, and Cu^{2+} ($E° = 0.74, 1.13,$ and 0.34, respectively) [28].

The goal of our research was to characterize key reactions that occur during the preparation of Pt/Mo_2C catalysts, and to systematically compare the compositional, structural and functional properties of unpassivated and passivated Mo_2C supported metal catalysts. Initial work focused on confirming the presence of redox chemistry between depositing H_2PtCl_6 and the unpassivated Mo_2C support by monitoring the reaction via cyclic voltammetry or monitoring the oxidation states of Pt and Mo throughout the wet impregnation process using X-ray photoelectron and adsorption spectroscopies.

The influence of surface redox chemistry on Mo_2C-supported metal catalysts is then explored. The required surface passivation of Mo_2C due to its inherent pyrophoricity enabled the comparison of a reduced and oxidized support surface with which to control the redox reaction. Extensive physical characterization of the passivated and unpassivated supports was performed, along with characterization of the materials following exposure to aqueous solutions. Further, interactions between metal precursors and the Mo_2C supports during wet impregnation were characterized to better understand the role of redox chemistry in this process. These experiments were also extended to an isolated form of the oxycarbide passivation layer to understand its role in the interaction between metals and passivated Mo_2C. Lastly, the compositional and structural differences between catalysts synthesized with and without redox chemistry were explored, focusing on the impact to their water gas shift activities. The water-gas shift reaction rates are compared

to those for a commercial Cu-ZnO/Al$_2$O$_3$ catalyst, allowing a connection with the broader literature regarding water gas shift catalysis.

3.2.   Experimental Methods

3.2.1. Catalyst Synthesis

Molybdenum carbide (Mo$_2$C) was synthesized via temperature-programmed reaction (TPR) as previously reported [29,30,31]. Approximately 1.3g of ammonium paramolybdate (AM, Alfa Aesar, 81-83% as MoO$_3$, particle size 125-250μm) was loaded into a quartz flow-through reactor, supported by a bed of quartz wool, and secured in a vertical furnace. The precursor was heated from room temperature to 350°C under H$_2$ flow (400 mL/min) at a heating rate of 5°C/min followed by a 12 hr soak at this temperature. Following the soak step, 15% CH$_4$/H$_2$ gas was introduced (400mL/min) and the material was heated to 590 °C at 2.67 °C/min followed by a 2 hr soak. Upon completion, the reactor was removed from the furnace and allowed to cool to room temperature under 15% CH$_4$/H$_2$ gas flow.

When the reactor had cooled to below 30°C, the material was treated in one of four ways: (1) transfer into an inert atmosphere glovebox without air exposure (referred to as Mo$_2$C), (2) surface passivation (material referred to as p-Mo$_2$C), (3) metal deposition onto Mo$_2$C followed by reduction and passivation (to produce [Metal]/Mo$_2$C), or (4) metal deposition onto p-Mo$_2$C followed by reduction and passivation (to produce [Metal]/p-Mo$_2$C). To obtain the unpassivated Mo$_2$C, the reactor was sealed and transferred into an inert atmosphere glove box without exposure to air. To passivate the surface, the material was exposed to 1% O$_2$/He flowing at 20mL/min for at least five hours. The third and fourth treatments involve the deposition of metal onto the

105

unpassivated or passivated Mo_2C support via a wet impregnation method previously reported in detail for Mo_2C [31]. In brief, the unpassivated or passivated Mo_2C was transferred from the quartz reactor (without exposure to air) into a deaerated, aqueous solution of the metal precursor salt (H_2PtCl_6, $(NH_3)_4Pd(NO_3)_2$, $Cu(NO_3)_2$, $Ni(NO_3)_2$, and $Co(NO_3)_2$), which was continuously sparged with Ar. The target loading (approximately 10% surface coverage based on 105 m^2/g and 10 sites/nm^2) was selected to be consistent with previous work [29,30]. The metals were allowed to deposit for 8 hrs. Following deposition, the catalyst was transferred back to the quartz reactor under argon blanket then reduced with H_2 at 110°C for 2 hr, followed by 450°C for 4 hr. The material was then cooled and passivated as described above in order to inhibit bulk oxidation.

Al_2O_3-supported Mo_2C materials were synthesized for X-ray absorption spectroscopy (XAS) experiments. γ-Al_2O_3 (Alfa Aesar, 78 m^2/g, pore volume of 0.40 cm^3/g) was dry impregnated with AM. After drying, the resulting material was carburized via temperature-programmed reaction using conditions described above. These materials were either (1) passivated for characterization or (2) transferred directly into an inert glove box and pelletized (60 mg pellets) for use in the X-ray absorption experiments.

3.2.2. Catalyst Characterization

3.2.2.1. X-ray Powder Diffraction

The crystal structure of the synthesized catalysts was determined via X-ray powder diffraction using a Rigaku Miniflex X-ray diffractometer employing a Cu Kα X-ray source and a Ni filter. Experimental and analysis procedures were described previously in Chapter 2 (Section 2.2.2.1.).

3.2.2.2.   N$_2$ Physisorption Measurements

Material surface areas were calculated using the Brunauer-Emmett-Teller (BET) method applied to a N$_2$ physisorption isotherm measured using a Micromeritics ASAP 2020. A brief description of the experiment and analysis can be found in Chapter 2 (Section 2.2.2.2).

3.2.2.3.   Elemental Analysis

Catalyst compositions were determined via elemental analysis performed using Inductively Coupled Plasma-Optical Emission Spectroscopy (ICP-OES). First, roughly 15-20 mg of the catalyst was dissolved in 3 mL of aqua regia (2.25 mL hydrochloric acid, 0.75 mL nitric acid). The powders were allowed to digest in the aqua regia overnight. Following digestion, 1 mL of each sample was diluted with 13 mL of deionized water (two diluted samples per each 15 mg sample). ICP-OES was performed on a Varian 710-ES spectrometer. Sample spectra were compared to a 5-point calibration curve using elemental standards of known concentrations to quantify the elements in each sample.

For metal deposition studies, during wet impregnation of the passivated or unpassivated Mo$_2$C, 1.3 mL aliquots were extracted from the 70 mL metal precursor solution at discrete time intervals (0, 15, 30, 45, 60, 90, … 480 minutes). The aliquots were filtered (Fisher, Sterile Nylon filters, 0.2 μm pore size). 1 mL of each sample solution was diluted with 13mL of deionized water, and analyzed on the ICP-OES.

3.2.2.4.   H$_2$ Temperature-Programmed Reduction

Hydrogen temperature-programmed reductions (H$_2$-TPRs) were conducted on a Micromeritics Autochem 2920, equipped with a thermal conductivity detector (TCD) and

a Pfeiffer Vacuum Quadstar GSD-301 Mass Spectrometer (MS). Detailed experimental conditions and analyses are described in Chapter 2 (Section 2.2.2.4).

3.2.2.5. CO Uptake

CO uptake chemisorption was performed on a Micromeritics Autochem 2920, described previously. Approximately 0.1 g of catalyst was supported on a quartz wool plug in the quartz U-tube reactor for each experiment. The catalyst was first pretreated at 590°C for 4 hr under 15% CH_4/H_2 flow (70 mL/min). After the 4 hr pretreatment, the gas flow was switched to He (70 mL/min) and the temperature was increased to 600°C to purge the surface. The reactor was then cooled to room temperature in He. After reaching room temperature, the reactor was heated to 35°C and the material was exposed to pulses of CO (5% CO/He in either a 500 μL or a 5 mL loop). During pulsing, the effluent gas was analyzed using both TCD and MS detectors. CO was pulsed until the site saturation as indicated by constant peak areas in the TCD towards the latter part of the experiment.

3.2.2.6. Point of Zero Charge, Isoelectric Point

The point of zero charge (PZC, measured by pH) measurements were carried out using procedures described in the literature [31,32,33]. The desired surface loading for PZC determination of Mo_2C and p-Mo_2C was $500m^2/L$; the Mo_2C-based catalyst weight was maintained at approximately 40 mg per solution while the solution volume was varied to maintain the surface loading. The pH of the starting solution (deionized water purged with Ar) was adjusted using concentrated hydrochloric acid or ammonium hydroxide to meet a target starting pH value. The catalyst sample was added to the solution, and the pH was recorded as a function of time until it stabilized at a final pH

value. Due to the low surface area of MoO_2 (~4 m^2/g), 500 mg of material was used in order to achieve the desired surface loading.

3.2.2.7.   Scanning Electron Microscopy

Scanning electron micrographs of the catalysts and supports were obtained using FEI Nova Nanolab Dualbeam (FIB/SEM) at the Michigan Center for Materials Characterization. The materials were supported on sample holders using copper tape and were gold sputter coated to improve conductivity. Elemental analyses of specific micrographs were obtained using Energy Dispersive X-ray Spectroscopy (EDX).

3.2.2.8.   Cyclic Voltammetry

Cyclic voltammetry was conducted on an electrode composed of 80% p-Mo_2C, 10% polyvinylidene fluoride (PVDF) binder, and 10% SuperPLi carbon using an Autolab PGSTAT302N potentiostat and a three electrode cell employing Pt as the counter and reference electrodes. The materials were combined and formed into a slurry using N-methylpyrrolidone as the solvent. The slurry was then pasted onto titanium foil and dried at 80°C overnight. Cyclic voltammograms were conducted in 0.1M HCl. After 10 cycles, H_2PtCl_6 (nominally at ~300% of a monolayer) was added to the solution and cyclic voltammograms were again collected.

3.2.2.9.   X-ray Photoelectron Spectroscopy

X-ray Photoelectron Spectroscopy (XPS) was performed to investigate the surface composition and species of the Mo_2C catalysts. The XPS analysis was conducted on a Kratos Axis Ultra X-ray photospectrometer equipped with an Al anode operating at 8 mA and 14 kV (K_α radiation, 1486.6 eV).

The passivated catalyst samples were loaded as-is while the unpassivated samples

post-impregnation were transferred to the XPS sample transfer chamber under a meniscus of water from the wet impregnation solution. The water was removed from the sample during the evacuation process to achieve ultra-high vacuum ($< 10^{-8}$ torr). All spectra were deconvoluted using a combination of Gaussian (80%) and Laurentzian (20%) peak distributions. C 1s and O 1s spectra were deconvoluted using linear backgrounds while Mo 3d and Pt 4f spectra were fit employing a Shirley background. Constraints were placed on certain parameters for the Mo 3d and Pt 4f spectra to account for the spin-orbit coupling. In particular, the Mo 3d and Pt 4f spectra were fit using doublets with the peaks separated by 3.2 eV and 3.3 eV, respectively, having the same full-width half maximum (FWHM), and a peak area ratio of 3:2 for the Mo $3d^{5/2}$ and $3d^{3/2}$ peaks and 4:3 for the Pt $4f_{7/2}$ and $4f_{5/2}$ peaks for Mo and Pt, respectively. The accuracy of the peak envelope developed from the peak deconvolution was evaluated by the residual standard error (STD). The peak parameters (area, binding energy, FWHM) were altered to minimize the residual STD. Peak areas were normalized using atomic sensitivity factors.

In one set of experiments, ~200 mg of unpassivated Mo_2C was exposed to three solutions for 24 hours: (1) ultrapure H_2O, (2) 15 mM HCl, and (3) 18.3 mM H_2PtCl_6 (~100% of a monolayer). The concentrations were chosen in order to maintain a similar pH. The Mo_2C powders were then loaded directly into the XPS transfer chamber under a meniscus of water (to prevent oxygen exposure) and the chamber was evacuated.

In a separate experiment, passivated Mo_2C was exposed to a solution of ultrapure water for 24 hours. The powder was then loaded directly into the XPS transfer chamber as described for the previous experiment. This spectrum was compared to the spectrum for passivated Mo_2C without water exposure.

3.2.2.10. X-ray Absorption Spectroscopy (XAS)

X-ray absorption is an extremely powerful technique capable of probing the electronic properties and local geometry of specific elements in materials or compounds [34]. XAS employs high intensity, highly resolved X-rays to excite core electrons to unpopulated electron states and, ultimately, eject an electron in the form of a photoelectron wave. Each element has a characteristic energy required to excite electrons through specific transitions. This energy is known as the edge energy. X-ray absorption can be monitored by measuring the difference in photon flux before and after the material under investigation. The energy range immediately before and after (±30 eV around the edge) is commonly referred to as the X-ray absorption near edge structure (XANES) region, which can yield information regarding geometry (i.e., tetrahedral vs. octahedral), oxidation state of the element, and the density of states. The energy range following the edge (~40-1000 eV beyond) is often characterized by oscillations resulting from constructive and destructive interference of spectral waves caused by interactions between ejected photoelectrons and nearby atoms. After mathematical transformations, these oscillations can yield information regarding bond distances, coordination numbers, and the neighboring elements [34].

The dynamic deposition and spontaneous reduction (previously reported by Schaidle et al. [31]) of Pt upon interaction with Mo_2C was investigated using *in situ* X-ray absorption spectroscopy. A custom Teflon cell was designed and built for the experiments to prevent air exposure. Exploded view diagrams of the cell design are shown in Figure 3.1, while photos of the cell can be seen in Figure 3.2. The cell consisted of two separate Teflon blocks. One block simply has a 125 μm thick Teflon window and

countersunk holes for hex nuts. The other block contains a cylindrical chamber capable of holding 15 mL of liquid. Another 125 μm thick Teflon window was cut at the base of this chamber; the heights of the two windows were designed to be equal to allow for X-rays to pass through. Three holes were cut, with 1/8" NPT fittings at the end to allow for gas flow (inlet and outlet on the sides of the cell) and liquid injection (at the top of the cell). The top connection was equipped with a septum to allow for air-tight introduction of the metal salt solution. To secure a sample pellet in the cell, a small notch was made in the Teflon next to the 125 um window for the pellet. An O-ring was used in an O-ring groove to seal the two blocks together. Three-way valves were used to purge the lines of any lingering oxygen prior to introduction of the UHP N_2 gas through the cell.
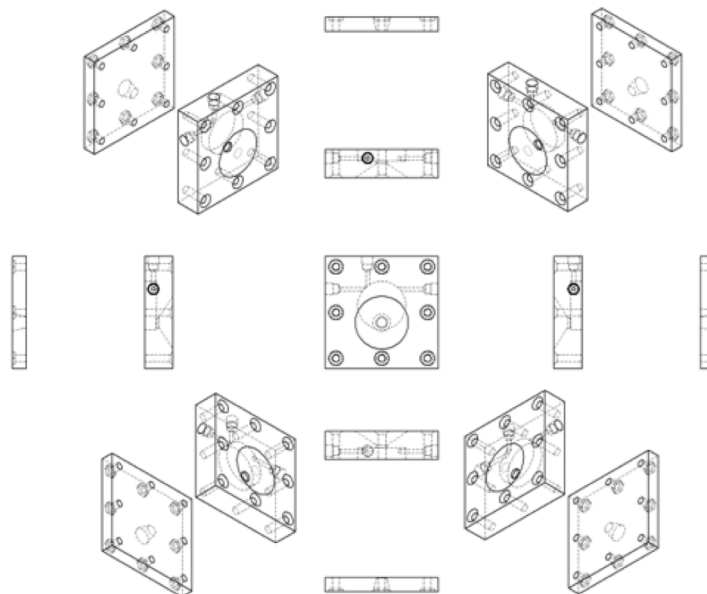
Figure 3.1. Schematic of *in situ* XAS cell in multiple views
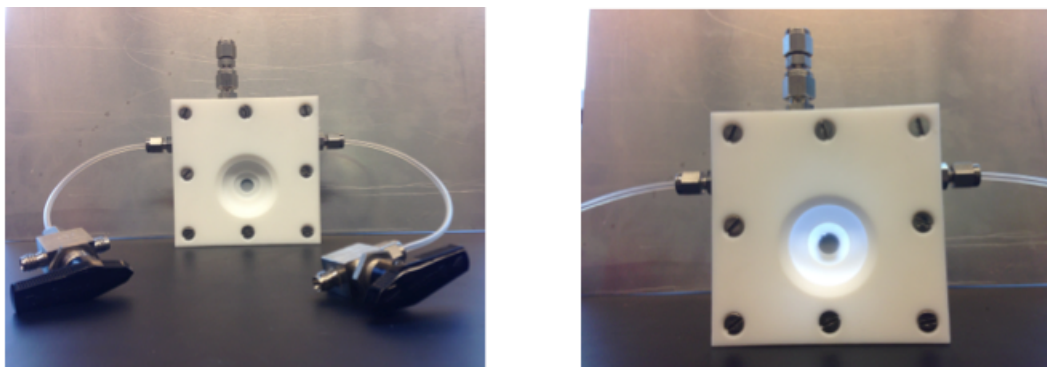
Figure 3.2. Photos of the custom Teflon cell. At the top of the photos are Swagelok fittings equipped with a septum. Gas inlet and outlet lines are shown on the sides and the pelletized sample can be seen in the "window."

X-ray absorption spectroscopy (XAS) experiments were conducted at the 10-BM beamline (MRCAT) of the Advanced Photon Source at Argonne National Lab. The beam size was set to 0.5x0.5 mm. All results reported here were obtained in transmission mode, using a metal reference (Mo or Pt foils) between I_t and I_{ref} to align samples. Data analysis was performed using Athena, a free online software package [35]. Background removal and spectrum normalization were conducted using standard analysis procedures [35]. Oxidation states of the sample spectra were calculated by linear combination fitting of the spectra to known standards (Pt: H_2PtCl_6, Pt^0; Mo: MoO_3, MoO_2, Mo^0).

During an experiment, a 60 mg pellet of material (Mo_2C or Mo_2C/Al_2O_3) was secured in the cell in an inert atmosphere glove box. The cell was sealed, removed from the glove box, and installed at the beam. A Mo K edge spectrum ($E_0 = 20,000$ eV) of the material was taken prior to liquid injection. The metal salt solution was prepared by dissolving either 16.0 mg or 2.6 mg of chloroplatinic acid (H_2PtCl_6, SigmaAldrich) in 12 mL of deionized water for the Mo_2C and Mo_2C/Al_2O_3 experiments, respectively. The metal salt solution was then deaerated with N_2 for 15 minutes to remove any dissolved oxygen. Two mL of the solution were collected prior to injection for elemental analysis back at UM. The metal salt solution (10 mL) was then injected into the cell through the

septum and spectrum (~6 minutes each) were taken continuously for approximately 4 hours. After 4 hours, a longer collection time spectrum was recorded in order to obtain data for EXAFS analysis. The beam energy was then changed to Pt L_{III} ($E_0 = 11,653$) and spectra were taken. The experiment was then repeated while recording spectra at the Pt L3 edge.

3.2.2.11. Water-gas Shift

The water-gas shift activities were determined using a flow reactor equipped with a GC-TCD (SRI 8610, with a Carboxen 1000 column). Prior to obtaining activity data, all of the Mo_2C-based catalysts were pretreated in 15% CH_4/H_2 at 590°C for 4hr (10°C/min heat rate) to remove the passivation layer. The commercial $Cu-ZnO/Al_2O_3$ was pretreated in 4% H_2/N_2 at 200°C for 4 hr (3°C/min heat rate) per vendor specifications. The reactant feed consisted of 11% CO, 21% H_2O, 6% CO_2, 43% H_2, and 19% N_2 (262 mL/min, 125,000 hr^{-1}) to simulate commercial reformate streams and the temperature was varied between 200 and 240°C. Prior to GC injection, the effluent stream flowed through a condenser, held at 0°C to remove water from the stream.

Differential conditions were maintained by limiting the conversions to 10% through adjustments to the catalyst weight. The catalyst was diluted with low surface area SiO_2 (Alfa Aesar, 99.995% metals basis) in order to maintain a constant bed height and volume. Hydrogen production rates were determined by monitoring the consumption of CO (Equation 3.1); mass balance closure was confirmed by quantifying the formation of CO_2. Direct measurement of H_2 was not possible because He was used as the carrier gas. Arrhenius plots for the turnover frequencies (TOF, s^{-1}), CO consumption rates normalized by CO uptakes, are reported for each of the catalysts.

$$r_{CO\ Consumption} = \frac{dX_{CO}}{dW} F_{CO} \approx \frac{F_{CO} * X_{CO}}{W_{cat}} \tag{3.1}$$

3.3. Results

3.3.1 Mechanism for *in situ* Metal Reduction during Wet Impregnation

The initial goal of this work was to confirm the cause of metal reduction during wet impregnation of certain metals onto Mo_2C, a direct follow-up from the work of Schaidle et al. [26]. Schaidle and coworkers proposed metal reduction coincident with Mo_2C oxidation based on differences in Gibbs free energies driving reduction of certain metals and not others.

Our study examines the Pt/Mo_2C system given the substantial literature on these catalysts [11,22,23,26,36]. A diagram of the synthesis method and conditions for the wet impregnation procedure is shown in Figure 3.3. Mo_2C is submerged in a deaerated solution of H_2PtCl_6 in H_2O, which is continuously sparged with pure Ar. There are two possible explanations for the observed Pt reduction: (1) chloroplatinic acid is not stable under these conditions in water and (2) a species in the wet impregnation solution acts as a reducing agent for the Pt. The first explanation can be eliminated based on previous speciation studies for aqueous solutions of chloroplatinic acid. At the pH used for wet impregnation (~2.3), the solution would be dominated by $[PtCl_6]^{2-}$ and $[PtCl_5(H_2O)]^{-1}$ species, both of which are stable and soluble according to Spieker et al. [37]. Therefore, the only explanation is the presence of a reducing agent in solution. The only possible reducing agent in the system is the highly reduced surface of Mo_2C. It is proposed that
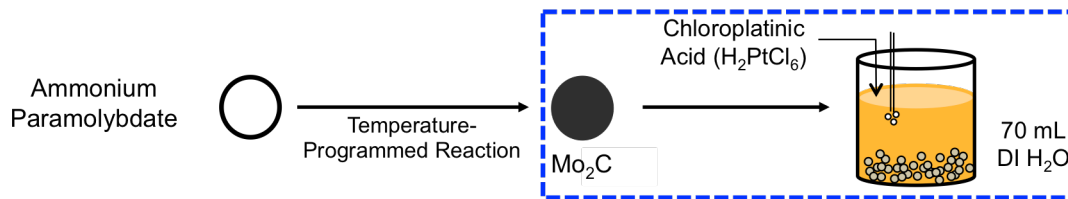
Figure 3.3. Procedure for wet impregnation of metals (in this case Pt from H_2PtCl_6) onto unpassivated Mo_2C.

redox reactions occurred between the Mo_2C surface and metal precursor, such that metal

reduction would be accompanied by Mo oxidation.

There are a few techniques that can be used for confirming surface redox: cyclic

voltammetry, X-ray photoelectron spectroscopy, and X-ray absorption spectroscopy.

Cyclic voltammetry (CV) sweeps through a range of potentials and monitors the current

response. When a potential is applied that initiates oxidation or reduction of a material,

this will be reflected in the current responses (negative current for reduction, positive

current for oxidation). X-ray photoelectron spectroscopy (XPS) affords information

regarding the oxidation of elements and their relative surface atomic percentages, and is a

surface specific technique. X-ray absorption spectroscopy utilizes a similar phenomenon

as XPS, but yields more information (e.g., local geometry, bond lengths) than XPS. XAS

is a bulk technique, and requires very intense X-rays, which are only available at

synchrotron sources.

3.3.1.1.   Cyclic Voltammetry of Pt deposition on Mo_2C

Given the availability of CV and XPS on site at the University of Michigan, these

methods were tested first. The voltammogram before and after H_2PtCl_6 (not shown)

failed to show any reduction or oxidation peaks for Mo_2C or Pt. It is unlikely that a

current response would be observed for this particular system, since any electron

movement (e.g., Mo_2C donating e⁻ directly to the adsorbing $[PtCl_6]^{2-}$ anions) would be

116

expected to only occur at the material surface and not pass through the external circuit between the working and counter electrodes. As a result, CV was deemed an inappropriate technique for further investigation.

3.3.1.2. X-ray Photoelectron Spectroscopic Analysis of Pt/Mo$_2$C

X-ray photoelectron spectroscopy was therefore employed in an attempt to observe Pt reduction and Mo oxidation post-wet impregnation. Three cases were studied in which Mo$_2$C was exposed to: (1) ultrapure H$_2$O, (2) 15 mM HCl, and (3) 18.3mM H$_2$PtCl$_6$ (~100% of a monolayer). Case 2 represents an acidic solution with an identical pH to that of case 3 in the absence of Pt metal to test for Mo oxidation due to exposure to acidic media. The Mo 3d and Pt 4f XPS spectra for these materials are shown in Figure 3.4 and Figure 3.5. Mo oxidation states and relative atomic percentages are provided in Table 3.1. The deconvoluted Mo 3d spectra of the Mo$_2$C-based catalysts contained four doublets each. These doublets are assigned to Mo species via comparisons with literature: Mo 3d$_{5/2}$ peak at ~232.2 ± 0.1 assigned to MoO$_3$ (Mo^{6+}) species [23,38,39,40,41]; Mo 3d$_{5/2}$ peak at ~230.1 ± 0.1 assigned to MoO$_2$ (Mo^{4+}) [23,38,41,42]; Mo 3d$_{5/2}$ peaks at 285.5 assigned to a reduced MoO$_2$ (likely associated with a Mo$^{\delta+}$ where δ exists between 2 and 4) [23,38,41]; and the 228.1 ± 0.1 eV peak assigned to a Mo^{2+} species (likely for the Mo in Mo$_2$C) [19,23,38,41]. The results are summarized by monitoring the shift in Mo oxidation state with different treatments. The Mo remains in a predominantly reduced state following treatment in both water and 15 mM HCl, with average oxidation states of +3.2 and +3.2, respectively. Only negligible differences in the percentages of Mo species are observed. However, the Mo 3d spectra following treatment with H$_2$PtCl$_6$ exhibited differences relative to the spectra following the other two treatments. Noticeable Mo

oxidation is observed as indicated by growth of the doublet (at 231.8 and 234.9 eV for $3d_{5/2}$ and $3d_{3/2}$, respectively) corresponding to Mo (VI) species is observed. The average Mo oxidation state increased to +3.7 compared to that following water treatment (+3.2) based on deconvolution fits.
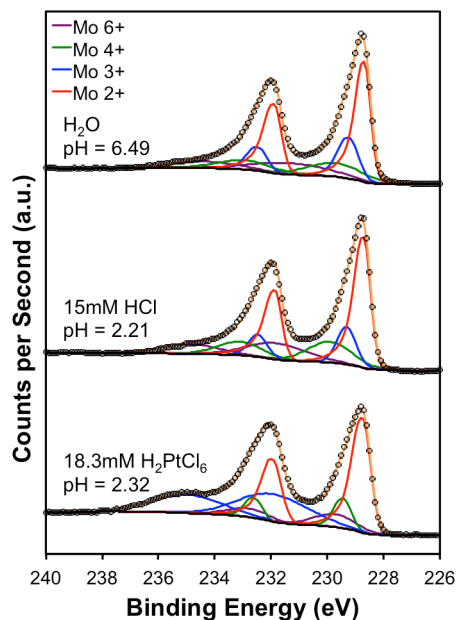
Figure 3.4. Mo 3d spectra of Mo_2C following 24 hour exposure to 3 different deaerated solutions: (top) ultrapure water, (middle) 15 mM HCl, and (bottom) 18.3 mM H_2PtCl_6.
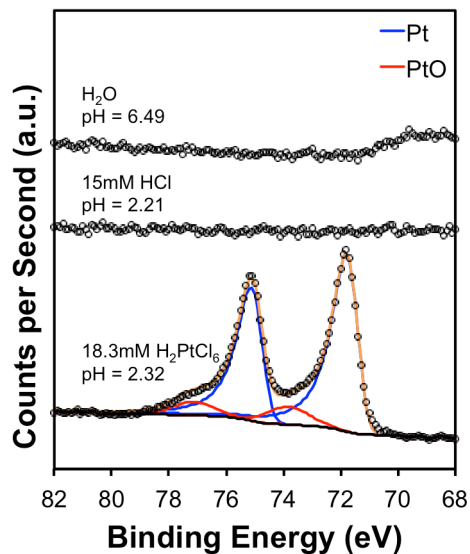
Figure 3.5. Pt 4f spectra of Mo_2C following 24 hour exposure to 3 different deaerated solutions: (top) ultrapure water, (middle) 15 mM HCl, and (bottom) 18.3 mM H_2PtCl_6.

The Pt 4f spectra were also analyzed for all of the samples. The spectra were fit to a series of doublets. Doublets containing a $4f_{7/2}$ peak at 71.5 eV are consistent with metallic Pt [22,23,43] and doublets with a $4f_{7/2}$ peak at ~74.0 eV are typically assigned to Pt^{2+} or PtO species [22,23,43]. As expected, no Pt signal was observed for the samples following treatment in water and HCl. A significant platinum signal is seen for the sample treated with chloroplatinic acid, indicating metal adsorption onto the Mo_2C support. Following deconvolution, the Pt is observed to exist as 88% Pt metal and 12% PtO, the chloroplatinic acid is reduced from its Pt^{4+} state upon interaction with Mo_2C, as previously observed by Schaidle et al. [26]. From these results, it is evident that redox chemistry is occurring between Pt and Mo_2C; and that the presence of Pt^{4+} instead of simply acidic conditions results in the oxidation of Mo.

Table 3.1. Binding energies and percentages for surface species associated with Mo_2C following 24 hour exposure to 3 different deaerated solutions

Catalyst Treatment	Mo $3d_{5/2}$ (eV)[1]				
	Mo^{6+}	Mo^{4+}	$Mo^{\delta+}$	Mo^{2+}	Avg. Mo Ox. State
Mo_2C, water	231.7 (17%)	229.9 (17%)	229.3 (19%)	228.7 (47%)	+3.2
Mo_2C, HCl	231.5 (18%)	229.7 (19%)	229.2 (14%)	228.7 (50%)	+3.2
Mo_2C, H_2PtCl_6	231.8 (35%)	229.7 (10%)	229.4 (10%)	228.7 (45%)	+3.7

[1] The first number listed represents the binding energy of the peak following deconvolution. The number in parentheses represents the atomic percentage of the species relative to other species of the same element.

While these results are consistent with the hypothesis, materials were still transferred *in air* from the aqueous solutions into the XPS sample transfer chamber, albeit it under a meniscus of water. Based on the results and the control experiments with deaerated water and HCl, it would appear that the water meniscus protects the carbide during the transfer and there is little oxidation. However, to conclusively prove the presence of Mo-Pt redox, X-ray absorption spectroscopy was employed.

3.3.1.3.   *In Situ* X-ray Absorption Spectroscopic Analysis of Mo-Pt Redox

Use of X-ray absorption spectroscopy (XAS) allows for the monitoring of Mo and Pt oxidation states *in situ* during wet impregnation of H_2PtCl_6 onto an unpassivated Mo_2C in a controlled, inert environment. Prior to the XAS experiments, the physical characteristics of Mo_2C pellets to be used for XAS analysis were compared with Mo_2C powder using BET and SEM. Micrographs (Figure 3.6) suggest that there is some loss of porosity on the surface for the pelletized sample relative to the powder sample. BET surface areas were almost identical (163 and 159 m^2/g for the powder and pellet samples, respectively); and pore volumes were also quite close (0.130 and 0.128 cm^3/g for the powder and pellet samples, respectively). While the surface may visibly appear less porous, only negligible differences are observed for the porosity and available surface area for metal adsorption.
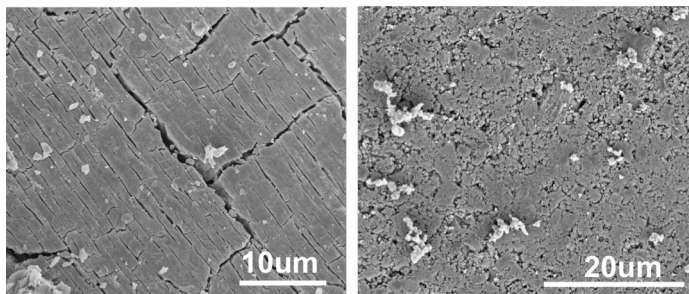
Figure 3.6. SEM micrographs of the powder (left) and pelletized (right) Mo_2C samples.

For the *in situ* wet impregnation experiments, chloroplatinic acid deposition was performed at ~7.7wt% Pt (25% surface coverage) onto Mo_2C in the custom built, air-tight *in situ* cell (see Experimental section) while monitoring the Mo and Pt oxidation states. The initial and final Mo K and Pt L3 edge spectra for wet impregnation of H_2PtCl_6 onto an unpassivated Mo_2C are shown in Figure 3.7 along with standard species for reference. The Pt L3 edge spectrum pre-deposition was consistent with that for chloroplatinic acid;

while after metal deposition, the platinum was highly reduced with spectra nearly identical to that for Pt foil (Figure 3.7a). ICP-OES analysis of the supernatant solution after the *in situ* wet impregnation indicated only 68% adsorption of H_2PtCl_6 over the 5 hr adsorption experiment, which may explain the small degree of oxidation still apparent in the Pt/Mo_2C spectra following deposition. The spectra likely represents an average oxidation state between the metallic platinum adsorbed on the Mo_2C surface and the Pt^{4+} species remaining in solution, but still in the path of the X-ray beam.
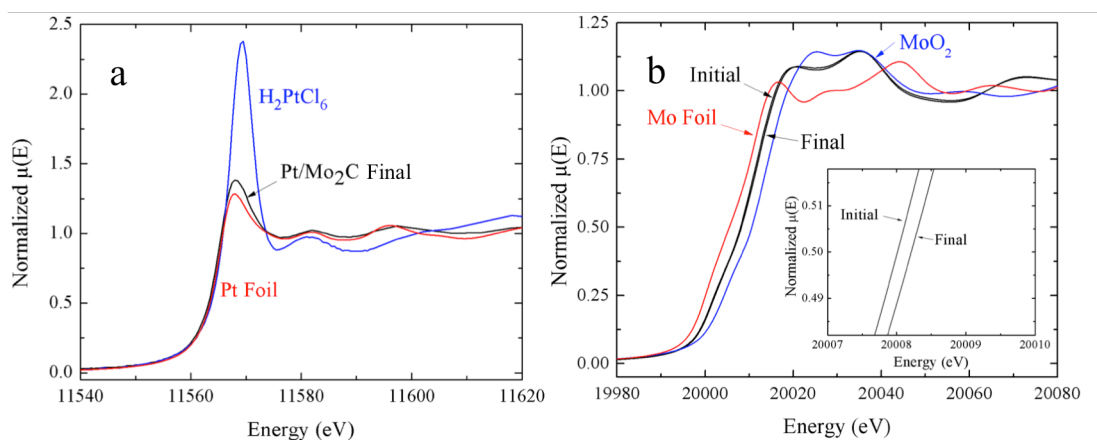
Figure 3.7. X-ray absorption spectra for (a) Pt L3 and (b) Mo K edges during the wet impregnation of H_2PtCl_6 onto an unpassivated Mo_2C. Only initial and final spectra are shown for ease of viewing. Known standards are shown in blue and red for reference.

The Mo K edge spectra before and after metal deposition are shown in Figure 3.7b along with Mo foil and MoO_2 as reference materials. There is a small shift in the Mo spectrum to higher edge energies, as seen in the inset image, which is consistent with oxidation. Oxidation state changes of Pt and Mo were calculated by fitting each spectrum to a weighted sum of the known standards, a technique known as linear combination fitting. The Pt oxidation state decreased from +4 prior to deposition to +0.4 after Pt deposition, while the Mo oxidation state increased from +2.6 to +2.8. Based on the mass of Mo_2C and the amount of Pt adsorbed in this experiment, the expected oxidation state

121

change for Mo is +0.20, which is close to the observed shift in oxidation state. These results corroborate the XPS results indicating the presence of Pt-Mo redox chemistry during wet impregnation.

While these results are convincing, XAS is a bulk technique; so the oxidation states and chemical character of bulk Mo are averaged with those of surface Mo, thereby diluting the change in oxidation state. Since this is a surface specific phenomenon, increasing the percentage of surface Mo atoms relative to bulk Mo atoms should enhance the differences observed via XAS. Supported Mo_2C would provide a greater surface-to-bulk ratio for the materials, so Al_2O_3-supported Mo_2C was synthesized for use in the *in situ* XAS experiments.

Prior to use, the physical and chemical properties of Mo_2C/Al_2O_3 (20 wt%) were compared to those of Mo_2C. CO uptake capacity for the Al_2O_3-supported Mo_2C was calculated at 73 μmol/g compared to 404 μmol/g for the unsupported Mo_2C. Since Al_2O_3 does not uptake CO itself, it is evident that Mo species are present. Furthermore, H_2 temperature programmed reduction spectra are very comparable for the supported and unsupported Mo_2C samples (Figure 3.8), indicating a similar oxidation state and chemical structure. As a final check, adsorption of H_2PtCl_6 was observed onto a Mo_2C/Al_2O_3 pellet under typical wet impregnation conditions (not shown). Adsorption was slightly slower, perhaps due to the use of a pellet instead of a powder, but proceeded to completion within 5 hours. From these collective experiments, it was evident that the Mo_2C/Al_2O_3 materials behave similarly to unsupported Mo_2C in the XAS experiments.
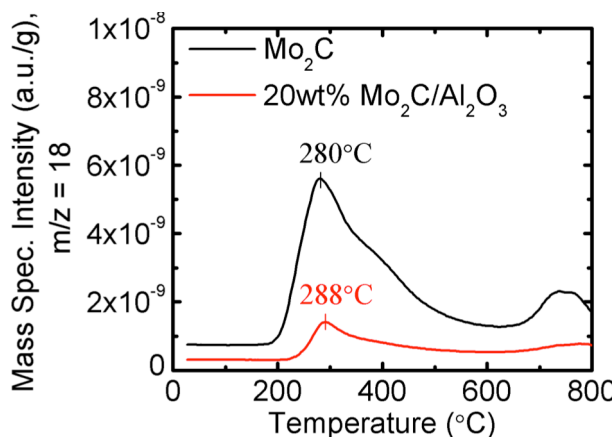
Figure 3.8. H_2 temperature-programmed reduction for the unsupported Mo_2C and Mo_2C/Al_2O_3 materials. Spectra taken in 10% H_2/Ar at 20 K/min.

Pt (nominally 6wt%) was deposited onto unpassivated Mo_2C/Al_2O_3 (20wt%) while recording XAS spectra for the Pt L3 or Mo K edges. Given the differences in energy (20,000 vs. 11,563 eV for $E_{0,Mo}$ and $E_{0,Pt}$, respectively), it is impossible to measure both spectra during the same experiment, so two adsorption experiments were run to separately obtain spectra for Mo and Pt. Select spectra for the Pt L3 and Mo K edges taken during these experiments are shown in Figure 3.9. With increasing deposition time, the Pt L3 spectra shift from H_2PtCl_6 spectra towards that of Pt foil. The Mo K spectra shift from ~20008.5 to ~20009 eV at a normalized $\mu(E)$ of 0.5 over the deposition period, again indicative of oxidation. Through linear combination fitting, the spectra were converted into oxidation states and plotted as a function of deposition time (Figure 3.10). The timeframes of Pt reduction and Mo oxidation appear concurrent based on the trend of the data. An anticipated Mo oxidation state change of +0.54 was calculated based on the amount of platinum adsorbed and the mass of Mo in the pellet. This value is close to the observed change of +0.42 and likely within the error for the experimental setup and calculations based on the appropriate assumptions. Based on these results, it appears conclusive that Pt reduction is occurring through oxidation of Mo. To ensure that water is

not the cause for the observed oxidation, a control experiment was performed in which Mo$_2$C/Al$_2$O$_3$ was exposed to deaerated water in the absence of a metal salt. No oxidation state changes were observed indicating that any apparent oxidation resulted from the support's interaction with the Pt salt.
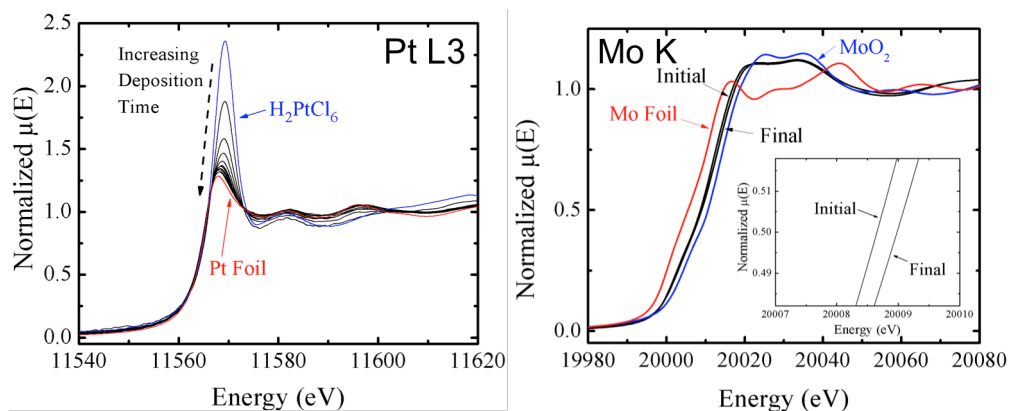
Figure 3.9. (left) Pt L3 edge XANES spectra during Pt (6 wt%) deposition onto Mo$_2$C /Al$_2$O$_3$. The spectrum for H$_2$PtCl$_6$ (blue) is at the top. The reference spectrum for metallic Pt is shown at the bottom (red). (right) Mo K edge XANES spectra of Mo$_2$C /Al$_2$O$_3$ before and after Pt deposition. The inset represents a closer view of the edge shift. Metallic Mo (red line) and Mo (IV) oxide (blue line) are shown for reference.
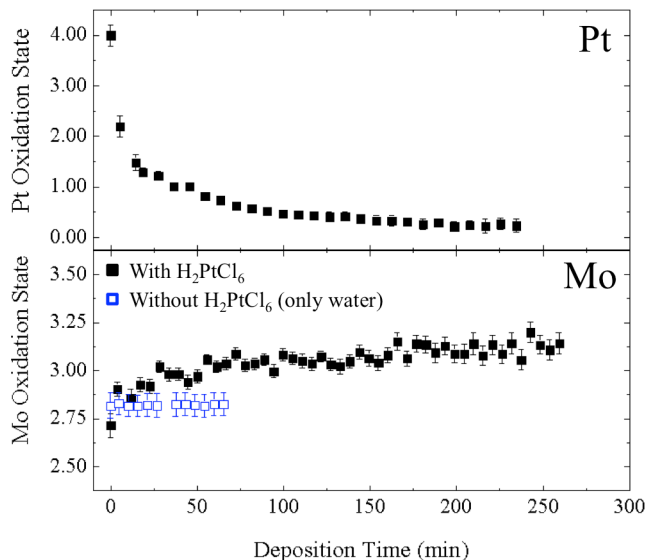
Figure 3.10. Pt and Mo oxidation states as a function of metal deposition time (6wt% Pt onto 20wt% Mo$_2$C/Al$_2$O$_3$). Open blue points in the Mo figure represent a control experiment (only deaerated water, no H$_2$PtCl$_6$).

124

In addition to obtaining information about metal oxidation states, XAS is a useful technique for monitoring changes in the local geometry and bonding of the metal atoms, namely the Extended X-ray Absorption Fine Structure (EXAFS) region at higher energies than the metal edge. This can be accomplished by utilizing the same spectra as those shown in Figure 3.9, converting the post edge data into k space by utilizing a k^2 weighting, and ultimately converting the k space to R space using a Fourier Transform. No measurable changes were detected in the EXAFS spectra for Mo during metal deposition. Conversely, distinct changes in the Pt coordination and bonding are seen as a result of Pt deposition (Figure 3.11). The spectra were fit using theoretical nearest neighbor Pt-Pt and Pt-Cl scattering amplitudes and phase shift functions generated via FEFF [44]. Using these fits, the spectra could be converted into corresponding Pt-Cl and Pt-Pt coordination numbers. Coordination numbers are plotted as a function of deposition time in Figure 3.12. The Pt-Pt coordination number increases from 0 to a stabilized value at ~11 ± 1 by ~90 minutes adsorption time (coordination number for bulk Pt is 12). This timeframe is similar to the time required for the Pt oxidation state to stabilize around +0.5. Similarly, the Pt-Cl coordination (such as that from the $[PtCl_6]^{2-}$ anions) decreased from 6 to ~0 after 120 minutes. The trends developed from the EXAFS results are consistent with the conclusions from the XANES work that Pt is adsorbing and reducing to generate Pt nanoparticles on Mo_2C with oxidation of Mo.
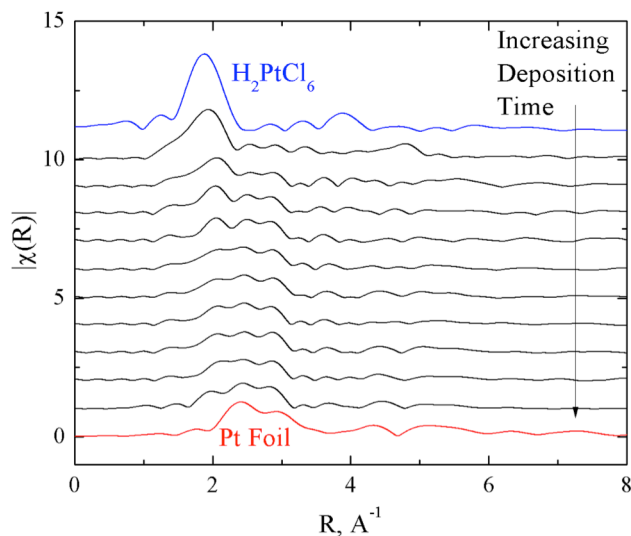
Figure 3.11. EXAFS spectra of the Pt L3 edge from the metal deposition of H_2PtCl_6 onto unpassivated Mo_2C/Al_2O_3. k-weight = k^2.
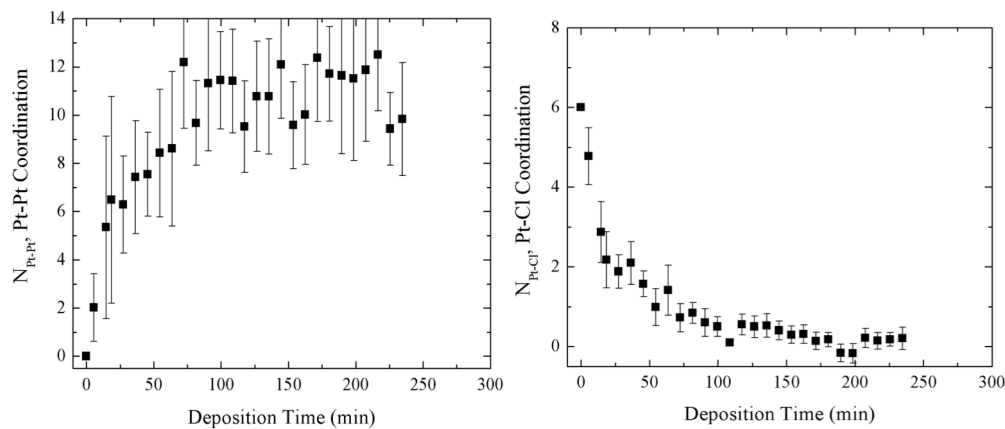
Figure 3.12. Pt-Pt (left) and Pt-Cl (right) coordination numbers as a function of metal deposition time.

As the primary goal was to obtain oxidation state information and to observe the dynamics of the reduction/oxidation, more data points were collected in the XANES region of the spectra and fewer in the EXAFS, resulting in larger error values for the latter results. A high resolution spectrum was also obtained after the deposition process where the data collection time was increased to 30 minutes and data was collected at high k-space values. This spectrum (shown in Figure 3.13) was analyzed similarly and Pt-Pt and Pt-Cl coordination numbers were obtained and determined to be 9.9 and 0.0.

126
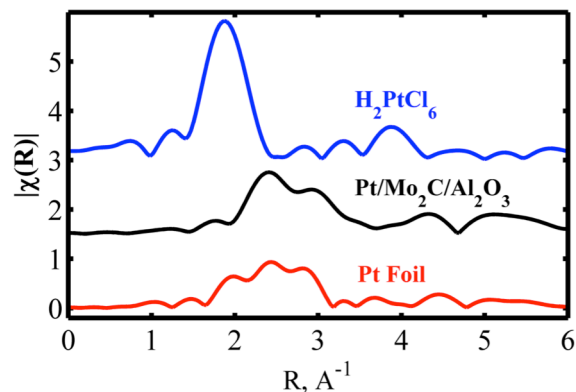
Figure 3.13. EXAFS spectra of the Pt L3 edge for 3 samples: (1) H_2PtCl_6 standard, (2) $Pt/Mo_2C/Al_2O_3$ after metal deposition, and (3) Pt foil standard. k-weight = k^2.

The overall XAS results together indicate the presence of Pt-Mo redox chemistry during wet impregnation metal deposition of chloroplatinic acid onto either unsupported or supported molybdenum carbide. Pt interaction with unpassivated Mo_2C leads to the formation of small metallic Pt particles on the order of 2-4 nm [45,46,47] in diameter along with the formation of an oxidized Mo surface. Based on the results of Schaidle et al., it is logical to expect that $(NH_3)_4Pd(NO_3)_2$ and $Cu(NO_3)_2$ precursors undergo the same redox chemistry during their spontaneous reduction when interacting with Mo_2C [26]. It should be noted that the character of the oxidized Mo surface post-impregnation is not well understood, but may exist as an oxycarbide [48]. The observed redox chemistry can potentially be exploited to regulate particle morphology or metal oxidation state through controlled catalyst syntheses. This idea will be studied in the next section.

3.3.2 Effect of Passivation on Interaction & Spontaneous Metal Reduction

Redox chemistry between Pt and Mo_2C could impact the resulting catalyst performance by aiding the degree of metal dispersion. One approach to test the impact on catalytic behavior of this surface redox reaction during wet impregnation is to oxidize the Mo_2C surface by generating a passivation layer prior to wet impregnation with Pt.

Passivating the Mo_2C should eliminate the reducing agent in the system (reduced Mo_2C) and lessen the driving force for deposition and metal reduction. Initial work focused on the effect of passivation on physical structure. The similarities and differences in Pt deposition trends for these supports were also explored. Lastly, the implications of these differences on deposited metal structure and water-gas shift reactivity are reported.

3.3.2.1.   Material Characterization

X-ray diffraction patterns for the Mo_2C and p-Mo_2C materials contained peaks characteristic for α-MoC_{1-x} and β-Mo_2C (Figure 3.14). No oxide phases were evident indicating that carburization was complete and that formation of the passivation layer was restricted to the surface, or that any other species were amorphous or below the detection limits for the diffractometer (<~5nm crystallites). The surface area decreased significantly from 162 to 103 m^2/g upon passivating the Mo_2C materials. This loss of surface area corresponds to the loss of micropores during passivation as observed in the pore size distributions (Figure 3.15); the mesopore distributions are very similar.
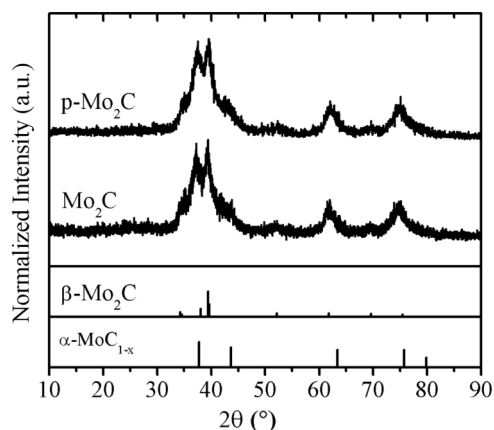
Figure 3.14. X-ray diffraction patterns for the studied supports, including standards from ICDD (β-Mo_2C [PDF #04-001-2151], α-MoC_{1-x} [PDF #04-001-2968]).
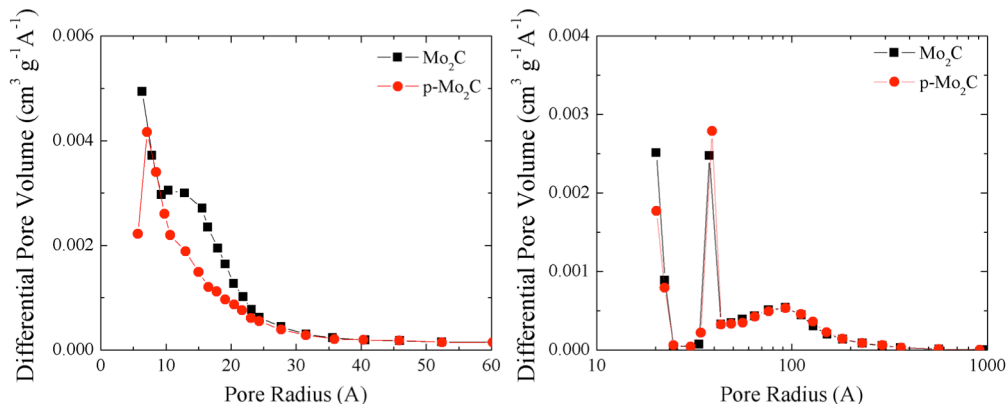
Figure 3.15. Pore size distributions in unpassivated and passivated Mo_2C for (a) micropores determined using the Horváth-Kowazoe (HK) method and (b) mesopores determined using the Barrett-Joyner-Halenda (BJH) method.

3.3.2.2. Metal Deposition on Mo_2C and p-Mo_2C supports

Interactions between metal salts and the passivated and unpassivated supports were explored to determine the effect of the redox chemistry on metal deposition. The deposition of metals (Pt, Pd, Cu, Ni, Co) onto the Mo_2C and p-Mo_2C supports was quantified by monitoring the concentration of metal in the supernatant solution (during wet impregnation) as a function of deposition time. These adsorption profiles are shown in Figure 3.16 plotted as normalized metal concentration as a function of minutes of adsorption. Profiles for metal deposition onto the unpassivated Mo_2C surface are consistent with previous work [31]. Deposition of Pt, Pd, and Cu occurs rapidly, with complete adsorption occurring within the first 120 to 180 minutes. Conversely, Co and Ni exhibit slightly slower adsorption behavior, requiring deposition times of ~300-360 minutes for complete adsorption. Metal deposition onto passivated Mo_2C was not as straightforward as that onto the unpassivated support. While Pd exhibited very comparable adsorption behavior, incomplete adsorption was observed for Cu, Co, and Ni. Cu adsorbed to ~8% of a monolayer while Co and Ni only adsorbed up to ~3.5% of a monolayer. Pt displayed a strikingly different adsorption profile, consisting of a 150
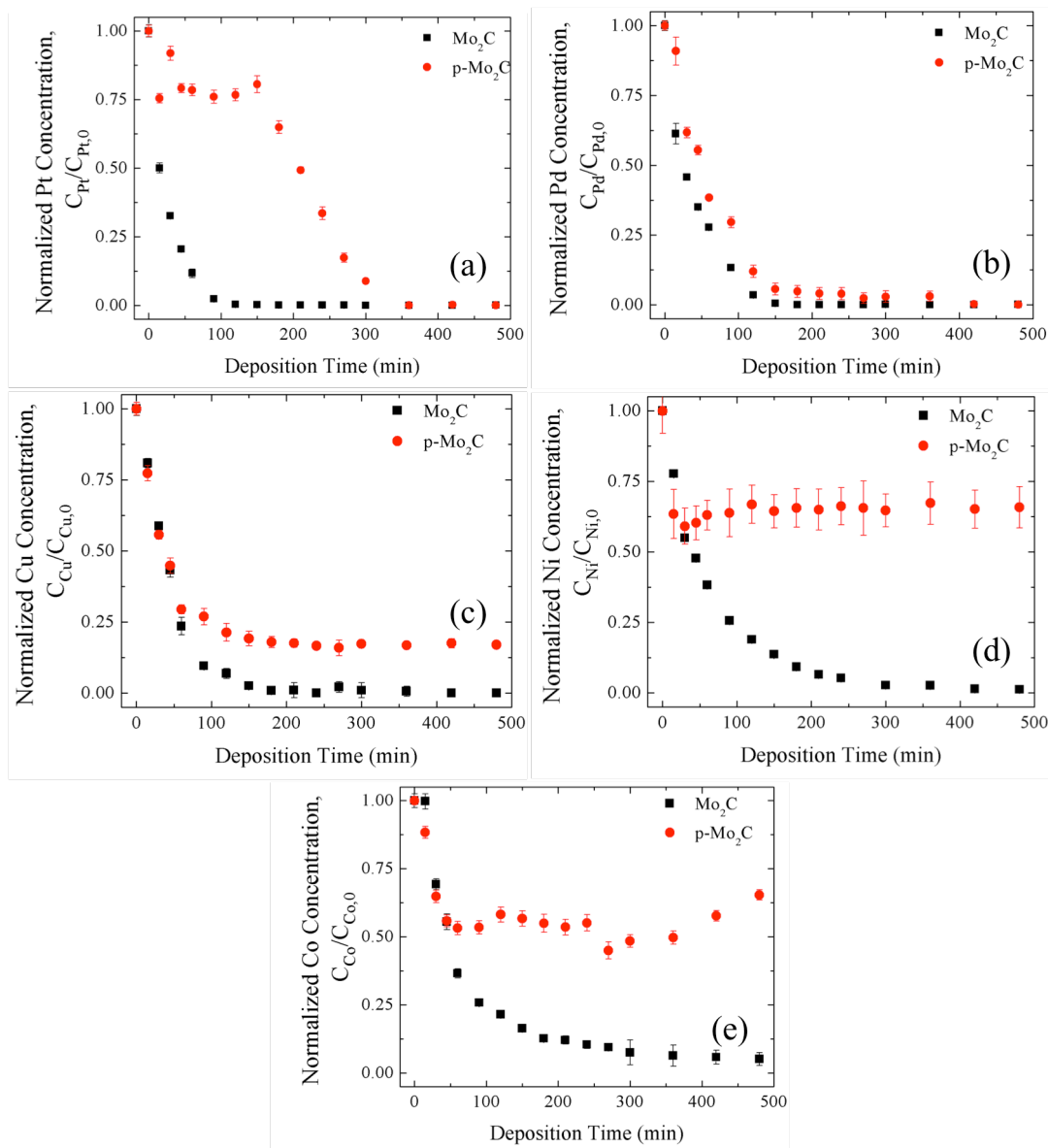
Figure 3.16. Metal deposition profiles as a function of deposition time for the Mo_2C-supported metal catalysts. Nominal metal loadings were 10% monolayer coverage, based on 105 m^2/g and 10 sites/nm^2. Error bars stem from the average concentration from different wavelengths for ICP-OES.

minute induction period followed by complete adsorption within ~360 minutes. As stated above in the introduction, Schaidle et al. observed that certain metals (i.e., Pt, Pd, and Cu) were spontaneously reduced to their zero-valent state following wet impregnation while others (Ni, Co) were not [31]. The adsorption and reduction of metals trended with the

standard reduction potential of the speciated metal salts. The adsorption profiles on passivated Mo_2C appear to follow a similar trend. The extent of metal adsorption onto p-Mo_2C decreased in the following order: Pt ~ Pd > Cu > Ni ~ Co, while the standard reduction potentials of the metal salts were 0.77V, 1.14V, 0.34V, -0.239V, and -0.283V for the Pt, Pd, Cu, Ni, and Co salts, respectively. However, this correlation is not as direct as that observed by Schaidle et al. for the unpassivated Mo_2C [31]. Instead, the materials appear to be saturated at certain metal loadings; in addition, the behavior of Pt is not consistent with that of other metals.

Differences between metal deposition profiles and compositions for the Mo_2C and p-Mo_2C supports suggest different deposition mechanisms. Pt deposition onto Mo_2C from a chloroplatinic acid salt solution proceeds differently for the unpassivated and passivated cases. Rapid adsorption proceeds to completion in approximately two hours on the unpassivated surface. The deposition is coincident with a solution color change from yellow to clear (see images at bottom of Figure 3.17). Conversely, Pt deposition onto the passivated surface proceeds with an initial rapid adsorption of ~25% of the platinum in solution. Minimal color changes are observed during this initial deposition period with the solution remaining predominantly yellow (see images at top of Figure 3.17). Between 120 and 180 minutes, a visible color change from yellow to blue is observed. This color change is coincident with the onset of further Pt loss from solution. Full loss of Pt from solution is observed after 360 minutes and the color of the final solution is a deep blue.
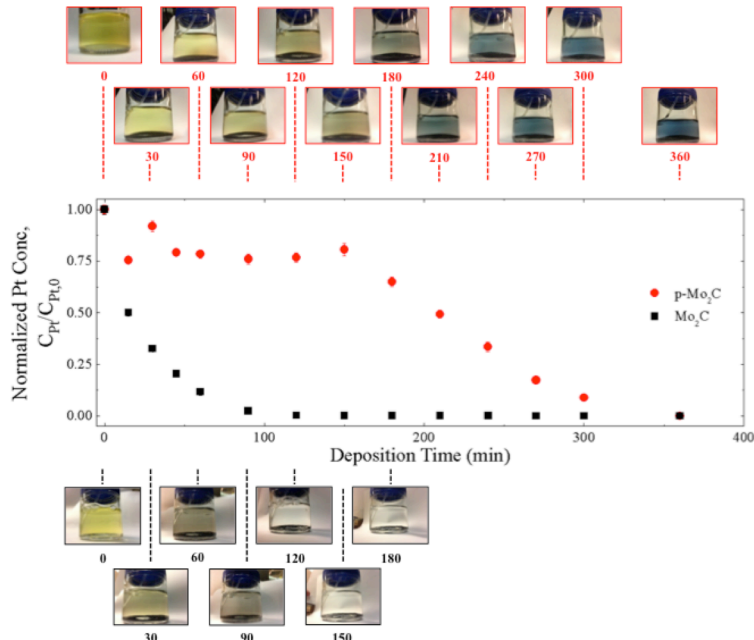
Figure 3.17. Deposition profiles for Pt onto passivated and unpassivated Mo₂C supports, including color changes observed visually during the experiments.

3.3.2.3. Behavior and Material Characterization of Passivated Mo₂C in Water

This blue color has also been observed in a slurry of passivated Mo₂C in deaerated, deionized water (in the absence of metal salts) and is hypothesized to result from partial or complete dissolution of the molybdenum oxycarbide passivation layer (see Figure 3.18). Unlike the time delay for appearance of the blue color in the chloroplatinic acid solution, the color change occurs immediately upon placing p-Mo₂C into water. After exposure of passivated Mo₂C to deaerated water for an extended period of time, the liquid was decanted into a beaker, separating the dark blue solution from the remaining Mo₂C powder. The solution was then vacuum dried overnight at room temperature to obtain a blue powder (referred to as "blue oxycarbide"). X-ray diffraction on the resulting powder showed an entirely amorphous solid (Figure 3.19). This diffraction pattern is consistent with previous work [48]. Elemental analysis (ICP-OES)

132

results showed that the material contained 62 ± 7 wt% Mo. The results are not inconsistent with the blue material being an oxycarbide, since MoO_3 contains 67 wt% Mo and MoO_2 contains 75 wt% Mo.
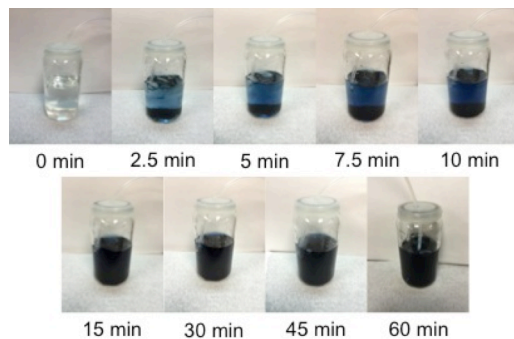
Figure 3.18. Images of 500mg of p-Mo_2C in 50mL of deionized deaerated water.
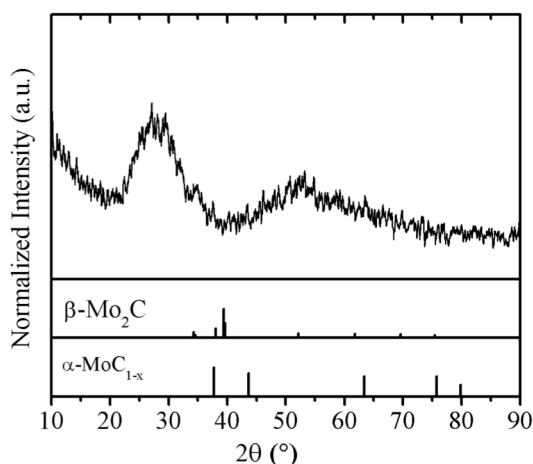
Figure 3.19. X-ray diffraction pattern for the "blue oxycarbide" powder isolated from p-Mo_2C in water

It is possible that the onset of further adsorption after 180 minutes of deposition time is due to the exposure of underlying reduced Mo_2C as a result of the dissolution of the oxycarbide passivation layer. This can be observed by analyzing the chemistry of the surface following dissolution of the passivation layer. To test this hypothesis, X-ray photoelectron spectroscopy was performed on passivated Mo_2C before and after 24 hr exposure to water to monitor changes in the surface chemistry. The XPS spectra for the

Mo 3d, C 1s, and O 1s energies are shown in Figure 3.20 and summarized in Table 3.2. There is little difference in the spectra for p-Mo_2C before and after water exposure. Deconvolution of the spectra show comparable relative atomic percentages for all elements (Mo, C, and O). Furthermore, the Mo:C ratios for the samples before and after water treatment were 0.65 and 0.65; the Mo:O ratios were 1.72 and 1.68, respectively. These results indicate that the dissolution of the oxycarbide passivation layer to generate the blue color in aqueous solutions does not significantly alter the surface chemistry of the p-Mo_2C catalysts. Instead, the surface remains highly oxidized, in a state very similar to that of the catalyst prior to water exposure. Therefore, removal of the passivation layer via oxycarbide dissolution does not expose underlying reduced Mo_2C with which redox chemistry can occur. The eventual continued loss of Pt from solution during wet impregnation on p-Mo_2C must have occurred via an alternative mechanism.

Table 3.2. Binding energies (BE) and relative atomic percentages for the deconvoluted Mo 3d, C 1s, and O 1s spectra for p-Mo_2C catalysts before and after 24 hr water exposure

Catalyst	Treatment	Mo 3d$_{5/2}$ (eV)[1]			
		Mo^{6+}	Mo^{4+}	Mo$^{\delta+}$	Mo^{2+}
p-Mo_2C		231.9 (40%)	229.6 (18%)	229.0 (20%)	228.4 (23%)
p-Mo_2C	H_2O[2]	232.2 (38%)	229.9 (20%)	229.1 (20%)	228.5 (22%)
		C 1s (eV)[1]			
		Carbidic	Adventitious	C-O	C=O
p-Mo_2C		283.5 (29%)	284.8 (33%)	286.1 (32%)	288.8 (7%)
p-Mo_2C	H_2O[2]	283.5 (35%)	284.8 (19%)	286.0 (37%)	288.9 (9%)
		O 1s (eV)[1]			
		MoO$_x$		-OH, =O, H_2O	
p-Mo_2C		530.4 (63%)		531.9 (37%)	
p-Mo_2C	H_2O[2]	530.3 (65%)		532.2 (35%)	

[1] The first number listed represents the BE. The number in parentheses represents the atomic percentage of the species relative to other species of the same element.
[2] H_2O treatment by exposure of passivated Mo_2C to deaerated H_2O for 24 hr
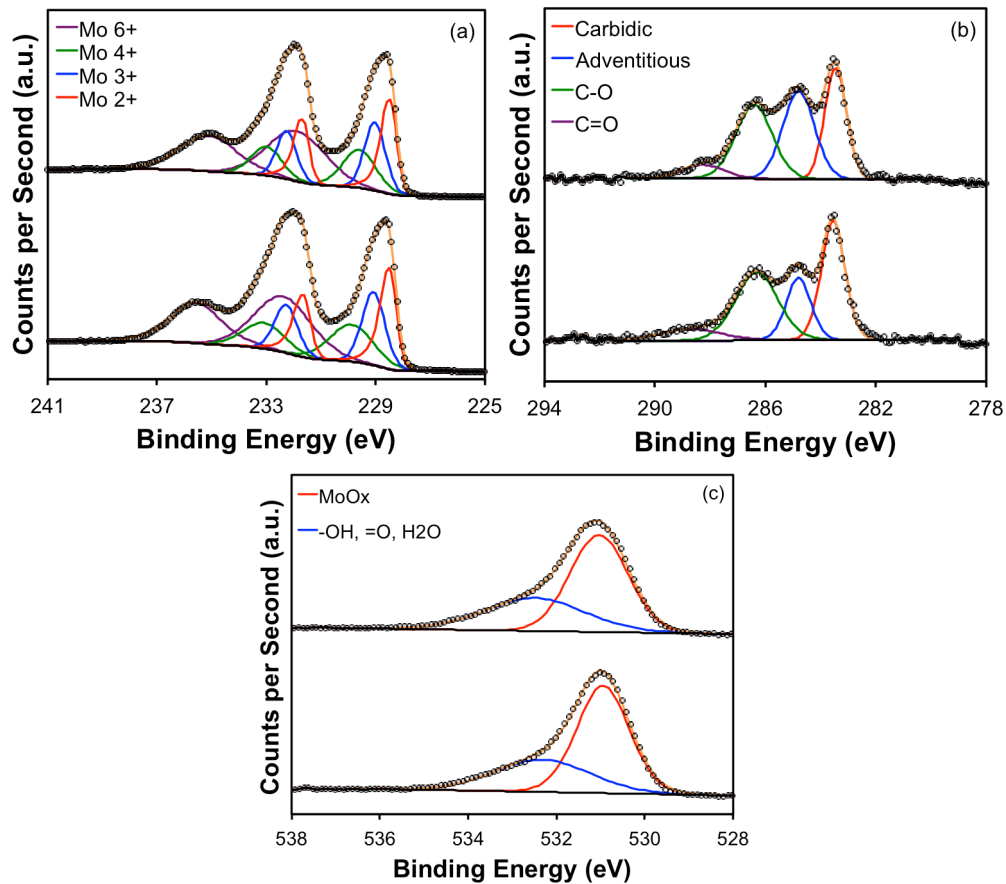
Figure 3.20. XPS for the passivated Mo_2C supports before (top) and after (bottom) water exposure. The spectra collected are (a) Mo 3d, (b) C 1s, and (c) O 1s.

3.3.2.4. Composition of Pt-Mo₂C Catalysts and Pt Mass Balance Closure

Analysis of the resulting Pt-Mo_2C catalysts powders indicated that the Pt/Mo_2C and Pt/p-Mo_2C catalysts contained 3.7wt% and 1.1wt% Pt, respectively. The actual Pt loading for the Pt/Mo_2C catalyst was within experimental error of the amount of Pt removed from the deposition solution (equivalent to 3.9wt% Pt). Conversely, The Pt loading for the Pt/p-Mo_2C catalyst was significantly less than that removed from solution (3.8 wt%). The difference in Pt metal content determined via analysis of the supernatant solution versus the dried powder indicates that Pt must be instead precipitating out of solution or depositing onto another material surface. It is highly unlikely that Pt is simply

135

precipitating from solution based on the findings of Spieker et al. showing the stability of chloroplatinic acid in aqueous solutions over a wide range of pH [49]. A more rational explanation for the difference in Pt loadings is the deposition or complexation of the $[PtCl_6]^{2-}$ anion on or with the blue oxycarbide that appears to dissolve from the catalyst surface into solution at the same time as the onset of continued Pt loss from solution.

Two experiments were designed and conducted to test this possibility. In the first experiment, analyses were performed in an attempt to close the Pt mass balance for a typical wet impregnation of H_2PtCl_6 onto p-Mo_2C; to achieve this, samples were taken to analyze all possible destinations for Pt. First, an aliquot of the starting H_2PtCl_6 solution was collected, filtered, and stored prior to introduction of p-Mo_2C to the solution; this sample served as a reference to the total Pt in the system. The p-Mo_2C was then introduced to the solution. After H_2PtCl_6 was allowed to adsorb onto p-Mo_2C for 12 hours, the solid material (Pt/p-Mo_2C) was collected, dried, and passivated. An aliquot of the final H_2PtCl_6 solution was collected, filtered, and stored. Lastly, the remaining supernatant solution (~65 mL) of the wet impregnation was dried under vacuum for 48 hours. ICP analysis was performed on these four samples (solution before, solution after, solid material after, blue oxycarbide) and the results are shown in Table 3.3. All Pt is lost from solution following wet impregnation onto p-Mo_2C. Based on the amount of Pt lost from solution, the expected weight percent for Pt/p-Mo_2C is 3.1, which differs from the measured Pt wt% of 2.2 for the solid material. The Pt balance does not close as approximately 7.2 mg remain unaccounted for. Surprisingly, a significant amount of Pt is observed in the digested oxycarbide sample indicating that the absent Pt atoms may be incorporated into the blue oxycarbide, which is typically filtered out from the sample

aliquots prior to ICP-OES analysis. This result is corroborated by Pt diffraction peaks for the blue oxycarbide material following exposure of p-Mo$_2$C to H$_2$PtCl$_6$ (Figure 3.21). Results conclusively indicate the presence of an interaction between the blue oxycarbide generated by dissolution of parts of the Mo$_2$C passivation layer and H$_2$PtCl$_6$.

Table 3.3. Pt concentrations as determined by ICP-OES for the 4 samples associated with Pt adsorption onto p-Mo$_2$C aimed at closing the Pt mass balance.

Sample	[Pt], mg/L	Eq. Pt wt% on Mo$_2$C
Solution *Before*	34.3	3.1
Solution *After*	0.1	
Pt/p-Mo$_2$C	103.3	2.2
Pt/Oxycarbide	305.4	36.7
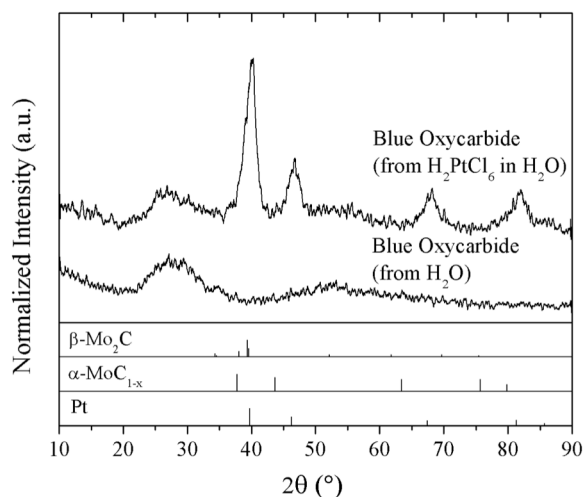
Figure 3.21. X-ray diffraction patterns for the recrystallized blue oxycarbide material following p-Mo$_2$C exposure to H$_2$O or H$_2$PtCl$_6$ in H$_2$O.

In the second experiment, the blue molybdenum oxycarbide powder was isolated and recrystallized. A metal deposition experiment with H$_2$PtCl$_6$ was conducted on the blue oxycarbide powder. Similar to previous tests, an aqueous precursor solution of H$_2$PtCl$_6$ was deaerated for 15 minutes, followed by introduction of the crystallized blue oxycarbide (~100 mg). Samples of the supernatant solution were taken at discrete time intervals during the metal deposition to monitor the concentration (or uptake) of Pt by the blue oxycarbide as a function of deposition time, shown in Figure 3.22. Results indicate

that the blue oxycarbide interacts with the chloroplatinic acid very rapidly as indicated by the loss of ~50% of Pt from solution in the first 5 minutes. However, the interaction is complex as Pt is observed to re-enter solution as a function of time, eventually returning to the initial concentration after approximately 90 minutes. The concentration of Mo in solution increases as a function of time to an asymptotic value after ~180 minutes. One explanation for these results is that Pt readily interacts with the solid oxycarbide, but does not interact as strongly with the dissolved oxycarbide under the conditions studied. This is supported by the similar trends of the Mo concentration and normalized Pt concentration curves. Initially, the blue oxycarbide may exist as a solid (low Mo concentration) and Pt interacts with this material, but as the solid dissolves into solution and increases the Mo concentration, the Pt also dissolves back into solution.
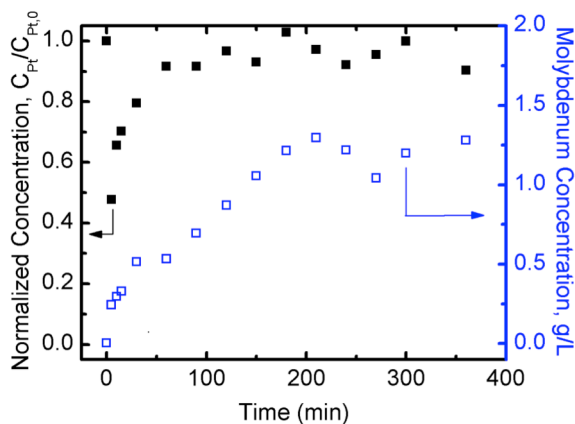
Figure 3.22. Adsorption profiles for H_2PtCl_6 with the blue oxycarbide as a function of deposition time. Normalized Pt concentration is shown on the left axis while Mo concentration (g/L) is shown on the right.

It should be noted that clear physical color changes occurred during the wet impregnation onto the blue oxycarbide. Prior to introducing the blue oxycarbide, the solution was bright yellow, consistent with the results in Figure 3.17. Following addition of the blue oxycarbide, the solution immediately turned dark blue, as expected. However,

138

with increasing time, the solution color shifted from dark blue to the initial yellow after 6 hours. It is not known what caused this physical change. However, it is possible that the presence of Mo_2C is necessary to maintain the blue oxycarbide in a solution of chloroplatinic acid. It is possible that this experimental design is insufficient for maintaining comparable conditions to those in a typical wet impregnation of H_2PtCl_6 onto p-Mo_2C. However, interactions between the blue oxycarbide and H_2PtCl_6 are evident and likely contribute to the previously observed Pt mass balance discrepancy.

3.3.2.5. Point of Zero Charge Analysis for Molybdenum Carbides and Oxides

The deposition of Pt onto Mo carbides has been reported to proceed via electrostatic adsorption of the Pt ions on the Mo_2C followed by reduction [26]. The point of zero charge (PZC) is a useful metric with regard to the surface chemistry of materials in solution [32,33]. The PZC of a material characterizes the point at which surface functional groups (e.g. hydroxyl) equilibrate with the solution such that no net protonation or deprotonation of surface –OH groups occurs. Solutions of initial pH above or below the PZC will deprotonate and protonate surface hydroxyls, respectively, in an attempt to equilibrate the material-solution system. For example, if the PZC of Mo_2C or p-Mo_2C lies sufficiently far above the pH of the H_2PtCl_6 solution, the material surface will generate a positive charge and will attract the $[PtCl_6]^{2-}$ anions.

Results from the PZC experiments for Mo_2C, p-Mo_2C, and MoO_2 are shown in Figure 3.23. The flat portion of each curve represents the point of zero charge. The PZC for Mo_2C is approximately pH 5, while PZCs for the p-Mo_2C and MoO_2 materials are very similar and approximately pH 3. These results not only indicate that surface chemistries of the unpassivated and passivated Mo_2C surfaces are different, but that the

charge on the p-Mo$_2$C surface in solution at a given pH resembles that of MoO$_2$. For completeness the PZC for MoO$_3$ was estimated and found to be approximately pH 3 in acidic solutions, but this result is not reported since MoO$_3$ dissolves in basic solutions. The H$_2$PtCl$_6$ solution pH was consistently ~2.2. As such, [PtCl$_6$]$^{2-}$ anions would be attracted to the unpassivated Mo$_2$C surface, given its PZC of 5, while the p-Mo$_2$C will not gain charge due to the negligible difference between its PZC (~3) and the pH in solution (~2.2.). This may also help to rationalize the adsorption results.
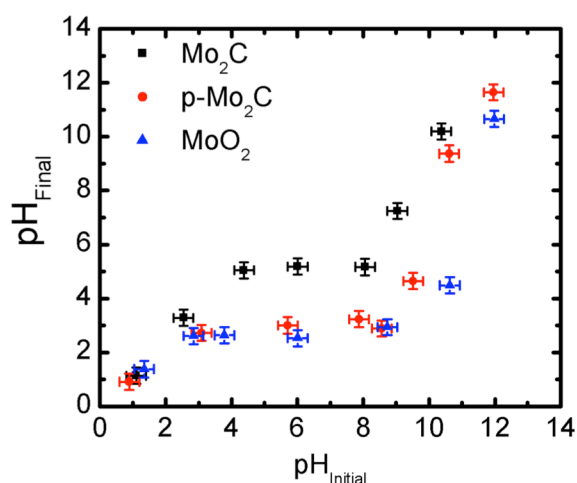
Figure 3.23. Point of zero charge determination for Mo$_2$C, p-Mo$_2$C and MoO$_2$ materials.

3.3.3. Effect of Passivation on Catalyst Structure and Catalytic Performance

3.3.3.1. Scanning Electron Microscopy of Pt-Mo$_2$C Catalysts

Scanning electron micrographs were collected to analyze the surface morphologies of the Pt-Mo$_2$C catalysts. Micrographs for Pt/Mo$_2$C and Pt/p-Mo$_2$C catalysts are shown in Figure 3.24 and Figure 3.25. Small crystallites (~100nm) were observed on the Pt/Mo$_2$C catalysts, presumably nanoscale Pt. Conversely, large globules were observed sporadically on the surface for Pt/p-Mo$_2$C. Small crystallites similar to those observed on Pt/Mo$_2$C were not observed in the Pt/p-Mo$_2$C micrographs. As a result of these differences, energy dispersive X-ray (EDX) mapping was performed on the

material surfaces to map the location of Pt and Mo in the images. EDX images for the micrographs are shown in Figure 3.26. Pt appears highly dispersed on the Pt/Mo$_2$C catalyst, showing uniform Pt signal in the SEM-EDX map for both micrographs studied. In contrast, the large agglomerates observed in the micrographs of Pt/p-Mo$_2$C were confirmed to be Pt as indicated by the localized yellow in the EDX map, existing as large (10-20 µm) particles. These results indicate that metal dispersion is strongly impacted by the presence or absence of redox chemistry in the Pt-Mo$_2$C system.
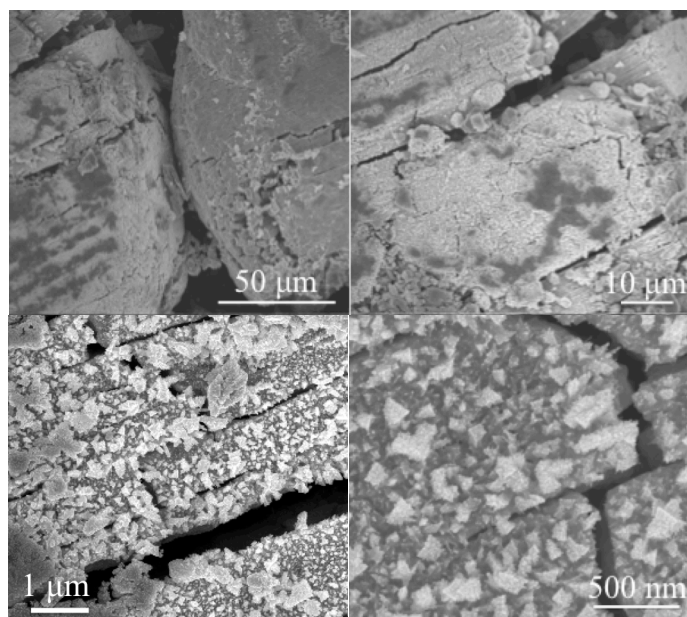
Figure 3.24. SEM micrographs of the nanostructured Pt/Mo$_2$C catalysts
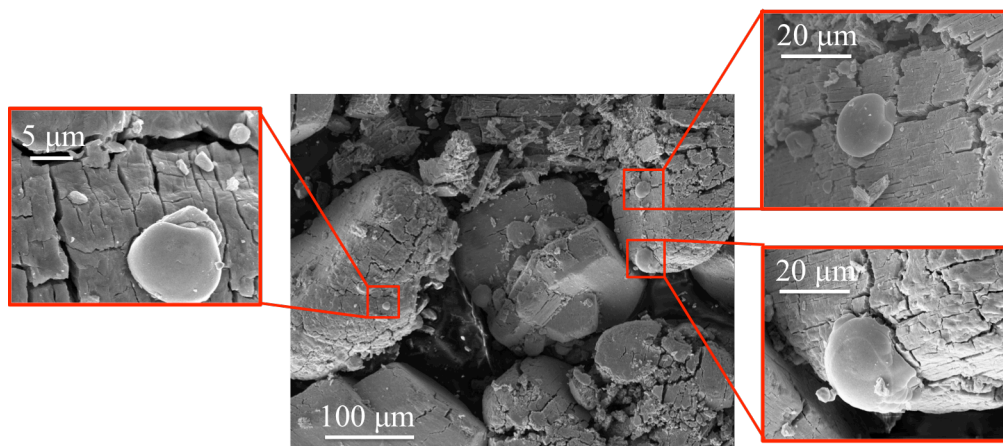
Figure 3.25. SEM micrographs of the nanostructured Pt/p-Mo$_2$C catalysts
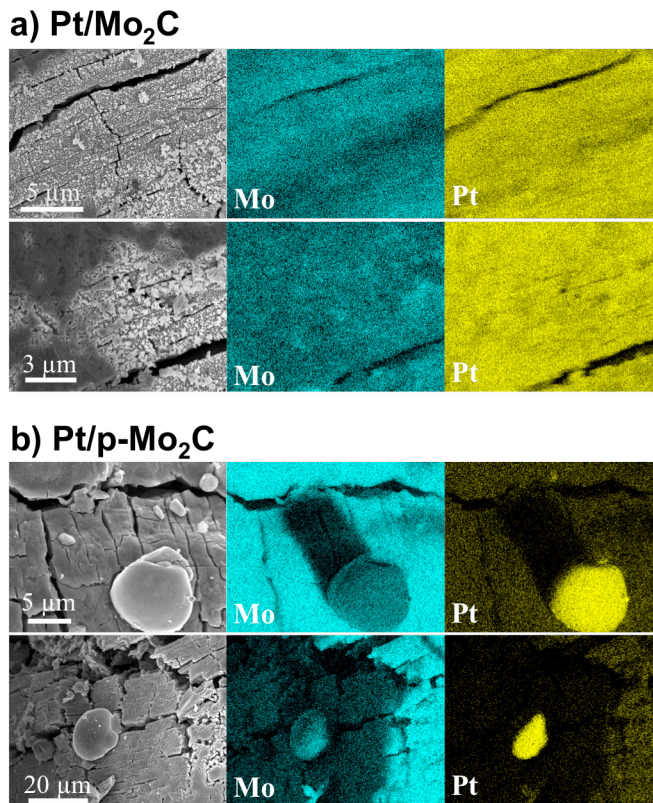
Figure 3.26. SEM-EDX mapping of Mo and Pt for the a) Pt/Mo$_2$C and b) Pt/p-Mo$_2$C catalysts

3.3.3.2.   Water-Gas Shift Results for Pt-Mo$_2$C Catalysts

The performance of Pt-Mo$_2$C catalysts for the water-gas shift (WGS) reaction is extensively reported in literature [11,23,36,48,50]. Schweitzer et al. reported the WGS active site occurred at the interface between Pt domains and the Mo$_2$C support, where Pt was responsible for CO adsorption and Mo$_2$C activated the H$_2$O [11]. The surface species then could react at the interface where Pt particles came in contact with Mo$_2$C. Raft-like Pt domains, which generate a high interfacial area, as determined by XAS and density functional theory calculations, only enhanced the promotional effect of Pt. In a separate study, Sabnis et al. hypothesized that the WGS active sites for Pt-Mo$_2$C were formed by Pt-Mo alloy nanoparticles in contact with the Mo$_2$C support [36]. Furthermore, for

142

supported Pt-Mo$_2$C catalysts (either on carbon nanotubes [36] or aluminum oxide [50]), the Pt was found to preferentially bind to Mo$_2$C particles over the other supports. As a result of these studies, it is expected that differences in Pt dispersion will impact that WGS rate. Given the larger Pt particles, Pt/p-Mo$_2$C is expected to show a smaller Pt promotional enhancement of Pt than for Pt/Mo$_2$C.

Gravimetric water-gas shift rates for Mo$_2$C, Pt/Mo$_2$C, and Pt/p-Mo$_2$C are shown in an Arrhenius plot (Figure 3.27). The performance of a commercial WGS catalyst, Cu-ZnO-Al$_2$O$_3$, is included as a reference. It should be noted that all Mo$_2$C catalysts were pretreated in 15% CH$_4$/H$_2$ at 590°C for 4 hr prior to reactivity testing. Cu-ZnO-Al$_2$O$_3$ was pretreated based on vendor specifications (200°C for 4 hr in 4% H$_2$/N$_2$, 3°C/min heat rate). Pt/Mo$_2$C exhibited the highest gravimetric rate, nearly 4-5 times higher than bare Mo$_2$C. Interestingly, Pt/p-Mo$_2$C exhibited very similar performance to Mo$_2$C indicating that the ~1.1wt% of Pt present does not have a significant promotional effect, supporting the hypothesis. In addition, Pt/Mo$_2$C far exceeded the performance of the commercial Cu-ZnO-Al$_2$O$_3$ catalyst, as has been reported previously [23]. Activation energies for the
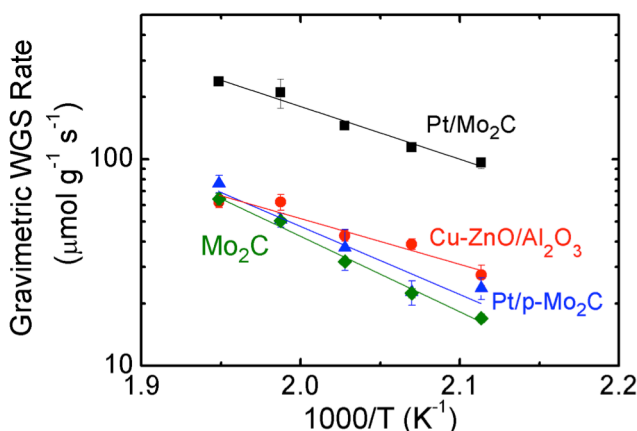
Figure 3.27. Gravimetric water-gas shift reaction rates for Mo$_2$C, Pt/Mo$_2$C, Pt/p-Mo$_2$C, and Cu-ZnO-Al$_2$O$_3$

Table 3.4. Summary of Physical and Surface Chemical Properties, and Water Gas Shift Activities.

Catalyst	Surface Area (m^2/g)	CO Uptake ($\mu mol/g$)[b]	N_2O Uptake ($\mu mol/g$)	Site Density (sites /m^2 x 10^{18})[c]	TOF (s^{-1})[d]	$E_{a,App}$ (kJ/mol)
p-Mo$_2$C	103[a]	404	-	2.36	0.16	68 ± 6
3.7% Pt/Mo$_2$C	115[a]	330	-	1.73	0.72	49 ± 4
1.1% Pt/p-Mo$_2$C	108[a]	420	-	2.34	0.18	63 ± 15
Cu/ZnO/Al$_2$O$_3$ [23]	60	-	192	1.93	0.38	42 ± 9

[a] BET surface areas determined for the passivated catalysts
[b] All catalysts pretreated in 15% CH_4/H_2 at 590°C for 4 hours prior to CO pulse chemisorption. Without the pretreatment step and removal of the passivation layer, CO chemisorption uptakes were very low (e.g. 6 $\mu mol/g$ for p-Mo$_2$C).
[c] Site densities were calculated based on the CO chemisorption and BET surface area results.
[d] Turnover frequencies (TOF) were calculated by normalizing the CO consumption rates measured at 240°C by the number of active sites estimated by CO chemisorption.

catalysts ranged from 42 kJ/mol for Cu/ZnO/Al$_2$O$_3$ to 68 kJ/mol for Mo$_2$C. Pt/Mo$_2$C had a lower activation energy than Mo$_2$C indicating a change in the rate determining step while Pt/p-Mo$_2$C exhibited an activation energy similar to that of Mo$_2$C. Interestingly, when normalized by the Pt content, activities for the Pt/p-Mo$_2$C (1.4 mol$_{CO}$ mol$_{Pt}^{-1}$ s^{-1}) and Pt/Mo$_2$C (1.3 mol$_{CO}$ mol$_{Pt}^{-1}$ s^{-1}) catalysts were similar at 240°C. This similarity will be considered in the Discussion section. The Pt normalized rate for the Pt/Mo$_2$C catalysts matches closely with those reported by Schweitzer et al. (~1.4 mol$_{CO}$ mol$_{Pt}^{-1}$ s^{-1}) [11].

Gravimetric rates were normalized by both surface area and proposed active site (based on CO and N_2O chemisorption for Mo$_2$C-based and Cu-ZnO-Al$_2$O$_3$, respectively). Surface areas, CO/N_2O uptakes, and calculated site densities are provided in Table 3.4. Areal rates (rates normalized by surface area) and turnover frequencies (rates normalized by CO or N_2O) are shown in Figure 3.28 and Figure 3.29, respectively. It is clear that Mo$_2$C and Pt/p-Mo$_2$C exhibit the lowest rates, while Pt/Mo$_2$C exhibits the highest rate. The commercial Cu-ZnO/Al$_2$O$_3$ catalyst exhibits rates in between Pt/Mo$_2$C and Mo$_2$C. Based on these results, it is evident that the presence of the passivation layer during

synthesis of Pt-Mo$_2$C catalysts has an adverse effect on the performance of these catalysts. The presence of redox chemistry during catalyst synthesis resulted in catalysts with exhibited higher Pt dispersions, higher Pt loadings, and higher WGS rates compared to catalysts synthesized without the driving force for redox.
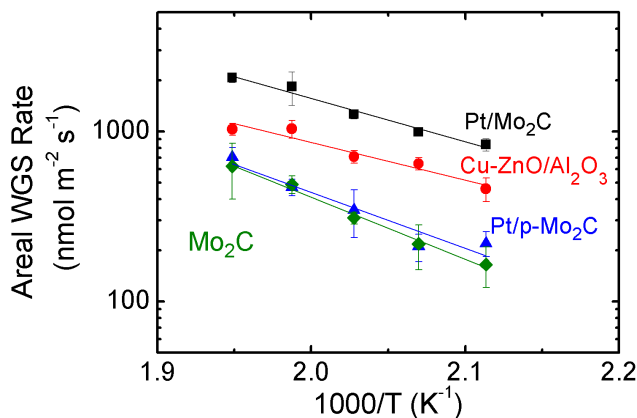
Figure 3.28. Areal water-gas shift reaction rates for Mo$_2$C, Pt/Mo$_2$C, Pt/p-Mo$_2$C, and Cu-ZnO-Al$_2$O$_3$
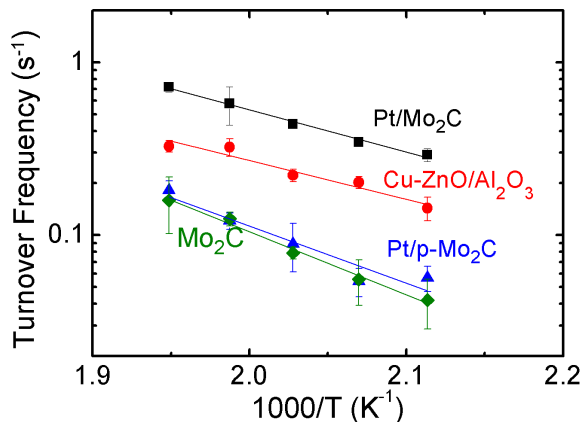
Figure 3.29. Turnover frequencies for Mo$_2$C, Pt/Mo$_2$C, Pt/p-Mo$_2$C, and Cu-ZnO-Al$_2$O$_3$ (gravimetric rates normalized by CO or N$_2$O uptakes)

3.4. Discussion

The spontaneous reduction of metals on unpassivated Mo$_2$C and its effect on catalyst structure and reactivity were explored in this chapter. Schaidle et al. hypothesized the presence of surface redox chemistry between Mo and depositing metals (i.e., Pt, Pd, Cu) during wet impregnation of metal salts onto unpassivated Mo$_2$C based

145

on standard reduction potentials [26]. In that study, while reduction of the depositing metal was observed, no analysis was conducted to test for oxidation of the Mo_2C support. A goal of the work reported here was to observe Mo oxidation concomitant with metal reduction during wet impregnation.

It is important to note that spontaneous reduction of metal ions on supports has been observed previously in other systems through galvanic displacement on both metallic and semiconductor surfaces. Galvanic displacement is an oxidation-reduction reaction driven simply by thermodynamics, where reduction of one species is concomitant with oxidation of another species. These redox reactions are governed by the standard reduction potential for the oxidation/reduction reactions and will proceed spontaneously if the change in Gibbs free energy is negative, (equations 3.2 and 3.3 with E_A^0 larger than E_B^0 where A and B represent half reactions). Galvanic displacement reactions can occur between two ionic species, such as the transition of Cu (II) and Cr (II) to Cu (I) and Cr (III) [$E^0_{Cu(II)/Cu(I)}$ = 0.16 V, $E^0_{Cr(III)/Cr(II)}$ = -0.50 V] or between a solid and metal ions, such as between Cu (II) and Fe metal, where metallic Cu displaces the Fe, forming Fe ions in solution [$E^0_{Cu(II)/Cu(0)}$ = 0.34 V, $E^0_{Fe(II)/Fe(0)}$ = -0.44 V].

$$E_i^0 = \frac{\Delta G_{Products} - \Delta G_{Reactants}}{nF} \tag{3.2}$$

$$\Delta G_{Red-ox} = -nF(E_A^0 - E_B^0) \tag{3.3}$$

For example, Wen et al. deposited thin layers of Au onto Cu_2S wires by simply exposing the Cu_2S to a chloroauric solution [51]. Due to differences in redox potential, Cu (E^0 = 0.34V) donates electrons to Au (E^0 = 1.002V) such that Au displaces Cu on the solid surface. Au has also been deposited onto semiconductor substrates, such as Si (E^0 = -1.20V) and Ge (E^0 = 0.12V), using this phenomenon [52]. Choi et al. also observed

reduction of Au and Pt chlorides onto carbon nanotubes (CNT), noting that the standard reduction potential of CNT was 0.5V compared to 1.002 and 0.775V for the $AuCl_4^-$ and $PtCl_4^{2-}$, respectively [53]. The authors noted increased conductivity in the CNT resulting from the donation of electrons to the depositing metals and generation of holes.

These literature reports indicate that a variety of species can support redox chemistry with highly reducible metals such as Pt and Au. The results reported in this chapter confirm the presence of redox chemistry between the depositing Pt and the Mo_2C support and reveal significant differences between the synthesis adsorption chemistries, structures and compositions of catalysts produced by depositing Pt onto unpassivated and passivated Mo_2C supports. Using both X-ray absorption spectroscopy and X-ray photoelectron spectroscopy, Mo oxidation and Pt reduction were observed during deposition of $[PtCl_6]^{2-}$ anions onto an unpassivated Mo_2C support. Similar results were also observed for Al_2O_3-supported Mo_2C. For the Mo_2C material, the XAS results indicated that the Pt^{4+} in $[PtCl_6]^{2-}$ was reduced to $\sim Pt^0$ with concomitant oxidation of Mo, perhaps according to the reaction in Equation 3.4.

$$Mo_2^x C + \delta[PtCl_6]^{2-} \rightarrow Mo_2^{x+4\delta} C + \delta Pt^0 + 6\delta\, Cl_{(ads)}^- \tag{3.4}$$
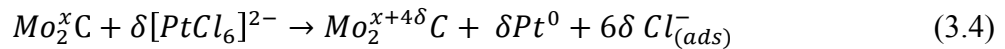
It is not surprising that Mo_2C is capable of this chemistry given its highly reduced state and low thermodynamic barrier for oxidation. However, it is difficult to determine the exact thermodynamics (i.e., standard reduction potential) of Mo_2C oxidation during metal deposition for two reasons. First, the exact Mo surface species following metal deposition is unknown, making it difficult to determine what oxidation reactions would be appropriate. Second, comprehensive thermodynamic data for Mo_2C are not available at the conditions used. Despite this, we can estimate the standard reduction potential of

Mo$_2$C by looking at thermodynamic data for Mo oxidation. Based on XAS results reported by Schaidle et al., Pt, Pd, and Cu were reduced during deposition on Mo$_2$C while Fe and Co were not, so the standard reduction potential of Mo$_2$C likely falls between the standard potential for Cu^{2+} (E^0 = 0.34V) and Fe^{3+} (E^0 = -0.02V) [26]. While comprehensive thermodynamic data is not available for Mo$_2$C systems, estimates can be made from the thermodynamic data for Mo oxidation reactions (equations 3.5-3.8) [28,54]:

$$Mo \rightarrow Mo^{3+} + 3\,e^-, \qquad\qquad\qquad E^0 = 0.20\,V \qquad (3.5)$$

$$Mo + 2H_2O \rightarrow MoO_2 + 4H^+ + 4e^-, \qquad\qquad E^0 = 0.152\,V \qquad (3.6)$$

$$Mo^{3+} + 2H_2O \rightarrow MoO_2 + 4H^+ + e^-, \qquad\qquad E^0 = 0.008\,V \qquad (3.7)$$

$$Mo + 3H_2O \rightarrow MoO_3 + 6H^+ + 6e^-, \qquad\qquad E^0 = -0.075\,V \qquad (3.8)$$

The standard potentials for the Mo oxidation reactions fall within the expected thermodynamic reduction potential range for Mo$_2$C.

It is necessary to comment on the specifics of Equation 3.4, in particular as it relates to charge balancing, adsorbed chlorine, and the Mo oxidation product. Following Pt reduction and Mo oxidation, positively charged Mo remains on the Mo$_2$C surface and requires charge balancing. Since these materials exhibit high conductivities [13], the charge could potentially be distributed throughout the bulk. Conversely, the generated surface charge may also be balanced by oxygen, hydroxyl groups, or adsorbed chloride ions, as illustrated in Figure 3.30. Oxygen from water can potentially incorporate into the lattice to form an oxycarbide or Mo oxide species, similar to those generated by passivating Mo$_2$C. However, no blue oxycarbide was observed to dissolve from the Pt/ Mo$_2$C surface following Pt deposition and redox indicating that the species formed is

likely not an oxycarbide. Schaidle et al. observed chlorine by XPS on the surfaces of the

materials following the deposition of Pt from H_2PtCl_6 solutions [26]. It is possible that

chloride anions complex with the surface following Pt reduction in order to balance

surface charge. While there is proof of a more oxidized Mo surface, it is difficult to

discern what species balances the charge from the oxidized Mo.
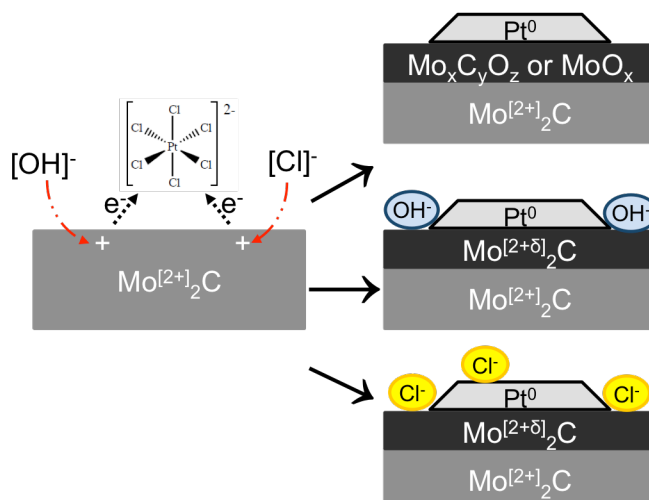
Figure 3.30. Schematics of proposed interactions between $[PtCl_6]^{2-}$ and unpassivated Mo_2C during metal deposition

Passivation of the Mo_2C surface would be expected to inhibit the observed redox

chemistry with the Pt salts and, based on the results presented in this chapter, produces

very different structural and compositional properties compared to materials prepared

using unpassivated materials. Wet impregnation of Pt onto unpassivated and passivated

Mo_2C yielded different adsorption profiles based on the Pt concentration remaining in

solution. Pt deposited rapidly onto unpassivated Mo_2C. In the case of passivated Mo_2C,

an initial adsorption period was followed by an induction period of ~2-3 hours and then

subsequent adsorption accompanied by a solution color change from yellow to blue due

to dissolution of the oxycarbide passivation layer. Elemental analysis of the resulting

catalysts showed that the Pt composition on p-Mo_2C was significantly lower than would

be expected based on the adsorption studies. Based on additional experimental analysis, it is proposed that after the induction period the Pt salt complexes with the blue oxycarbide in solution to form a suspended precipitate, which is filtered out prior to elemental analysis of the supernatant solution. SEM micrographs indicated large agglomerates of Pt on the p-Mo_2C support and small Pt crystallites on the Mo_2C support. Surface redox chemistry facilitated this higher dispersion on unpassivated Mo_2C, as the rate of nucleation would exceed the rate of growth of particles due to the fast redox reactions present between Pt and unpassivated Mo_2C.

The WGS rates and TOFs for the Pt/Mo_2C catalyst were higher than those for the Pt/p-Mo_2C catalyst. Since both catalysts were recarburized prior to the rate measurements similar performance characteristics including activation energies might be expected, however, this was not the case. Given the higher activities, depositing Pt directly onto the carbide surface is preferred. Differences between TOFs and activation energies for the Pt/Mo_2C and Pt/p-Mo_2C catalysts suggest that active sites for these catalysts are different. Schweitzer et al. [11] proposed that the interface between the Pt particle and Mo_2C surface was the most active site for WGS on the Pt/Mo_2C catalyst. At this interface, Mo_2C activates H_2O producing oxygen for subsequent reaction with CO, while Pt facilitates adsorption of CO. Further, Sabnis et al. hypothesized that the WGS active site was at the interface between a Pt-Mo alloy nanoparticle and the Mo_2C support [36]. Given that rates, TOFs, and activation energies for the passivated Mo_2C catalysts (Pt/p-Mo_2C and p-Mo_2C) were nearly identical, it appears that most of the activity was derived from p-Mo_2C and that Pt was relatively inactive. This is not inconsistent with the very large particle sizes for Pt on the Pt/p-Mo_2C catalyst. Assuming 18.8 μm particles, the Pt

would account for 1.6×10^{-4} m^2 or less than 0.001% of the surface area of the 1.1% Pt/p-Mo$_2$C catalyst.

Finally, a comment about similarities between rates for the Pt/Mo$_2$C and Pt/p-Mo$_2$C catalysts when normalized based on the Pt content. This similarity was likely a coincidence as Mo$_2$C is itself an active support. Rates normalized by metal content are more applicable in systems where the added metal is the only active species. For catalysts where the activity is dominated by p-Mo$_2$C, mathematically, there will be one loading where the Pt normalized rates for the enhanced Pt/Mo$_2$C and Pt/p-Mo$_2$C catalysts should be identical. For example, bare Mo$_2$C itself has an appreciable WGS rate. If addition of a metal promoter increases the rate by a factor of 5 in one case, but has a negligible effect in a separate case (as was observed for the unpassivated and passivated Mo$_2$C supports), when normalized to the moles of metal added, the normalized rates will be identical for metal loadings differing by a factor of 5 (with the catalyst with the lower metal content exhibiting the lower rate). This is mathematically true for all cases.

Some further insight can be gained from the report by Schweitzer et al of a Pt-normalized rate of ~2.4 mol$_{CO}$ mol$_{Pt}^{-1}$ s^{-1} for 1wt% Pt/Mo$_2$C,, nearly double that of the 1.1wt% Pt/p-Mo$_2$C catalyst in our work (1.4 mol$_{CO}$ mol$_{Pt}^{-1}$ s^{-1}) [11]. Another rate comparison approach involves removing the background activity generated by Mo$_2$C and only analyzing the rate enhancement with Pt addition. On a per mole Pt basis, the rate enhancement relative to Mo$_2$C for Pt/Mo$_2$C and Pt/p-Mo$_2$C is 0.92 and 0.12 mol$_{CO}$ mol$_{Pt}^{-1}$ s^{-1}, respectively.

3.5. Summary

The presence and implications of surface redox between Mo_2C and depositing metals during catalyst synthesis were explored. Redox chemistry was observed between depositing Pt and the Mo_2C support using both XPS and *in situ* XAS. During wet impregnation, complete reduction of Pt was observed while Mo was oxidized in the process. The electron balance was within error indicating that the oxidation resulted entirely from a galvanic-type interaction between Mo and Pt. To our knowledge, this is the first experimental observation of redox chemistry occurring between the support and depositing metal during actual metal deposition.

The effects of metal-support interactions on catalysis over these materials were probed. Passivation of Mo_2C was utilized to inhibit redox chemistry by oxidizing the surface prior to exposure to the Pt salt. The differences in composition, structure, and reactivity of catalysts synthesized via deposition onto an unpassivated (reduced) and a passivated (oxidized) support surface suggest a strong effect of the redox chemistry. Pt adsorption and dispersion were greatly diminished by suppression of redox. In addition, the intrinsic water-gas shift rates of these catalysts differed greatly despite identical reaction conditions and pretreatments. The Pt/Mo_2C catalyst was much more active than the $Pt/p-Mo_2C$ catalyst.

It is hypothesized that other, more reducible metals (e.g., Cu, Ag, Au, Pd, Ru, Rh, etc.) will exhibit different catalyst structures when deposited on unpassivated versus passivated Mo_2C. The passivation layer has a larger impact on metal-support interactions than has been discussed to date and should be considered during synthesis of carbide- and nitride-supported metal catalysts.

3.6. References

[1]   M. Delgado, C.C. Santini, F. Delbecq, R. Wischert, B. Le Guennic, G. Tosin, R. Spitz, J.-M. Basset, P. Sautet, J. Phys. Chem. C, 114 (2010) 18516-18528.

[2]   X. Wang, J.A. Rodriguez, J.C. Hanson, D. Gamarra, A. Martínez-Arias, M. Fernández-García. J. Phys. Chem. B, 110 (2006) 428-434.

[3]   S.J. Tauster, Acc. Chem. Res., 20 (1987) 389–394.

[4]   B.L. Mojet, M.J. Kapper, J.T. Miller, D.C. Koningsberger, Studies in Surf. Sci. and Cat., 101 (1996) 1165-1174.

[5]   K. Keyvanloo, H.C. Hecker, B.F. Woodfield, C.H. Bartholomew, J. Catalysis., 319 (2014) 220–231.

[6]   K. Cheng, V.V. Ordomsky, M. Virginie, B. Legras, P.A. Chernavskii, V.O. Kazak, C. Cordier, S. Paul, Y. Wang, A.Y. Khodakov, Appl. Cat. A: General, 488 (2014) 66–77.

[7]   K.G. Azzam, I.V. Babich, K. Seshan, L. Lefferts, J. Catalysis, 251 (2007) 153–162.

[8]   A. Centeno, E. Laurent, B. Delmon, J. Catalysis, 154 (1995) 288–298.

[9]   D.V. Esposito, S.T. Hunt, Y.C. Kimmel, J.G. Chen, J. Am. Chem. Soc., 134 (2012) 3025-3033.

[10]   J.A. Rodriguez, P. Liu, Y. Takahashi, K. Nakamura, F. Viñes, F. Illas, J. Am. Chem. Soc., 131 (2009) 8595-8602.

[11]   N.M. Schweitzer, J.A. Schaidle, O.K. Ezekoye, X. Pan, S. Linic, L.T. Thompson, J. Am. Chem. Soc., 133 (2011) 2378-2381.

[12]   N. Perret, X. Wang, L. Delannoy, C. Potvin, C. Louis, M.A. Keane, J. Catalysis., 286 (2012) 172-183.

[13]   S.T. Oyama, Catal. Today. 15 (1992) 179–200.

[14]   R.J. Colton, J.J. Huang, R.W. Rabalais, Chem. Phys. Letters., 34 (1975) 337-339.

[15]   M. Lewandowski, A. Szymańska-Kolasa, P. Da Costa, C. Sayag, Catal. Today, 119 (2007) 31-34.

[16]   A. Guerrero-Ruiz, Y. Zhang, B. Bachiller-Baeza, I. Rodríguez-Ramos. Catal. Letters. 55 (1998) 165-168.

[17]   M. Xiang, D. Li, H. Xiao, J. Zhang, W. Li, B. Zhong, Y. Sun, Catal. Today, 131 (2008) 489-495.

[18]   H. Shou, R.J. Davis, J. Catalysis, 282 (2011) 83-93.

[19]   A, Griboval-Constant, J. Giraudon, G. Leclercq, L. Leclercq, Appl. Cat. A: General, 260, (2004) 35-45.

[20]   A. Griboval-Constant, J. Giraudon, I. Twagishema, G. Leclercq, M.E. Rivas, J. Alvarez, M.J. Pérez-Zurita, M.R. Goldwasser, J. Molec. Cat. A: Chemical, 259 (2006) 187-196.

[21]   W. Setthapun, S.K. Bej, L.T. Thompson, Top. Catal., 49 (2008) 73-80.

[22]   A.C. Lausche, J.A. Schaidle, L.T. Thompson, Appl. Cat. A: General, 401 (2011) 29-36.

[23]   J.A. Schaidle, A.C. Lausche, L.T. Thompson, J. Catalysis., 272 (2010) 235-245.

[24]   I.J. Hsu, Y.C. Kimmel, X. Jiang, B.G. Willis, J.G. Chen, Chem. Commun., 48 (2012) 1063-1065.

[25] R. Venkataraman, H.R. Kunz, J.M. Fenton, J. Electrochem. Soc., 150 (2003) A278-A284.

[26] J.A. Schaidle, N.M. Schweitzer, O.T. Ajenifujah, L.T. Thompson, J. Catalysis, 289 (2012) 210-217.

[27] H. Shou, D. Ferrari, D.G. Barton, C.W. Jones, R.J. Davis, ACS Catal., 2 (2012) 1408−1416.

[28] D.D. Wagman, W.H. Evans, V.B. Parker, I. Halow, S.M. Baily, R.H. Schumm. Selected Values of Chemical Thermodynamic Properties, Institute for Basic Standards, National Bureau of Standards, Washington D.C., 1965.

[29] N.M. Schweitzer, J.A. Schaidle, O.K. Ezekoye, X. Pan, S. Linic, L.T. Thompson, J. Am. Chem. Soc., 133 (2011) 2378-2381.

[30] J.A. Schaidle, A.C. Lausche, L.T. Thompson, J. Catalysis, 272 (2010) 235-245.

[31] J.A. Schaidle, N.M. Schweitzer, O.T. Ajenifujah, L.T. Thompson, J. Catalysis, 289 (2012) 210-217.

[32] L. Jiao, J.R. Regalbuto, J. Catalysis, 260 (2008) 329–341.

[33] T.E. Feltes, L. Espinsoa-Alonso, E. de Smit, L. D'Souza, R.J. Meyer, B.M. Weckhuysen, J.R. Regalbuto, J.R. J. Catalysis, 270 (2010) 95–102.

[34] Bencze, K.Z.; Kondapalli, K.C.; Stemmler, T.L. "X-ray Absorption Spectroscopy" in *Encyclopedia Absorption Spectroscopy*. John Wiley & Sons: New York, NY 2011.

[35] B. Ravel, M. Newville, Journal of Synchrotron Radiation, 12 (2005) 537–541.

[36] K.D. Sabnis, M.C. Akatay, Y. Cui, F.G. Sollberger, E.A. Stach, J.T. Miller, W.N. Delgass, R.H. Ribeiro. J. Catalysis, 330 (2015) 442-451.

[37] W.A. Spieker, J. Liu, L.T. Miller, A.J. Kropf, J.R. Regalbuto, Appl. Cat. A: General 232 (2002) 219-235.

[38] J.A. Schaidle, J. Blackburn, C.A. Farberow, C. Nash, K.X. Steirer, J. Clark, D.J. Robichaud, D.A. Ruddy. *ACS Catal.* 6 (2016) 1181-1197.

[39] Reddy, B.M.; Chowdhury, B.; Reddy, E.P.; Fernández, A. Appl. Cat. A: General 213 (2001) 279-288.

[40] Delporte, P.; Meunier, F.; Pham-Huu, C.; Vennegues, P.; Ledoux, M.J.; Guille, J. Catalysis Today 23 (1995) 251-267.

[41] Cheekatamarla, P.K.; Thomson, W.J. Appl. Cat. A: General 287 (2005) 176-182.

[42] Castañeda, S.I.; Montero, I.; Ripalda, J.M.; Díaz, N.; Galán, L.; Rueda, F. J. Applied Physics 85 (1999) 8415-8418.

[43] G.M. Bancroft, I. Adams, L.L. Coatsworth, C.D. Bennewitz, J.D. Brown, W.D. Westwood, Anal. Chem. 47 (1975) 586.

[44] Ravel, B. and M. Newville, Journal of synchrotron Radiation 12 (2005) 537-541.

[45] S. Calvin, S.X. Luo, C. Caragianis-Broadbridge, J.K. McGuinness, E. Anderson, A. Lehman, K.H. Wee, S.A. Morrison, L.K. Kurihara. Appl. Phys. Lett. 87 (2005) 233102

[46] A.M. Karim, V. Prasad, G. Mpourmpakis, W.W. Lonergan, A.I. Frenkel, J.G. Chen, D.G. Vlachos. J. Am. Chem. Soc. 131 (2009) 12230-12239.

[47] A.I. Frenkel, C.W. Hills, R.G. Nuzzo. J. Phys Chem. B 105 (2001) 12689-12703.

[48] J. Patt. PhD. Thesis. University of Michigan, 2003.

[49]   W.A. Spieker, J. Liu, L.T. Miller, A.J. Kropf, J.R. Regalbuto, Appl. Cat. A: General 232 (2002) 219-235.

[50]   G. Wang, J.A. Schaidle, M.B. Katz, Y. Li, X. Pan, L.T. Thompson, J. Catalysis 304 (2013) 92-99.

[51]   X. Wen, S. Yang, Nano Letters 2 (2002) 451-454.

[52]   L. Magagnin, R. Maboudian, C. Carraro. J. Phys. Chem. B 106 (2002) 401-407.

[53]   H.C. Choi, M. Shim, S. Bangsaruntip, H. Dai. J. Am. Chem. Soc. 124 (2002) 9058-9059.

[54]   A.J. Bard, R. Parsons, J. Jordan. *Standard Potentials in Aqueous Solution*, CRC Press, Inc., 1985.

CHAPTER 4

Fischer-Tropsch Synthesis over Mo_2C-supported Metal Catalysts

4.1. Introduction

Molybdenum carbide (Mo_2C)-supported metals have been evaluated as catalysts for Fischer-Tropsch synthesis (FTS) or CO hydrogenation, a potential process to convert biomass or methane from shale gas into useful synthetic fuels. Through biomass gasification or steam reforming of methane upstream, syngas (mixture of CO and H_2) can be obtained for conversion to useful fuels through the Fischer-Tropsch process. An in depth description of this process and the reactions involved can be found in Section 1.3.

The reactivity of transition-metal carbides and nitrides for the Fischer-Tropsch reaction is well documented [1-6]. To briefly summarize these reports, the primary products typically are the undesirable CH_4 and CO_2 and light hydrocarbons although chain propagation does occur. As discussed in Chapter 1, these carbides and nitrides have also been explored as active catalyst supports for active metallic phases for Fischer-Tropsch Synthesis [7,8], among other reactions [9-20]. Strong metal-support interactions have been hypothesized as the cause for some of the promising catalytic results.

Griboval-Constant et al. explored the use of Mo_2C- and WC-supported Co and Ru for FTS [7,8], reporting improved CO consumption rates with metal addition compared to the base carbide support. Negligible changes to the C_{5+} selectivity were observed for the Mo_2C-supported metal catalysts [7]; conversely, on WC, selectivity to C_{5+} hydrocarbons

156

was significantly increased with Co and Ru addition [8]. For these materials, the surface areas of supports were quite low (3-9.2 m^2/g) and the nominal loadings of Co and Ru were 1 wt%. Assuming 10 sites nm^{-2} and an average surface areas of ~ 6 m^2 g^{-1} for Mo$_2$C and WC, respectively, the surface coverage of Co and Ru were ~100 and 175% of a monolayer. As a result of these high surface coverages, the Fischer-Tropsch performance of the catalysts was probably dominated by the chemistry of the deposited metal. In another study, Shou et al. reported on the effect of Rb addition to Mo$_2$C, noting that Rb shuts down hydrocarbon production over Mo$_2$C without greatly improving alcohol synthesis [13]. Schaidle recently analyzed the effect of metal addition to Mo$_2$C on FTS with low metal surface coverages (nominal 10% based on 120 m^2 g^{-1} and 10 sites nm^{-2}) [6]. However, Schaidle found very minor changes in the product selectivity with metal addition and only small changes in CO consumption rate, primarily with Ni and Co (see Figure 4.1). As Griboval et al. and Shou et al. observed changes to the FTS performance using high surface coverages of the metal, the negligible changes observed by Schaidle et al. were speculated to be due to the low surface coverages used, where the innate Mo$_2$C chemistry for FTS dominates and the supported metal adds only limited active sites and
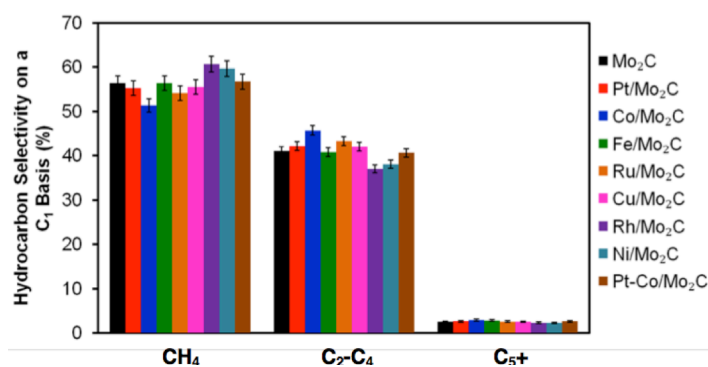
Figure 4.1. Hydrocarbon selectivity for Mo$_2$C supported metal catalysts. Conditions: 270-300°C, 25 bar, H$_2$:CO = 2:1, GHSV = 44,000 hr^{-1}. Selectivities reported for 290°C data points. Taken from [6].

157

hence, fails to greatly alter the catalyst performance. A similar evaluation of the FTS performance of these catalysts employing higher weight loadings of deposited metals may provide some noticeable differences in FTS performance as the surface is changed more drastically from a Mo_2C rich surface.

While these materials represent very promising catalysts, one practical challenge associated with the use of these carbides and nitrides is their pyrophoricity; consequently, prior to exposure to air, these materials are typically treated with oxygen to form a passivation layer that prohibits bulk oxidation. Thus, most carbide- or nitride-supported metal catalysts reported in the literature were prepared by deposition or impregnation of the metal onto the passivated carbide or nitride surface due to simplicity [10-12,7,8,20]. The effects of passivation on the synthesis, structure and composition of Mo_2C-supported Pt catalysts were discussed in Chapter 3. Work performed in this chapter attempted to expand this analysis to FTS active metals.

The primary objectives of the research described herein are two-fold: (1) evaluate the effect of metal promoters and loadings on Mo_2C and (2) explore the effect of passivation on the resulting catalyst structure and activity for Fischer-Tropsch synthesis. Molybdenum carbide was chosen as the support for this study as it represents an exemplary early transition-metal carbide and has been reported highly active for FTS [1,3,6,7,13].

4.2.   Experimental Methods

4.2.1. Catalyst Synthesis

Molybdenum carbide (Mo_2C) was synthesized via temperature-programmed reaction (TPR) as previously reported [16,17,21] and described previously in Section

3.2.1. Approximately 1.3g of ammonium paramolybdate was supported by a bed of quartz wool in a flow-through reactor, and secured in a vertical furnace. The precursor was heated from room temperature to 350°C under H_2 flow (400 mL/min) at a heating rate of 5°C/min followed by a 12 hr soak at this temperature. Following the soak step, 15% CH_4/H_2 gas was introduced (400mL/ min) and the material was heated to 590 °C at 2.67 °C/min followed by a 2 hr soak. The reactor was then removed from the furnace and allowed to cool to room temperature under 15% CH_4/H_2 gas flow.

When the reactor had cooled to below 30°C, the material was treated in one of three ways. To prepare the bare Mo_2C catalysts without metal promotion, the resulting material was exposed to 1% O_2/He flowing at 20 mL/min for at least six hours to form a protective oxide layer on the surface aimed at protecting the bulk phase. Metal deposition onto the passivated or unpassivated carbide was performed in one of two ways, wet impregnation and incipient wetness impregnation. Wet impregnation employs metal precursor solution volumes in excess of the pore volume of the solid support; such a technique typically allows metals to deposit through a chemical or electrostatic interaction [22,23]. Conversely, incipient wetness impregnation (also referred to as dry impregnation) utilizes a metal precursor solution volume exactly equal to the pore volume of the material support. The metal solution fills the pores and upon drying, metal nanoparticles are deposited on the walls of the pores.

Wet impregnation involves the deposition of a metal precursor onto the Mo_2C support previously reported in detail for Mo_2C [21] and was described in detail in Section 3.2.1. In short, the unpassivated or passivated Mo_2C was transferred from the quartz reactor (without exposure to air) into a deaerated, aqueous solution of the metal

precursor, which was continuously sparged with Ar. The metal precursors included Ni(NO$_3$)$_2$•6H$_2$O (Fisher, 99%) and Co(NO$_3$)$_2$•6H$_2$O (Alfa Aesar, ACS, 98.0-102.0%). These metals were chosen based on reports of their performance as active metals or promoters for Fischer-Tropsch synthesis. The target loadings were selected at 10% or 50% of a monolayer, assuming two-dimensional growth and a site density of 10 sites/nm^2, based on the site density of most metals [24]. Metals were allowed to deposit for up to 8 hr with intermittent stirring. Following deposition, the catalyst was transferred back to the quartz reactor under argon blanket then reduced with H$_2$ at 110°C (1.67°C/s ramp) for 2 hr, then at 450°C (5.67°C/s ramp) for 4 hr. The material was then cooled and passivated as described above in order to inhibit bulk oxidation.

For dry impregnation, the Mo$_2$C was first directly transferred into an argon glove box from the synthesis reactor without exposure to air. The material was then weighed, and transferred into a water-tolerant, nitrogen glove box, with the correct amount of metal precursor and deaerated water. The metal precursors included Ni(NO$_3$)$_2$•6H$_2$O (Fisher, 99%), Co(NO$_3$)$_2$•6H$_2$O (Alfa Aesar, ACS, 98.0-102.0%), Cu(NO$_3$)$_2$•3H$_2$O (Alfa Aesar, 99+%), Fe(NO$_3$)$_3$•9H$_2$O (Fisher, 99.6%), RuCl$_3$•3H$_2$O (Alfa Aesar, 99.9% (PGM basis), Ru 38% minimum), Ru(acac)$_3$ (Sigma-Aldrich, 97%), and K$_2$CO$_3$ (Sigma-Aldrich, SigmaUltra, minimum 99.0%). The glove box atmosphere was maintained by a constant flow of nitrogen; oxygen concentration levels in the glove box were tested using a titanium metallocene complex that changes colors with oxygen levels above 5 and 20 ppm [25]. The glove box was not used unless oxygen levels below 5 ppm were observed. The metal precursor was first dissolved in the appropriate amount of deaerated water, based on the support material pore volume, determined using both nitrogen physisorption

and empirical methods. Metal precursor hydration amounts were accounted for in calculation of required water. The metal precursor solution was dropped in 50 μL increments onto the Mo_2C powder and stirred/agitated extensively between additions. Following impregnation, the resulting powder was heated to 100°C on a hot plate in the nitrogen glove box in order to evaporate the water and dry the powder. The dried material was then transferred back into an argon glove box, and loaded into a quartz flow-through reactor, supported by a bed of quartz wool. The reactor ends were sealed, and secured back into the vertical furnace under excess hydrogen flow to prevent exposure to air. The catalyst was then reduced via the same method as for wet impregnation.

Two catalysts were prepared for each metal promoter on passivated and on unpassivated Mo_2C supports. The synthesis for both was identical to the methods described above with the only differences being the exposure to 1% O_2/He at 20 mL/min for 6 hours (passivation) prior to metal impregnation and adjustment of the volume of water used in dry impregnation to account for the difference in pore volume after passivation. Otherwise, all transfers, wet impregnation, dry impregnation and reduction steps were identical. The resulting catalysts will be referred to as Metal/Mo_2C and Metal/p-Mo_2C for the metal deposited on the unpassivated and passivated Mo_2C, respectively.

Silica-supported metal catalysts were synthesized by incipient wetness impregnation of a silica support. Cab-o-Sil L-90 commercial silica was obtained from Cabot Corporation®. The silica support was first calcined at 500°C for 10 hr in air at 200 mL/min. The material was heated at a constant rate of 5°C/min. The calcined material

was then dried in a vacuum oven to remove any lingering water. Incipient wetness impregnation was used to deposit the metal at the target loading, consistent with Mo_2C-based catalyst metal loadings, as described above. Identical to the Mo_2C-based catalysts, the subsequent material was dried at 110°C, then reduced in H_2 as described previously.

4.2.2. Catalyst Characterization

4.2.2.1. X-ray Powder Diffraction

The crystal structure of the synthesized catalysts was determined via X-ray powder diffraction using a Rigaku Miniflex X-ray diffractometer employing a Cu Kα X-ray source and a Ni filter. Experimental and analysis procedures were described previously in Chapter 2 (Section 2.2.2.1).

4.2.2.2. N_2 Physisorption Measurements

Material surface areas were calculated using the Brunauer-Emmett-Teller (BET) method applied to a N_2 physisorption isotherm. A brief description of the experiment and analysis can be found in Chapter 2 (Section 2.2.2.2).

4.2.2.3. Elemental Analysis

Catalyst compositions were determined via elemental analysis performed using Inductively Coupled Plasma-Optical Emission Spectroscopy (ICP-OES) using a Varian 710-ES spectrometer. Roughly 15-20 mg of the catalyst was dissolved in 3 mL of aqua regia (3 parts hydrochloric acid, 1 part nitric acid) and analyzed by comparing the wavelength intensities for various elements to the intensities of known standards.

4.2.2.4. H_2 Temperature-Programmed Reduction

Hydrogen temperature-programmed reductions (H_2-TPRs) were conducted on a Micromeritics Autochem 2920, equipped with a thermal conductivity detector (TCD) and

a Pfeiffer Vacuum Quadstar GSD-301 Mass Spectrometer (MS). Detailed experimental conditions and analyses are described in Chapter 2 (Section 2.2.2.3).

4.2.2.5. CO Uptake

CO uptake chemisorption was performed on a Micromeritics Autochem 2920, as described previously in Chapter 3 (Section 3.2.2.5). CO uptake chemisorption was used to probe the number of metallic sites over catalysts. Catalysts were pretreated at different conditions (various temperatures and either 15% CH_4/H_2 or H_2 gas) prior to CO pulsing. During pulsing, the effluent gas was analyzed using both TCD and MS detectors. CO was pulsed until the surface became saturated as indicated by the constant peak area in the TCD towards the latter part of the experiment.

4.2.2.6. Fischer-Tropsch Synthesis

The performance of these catalysts for Fischer-Tropsch synthesis was evaluated using a high-pressure, fixed bed, U-shaped, stainless steel reactor. The catalyst bed height was held constant at 15 mm for a bed volume of 0.25 cm^3. Total flow rates were maintained between 20 mL/min and 180 mL/min, or gas hourly space velocities (GHSV) between 4,800 and 43,200 hr^{-1}. Typical reaction conditions consist of between 50-200 mg of catalyst, 25 bar pressure, CO:H_2 ratios of 1:2, a temperature regime between 200-250°C, and conversions <10% in order for differential reaction conditions to hold. To limit the conversion, the weight of catalyst loaded or the flow rates were adjusted; less catalyst or higher flow rates lessen the conversion as the time of interaction between the reactants and the active catalyst decreases with each change. The catalyst samples were diluted with low surface area SiO_2 (Alfa Aesar, 125-250 μm, <1 m^2/g) in order to maintain a constant bed height as well as prevent channeling. The reactant stream

consisted of CO (99.99%), H_2 (UHP Grade), and N_2 (UHP Grade, used as an internal standard to adjust for changes in molar flow). The gas flow rates were controlled and monitored by Teledyne Hastings mass flow controllers (200 Series MFCs, rated to 500 psig). The system pressure was increased using a backpressure regulator downstream of the reactor. The feed was preheated to 150°C prior to introduction into the reactor. All lines downstream of the reactor were heated to 150°C as well in order to ensure that products remained in the gas phase. This temperature is sufficient for keeping C_9 compounds in the gas phase. In the event that compounds greater than 10 carbon atoms were formed, a trap was provided, although no liquid buildup has ever been observed in this trap. The effluent stream was introduced into a Varian CP-3800 gas chromatograph equipped with air actuated Valco valves for sample introduction and thermal conductivity detectors (TCD) for monitoring N_2, CO, CO_2, and H_2, and a flame ionization detector (FID) for monitoring all of the hydrocarbons and alcohols. The front TCD, used for monitoring N_2, CO, and CO_2 used He carrier gas, while the middle TCD (H_2 monitoring) and FID used Ar carrier gas. Response factors were obtained for all reactants/products and were continually checked for accuracy every 6 months. A typical GC run is shown in Figure 4.2; a run typically lasted 40 minutes with a 5 minute cooldown and stabilization period prior to the next injection.
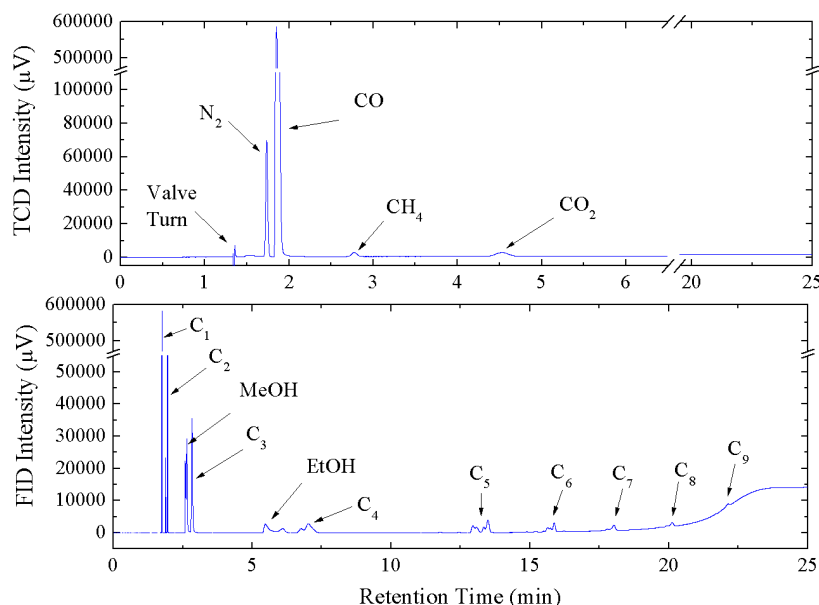
Figure 4.2. Example chromatograms for a typical Fischer-Tropsch synthesis reaction run. GC traces for the TCD (top) and FID (bottom) detectors are shown along with the species identification of the peaks.

In a typical FTS run, a tightly packed quartz wool plug was placed at the bottom of the U-tube reactor. The desired catalyst loading was then supported on top of the quartz wool bed and low surface area SiO_2 was added to reach a bed height of 15 mm. The catalyst/SiO_2 mixture was mixed to ensure a homogeneous catalyst bed to minimize temperature gradients. The U-tube reactor was installed into the reactor system; a pressure check at 25 bar was conducted to ensure that no leaks were present. The catalyst was then pretreated in either 15% CH_4/H_2 at 590°C for 4 h or pure H_2 at 450°C for 4 h, depending on the desired experimental design. Following pretreatment, the reactor was cooled to 150°C, where the catalyst was then exposed to N_2 for 15 minutes to purge the surface. The pressure was then increased to 25 bar. The nitrogen flow rate was then reduced and hydrogen was introduced to the system. The temperature was immediately increased at 1°C/min to 240°C. Once at 240°C, CO was introduced to the reactor. Given the highly exothermic nature of FTS, the reactor was monitored for a half hour in order to

maintain the reaction temperature and prevent a runaway reaction. The first GC sample was taken 10 minutes after the introduction of CO. The catalysts were allowed to deactivate for 12 h before the temperatures were randomly varied between 200 and 250°C to obtain the steady-state rates. Each temperature was held for 4 h in order to obtain 5-6 data points for each. The temperature was returned to 240°C in order to check for further deactivation with time on stream.

The reaction rates and selectivity were calculated for each GC injection. As the GC monitored the evolution of both CO and products, it was possible to check for mass balance closure and to compare the calculated rates based on CO consumption or product formation. Mass balance closure was typically observed to be within 5%. CO consumption rates were calculated using Equation 4.1, the reduced equation for a packed bed applicable only under differential conditions, where F_{CO} is the flow rate of CO into the reactor, χ_{CO} is the conversion of CO, and W_{cat} is the catalyst weight. However, most of the rates reported were computed by quantifying the products formed on a C1 basis (e.g., production of 1μmol of hexane, a C6 compound, is equivalent to the formation of 6μmol of methane, a C1 compound), since the resolution of FID detectors are far superior to TCD detectors. This approach allows for a comparison of the relative efficiency of the reaction per CO molecule reacted. The product formation rates were calculated using Equation 4.2, where F_{CO} is the flow rate of CO into the reactor, ε is a factor accounting for changes in molar flow rate since multi-carbon compounds are made from CO during the reaction calculated by monitoring the concentration of N_2 in the influent and effluent streams, W_{cat} is the catalyst weight, C_i is the concentration of component i obtained from the GC analysis, and Z_i is the number of carbon atoms in component i.

$$r_{CO\ Consumption} = \frac{dX_{CO}}{dW}F_{CO} \approx \frac{F_{CO}*X_{CO}}{W_{cat}} \tag{4.1}$$

$$r_{Product\ Formation,C1} = \left(\frac{F_{CO}*(1-\varepsilon)}{W_{cat}}\right)\sum_i C_i Z_i \tag{4.2}$$

Selectivities, either total or hydrocarbon only, were calculated on a C1 basis using Equation 4.3:

$$S_i = \frac{C_i Z_i}{\sum_i C_i Z_i} \tag{4.3}$$

where S_i is the selectivity for product i, C_i is the concentration of component i obtained from the GC analysis, and Z_i is the number of carbon atoms in component i. Conversions were adjusted to between 3 and 4% at 240°C to allow for an objective selectivity comparison as reaction conversion can influence the FTS selectivity [26].

A common metric used for characterizing the performance of Fischer-Tropsch synthesis catalysts is the Andersen-Schultz-Flory model [27], which describes the distribution of hydrocarbons based on a single parameter, α, termed the C-C chain growth probability. The Andersen-Schultz-Flory model is listed in Equation 4.4; here W_n is the weight fraction of the products containing n carbons and α is the C-C chain growth probability. By taking the natural log of Equation 4.4, it is possible to linearize the equation found in Equation 4.5; thus, the α value can be directly calculated from the slope of the line from a data set plotted as $\ln(W_n/n)$ vs. n. W_n/n can be thought of as a relative mole fraction of each hydrocarbon with respect to the other hydrocarbons.

$$W_n = (1 - \alpha)^2 n \alpha^{n-1} \tag{4.4}$$

$$\ln\left(\frac{W_n}{n}\right) = \ln\left[(1-\alpha)^2\right] + (n-1)\ln(\alpha) \tag{4.5}$$

4.3. Results

4.3.1. Low Loading (1wt%) Metal/Mo$_2$C Fischer-Tropsch Catalysts (Co, Ni)

Initial work focused on analyzing the effect of metal promoters on Mo$_2$C-based Fischer-Tropsch catalysts, as well as determining the effect, if any, of the presence of the passivation layer during synthesis on the resulting catalysts. Ni- and Co-based catalysts supported on Mo$_2$C were studied given previous results by Schaidle showing these metals to have the largest effect on FTS performance when supported on Mo$_2$C [6]. In prior work, Co and Ni additions slightly reduced and slightly increased the FTS activity, respectively, and Co/Mo$_2$C produced slightly higher C$_{2+}$ selectivity while Ni/Mo$_2$C produced more CH$_4$ relative to bare Mo$_2$C.

Work here aimed to expand upon the work done in Chapter 3 investigating the effect of the passivation layer on these supported metal catalysts. Results from the adsorption (at 10% surface coverage assuming 10 sites/nm^2 and 105 m^2/g) of Ni and Co from nitrates onto the unpassivated (referred to hereafter as Mo$_2$C) and passivated (referred to hereafter as p-Mo$_2$C) molybdenum carbide catalyst surfaces were previously shown in Chapter 3. Ni and Co adsorb to near completion on unpassivated Mo$_2$C after ~5 hours while Ni and Co appear to reach a point of saturation at ~40% adsorption after only 0.5-1 hour. These results indicate that the passivation layer affects the adsorption as was previously discussed in detail in Chapter 3.

The resulting metal weight loadings (Table 4.1) are lower than the targeted loadings for the passivated Mo$_2$C supports due to the incomplete adsorption. X-ray diffraction patterns for the catalysts (Figure 4.3) resemble the characteristic Mo$_2$C pattern with a mixture of α and β phases. It is difficult to comment on the dispersion of the metal

on these supports based on XRD results. While the diffraction patterns contain small peaks at 2θ values of ~44°, it is difficult to determine the origin of this diffraction feature since the Co (111), Ni (111) and MoC_{1-x} (200) diffraction planes fall very close to one another (43.7, 44.2, and 44.5°, respectively).

Table 4.1. Target and actual metal loadings, BET surface areas, and CO uptake capacities for Mo_2C-supported Co and Ni catalysts at low monolayer coverages (10%).

Catalyst	Target Metal Loading (wt %)	Actual Metal Loading (wt %)[1]	BET Surface Area (m^2/g)	CO Uptake Capacity ($\mu mol/g_{cat}$)[2]
Mo_2C	--	--	109	446
Co/Mo_2C	1.0	1.0 ± 0.2	105	414
Co/p-Mo_2C		0.4 ± 0.2	98	383
Ni/Mo_2C	1.0	0.9 ± 0.1	103	439
Ni/p-Mo_2C		0.5 ± 0.2	101	433

[1] Actual metal loadings determined via ICP-OES
[2] BET surface areas were calculated from a N_2 physisorption isotherm
[3] CO uptake capacity calculated via pulse chemisorption of a 5% CO/He mixture over the catalyst at 35°C following pretreatment in 15% CH_4/H_2 at 590°C for 4 h.
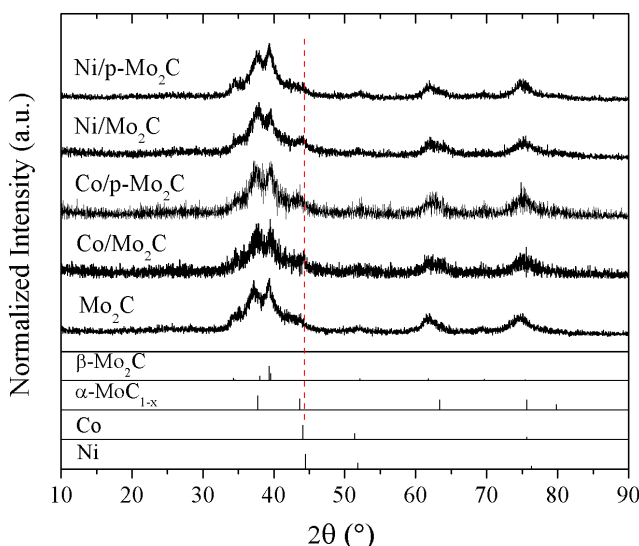
Figure 4.3. X-ray diffraction patterns for the Ni and Co-based Mo_2C catalysts at 10% surface coverage.

These catalysts were further characterized using N_2 physisorption and chemisorption techniques (Table 4.1). BET surface areas and CO uptakes were relatively unaffected by both the metal addition and the presence of the passivation layer, indicating that (1) metals do not occupy CO adsorption sites on Mo_2C, (2) the metal nanoparticles

formed have similar CO adsorption capacities as Mo_2C on an areal basis, and/or (3) the presence of the passivation layer during wet impregnation does not drastically effect the catalyst surface chemistry following drying, reduction, and subsequent passivation.

An example Fischer-Tropsch synthesis run for Mo_2C can be found in Figure 4.4, detailing the rate data collected as a function of time on stream and varying temperature. An Arrhenius plot (shown as ln(rate) vs 1000/T) can be constructed from these results and this process repeated for all catalysts studied (Figure 4.5a). The product formation rates on a C1 basis appear very similar for all of the catalysts with perhaps a slight enhancement in rate for Ni/Mo_2C and $Ni/p-Mo_2C$ and a slight decrease in activity for the $Co/p-Mo_2C$ catalysts. Both Ni and Co are known active metals for Fischer-Tropsch; the negligible enhancement in rate is quite striking. However, the CO uptakes and metal weight loadings were different for these catalysts. To generate a more relevant comparison, rates are often normalized to the number of active sites on the catalyst surface to form a quantity often referred to as the intrinsic turnover frequency (TOF) of the catalyst. By assuming that the FTS reaction occurs at CO adsorption sites on Mo_2C, a TOF can be generated (shown in Figure 4.5b). It should be stressed that the CO uptake-normalized gravimetric rates may not truly represent TOFs as CO chemisorption sites are
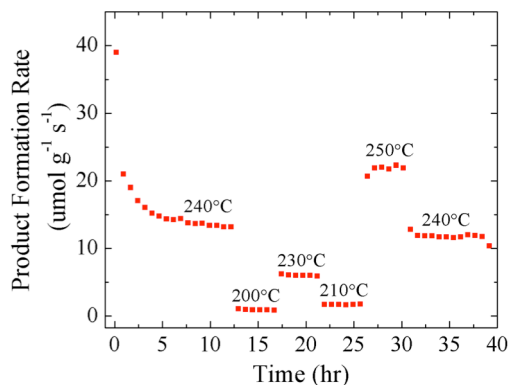
Figure 4.4. Product Formation Rate from CO as a function of time. Fischer-Tropsch run for Mo_2C. Operating Conditions: 200-250°C, 25 bar, $H_2:CO = 2$, GHSV = 43,200 hr^{-1}.

not definitively characterized as the active site for FTS over Mo_2C; this is compounded by the fact that CO is capable of adsorbing to both Mo_2C and the deposited metals. A more apparent trend is observed for the turnover frequencies: $Ni/Mo_2C \sim Ni/p-Mo_2C >$ $Mo_2C \sim Co/Mo_2C \sim Co/p-Mo_2C$. It is surprising that Co showed no effect in the activity of the Co/Mo_2C catalyst. That being said, metal promotion may not enhance the activity on Mo_2C drastically, but may have an influence on the selectivity of the catalysts to generate the desired long-chain hydrocarbons, which is of interest for FTS.
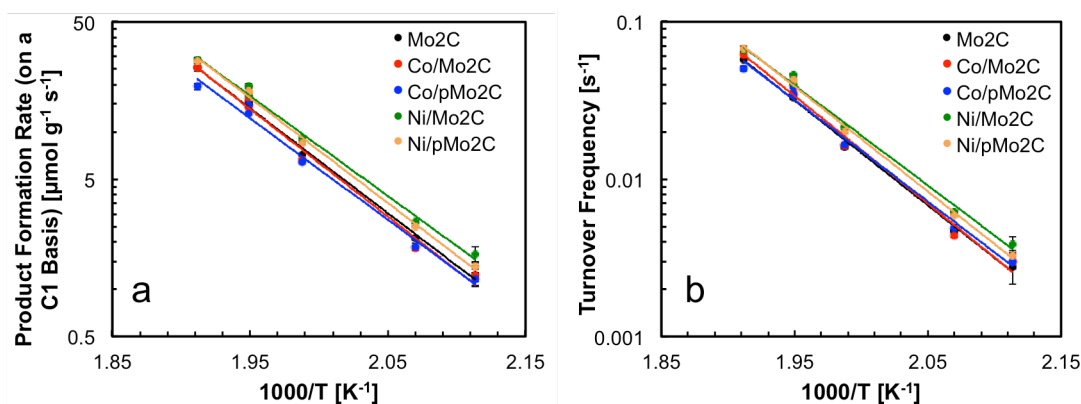
Figure 4.5. Arrhenius plots showing the (a) product formation rate on a single carbon basis and (b) turnover frequency as a function of inverse temperature for the Mo_2C-based catalysts being studied. Reaction conditions: 25 bar, $CO:H_2 = 1$, GHSV = 43,200 hr^{-1}, 200-250°C. Pretreatment in 15% CH_4/H_2 at 590°C for 4 hr.

Activation energies for the studied catalysts were calculated to be 128 ± 4, 131 ± 8, 124 ± 7, 122 ± 5, and 128 ± 4 kJ/mol for Mo_2C, Co/Mo_2C, $Co/p-Mo_2C$, Ni/Mo_2C, and $Ni/p-Mo_2C$, respectively. These values are not statistically different, so the metal addition failed to alter the energy requirements for the rate-limiting step in the Fischer-Tropsch reaction. These activation energies are consistent with those found in literature. Griboval-Constant et al. reported activation energies between 120 and 170 kJ/mol, depending on reaction conditions [7]. Schaidle et al. reported activation energies 107 and 98 kJ/mol for Mo_2C at temperature ranges of 200-250 and 270-320°C, respectively [28]. Vo et al.

reported activation energies between 51 and 158 kJ/mol for alumina-supported Mo_2C catalysts [29].

The overall total CO conversion selectivity of the Mo_2C-based catalysts is shown in Figure 4.6 (left). The total selectivities are consistent for all catalysts, generating hydrocarbons from roughly 60% of the CO converted, alcohols from ~5-8%, and CO_2 from ~35% of the CO converted. Carbon dioxide is a by-product from the side reaction between CO and the H_2O formed via hydrocarbon formation. Further comparisons can be drawn between catalysts by comparing the hydrocarbons formed during FTS (Figure 4.6, right). While the hydrocarbon selectivities for the Co-based catalysts are no different than that of bare Mo_2C, Ni/Mo_2C and Ni/p-Mo_2C show an increase in CH_4 selectivity accompanied with slight decreases in the C_2-C_4 and C_{5+} selectivities. This is not surprising as nickel is a well-known catalyst for CO methanation [30,31]. The overall chain probability factor (α) for these catalysts was calculated to be 0.42 for Mo_2C, Co/Mo_2C and Co/p-Mo_2C, and 0.40 for Ni/Mo_2C and Ni/p-Mo_2C. Commercial catalysts tested at 230°C were observed to have α of 0.65 and 0.66 for Fe/SiO_2 and Co/Al_2O_3, respectively [6].
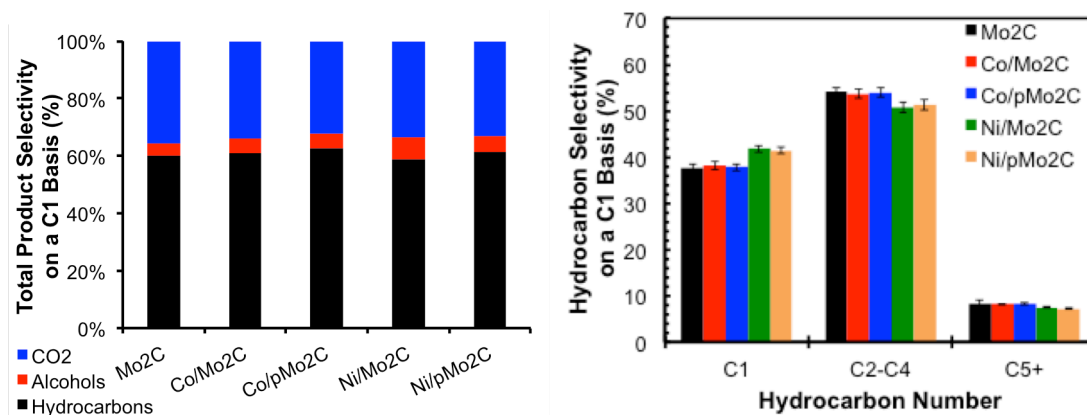
Figure 4.6. (left) Overall total product and (right) hydrocarbon selectivity for the Fischer-Tropsch synthesis reaction over the Mo_2C-based catalysts. Selectivity reported at 240°C.

The unusual absence of significant differences in rate and selectivity for Co and Ni, two well-known Fischer-Tropsch catalysts, when supported on Mo_2C is a phenomenon that warrants further investigation. As a result of these small differences in performance, it is difficult to draw conclusions on the effect of the metal promoter, as well as the presence of the passivation layer during synthesis. Potential reasons for the relative inactivity of Co and, to a lesser extent, Ni, include: (1) insufficient metal loading to provide a noticeable enhancement, (2) deactivation of metal by the pretreatment in 15% CH_4/H_2, (3) strong metal-support interactions (SMSI) [32] exist between the metal and Mo_2C, changing the character of the metal through electronic or geometric perturbations, and (4) metal particles are too small to be active for FTS. Considering the first case, as Mo_2C is highly active for FTS, the performance of the deposited metal could be diluted by the intrinsic Mo_2C activity such that no promotional enhancement is observed for the metal. For the second case, it is possible that the pretreatment conditions are not conducive towards generating an active FTS Co phase. High temperatures in 15% CH_4/H_2 may generate a cobalt carbide phase (i.e., Co_2C) that is inactive for CO hydrogenation. The literature supports the third case, since SMSI has commonly been cited as the cause for differences in the performance of Co, Ni, Ru, or Fe when deposited on various supports [33,34,35,36,37,38]. Lastly, particle size has been reported to have a significant effect on the turnover frequencies of Ru [39,40,41] and Co-based [42,43,44] catalysts, and to a lesser extent Fe [45]. In general, the turnover frequencies over Ru, Co, and Fe increase by a factor between 3 and 10 as the particle size increases from 1 to ~15nm with a more drastic effect observed for Ru and Co, than for Fe.

4.3.2. Moderate Loading (~5wt%) Metal/Mo₂C Fischer-Tropsch Catalysts

The first two cases listed above are the most straightforward to test. By increasing the weight loading of the deposited metal, the surface will have a higher density of the promoter, perhaps yielding a more apparent enhancement. The nominal weight loading was increased to 50% of a monolayer from 10. To test the feasibility of using this weight loading with current synthesis techniques, an adsorption study for $Co(NO_3)_2$ deposition onto passivated and unpassivated Mo_2C via wet impregnation at this higher weight loading was performed. However, adsorption profiles of the metal deposition process show that $Co(NO_3)_2$ fails to adsorb entirely onto even unpassivated Mo_2C (Figure 4.7). Instead, maximum Co loadings were observed at ~ 14% and ~6% of a monolayer for unpassivated and passivated, respectively, as opposed to the targeted 50%. The incomplete adsorption onto p-Mo_2C is similar to that observed for lower loadings (1wt%) above. To increase the weight loading of the deposited metal, dry impregnation was employed.
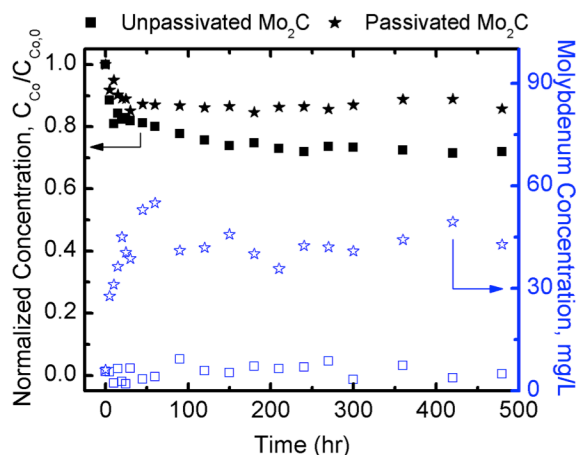
Figure 4.7. Adsorption profiles for 50% of a monolayer of $Co(NO_3)_2$ onto unpassivated (n) and passivated (★) Mo_2C. Normalized Co concentration is shown on the left axis while Mo concentration (mg/L) is shown on the right (unfilled blue symbols).

Unpassivated and passivated Mo_2C were dry impregnated with the metal precursors at weight loadings equivalent to 50% surface coverage, assuming 10 sites/nm^2 and the surface area for passivated Mo_2C (105 m^2/g) in order to maintain a constant weight loading for the two scenarios. SiO_2-supported metal catalysts were also synthesized for comparison. Since it represents a common, well-understood, inactive support for FTS catalysts, SiO_2 (Cab-o-Sil L-90, 101 m^2/g) was chosen to provide a true comparison to Mo_2C with respect to surface and weight loading.

Prior to these studies, a control experiment was performed using unpromoted Mo_2C to measure the effect that water treatment and drying (as a result of dry impregnation) has on the Mo_2C surface and, ultimately, on FTS performance. Passivated and unpassivated Mo_2C were first dry impregnated with an aqueous solution without any metal salt. Subsequently, the materials were reduced in H_2 at 450°C followed by passivation for more than 6 hours, prior to FTS pretreatment and analysis. XRD patterns of these water-treated Mo_2C catalysts were consistent with α-MoC_{1-x} and β-Mo_2C phases. The absence of molybdenum oxide diffraction peaks indicated that no bulk oxidation occurred as a result of this water-treatment step. Surface areas were not impacted significantly by the water-treatment; however, CO uptake capacities decreased by approximately 10% with the water-treatment step (Table 4.2), which may lead to reduced FTS rates due to less available CO adsorption sites.

Table 4.2. BET surface areas and CO uptake capacities for the untreated and water-treated Mo_2C catalysts.

Catalyst	BET Surface Area (m^2/g)	CO Uptake Capacity (μmol/g$_{cat}$)[a]	CO Site Density (x10^{18} sites/m^2)
Mo_2C	103 ± 7	404	2.36
H_2O-treated Mo_2C	100	344	2.14
H_2O-treated p-Mo_2C	93	356	2.23

[a] CO uptake capacity calculated via pulse chemisorption of a 5% CO/He mixture over the catalyst at 35°C following pretreatment in 15% CH_4/H_2 at 590°C for 4 h.

Gravimetric rates on a C1 basis and CO uptake-normalized rates (TOFs) for Fischer-Tropsch synthesis are shown in Figure 4.8. A small reduction in gravimetric rate was observed for the H_2O-treated catalysts when compared to the untreated Mo_2C sample. However, when the rates are normalized to CO uptake capacity, the turnover frequencies for all of the catalysts appear within error, meaning the gravimetric activity loss is likely due to the decrease in CO adsorption sites resulting from these treatments. Activation energies for the catalysts remained relatively unchanged at 130±5, 122±5, 131±5, 127±4 kJ/mol for the untreated Mo_2C, hydrogen-pretreated Mo_2C, water-treated Mo_2C, and water-treated p-Mo_2C, respectively.

Total selectivities were similar, although it appears that water treatment results in a slight decrease in CO_2 selectivity (Figure 4.9, left). This may be due to the water treatment deactivating the catalyst's inherent WGS activity. It is possible that the reduction in WGS activity may entirely account for the decreased gravimetric CO
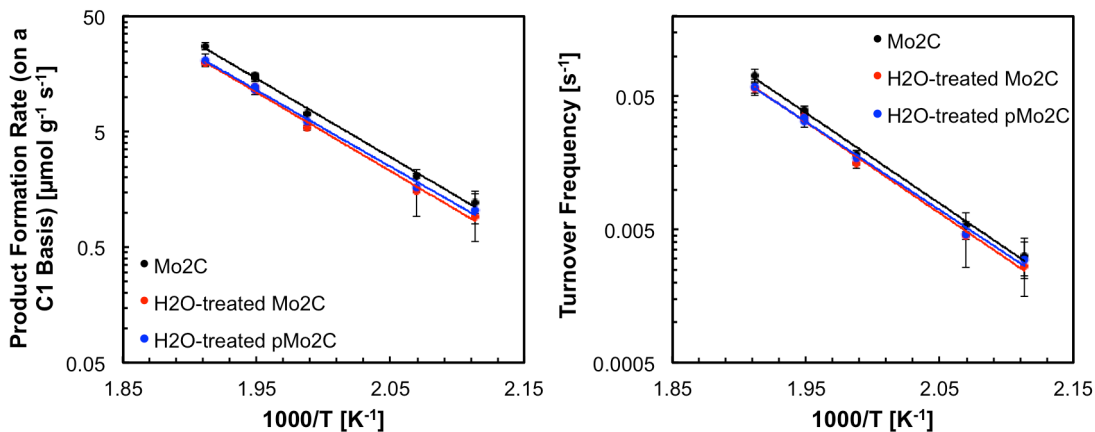
Figure 4.8. Gravimetric rates on a C1 basis and turnover frequencies (TOFs) for the Mo_2C and water-treated Mo_2C catalysts. TOFs were calculated by normalizing the gravimetric rates by CO uptake capacity. Catalysts were pretreated in 15% CH_4/H_2 at 590°C.
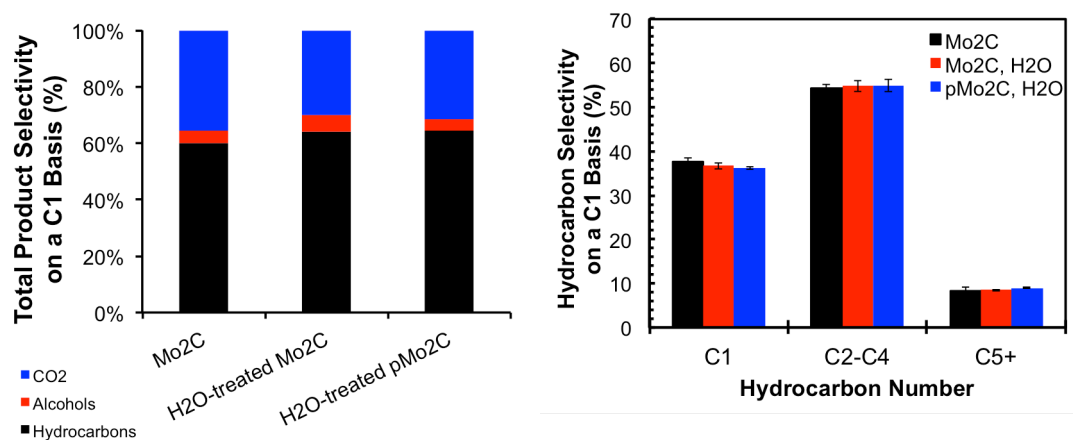
Figure 4.9. Total product selectivity (left) and hydrocarbon selectivity (right) for the Mo_2C and water-treated Mo_2C catalysts. Selectivity values were taken at 240°C.

consumption activity observed for these catalysts. However, as shown in Table 4.3, a reduction in gravimetric rate is still observed for the water-treated catalysts when comparing the CO_2-free rates, indicating that the reduction in rate is a combination of decreased FTS and WGS activity. Hydrocarbon selectivities (Figure 4.9, right) remained unchanged following treatment of Mo_2C. As a result of these analyses, it is apparent that any changes in the turnover frequency or the hydrocarbon selectivity of the Mo_2C-based catalysts are as a result of the deposited metal and not the treatment associated with syntheses by dry impregnation.

Table 4.3. Gravimetric rates for Mo_2C and H_2O-treated Mo_2C catalysts taken at 240°C.

Catalyst	Gravimetric Rate (µmol/g/s)	CO_2-free Rate (µmol/g/s)	WGS Rate (µmol/g/s)
Mo_2C	15.36	9.94	5.42
H_2O-treated Mo_2C	12.15	7.71	4.44
H_2O-treated pMo_2C	12.24	8.03	4.21

X-ray diffraction patterns for passivated and unpassivated Mo_2C- and SiO_2-supported metal catalysts are found in Figure 4.10-Figure 4.15 along with the baseline Mo_2C pattern and the relevant single crystal standards. The diffraction pattern for the

base Mo_2C shows the characteristic diffraction peaks for α-MoC_{1-x} and β-Mo_2C in nearly equal amounts based on weighted pattern fitting analysis. No noticeable changes are found in the diffraction patterns following treatment of unpassivated and passivated Mo_2C with deionized water when the material was then dried at 110°C in the oxygen-free N_2 glove box and reduced in the quartz tube reactor under hydrogen flow at 110°C for 2 hours followed by 450°C for 4 hours. The addition of water and subsequent reduction do not appear to affect the crystal structure nor cause bulk oxidation. Thus, any bulk structure changes observed in the diffraction patterns for supported metal catalysts are a direct consequence of interaction with the metal. In general, diffraction peaks were not observed for the deposited metal other than Cu (111) (42.8°), though small features are observed at 2θ values consistent with Ru (101) (44.4°), Ni (111) (44.7°), and Fe (110) (44.8°). However, these peaks line up fairly closely to the peak associated with the (200) plane of α-MoC_{1-x} (42.7°) making it difficult to definitively distinguish given the width of this weak feature. No features were observed at 2θ values consistent with the other crystal planes for these metals. These results indicate that the metals were either amorphous or were well dispersed with small crystallite sizes. It is not surprising that peaks were observed consistent with Cu as Cu is known to sinter at relatively low temperatures (>300°C) [46]. It should be noted that peaks associated with a ternary carbide, formed by dissolution of the deposited metal into the Mo_2C (e.g., Fe_3Mo_3C), were not observed in any of the diffraction patterns. However, the deposited metal is in relatively low concentrations relative to the bulk Mo carbide. As such, it is still possible that formation of a ternary carbide may be restricted to the surface, though there is currently no experimental evidence to support this claim.
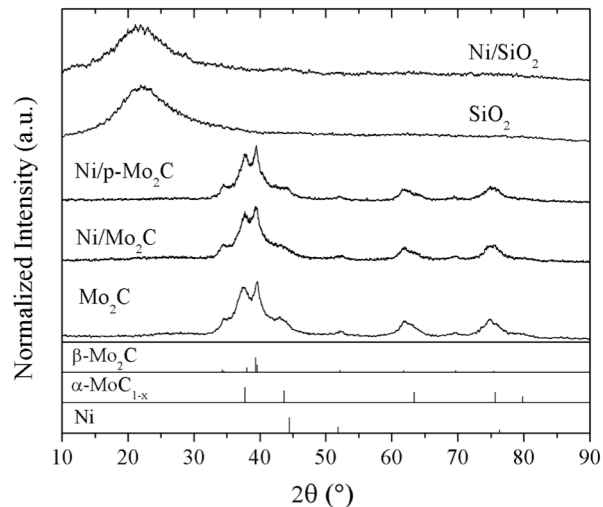
Figure 4.10. X-ray diffraction patterns for the as-synthesized Ni-based catalysts.
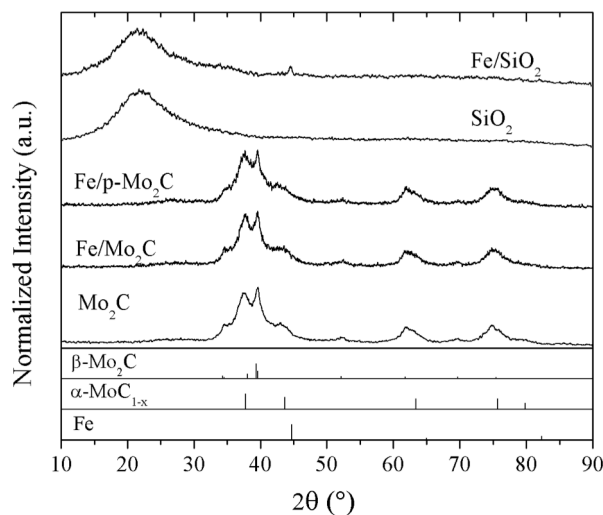
Figure 4.11. X-ray diffraction patterns for the as-synthesized Fe-based catalysts.
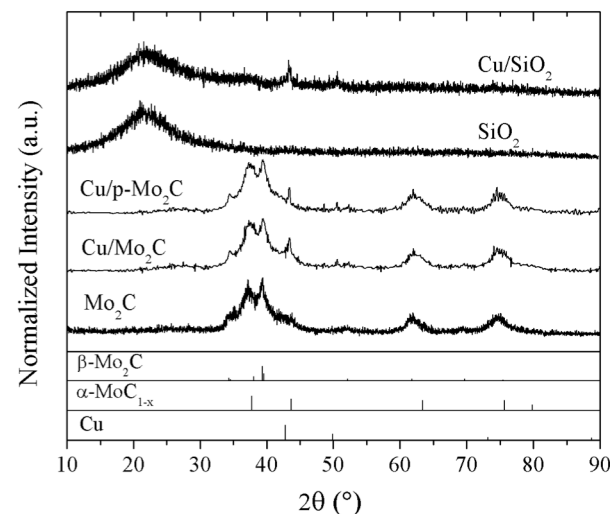
Figure 4.12. X-ray diffraction patterns for the as-synthesized Cu-based catalysts.
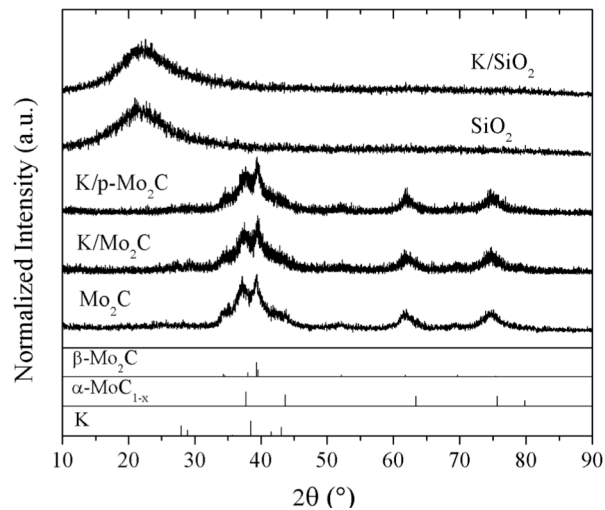
Figure 4.13. X-ray diffraction patterns for the as-synthesized K-based catalysts
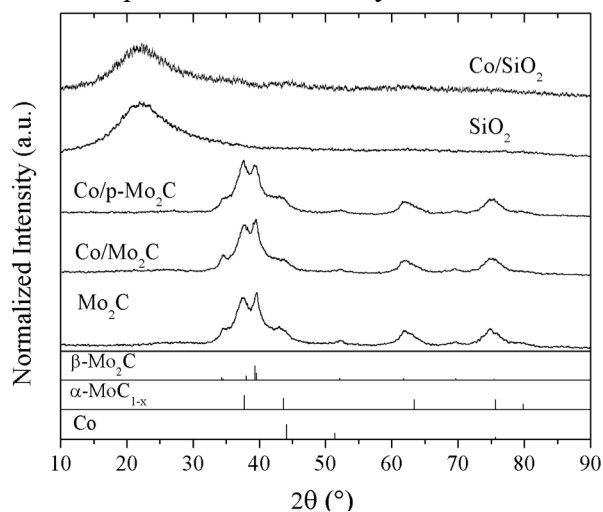
Figure 4.14. X-ray diffraction patterns for the as-synthesized Co-based catalysts
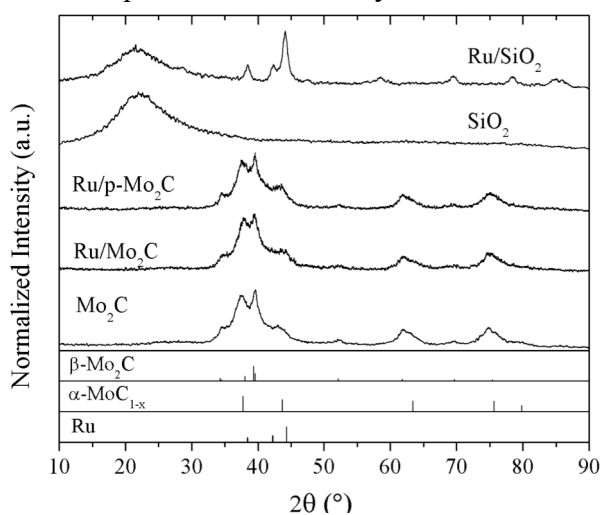
Figure 4.15. X-ray diffraction patterns for the as-synthesized Ru-based catalysts

Alternatively, many of the SiO$_2$-supported metal catalysts XRD patterns displayed features corresponding to metal crystal facets. The bare SiO$_2$ was entirely amorphous as illustrated by the broad feature at ~22°. Features were observed for the Fe, Cu, Ru, and Co-based SiO$_2$ catalysts. Using the Scherrer equation, the crystallite sizes for these catalysts were found to be 19, 34, 107, and 3 nm for Fe, Cu, Ru, and Co, respectively. Of particular note, Ru exhibited significant diffraction peaks, in stark contrast to the minute peak observed for the Ru/Mo$_2$C catalysts. It is likely that the Ru dispersion is very different for these two catalysts; in particular, Mo$_2$C seems to disperse the Ru phase better than SiO$_2$. Diffraction patterns for the Ni and K-based SiO$_2$ catalysts did not show features for metal nanoparticles, indicating a highly dispersed crystalline phase or an amorphous phase.

This section will focus on Mo$_2$C-based catalysts. Analogous SiO$_2$-supported metal catalysts will be discussed in the latter part of this chapter. Elemental analysis (ICP-OES) was performed on the Mo$_2$C-based catalysts to determine the actual weight percent for the deposited metal. The target and actual weight loadings for the Mo$_2$C-based catalysts are shown in Table 4.4. Actual weight loadings were reasonably close to the target values (within 1wt%, ±10% surface coverage).

The BET surface areas generally decreased by approximately 10-30% after depositing metals onto the Mo$_2$C surface, perhaps due to pore blocking by the metal nanoparticles. Cu had the highest surface area of the supported metal catalysts, while K had the lowest surface area. The CO uptake capacities for these catalysts followed a similar trend to surface area. With the exception of Ni and K, the CO uptake capacities scaled with surface area. The CO site densities ranged from 2.08 to 2.47 molecules per

Table 4.4. Target and actual metal loadings, BET surface areas, and CO uptake capacities for all Mo_2C and Mo_2C-supported metal catalysts studied.

Catalyst	Target Metal Loading (wt %)	Actual Metal Loading (wt %)[1]	BET Surface Area (m^2/g)[2]	CO Uptake Capacity $(\mu mol/g_{cat})$[3]
Mo_2C	--	--	103 ± 7	404
Fe/Mo_2C	4.7	5.0 ± 0.2	66	254
$Fe/p\text{-}Mo_2C$	--	5.2 ± 0.1	67	243
Ni/Mo_2C	5.2	5.7 ± 0.3	72	328
$Ni/p\text{-}Mo_2C$		6.0 ± 0.3	75	335
Cu/Mo_2C	5.6	6.5 ± 0.1	87	291
$Cu/p\text{-}Mo_2C$		6.9 ± 0.2	84	284
K/Mo_2C	3.7	4.4 ± 0.2	54	<1
$K/p\text{-}Mo_2C$		3.8 ± 0.5	31	<1
Ru/Mo_2C	8.6	8.9 ± 0.1	68	279
$Ru/p\text{-}Mo_2C$		7.5 ± 0.2	75	282
Co/Mo_2C	5.2	5.6 ± 0.3	77	284
$Co/p\text{-}Mo_2C$		5.8 ± 0.4	79	271

[1] Actual metal loadings determined via ICP-OES
[2] BET surface areas were calculated from a N_2 physisorption isotherm
[3] CO uptake capacity calculated via pulse chemisorption of a 5% CO/He mixture over the catalyst at 35°C following pretreatment in 15% CH_4/H_2 at 590°C for 4 h.

nm^2 for the Fe, Cu, Ru, and Co-based catalysts, compared to 2.36 for bare Mo_2C. The Ni/Mo_2C catalyst exhibited higher site densities of 2.74 and 2.69 sites per nm^2 for the unpassivated and passivated cases, respectively, perhaps attributable to nickel's intrinsic ability to adsorb CO [47,48]. Lastly, the K/Mo_2C catalysts showed no CO chemisorption uptake capacity, which is fairly consistent with previous literature on K/Mo_2C systems. Kotarba et al. observed a decrease in CO uptake from 270 to 200 μmol/g after adding 1.0 wt% of K [49]. Park et al. did not observe any measurable CO uptake for 12wt% K_2CO_3/Mo_2C, while Mo_2C was capable of 56 μmol/g uptake [50]. The cause of these changes in surface chemistry has been the subject of recent investigations [51,52], and findings suggest that K deposition causes surface reconstruction, which weakens the adsorption of CO on the surface.

The gravimetric FTS rates of these Mo₂C-supported metal catalysts (Figure 4.16A), with the exception of the Ni- and K-based catalysts, were of equal or slightly lower activity (~20% lower) compared to bare Mo₂C. In contrast, the activity of the K/Mo₂C catalysts were significantly lower (~90% lower) than that of bare Mo₂C. While this is an unexpected result, K addition has been reported to drastically reduce the activity of Mo₂C for FTS, although the cause for this is still under active investigation [13,53,54,55,56]. Some recent literature suggests that the addition of K or Rb to Mo₂C
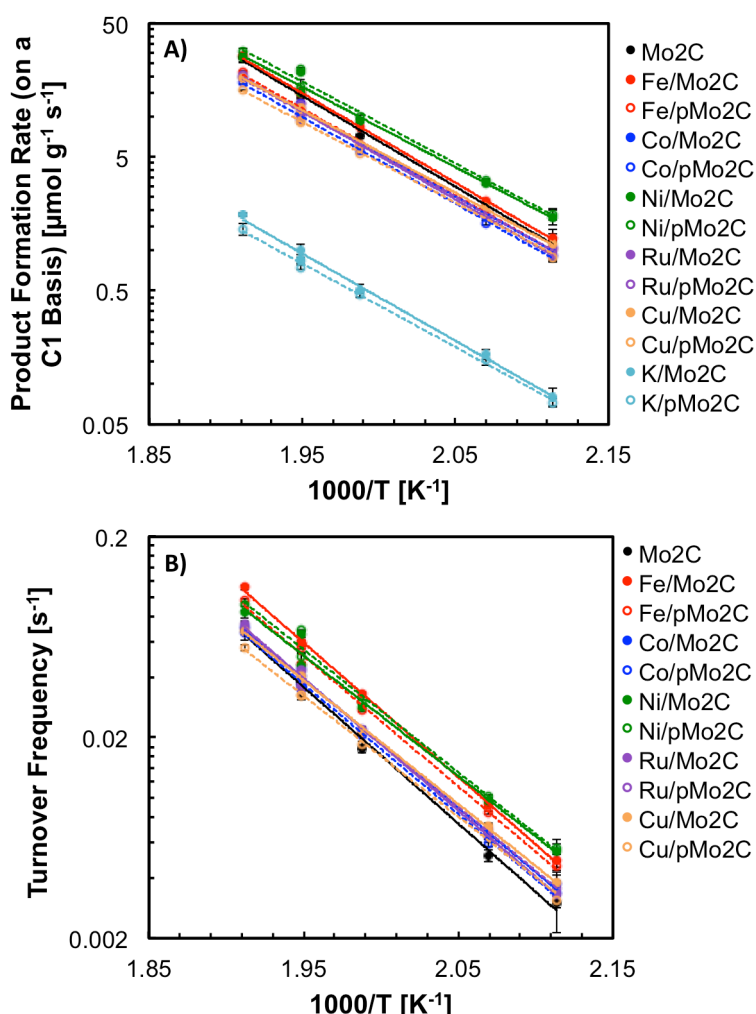
Figure 4.16. Arrhenius plots detailing the (A) gravimetric rates and (B) turnover frequencies (gravimetric rates normalized by CO uptake) for the Mo₂C-based catalysts using Fe (•), Co (•), Ni (•), Ru (•), Cu (•), and K (•) as the promoters and the unpassivated (–) or passivated (- -) Mo₂C support.

lowers the number of active sites for hydrocarbon synthesis via CO hydrogenation [13]. Further, the addition of K is hypothesized to enhance the deposition of carbon species on the catalyst surfaces, perhaps through the decomposition of two CO molecules to CO_2 and $C_{(ads)}$ [56]. The Ni/Mo$_2$C catalysts, on the other hand, showed ~40% increase in gravimetric reaction rate relative to bare Mo$_2$C.

The gravimetric rates were again normalized by CO uptake capacities to generate TOFs (Figure 4.16B). Ni and Fe showed enhancements of roughly 70 and 60% relative to bare Mo$_2$C, respectively, while the remaining metals (Co, Ru, Cu) exhibited nearly identical turnover frequencies to that of bare Mo$_2$C. TOFs could not be calculated for the K-promoted catalysts since negligible CO uptakes (<1 µmol/g) were observed.

The gravimetric rates for each family of products is provided in Table 4.5. There is a general trend of decreasing CO_2 formation with metal addition. Ni/Mo$_2$C showed a large increase in the CH_4 formation rate, owing to the intrinsic methanation capability of Ni [30,31]. Of note, the product formation rates of the Ni/Mo$_2$C catalysts for C_2-C_4 and alcohol products are also higher than those observed for bare Mo$_2$C, indicating that the

Table 4.5. Gravimetric product formation rates on a C1 basis for the Mo$_2$C-supported metal catalysts taken at 240°C, 25 bar, and a CO/H$_2$ ratio of 2. Apparent activation energies for the studied catalysts are also shown assuming an Arrhenius relationship.

Catalyst	Product Formation Rates on a C1 Basis (µmol/g/s)					$E_{a, Apparent}$ (kJ/mol)
	CO_2	CH_4	C_2-C_4	C_5+	Alcohols	
Mo$_2$C	5.51	3.38	5.16	0.76	0.70	130 ± 5
Fe/Mo$_2$C	2.86	3.58	5.97	1.23	0.97	128 ± 2
Fe/p-Mo$_2$C	2.36	2.61	4.40	0.98	1.13	124 ± 4
Co/Mo$_2$C	2.42	2.79	4.23	0.91	1.54	123 ± 4
Co/p-Mo$_2$C	2.27	3.02	3.92	0.89	1.21	124 ± 3
Cu/Mo$_2$C	1.86	3.12	4.43	0.65	0.99	118 ± 2
Cu/p-Mo$_2$C	1.73	2.75	3.62	0.47	0.71	115 ± 4
Ni/Mo$_2$C	3.79	7.15	6.64	0.97	2.83	115 ± 7
Ni/p-Mo$_2$C	4.48	7.72	7.08	1.01	2.55	117 ± 6
Ru/Mo$_2$C	1.79	2.61	4.47	0.70	0.64	126 ± 3
Ru/p-Mo$_2$C	1.95	2.53	4.31	0.63	0.55	121 ± 4
K/Mo$_2$C	0.48	0.11	0.22	0.04	0.02	125 ± 5
K/p-Mo$_2$C	0.46	0.09	0.16	0.02	0.02	120 ± 3

addition of Ni not only promoted CH_4 formation but also promoted the coupling of carbon bonds to longer chain hydrocarbon products, perhaps in a synergistic manner with Mo_2C. The activation energies of all catalysts were very similar. This indicates that the rate-limiting step for FTS likely remains unchanged with metal addition to Mo_2C.

The selectivities for the promoted Mo_2C catalysts are reported in Figure 4.17 for reactions conducted at 240°C. Metal addition appears to both reduce the material's propensity to catalyze the water-gas shift reaction and enhances the production of oxygenates such as alcohols. It is also of interest that Ni and Co promotion resulted in the most alcohols. However, K/Mo_2C was found to be an outlier in the catalyst series, as CO_2 is actually the dominant product and alcohols represent only a small fraction of the product distribution. Previous reports, however, indicate a high selectivity to alcohol products for K- or $Rb-Mo_2C$ catalysts [13,53,54,55,56]. It is possible that differences in the surface chemistry of the Mo_2C catalyst reported here versus in the literature may
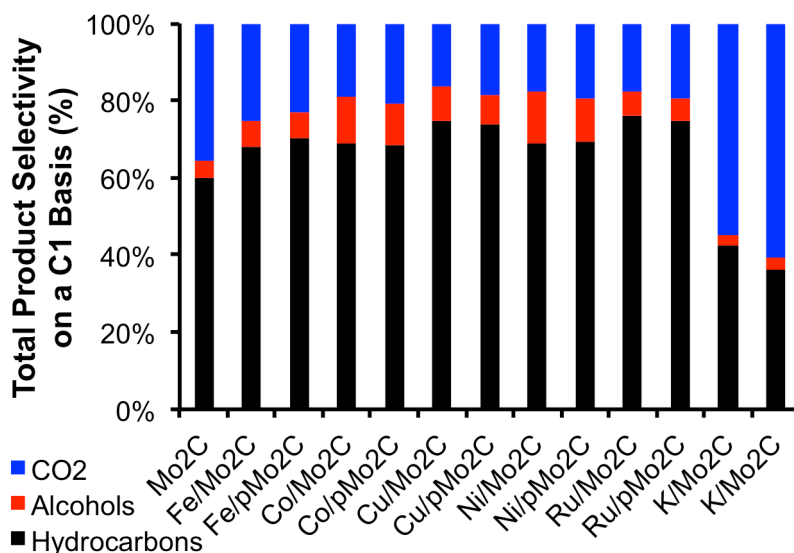
Figure 4.17. Overall total product selectivity for the Fischer-Tropsch synthesis reaction over the Mo_2C-supported metal catalysts. Selectivity values were taken at 240°C.

result in different interactions with K. Further, pretreatment conditions may have a profound effect on the catalyst performance. In many of the literature reports, these catalysts were not pretreated prior to CO hydrogenation [13,53,55]; whereas, the catalysts were pretreated under fairly harsh reducing conditions (590°C in 15% CH_4/H_2) in the work reported here.

The hydrocarbon selectivities of the catalysts (Figure 4.18) showed more drastic differences with Fe and K-promotion resulting in enhancements in the product selectivity towards higher hydrocarbons compared to bare Mo_2C. Nickel-promotion resulted in more CH_4 and less C_2+ production, and Co, Ru, and Cu failed to exhibit significant differences from the Mo_2C control case. The chain probability factors (α), calculated from the Anderson-Shultz-Flory model [27], (Table 4.6) follow the same trend, with only Fe and K showing improvements and Ni having a slight deleterious effect. Iron-based catalysts are known to catalyze the FTS reaction favoring the formation of higher hydrocarbons [57,58]. Similarly, alkali metals such as Rb and K have been reported to
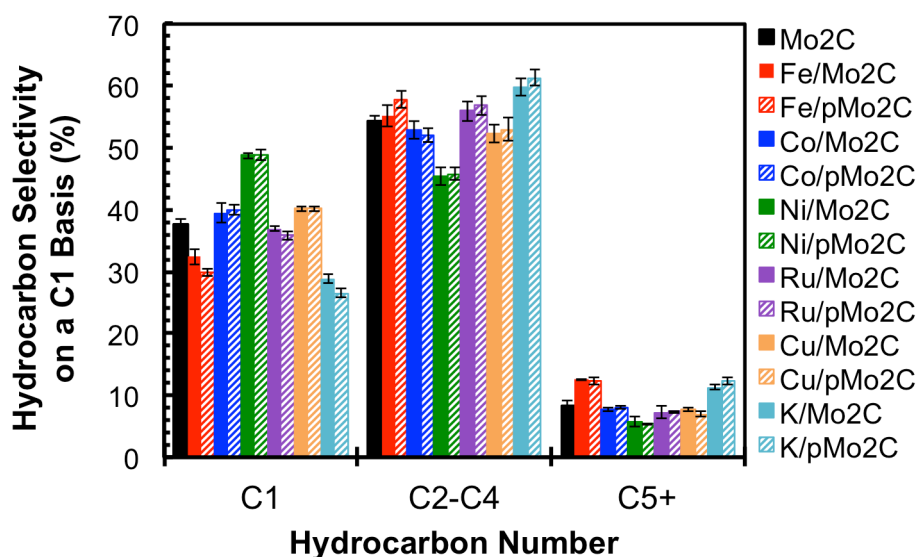
Figure 4.18. Hydrocarbon product selectivity for the Fischer-Tropsch synthesis reaction over the Mo_2C-supported metal catalysts. Selectivity values were taken at 240°C.

shift the hydrocarbon selectivity to longer chain hydrocarbons [53]. The increased

methane selectivity for Ni is not surprising since it is a known methanation catalyst as

discussed previously. Copper is not known to be active for hydrocarbon synthesis from

CO, but is commonly used in alcohol synthesis [59]. It is likely that no enhancement in

alcohol selectivity is observed for Cu as the active site for CO adsorption and FTS occurs

only on the Mo_2C. Quite surprisingly, Co and Ru, two of the most active metals for the

Fischer-Tropsch synthesis reaction [60], showed no promotional enhancement when

supported on Mo_2C.

Table 4.6. α-values for the Mo_2C-supported metal catalysts studied. Chain probabilities
calculated using data collected at 240°C.

Catalyst	α
Mo_2C	0.42 ± 0.2
Fe/Mo_2C	0.48 ± 0.1
$Fe/p\text{-}Mo_2C$	0.49 ± 0.1
Co/Mo_2C	0.41 ± 0.1
$Co/p\text{-}Mo_2C$	0.42 ± 0.1
Cu/Mo_2C	0.42 ± 0.2
$Cu/p\text{-}Mo_2C$	0.41 ± 0.1
Ni/Mo_2C	0.39 ± 0.1
$Ni/p\text{-}Mo_2C$	0.38 ± 0.1
Ru/Mo_2C	0.43 ± 0.1
$Ru/p\text{-}Mo_2C$	0.42 ± 0.1
K/Mo_2C	0.51 ± 0.1
$K/p\text{-}Mo_2C$	0.52 ± 0.1

4.3.4. Comparison of Mo_2C- and SiO_2-supported Metal Catalysts and the Effect of Pretreatment

In an attempt to determine the intrinsic activity of the deposited metals, the SiO_2-

supported metal catalysts were also tested using CO chemisorption, N_2 physisorption, and

Fischer- Tropsch reactivity. The CO chemisorption and BET surface area results for the

SiO_2-based catalysts are shown in Table 4.7. Aside from potassium, metal addition had

little effect on the surface area of the silica support. However, K addition reduced the

surface area by approximately 60%, possibly due to the high mobility of K resulting in

extensive sintering and pore blocking, or due to evaporation of the K species [61]. Significant CO uptake capacities were only observed for the Ru, Ni, and Co catalysts. Cu, K, and Fe are not known to chemisorb substantial amounts of CO; and these test conditions are not optimized for the adsorption of CO onto these metals. Iron, for example, is often probed via CO chemisorption at 195 K as opposed to 300 K [62] while Cu sites are typically probed using N_2O [63]. For the metals with measurable uptake capacity, TOFs will be calculated for comparison with Mo_2C-based catalysts.

Table 4.7. BET surface areas and CO uptakes for the Metal/SiO_2 catalysts

Catalyst	BET Surface Area (m^2/g)	CO Uptake Capacity (μmol/g_{cat})
SiO_2	101	<1
Fe/SiO_2	102	<1
Co/SiO_2	97	18
Ni/SiO_2	103	116
Ru/SiO_2	102	52
Cu/SiO_2	100	<1
K/SiO_2	37	<1

Gravimetric rates and, where applicable, TOFs for the SiO_2-supported catalysts were compared to the Mo_2C-supported metal catalysts (Figure 4.19-Figure 4.23). Rate data was typically captured after pretreatment in 15% CH_4/H_2 at 590°C for 4 hours. However, for the Fe and Co studies, catalysts were also pretreated in H_2 at 450°C to determine the effect of the pretreatment gas on TOF and seletivity and compared to Mo_2C following the same pretreatment. Bare SiO_2 was found inactive for FTS. This clearly states that, for the SiO_2-based catalysts, the reaction is entirely catalyzed by the deposited metal, with little influence of the SiO_2 support outside of dispersing the metal. This is not the case for Mo_2C, which is active for FTS.

It is evident that all of the Fe/Mo_2C catalysts (Figure 4.19) exhibit similar or slightly lower (particularly the H_2 pretreated Mo_2C and Fe/Mo_2C) gravimetric rates than the bulk Mo_2C. Compared to the Mo_2C-based catalysts, the Fe/SiO_2 catalysts exhibit a

188

lower rate, which is unaffected by the pretreatment method with the exception of slight differences in activation energy (83 and 109 kJ/mol for Fe/SiO_2 pretreated using 15% CH_4/H_2 versus H_2). The origin of this difference is not yet known, but might involve the formation of an active iron carbide species, given the carburizing conditions. It is well understood that carburized iron (i.e., Fe_7C_3, Fe_3C) represents the active phase for FTS over iron-based catalyst [64,65]. Turnover frequencies clearly show a rate enhancement for all Fe/Mo_2C catalysts and pretreatment combinations. Unfortunately, the Fe/SiO_2 catalysts did not uptake CO so TOFs could not be calculated.
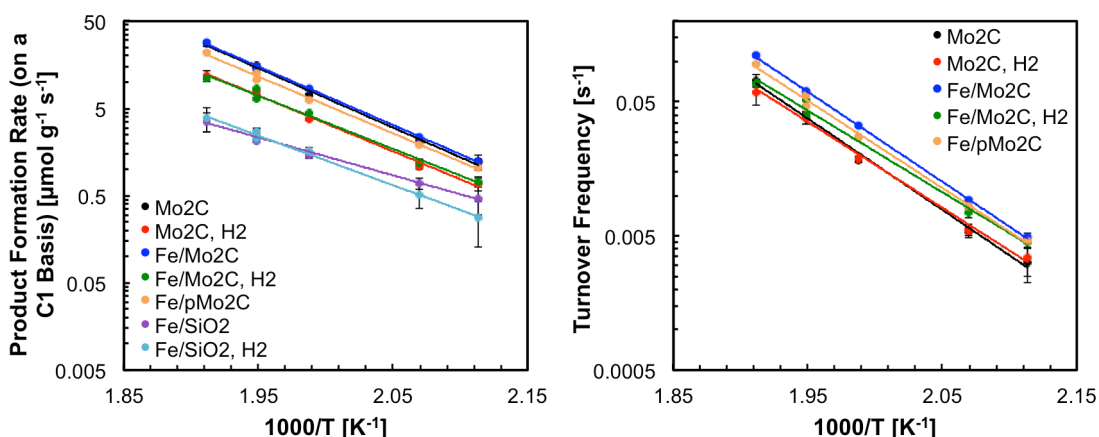
Figure 4.19. Gravimetric (left) and turnover frequencies (right) for the Mo_2C and Fe-based catalysts. TOFs could not be calculated for the Fe/SiO_2 catalysts due to negligible CO uptake. Catalysts were pretreated in 15% CH_4/H_2 at 590°C or pure H_2 at 450°C for 4 hours (designated by "H_2").

The Co/Mo_2C catalysts (Figure 4.20) yielded similar gravimetric rates to bulk Mo_2C, with again much lower gravimetric rate for H_2-pretreated than for CH_4/H_2-pretreated catalysts. Co/SiO_2 was found to be quite active, and matched the gravimetric rate of the Mo_2C catalysts at lower temperatures. The different pretreatment conditions did not impact the performance of the Co/SiO_2 catalysts. The activation energies for the Co/SiO_2 catalysts (98±8 and 103±9 kJ/mol) are consistent with previous literature reports [66,67]. TOF values observed for the Co-based catalysts show no promotional effect of

189

Co for the Mo$_2$C-based catalysts, while the CO-normalized rates for the Co/SiO$_2$ catalysts were almost an order of magnitude higher.

The Ni/SiO$_2$ catalyst performed rather poorly relative to the Mo$_2$C-based catalysts (Figure 4.21). Both the gravimetric and CO-normalized rates for the Ni/SiO$_2$ catalysts were between 10 and 20 times less active than the Ni/Mo$_2$C catalysts across the temperature range. The Ru/SiO$_2$ catalysts showed gravimetric activity similar to that of Fe, with CO-normalized rates exceeding that of the Mo$_2$C and Ru/Mo$_2$C catalysts (Figure 4.22). Cu/SiO$_2$ was found to be quite inactive for FTS, as expected (Figure 4.23). Given the negligible CO uptake of Cu/SiO$_2$, CO-normalized rates were not calculated. Lastly, gravimetric and CO-normalized rates are not reported for the K-based catalysts due to the immeasurable activity of K/SiO$_2$ and the lack of CO uptake capacity for all K-promoted catalysts.
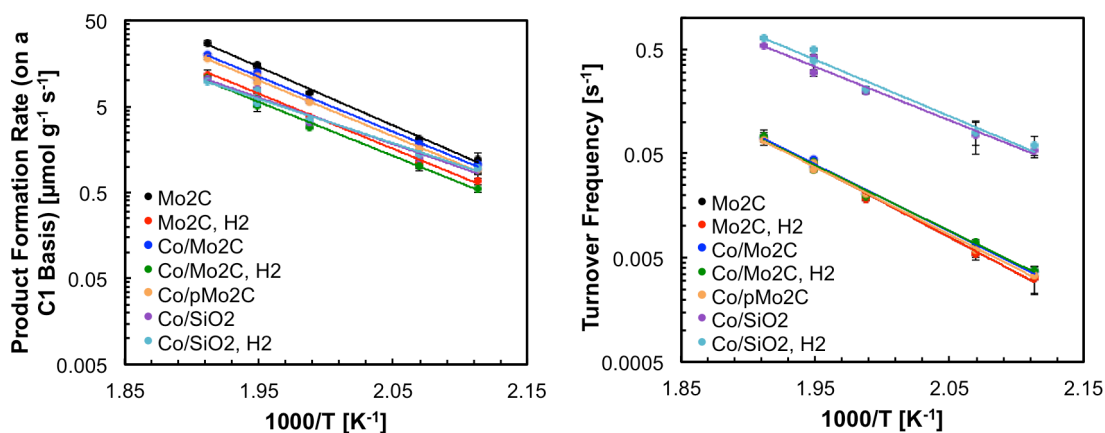
Figure 4.20. Gravimetric (left) and turnover frequencies (right) for the Mo$_2$C and Co-based catalysts. Catalysts were pretreated in 15% CH$_4$/H$_2$ at 590°C or pure H$_2$ at 450°C (designated by "H$_2$").
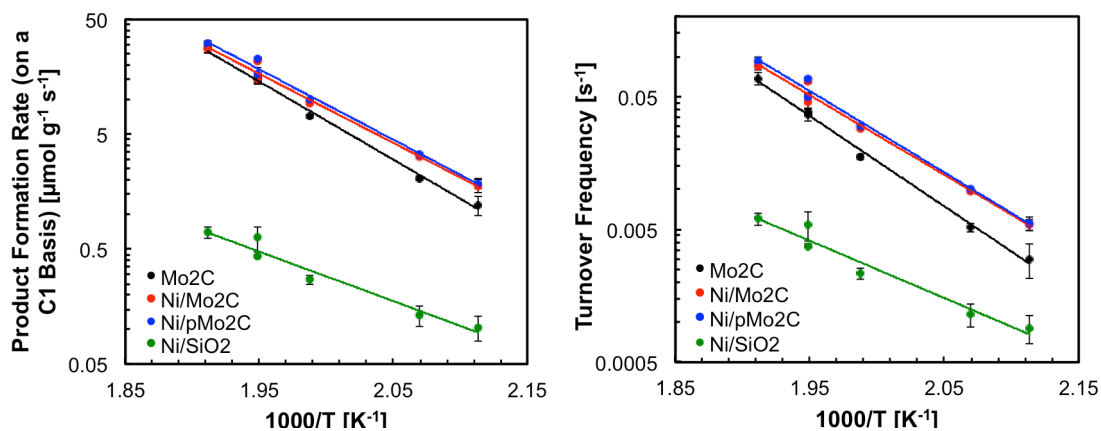
Figure 4.21. Gravimetric rates (left) and turnover frequency (right) for the Ni catalysts.
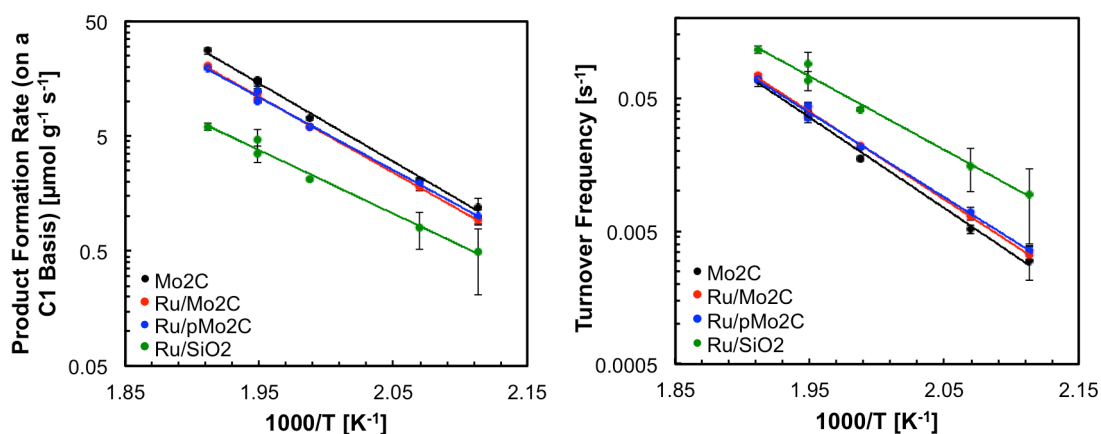
Figure 4.22. Gravimetric rates (left) and turnover frequency (right) for the Ru catalysts
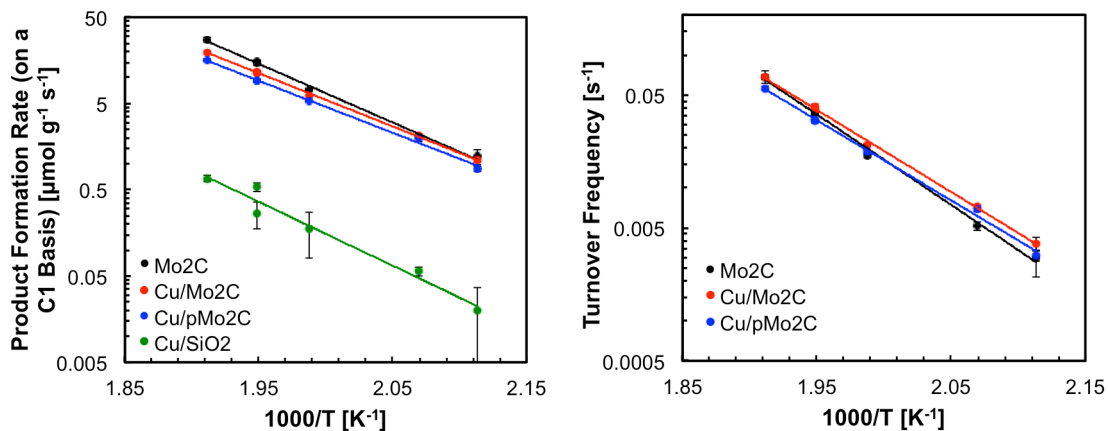
Figure 4.23. Gravimetric rates (left) and turnover frequency (right) for the Cu catalysts. TOFs could not be calculated for the Cu/SiO$_2$ catalysts due to negligible CO uptake.

Total and hydrocarbon selectivity comparisons for the Mo_2C- and SiO_2-supported metal catalysts are shown in Figure 4.24-Figure 4.28. Generally speaking, the metal/SiO_2 catalysts exhibited the expected FTS performance from a selectivity perspective, consistent with previous literature. Ru [39,40,68], Co [42,44], and Fe [45] are well known for their chain propagation capabilities, generating long-chain hydrocarbons from syngas. These metals represent the basis for FTS commercial catalysts, although Ru usage is limited due to its inherently high cost. The Fe/SiO_2, Co/SiO_2, and Ru/SiO_2 catalysts produced chain propagation probability factors of 0.62, 0.63, and 0.79, respectively. Nickel is an excellent methanation catalyst, as corroborated by the higher CH_4 selectivity for Ni/SiO_2 relative to bare Mo_2C, while Cu/SiO_2 shows higher CO_2 selectivity relative to bare Mo_2C.

Interestingly, for certain metals, the performance of the Mo_2C-supported metal catalysts appears to represent a weighted average of the activities of Mo_2C and the deposited active metal. Fe and Ni, which represent the two cases where higher CO-normalized rates were observed relative to Mo_2C, have hydrocarbon selectivities between those of the corresponding metal and the Mo_2C. For example, in Figure 4.24, the C_5+ selectivity for the Fe/Mo_2C catalysts lies in between the Mo_2C and the Fe/SiO_2 selectivities. Similarly, for Ni, the CH_4 selectivity of Ni/Mo_2C sits between the Mo_2C and the Ni/SiO_2 selectivities.
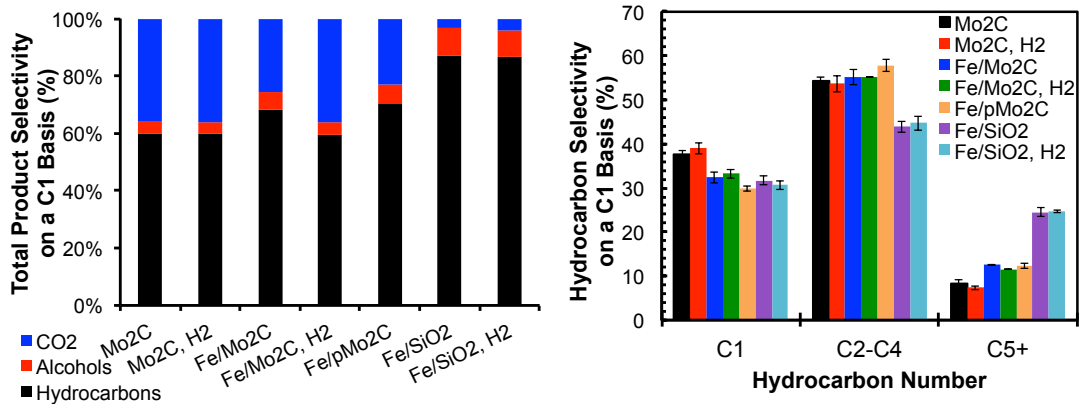
Figure 4.24. Total (left) and hydrocarbon (right) selectivity for the Mo_2C- and SiO_2-supported Fe catalysts studied. Hydrogen pretreatment at 450°C is indicated by the "H2" after the catalyst name in the legend. Selectivities were calculated from data at 240°C.
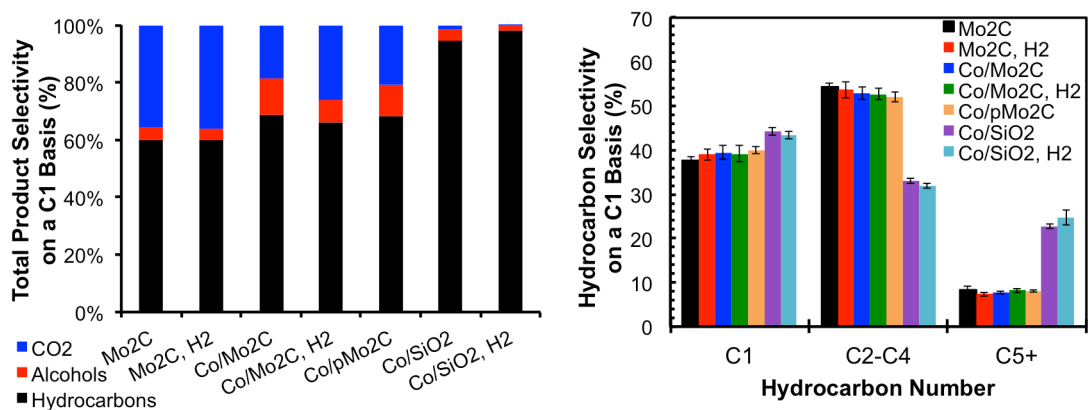
Figure 4.25. Total (left) and hydrocarbon (right) selectivity for the Mo_2C- and SiO_2-supported Co catalysts studied. Hydrogen pretreatment at 450°C is indicated by the "H2" after the catalyst name in the legend. Selectivities were calculated from data at 240°C.
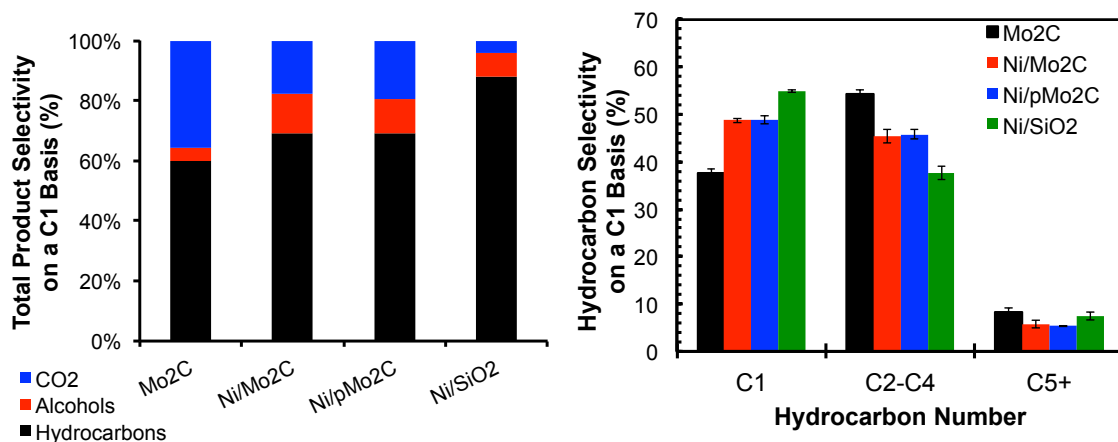
Figure 4.26. Total (left) and hydrocarbon (right) selectivity for the Mo_2C- and SiO_2-supported Ni catalysts studied. Selectivities were calculated from data at 240°C.
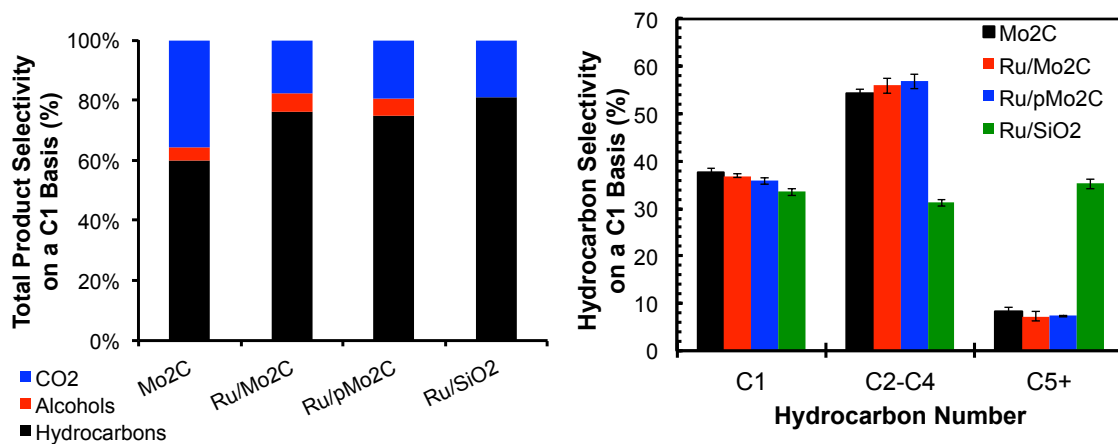
Figure 4.27. Total (left) and hydrocarbon (right) selectivity for the Mo_2C- and SiO_2-supported Ru catalysts studied. Selectivities were calculated from data at 240°C.
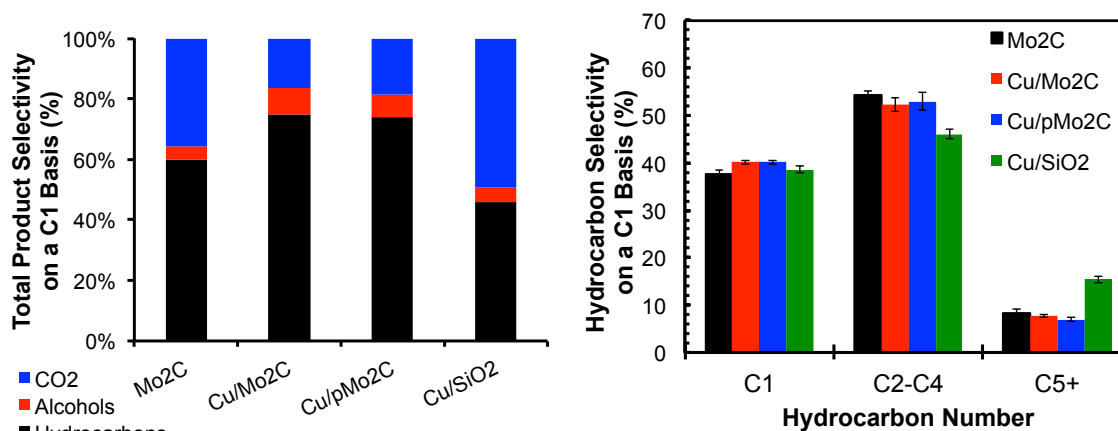
Figure 4.28. Total (left) and hydrocarbon (right) selectivity for the Mo_2C- and SiO_2-supported Cu catalysts studied. Selectivities were calculated from data at 240°C.

While changes in selectivity consistent with the intrinsic activity of the deposited metal are observed for the Fe and Ni catalysts, the performance of Co (Figure 4.25), Ru (Figure 4.27), and Cu (Figure 4.28) when supported on Mo_2C are inconsistent with the intrinsic performance of the metal as seen for the SiO_2-supported catalysts. The negligible differences for Cu are not unexpected as the intrinsic rate of CO hydrogenation over Cu/SiO_2 is quite low (Figure 4.23). While Co and Ru supported on SiO_2 generate hydrocarbons of C_5 or longer at selectivities of 25-35% on a C1 basis, these same metals supported on Mo_2C result in similar the selectivities to bulk Mo_2C. These Co/Mo_2C (50%

194

metal loading) results are consistent with those at lower surface loadings (10%), which indicates that the low metal loading does not explain the observed inactivity of Co and Ru [6]. Additionally, the performance of Co/Mo_2C was not statistically different after pretreatment in 15% CH_4/H_2 at 590°C versus H_2 at 450°C indicating that pretreatment gas is not specifically causing the deactivation of cobalt.

4.4. Discussion

In this chapter, the performance of Mo_2C-supported metal (Ru, Co, Ni, Fe, Cu, K) catalysts at high promoter weight loadings was described for the Fischer-Tropsch synthesis (FTS) reaction. Work focused on the effect of metal promoter addition as well as the effect of the presence of a passivation layer on Mo_2C during synthesis of Mo_2C-supported FTS active metal catalysts. Based on the turnover frequencies (TOF), the following trend in activity was observed: $Fe/Mo_2C \sim Ni/Mo_2C > Mo_2C \sim Cu/Mo_2C \sim Ru/Mo_2C \sim Co/Mo_2C$. TOFs for the Fe and Ni-based catalysts were ~2 times higher than bare Mo_2C. TOFs for the K/Mo_2C could not be calculated due to negligible CO uptake capacities. In addition, activation energies for all the Mo_2C-based catalysts were within 10% of each other, and not statistically different.

Selectivities for all of the catalysts were relatively similar to Mo_2C as well. Any differences from Mo_2C with respect to the hydrocarbon selectivities towards C_{5+} products were fairly small. The selectivities to the desired C_{5+} products trended as follows: $Fe/Mo_2C \sim K/Mo_2C > Mo_2C \sim Cu/Mo_2C \sim Co/Mo_2C \sim Ru/Mo_2C > Ni/Mo_2C$. The Fe/Mo_2C and K/Mo_2C exhibited C_{5+} selectivities close to 12-13% compared to ~8% for bulk Mo_2C. Also, with the exception of K/Mo_2C, metal addition resulted in a lower selectivity to CO_2 and a higher selectivity to alcohol oxygenates. These results indicate

195

that the metal addition had an influence on either the WGS activity or the removal or incorporation of oxygen into products. On the other hand, K/Mo$_2$C resulted in higher selectivity towards CO$_2$ production (60-65%) compared to hydrocarbons and alcohols. For Fischer-Tropsch synthesis, in the absence of alcohol production, the amount of water produced should be equal to the amount of hydrocarbons produced on a C1 basis. Therefore, the maximum CO$_2$ selectivity should be 50% assuming all CO$_2$ is produced via WGS. Thus, the 60-65% selectivity observed for K/Mo$_2$C suggests an alternative reaction is occurring as well, perhaps disproportionation of CO via the Boudouard reaction described in Equation 4.6 [69].

$$2\ CO \rightarrow CO_2 + C_{(ads)} \tag{4.6}$$
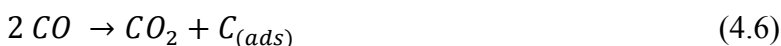
This possibility is supported by computational reports from Bugyi et al. indicating that CO dissociates more readily over a K/Mo$_2$C surface compared to a native Mo$_2$C surface [70].

The SiO$_2$-supported metal catalysts performed as expected based on reported literature [37,38,40,42,43]. SiO$_2$-supported Fe, Co, and Ru exhibited high selectivities to C$_{5+}$ hydrocarbons, Ni yielded high CH$_4$ selectivities, and Cu and K were relatively inactive. Based on comparisons of the results for the Mo$_2$C- and SiO$_2$-supported metal catalysts, the Fe-Mo$_2$C appears to produce additive performance, while the Ni-Mo$_2$C system may exhibit synergy. Other metals (Ru, Co, Cu) failed to show any enhancement on Mo$_2$C (discussed further below).

Considering the Fe-Mo$_2$C system, its additive performance may be estiamted mathematically. In theory, if the selectivities are a combination of the individual Mo$_2$C

and Fe/SiO$_2$ performance, the C$_{5+}$ selectivity of Fe/Mo$_2$C can be represented by Equation 4.7.

$$S_{5+,Fe/Mo2C} = \left[r_{Mo2C}(S_{C5+,Mo2C}) + r_{Fe/SiO2}(S_{C5+,Fe/SiO2})\right] * r_{Fe/Mo2C} \qquad (4.7)$$

where r_{Mo2C}, $r_{Fe/SiO2}$, and $r_{Fe/Mo2C}$ are the gravimetric rates of Mo$_2$C, Fe/SiO$_2$, and Fe/Mo$_2$C, respectively; and $S_{C5+,Mo2C}$ and $S_{C5+,Fe/SiO2}$ are the C$_{5+}$ selectivities for Mo$_2$C and Fe/SiO$_2$, respectively. Using the relative rates and selectivities for Mo$_2$C and Fe/SiO$_2$ at 240°C, together with the Fe/Mo$_2$C rate, an expected C$_{5+}$ selectivity for Fe/Mo$_2$C can be calculated. The calculated selectivity of 12.7% closely matches the observed value of 12.0% C$_{5+}$ selectivity. The close relationship between the calculated and actual selectivity values indicates that the deposited Fe metal and the Mo$_2$C support exist and perform independently of each other, without synergy.

Ni/Mo$_2$C, on the other hand, shows an improvement in gravimetric rate (~40%) over bulk Mo$_2$C not due to only additive performance between Mo$_2$C and Ni/SiO$_2$ since the activity of Ni/SiO$_2$ was quite low (0.4μmol/g/s). To achieve the enhancement in rate, the addition of nickel must either change the energetics of the rate limiting step or provide additional active sites for FTS. The apparent activation energy (E$_{a,App}$) for Ni/Mo$_2$C was 115 ± 7 kJ/mol compared to 130 ± 5 kJ/mol for Mo$_2$C (the E$_{a,App}$ for Ni/SiO$_2$ was 82 ± 10 kJ/mol). Although this decrease in E$_{a,App}$ is small, it is possible that the addition of Ni decreased the energy requirements for the rate limiting step. Another posibility is that the addition of Ni provides more sites for the dissociation of H$_2$ to generate a more H-rich surface or generates new sites between Ni and Mo$_2$C, as has been reported previously for the Pt-Mo$_2$C system [16,71].

The presence of a passivation layer on Mo_2C did not impact the reactivity of any of the catalysts studied. As discussed in Chapter 3, a passivation layer inhibits redox chemistry between the support and depositing metal, which can influence reactivity. Fe and Ni, the only two metals that showed noticeable differences in FTS rate performance relative to bare Mo_2C, are not spontaneously reduced during impregnation of Mo_2C with the precursor salt [21]. The metals expected to undergo redox chemistry (Ru, Cu) did not appear to influence the FTS reactivity.

The inactivity of or lack of enhancement from Ru and Co when supported on Mo_2C was unexpected since Ru and Co are known to be highly active metals for FTS [72,73]. FTS rates and selectivities for the Ru/Mo_2C and Co/Mo_2C catalysts were similar to those for bulk Mo_2C. However, performance consistent with the literature was observed for Co and Ru supported on SiO_2. Moderate rates and high C_{5+} selectivities (25-35%), far exceeding those observed on Mo_2C, were observed for the SiO_2-supported Co and Ru catalysts. The inactivity of Ru and Co appears to be specific to the Mo_2C support and its cause will be explored and discussed in Chapter 5.

4.5. Summary

The Fischer-Tropsch synthesis performance of Mo_2C-supported metal catalysts, employing 6 metal promoters (Ru, Co, Fe, Ni, Cu, K), was evaluated. Initial studies indicated that supported Ni and Fe exhibited enhanced turnover frequencies relative to Mo_2C alone. Furthermore, selectivity for C_{5+} products was lower for Ni and higher for Fe relative to Mo_2C. Performance for metal and support in the Ni/Mo_2C and Fe/Mo_2C catalysts appeared to be synergistic and additive, respectively. On the other hand, Co and Ru supported on Mo_2C were surprisingly inactive, exhibiting no promotional effect.

SiO$_2$-supported Co and Ru exhibited excellent FTS performance, suggesting the observed

inactivity is specific to and caused by the Mo$_2$C support.

4.6.   References

[1]   I. Kojima, E. J. Miyazaki. Catalysis, 89 (1984) 168-171.
[2]   P.M. Patterson, T.K. Das, B.H. Davis, Appl. Cat. A: General, 251 (2003) 449-455.
[3]   G. S. Ranhotra, A. T. Bell, J. A. Reimer, J. Catalysis 108 (1987) 40-49.
[4]   H.-G. Kim, K.H. Lee, J.S. Lee, Research Chem. Interm., 26 (2000) 427-443.
[5]   I. Kojima, E. Miyazaki, I.J.C.S. Yasumori, Chem. Comm. 1980 (573-574).
[6]   J.A. Schaidle, PhD Dissertation, University of Michigan, 2011.
[7]   A. Griboval-Constant, J. Giraudon, G. Leclercq, L. Leclercq, Appl. Cat. A: General, 260, (2004) 35-45.
[8]   A. Griboval-Constant, J. Giraudon, I. Twagishema, G. Leclercq, M.E. Rivas, J. Alvarez, M.J. Pérez-Zurita, M.R. Goldwasser, J. Molec. Cat. A: Chemical, 259 (2006) 187-196.
[9]   J.A. Rodriguez, P. Liu, Y. Takahashi, K. Nakamura, F. Viñes, F. Illas, J. Am. Chem. Soc., 131 (2009) 8595-8602.
[10]   M. Lewandowski, A. Szymańska-Kolasa, P. Da Costa, C. Sayag, Catal. Today, 119 (2007) 31-34.
[11]   N. Perret, X. Wang, L. Delannoy, C. Potvin, C. Louis, M.A. Keane, J. Catalysis, 286 (2012) 172-183.
[12]   M. Xiang, D. Li, H. Xiao, J. Zhang, W. Li, B. Zhong, Y. Sun, Catal. Today, 131 (2008) 489-495.
[13]   H. Shou, R.J. Davis, J. Catalysis, 282 (2011) 83-93.
[14]   W. Setthapun, S.K. Bej, L.T. Thompson, Top. Catal., 49 (2008) 73-80.
[15]   A.C. Lausche, J.A. Schaidle, L.T. Thompson, Appl. Cat. A: General, 401 (2011) 29-36.
[16]   N.M. Schweitzer, J.A. Schaidle, O.K. Ezekoye, X. Pan, S. Linic, L.T. Thompson, J. Am. Chem. Soc., 133 (2011) 2378-2381.
[17]   J.A. Schaidle, A.C. Lausche, L.T. Thompson, J. Catalysis, 272 (2010) 235-245.
[18]   Esposito, D.V.; Hunt, S.T.; Kimmel, Y.C.; Chen, J.G. J. Am. Chem. Soc., 134 (2012) 3025-3033.
[19]   I.J. Hsu, Y.C. Kimmel, X. Jiang, B.G. Willis, J.G. Chen, Chem. Commun., 48 (2012) 1063-1065.
[20]   R. Venkataraman, H.R. Kunz, J.M. Fenton, J. Electrochem. Soc., 150 (2003) A278-A284.
[21]   J.A. Schaidle, N.M. Schweitzer, O.T. Ajenifujah, L.T. Thompson, J. Catalysis, 289 (2012) 210-217.
[22]   J.P. Brunelle, Pure & Applied Chemistry 50 (1978) 1211-1229.
[23]   L. Jiao, J.R. Regalbuto, J. Catalysis 260 (2008) 329-341.
[24]   I.E. Wachs, Characterization of Catalytic Materials. Mometum Press: New York, New York, 2010.
[25]   R.S.P.Coutts, B. Kautzner, P.C. Wailes, Aust. J. Chem. 22 (1969) 1137-1141.

[26] G. P. Van Der Laan, A. A. C. M. Beenackers, Catalysis Reviews: Science and Engineering 41 (1999) 255-318

[27] R.B. Anderson, Catalysts for the Fischer-Tropsch Synthesis, Van Nostrand Reinhold, New York, 1956. Vol. 4.

[28] J.A. Schaidle, L.T. Thompson, Journal of Catalysis 329 (2015) 325-334.

[29] D-V.N. Vo, A.A. Adesina, Applied Catalysis A: General 399 (2011)221-232.

[30] D.W. Goodman, R.D. Kelley, T.E. Madey, J.T. Yates, Jr., Journal of Catalysis 63 (1980) 226-234.

[31] C.C. Kao, S.C. Tsai, Y.W. Chung, Journal of Catalysis 73 (1982) 136.

[32] S.J. Tauster, S.C. Fung, Journal of Catalysis 55 (1978) 29-35.

[33] A.A. Khassin, T.M. Yurieva, V.V. Kaichev, V.I. Bukhtiyarov, A.A. Budneva, E.A. Paukshtis, V.N. Parmon, Journal of Molecular Catalysis A: Chemical 175 (2001) 189–204

[34] R.P. Mogorosi, N. Fischer, M. Claeys, E. van Steen, Journal of Catalysis 289 (2012) 140-150.

[35] J.M.G. Carballo, E. Finocchio, S. García, S. Rojas, M. Ojeda, G. Busca, J.L.G. Fierro, Catalysis Science & Technology 1 (2011) 1013-1023.

[36] Zhang, J.; Chen, J.; Li, Y.; Sun, Y. Journal of Natural Gas Chemistry 11 (2002) 99-108.

[37] H. Jahangiri, J. Bennet, Mahjoubi, P.; Wilson, K.; Gu, S.; Catalysis Science & Technology 4 (2014) 2210.

[38] Spadaro, L.; Arena, F.; Granados, M.L.; Ojeda, M.; Fierro, J.L.G.; Frusteri, F. Journal of Catalysis 234 (2005) 451-462.

[39] J.M.G. Carballo, J. Yang, A. Holmen, S. García-Rodríguez. J. Catalysis, 284 (2011) 102-108

[40] X.-Y. Quek, I.A.W. Filot, R. Pestman, R. A. van Santen. Chem. Commun., 50 (2014) 6005-6008.

[41] D.L. King. J. Catalysis, 51 (1978) 386-397.

[42] G.L. Bezemer, J.H. Bitter, H.P.C.E. Kuipers, H. Oosterbeek, J.E. Holewijn, X. Xu, F. Kapteijn, A.J. van Dillen, K.P. de Jong. J. Am. Chem. Soc. 128 (2006) 3956

[43] T. Herranz, X. Deng, A. Cabot, J. Guo, M. Salmeron. J. Phys. Chem. B. 113 (2009) 10721-10727.

[44] J.P. den Breejen, P.B. Radstake, G.L. Bezemer, J.H. Bitter, V. Frøseth, A. Holmen, J. Am. Chem. Soc. 131 (2009) 7197-7203

[45] J.-Y. Park, Y.-J. Lee, P.K. Khanna, K.-W. Jun, J.W. Bae, Y.H. Kim. J. Mol. Catal. A: Chem., 323 (2010) 84-90.

[46] Twigg, M.V.; Spencer, M.S. Appl. Cat. A: General. 212 (2001) 161-174.

[47] Keane, M.A.; Patterson, P.M. J. Chem. Soc., Faraday Trans. 92 (1996) 1413-1421.

[48] Romanowski, W. Highly Dispersed Metals as Adsorbents, Wiley, New York, 1987, p. 171

[49] Kotarba, A.; Adamski, G.; Piskorz, W.; Sojka, Z.; Sayag, C.; Djéga-Maradassou, G. J. Phys. Chem. B 108 (2004) 2885-2892.

[50] Park, K.Y.; Seo, W.K.; Lee, J.S. Catalysis Letters 11 (1991) 349-356.

[51] C. Pistonesi, M.E. Pronsato, L. Bugyi, A. Juan. Catal. Today 181 (2012) 102-107.

[52] J.W. Han, L. Li, D.S. Sholl, J. Phys. Chem. C 115 (2011) 6870-6876.

[53] Shou, H.; Davis, R.J. Journal of Catalysis 282 (2011) 83-93.

[54] Shou, H.; Liwei, L.; Ferrari, D.; Sholl, D.S.; Davis, R.J. Journal of Catalysis 299 (2013) 150-161.

[55] Xiang, M.; Li, D.; Xiao, H.; Zhang, J.; Li, W.; Zhong, B.; Sun, Y. Catalysis Today 131 (2008) 489-495.

[56] Christensen, J.M.; Duchstein, L.D.L.; Wagner, J.B.; Jensen, P.A.; Temel, B.; Jensen, A.D. Industrial & Engineering Chemistry Research 51 (2012) 4161-4172.

[57] Davis, B.H. Catalysis Today 141 (2009) 25-33.

[58] Dry, M.E. Catalysis Letters 7 (1990) 241-252.

[59] Forzatti, P.; Tronconi, E.; Pasquon, I. Catalysis Reviews: Science and Engineering 33 (1991) 109-168.

[60] Vannice, M.A. Journal of Catalysis 37 (1975) 449-461

[61] Badini, C.; Saracco, G.; Serra, V.; Specchia, V. Appl. Catal. B 18 (1998) 137.

[62] Lee, J-F. Chern, W-S.; Lee, M-D. Dong, T-Y. Canadian Journal of Chem. Eng. 70 (1992) 511-515

[63] Narita, K.; Takezawa, N.; Kobayashi, H.; Toyoshima, I. React. Kinet. Catal. Letters 19 (1982) 91-94

[64] Mansker, L.D.; Jin, Y.; Bukur, D.B.; Datye, A.K. Appl. Cat. A: General 186 (1999) 277-296.

[65] Herranz, T.; Rojas, S.; Pérez-Alonso, F.J.; Ojeda, M.; Terreros, P.; Fierro, J.L.G. J. Catalysis 243 (2006) 199-211.

[66] Yan, Z.; Wang, Z.; Bukur, D.B.; Goodman, D.W. J. Catalysis 268 (2009) 196-200

[67] C.G. Cooper, T.-H. Nguyen, Y.-J. Lee, K.M. Hardiman, T. Safinski, F.P. Lucien, A.A. Adesina, Catal. Today 131 (2008) 255

[68] Ernst, B.; Libs, S.; Chaumette, P.; Kiennemann, A. Appl. Cat. A: General 186 (1999) 145-168

[69] J.M. Calo, M.T. Perkins, Carbon 25 (1987) 395-407.

[70] L. Bugyi, F. Solymosi, J. Phys. Chem. B. 105 (2001) 4337-4342.

[71] K.D. Sabnis, M.C. Akatay, Y. Cui, F.G. Sollberger, E.A. Stach, J.T. Miller, W.N. Delgass, F.H. Ribeiro, 330 (2015) 442-451.

[72] G. P. Van Der Laan, A. A. C. M., Catalysis Reviews: Science and Engineering 41 (1999) 255-318.

[73] M. A. Vannice, J. Catalysis 37 (1975) 449-461

CHAPTER 5

Understanding the Activity of Mo$_2$C-supported Ru or Co Catalysts for Fischer-Tropsch Synthesis

5.1. Introduction

Iron (Fe), cobalt (Co), and ruthenium (Ru) are known to be highly active metals for FTS favoring the production of long chain hydrocarbons [1,2,3]. We anticipated that the addition of these metals to Mo$_2$C would result in enhanced performance, however, as reported in Chapter 4, these metals appeared to be inactive when supported on the Mo$_2$C surface. This observation is unlike that reported for Pt/Mo$_2$C WGS catalysts [4]. In addition the SiO$_2$-supported Co and Ru catalysts at loadings comparable to those for the Mo$_2$C supported catalysts were active and highly selective for higher hydrocarbons (~25-35% C$_{5+}$). It should be noted that Mo$_2$C- and WC-supported Ru or Co catalysts have been studied previously [5,6] and enhancements in the rates and/or selectivities to C$_{5+}$ products were improved [6]. The authors did not explain the origin of the enhanced performance. The metal loadings were 1 wt%, but the catalyst surface areas were very low (3-9 m^2/g) so the Ru/Mo$_2$C and Co/Mo$_2$C catalyst surfaces were likely dominated by the supported metal (surface coverages of ~85-150% based on 10 sites/nm^2). Conversely, in a separate study, Schaidle reported very similar FTS performance for Ru/Mo$_2$C and Mo$_2$C, while very small (<10%) changes in rate and hydrocarbon selectivity were observed for Co/Mo$_2$C [7]. Schaidle's results are consistent with the results reported in Chapter 4 detailing the unanticipated FTS performance of Ru and Co when supported on Mo$_2$C.

Interestingly, there is a disconnect in the literature as to the impact of depositing Ru or Co metal on the surfaces of Mo_2C FTS catalysts, a gap that the work in this chapter aims to investigate.

Mo_2C-supported Ru and Co materials have been studied for other reaction systems with variable results. Chen reported lower methanol formation rates during CO_2 hydrogenation for the Ru/Mo_2C catalyst relative to bulk Mo_2C and Cu/Mo_2C, hypothesizing to be due to differences in the metal-support interactions, though no evidence was provided [8]. Patt [9] and King [10] reported that the addition of Ru to Mo_2C improved WGS rates relative to bulk Mo_2C. Porosoff et al. evaluated the performance of a 7.5wt% Co/Mo_2C catalyst for the reduction of CO_2, noting that the addition of Co had a negligible effect on conversion, but decreased the ability to reduce CO further to CH_4 (higher $CO:CH_4$ product ratio than bulk Mo_2C) [11]. On the other hand, Chen reported the enhanced formation of CH_4 and longer chain hydrocarbons from CO_2 for Co/Mo_2C relative to bulk Mo_2C [8]. These results suggest that FTS occurred for this catalyst as Chen hypothesized that the addition of Co facilitated the further reduction of CO (formed from CO_2) into CH_4 and other products. It should be noted that literature reviewed here involved the use different reaction conditions. For example, Chen's work was performed using a three-phase batch reactor (solid catalyst, 1,3-dioxane solvent, and dissolved and gas phase CO_2/H_2) compared to the flow reactors used in research by Patt, King and Porosoff [8-11].

There are a number of potential reasons for the unanticipated performance during FTS for the Ru/Mo_2C and Co/Mo_2C catalysts including: (1) particle size effects [12-17], (2) incomplete reduction of the metal precursor [18], (3) inhibition by chloride [19,20],

and/or (4) the presence of strong metal-support interactions (SMSI) [21] between the metal and Mo_2C, changing the character of the metal through electronic or geometric perturbations. According to a number of reports, turnover frequencies for FTS over Ru [12,13,14] and Co [15,16,17] based catalysts increase by a factor between 3 and 10 as the particle size increases from 1 to ~15nm, respectively. In general, in these works, it was hypothesized that the highly coordinated (~11-12 atoms) Ru and Co metallic sites are the most active sites for FTS. Additionally, metallic sites are known to be the active sites for FTS over Ru and Co [12-17]; if Ru on Mo_2C was not sufficiently reduced in comparison to behavior on SiO_2, one would expect lower activities. It is also possible that chloride ions from the $RuCl_3$ precursor were left on the surface, inhibiting activities for Ru. Chlorine has been reported to decrease FTS reaction rates for Ru-based catalysts [19,20]. Cobalt nitrate was used as the precursor for the Co/Mo_2C, and thus, catalyst poisoning by the precursor anion is not an expected form of deactivation for cobalt. Finally, SMSI have been cited to cause differences in the performance of Co, Ni, Ru, or Fe when deposited on various supports [18,22-26] and may have played a role in the observed behavior of the Ru/Mo_2C catalyst.

Work described in this chapter focuses on understanding the performance of Ru/Mo_2C and Co/Mo_2C catalysts for Fischer-Tropsch synthesis. The Ru/Mo_2C catalyst was synthesized using different conditions, characterized and then tested for FTS performance. The goal was to correlate the unanticipated inactivity of Ru with a root cause for the deactivation. The Ru/Mo_2C catalysts were initially chosen for the experiments in order to limit complexity. Catalyst syntheses were designed in order to alter the particle size of Ru by increasing the Ru weight loading used. Ruthenium

oxidation states for the Ru/Mo$_2$C catalysts were determined using X-ray photoelectron spectroscopy and compared to that for a Ru/SiO$_2$ catalyst; both the passivated and pretreated catalysts were characterized. To evaluate the effect of chloride on FTS over the Ru/Mo$_2$C catalysts, several catalysts were prepared using ruthenium acetylacetonate (Ru(acac)$_3$) instead of RuCl$_3$. Finally, the effect of reduction temperature was explored to investigate potential metal-support interactions. These evaluations, where applicable, were then applied to the Co/Mo$_2$C catalysts. Results and conclusions from this chapter will help inform the synthesis and application of Mo$_2$C-supported metal catalysts.

5.2. Experimental Methods

5.2.1. Catalyst Synthesis

Molybdenum carbide (Mo$_2$C) was synthesized via temperature-programmed reaction (TPR) as previously reported [27] and described in Section 3.2.1. Approximately 1.3g of ammonium paramolybdate was heated from room temperature to 350°C under H$_2$ flow (400 mL/min) at 5°C/min followed by a 12 hr soak. Following the soak step, the material was heated to 590°C at 2.67°C/min under 15% CH$_4$/H$_2$ gas followed by a 2 hr soak. The reactor was then removed from the furnace and allowed to cool to room temperature under 15% CH$_4$/H$_2$ gas flow. To prepare the bare Mo$_2$C catalysts without metal promotion, the resulting material was passivated by exposure to 1% O$_2$/He flowing at 20 mL/min for at least six hours to form a protective oxide layer on the surface of the bulk phase.

Alternatively, metal deposition onto unpassivated carbide was performed via dry impregnation. More details regarding the synthesis can be found in Section 4.2.1. In short, the Mo$_2$C was transferred into a water-tolerant, nitrogen glove box, and a metal

precursor solution (with volume equivalent to the material pore volume) was dropped in 15 μL increments onto the Mo$_2$C powder, which was stirred/agitated extensively between additions. The metal precursors included RuCl$_3$•3H$_2$O (Alfa Aesar, 99.9% (PGM basis), Ru 38% minimum), Ru(acac)$_3$ (Sigma-Aldrich, 97%), and Co(NO$_3$)$_2$•6H$_2$O (Alfa Aesar, ACS, 98.0-102.0%). Following impregnation, the water was evaporated using a hot plate in the glove box. The dried material was then transferred back into the quartz flow-through reactor, supported by a bed of quartz wool, under excess hydrogen flow to prevent exposure to air. The catalyst was then either passivated in 1% O$_2$/He flowing at 20 mL/min for at least six hours or reduced in H$_2$ at 110°C for 2 hours, then 450°C for 4 hours, followed by passivation.

Silica-supported metal catalysts were synthesized by dry impregnation of a silica support. Cab-o-Sil L-90 silica support was first calcined at 500°C for 10 hr in air at 200 mL/min. Incipient wetness impregnation was used to deposit the metal at the target loading, consistent with Mo$_2$C-based catalyst metal loadings, as described above. Identical to the Mo$_2$C-based catalysts, the subsequent material was dried in H$_2$ at 110°C for 2 hours, then reduced at 450°C as described previously. More details regarding the synthesis can be found in Section 4.2.1.

5.2.2. Catalyst Characterization

5.2.2.1. X-ray Powder Diffraction

The crystal structure of the synthesized catalysts was determined by X-ray powder diffraction using a Rigaku Miniflex X-ray diffractometer employing a Cu Kα X-ray source and a Ni filter. Experimental and analysis procedures were described previously in Chapter 2 (Section 2.2.2.1.).

Crystallite sizes for the crystalline facets were estimated using the Scherrer equation, found in Equation 5.1, where K is a shape factor (typically assumed to be 0.9, but varies with actual crystallite size), β is the full-width at half maximum (FWHM) for the facet diffraction peak, and θ is the angle of the diffraction peak.

$$Crystallite\ Size = \frac{K*\gamma}{\beta*\cos(\theta)} \tag{5.1}$$

5.2.2.2. N$_2$ Physisorption Measurements

Material surface areas were calculated using the Brunauer-Emmett-Teller (BET) method applied to a N$_2$ physisorption isotherm. A brief description of the experiment and analysis can be found in Chapter 2 (Section 2.2.2.2.).

5.2.2.3. Elemental Analysis

Catalyst compositions were determined by elemental analysis performed using Inductively Coupled Plasma-Optical Emission Spectroscopy (ICP-OES) using a Varian 710-ES spectrometer. Roughly 15-20 mg of the catalyst was dissolved in 3 mL of aqua regia (3 parts hydrochloric acid, 1 part nitric acid) and analyzed by comparing the wavelength intensities for various elements to the intensities of known standards.

5.2.2.4. H$_2$ Temperature-Programmed Reduction

Hydrogen temperature-programmed reductions (H$_2$-TPRs) were conducted on a Micromeritics Autochem 2920, equipped with a thermal conductivity detector (TCD) and a Pfeiffer Vacuum Quadstar GSD-301 Mass Spectrometer (MS). Detailed experimental conditions and analyses are described in Chapter 2 (Section 2.2.2.3.).

5.2.2.5. CO Uptake

CO uptake chemisorption was performed on a Micromeritics Autochem 2920, as described previously in Chapter 3 (Section 3.2.2.5). CO uptake chemisorption was used

to probe the number of metallic sites on catalysts. Catalysts were pretreated at different conditions (various temperatures and either 15% CH_4/H_2 or H_2 gas) prior to CO pulsing. During pulsing, the effluent gas was analyzed using both TCD and MS detectors. CO was pulsed until the surface became saturated as indicated by the constant peak area in the TCD towards the latter part of the experiment.

5.2.2.6. X-ray Photoelectron Spectroscopy

X-ray photoelectron spectroscopy (XPS) was conducted on a Kratos Axis Ultra X-ray photospectrometer equipped with an Al anode operating at 8 mA and 14 kV (K_α radiation, 1486.6 eV). Details for the analysis are found in Section 3.2.2.9. In addition to the analysis of the elements described therein, constraints were placed on parameters in the analysis of the Ru 3d and Cl 2p spectra. Ru 3d and Cl 2p peak splitting were set to 4.2 and 1.6 eV, respectively. Furthermore, peak area ratios were set to 3:2 ($3d^{5/2}$:$3d^{3/2}$) for the Ru 3d peaks and 1:2 ($2p^{3/2}$:$2p^{1/2}$) for the Cl 2p peaks, while the full-width half maximum were constrained to be similar for the two peaks. The Ru 3d and C 1s spectra overlap in binding energy and, thus, were deconvoluted together. Ru doublets were first added given the lower energy of Ru metal and oxides (279-282 eV). By fitting the Ru $3d_{5/2}$ peaks first, the $3d_{3/2}$ peaks were then calculated by applying the above assumptions. After applying the Ru 3d spectra, singlet peaks were added for adventitious carbon species (C-O, and C=O) and, where applicable, a peak for carbidic carbon was added.

Analysis was conducted on the passivated and pretreated Ru/Mo_2C and Ru/SiO_2 catalysts, respectively. Catalysts were pretreated in 15% CH_4/H_2 at 590°C for 4 hours. Following the temperature-programmed pretreatment and cooling to room temperature, the material was transferred without exposure to air into an inert glove box for short-term

208

storage. To transfer these materials to the XPS, the catalyst powders were pelletized by applying ~5000 ft-lb to the powder. Each pellet was then submerged in ~5 mL of isooctane and sealed in a 20 mL vial for transfer. At the XPS, the samples were quickly secured on Cu tape, topped with a meniscus of ~0.5 mL of isooctane, and secured in the XPS sample transfer chamber (STC), followed by immediate evacuation of the STC. Evacuation of the STC removed the remaining isooctane, leaving a dried catalyst pellet, albeit with residual isooctane on the catalyst surface. The chamber was allowed to evacuate down to ~1×10^{-8} torr, upon which the samples were transferred to the sample analysis chamber (SAC).

5.2.2.7. Fischer-Tropsch Synthesis

The Fischer-Tropsch synthesis reaction (described in more detail in Section 4.2.2.6) was performed using a high-pressure, fixed bed, U-shaped, stainless steel reactor. The catalyst bed height was held constant at 15 mm for a bed volume of 0.25 cm^3. Total flow rates were maintained between 20 mL/min and 180 mL/min, or gas hourly space velocities (GHSV) between 4,800 and 43,200 hr^{-1}. Typical reaction conditions consist of between 50-200 mg of catalyst, 25 bar pressure, CO:H$_2$ ratios of 1:2, a temperature regime between 200-250°C, and conversions <10% in order for differential reaction conditions to be applied. The weight of catalyst loaded or the flow rates were adjusted; less catalyst or higher flow rates lower the conversion due to decreased time of interaction between the reactants and the active catalyst. The catalyst samples were diluted with low surface area SiO$_2$ (Alfa Aesar, 99.999%, 125-250 μm, <1 m^2/g) in order to maintain a constant bed height and prevent channeling.

In a typical FTS run, a tightly packed quartz wool plug was placed at the bottom of the U-tube reactor. The desired catalyst loading was then supported on top of the quartz wool bed and low surface area SiO_2 was added to reach a bed height of 15 mm. The catalyst/SiO_2 mixture was mixed to ensure a homogeneous catalyst bed to minimize temperature gradients. The U-tube reactor was installed into the reactor system followed by a pressure check at 25 bar to ensure that no leaks were present. The catalyst was then pretreated in either 15% CH_4/H_2 at 590°C for 4 h or pure H_2 at 450°C for 4 h, depending on the desired experimental design. Following pretreatment, the reactor was cooled to 150°C, where the catalyst was then exposed to N_2 for 15 minutes to purge the surface. The pressure was then increased to 25 bar, the nitrogen flow rate was reduced, and hydrogen was introduced into the system. The temperature was immediately increased at 1°C/min to 240°C. Once 240°C was reached, CO was introduced into the reactor. Given the highly exothermic nature of FTS, the reactor was closely monitored for a half hour in order to maintain the reaction temperature and prevent a runaway reaction. The first GC sample was taken 10 minutes after the introduction of CO (a new sample was injected onto the GC every 45 minutes after the start). The catalysts were allowed to react and deactivate for 12 h at 240°C before the temperatures were randomly varied between 200 and 250°C to obtain the steady-state rates. Each temperature was held for 4 h in order to obtain 5-6 data points for each. The temperature was then returned to 240°C in order to check for further deactivation with time on stream.

5.3. Results

5.3.1 Effect of Particle Size

As stated previously, higher turnover frequencies were observed for larger Ru particles [12-14]. Work in Chapter 4 showed that no X-ray diffraction peaks were observed for Ru in the Ru/Mo$_2$C catalysts (Figure 4.15), indicating that the Ru is highly dispersed or amorphous on the Mo$_2$C. In contrast, large peaks were observed for Ru on SiO$_2$, with crystallite sizes of ~107 nm based on analysis using the Scherrer equation [28]. The differences in FTS catalyst performance between Ru/SiO$_2$ (high TOF and extremely high selectivity to C$_5$+) and Ru/Mo$_2$C (identical performance to Mo$_2$C) can possibly be explained by these differences in dispersion.

To explore the influence of Ru particle size on catalytic performance, a series of catalysts were synthesized aimed at varying particle size. As precise control over particle size was unachievable with current synthesis methods, the Ru loadings were increased in an attempt to generate larger particles. The metal loadings were equivalent to 50, 100, and 150% of a monolayer (ML), assuming 10 sites/nm^2 and 105 m^2/g. At higher metal loadings, diffraction peaks attributable to Ru became increasingly apparent indicating the formation of larger crystallites (Figure 5.1). Using the Scherrer equation, the crystallite sizes for the Ru catalysts increased from immeasurable to a maximum of 181 nm for 150% Ru/Mo$_2$C. Catalyst characterization by ICP-OES indicated reasonable agreement between the expected and actual Ru weight loadings (Table 5.1). Both CO uptake capacity and BET surface area decreased with increasing Ru surface coverage, indicating that the CO chemisorption is likely occurring solely on the Mo$_2$C support and not on Ru given the strong correlation between surface area and CO uptake.
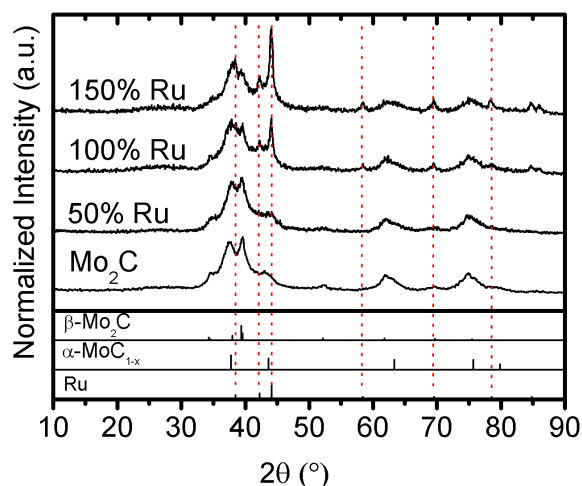
Figure 5.1. X-ray diffraction patterns for the Ru/Mo$_2$C catalysts at different monolayer coverages, assuming 10 sites/nm^2 and 105 m^2/g.

The gravimetric FTS rates and turnover frequencies for these catalysts are found in Figure 5.2. No difference in turnover frequency was found among the catalysts. As such, the difference in gravimetric rate is likely due to changes in the surface area, and hence CO adsorption sites, of the catalyst. Hydrocarbon selectivities are shown in Figure 5.3 for the catalysts studied. Again, no changes in the selectivity relative to bulk Mo$_2$C were observed for the catalysts with increasing Ru content. Based on these results, Ru particle size is not the cause of poor FTS performance for Ru when supported on Mo$_2$C.

Table 5.1. Ru weight loadings (via ICP), CO uptake capacities, and BET surface areas for the Ru/Mo$_2$C catalysts synthesized at different Ru loadings.

Catalysts	Ru wt% (Expected)	Ru wt% (Actual)	Ru Crystallite Size (nm)	CO Uptake Capacity (μmol/g)	BET Surface Area (m^2/g)
Mo$_2$C	-	-	-	410	101
50% Ru/Mo$_2$C	8	8.8	<5	239	69
100% Ru/Mo$_2$C	14.7	12.6	112	212	63
150% Ru/Mo$_2$C	20.6	17	181	201	61
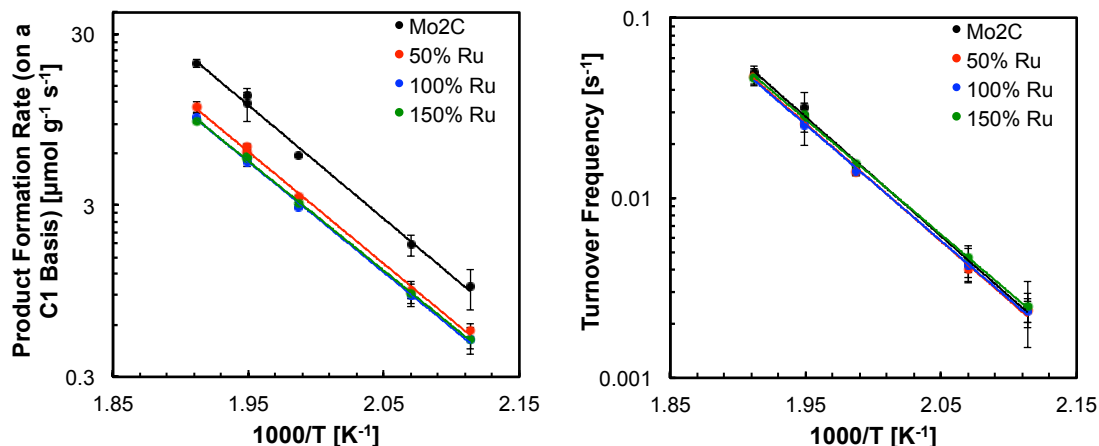
Figure 5.2. Gravimetric rates (left) and turnover frequencies (right) for the Ru-promoted Mo₂C catalysts at different Ru surface coverages.
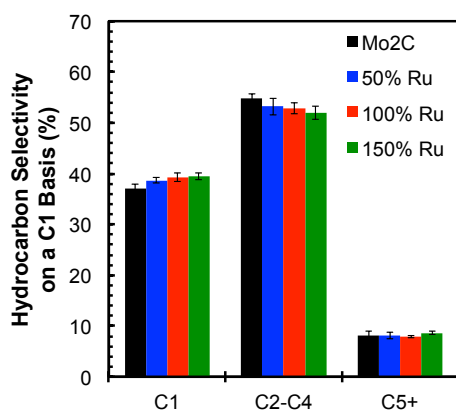
Figure 5.3. Hydrocarbon selectivity for the Ru-based catalysts at different monolayer coverages. Selectivity is reported at 240°C.

5.3.2. Ru Metal Oxidation State/FTS Inhibition via Chloride

Other possible explanations for the observed inactivity include the difference in Ru oxidation state when Ru is supported on Mo₂C vs. SiO₂, and/or the presence of chlorine, a potential catalyst poison, from the Ru precursor (RuCl₃). To test these two hypotheses, X-ray photoelectron spectroscopy was employed to analyze the surface chemistries of passivated and pretreated Ru/Mo₂C and Ru/SiO₂ catalysts. The passivated catalysts were stored in an inert glove box prior to use. The pretreated catalysts were exposed to typical pretreatment conditions (590°C in 15% CH_4/H_2 for 4 hours) in a

vertical reactor identical to those used for Mo_2C synthesis. For details on transferring the samples into the XPS, please refer to Section 5.2.2.6.

The Mo 3d, Ru 3d plus C 1s, O 1s, and Cl 2p spectra and their deconvolution fits are shown in Figure 5.4, Figure 5.5, Figure 5.6, and Figure 5.7, respectively. The deconvoluted Mo 3d spectra (Figure 5.4) of both Ru/Mo_2C catalysts each contained four doublets each. Based on comparisons with literature, the doublets were assigned as follows: Mo $3d_{5/2}$ peak at ~232.2 ± 0.1 eV assigned to MoO_3 (Mo^{6+}) species [29,30,31,32,33]; Mo $3d_{5/2}$ peak at ~230.1 ± 0.1 eV assigned to MoO_2 (Mo^{4+}) [29,30,32,33]; Mo $3d_{5/2}$ peaks at 285.5 assigned to a reduced MoO_2 likely associated with a $Mo^{\delta+}$ where δ exists between 2 and 4 [29,30,32]; and the peaks at 228.1 ± 0.1 eV assigned to a Mo^{2+} species, likely for the Mo in Mo_2C [29,30,32,34]. Pretreatment in 15% CH_4/H_2 resulted in a more reduced catalyst surface, almost entirely removing any Mo^{6+} character. Relative percentages of the elemental species can be found in Table 5.2.

The Ru $3d_{5/2}$ peaks were assigned as follows: 279.9 ± 0.2 eV to metallic Ru [35, 36]; 280.7 ± 0.3 eV to RuO_2 species [35,36]; 282.4 ± 0.2 eV to $RuCl_3$ species [35,36]; ~283.4 ± 0.1 eV are consistent with carbidic carbon associated with Mo_2C [34,29,30,37]; 286.1 ± 0.2 eV as C-O [30,32,33,37]; and 288.8 ± 0.2 eV as C=O [30,32, 33,37] features. Features centered at 284.8 eV are typically assigned to adventitious carbon [32,37] and are used to reference the other binding energies.

The O 1s spectra indicate the presence of four species. Peaks centered at 529.6 eV are consistent with RuO_x species [35,38], peaks at 530.3 ± 0.2 eV have commonly been assigned to Mo oxides (MoO_x) [29,30,32,37], and peaks located at 532.1 ± 0.2 eV are consistent with hydroxyl, carbonyl, and water species (-OH, C=O, H_2O) [29,30,32,37].

O 1s peaks associated with SiO_2 are typically located at 532.8 ± 0.1 eV [39]. Lastly, the Cl 2p species with a $2p_{3/2}$ peak centered at 198.7 ± 0.2 eV are consistent with metal chloride species [35,40].
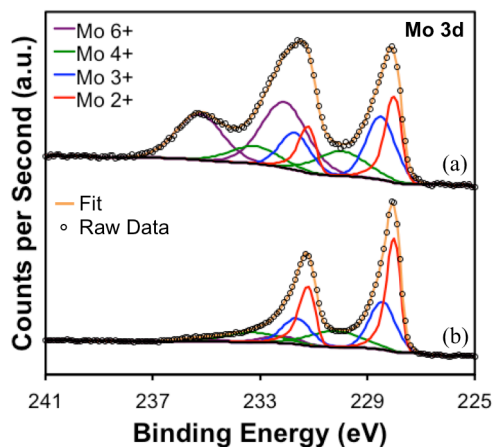
Figure 5.4. Molybdenum 3d spectra for Ru/Mo_2C catalysts that were (a) passivated and (b) pretreated in 15% CH_4/H_2 for 4 hours.
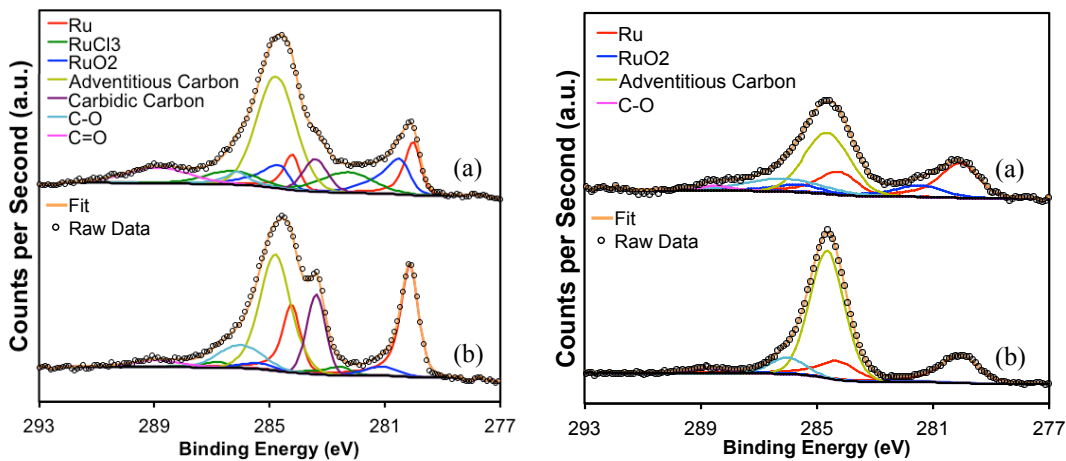
Figure 5.5. Ruthenium 3d and Carbon 1s spectra for Ru/Mo_2C (left) and Ru/SiO_2 (right) catalysts that were (a) passivated and (b) pretreated in 15% CH_4/H_2 for 4 hours.
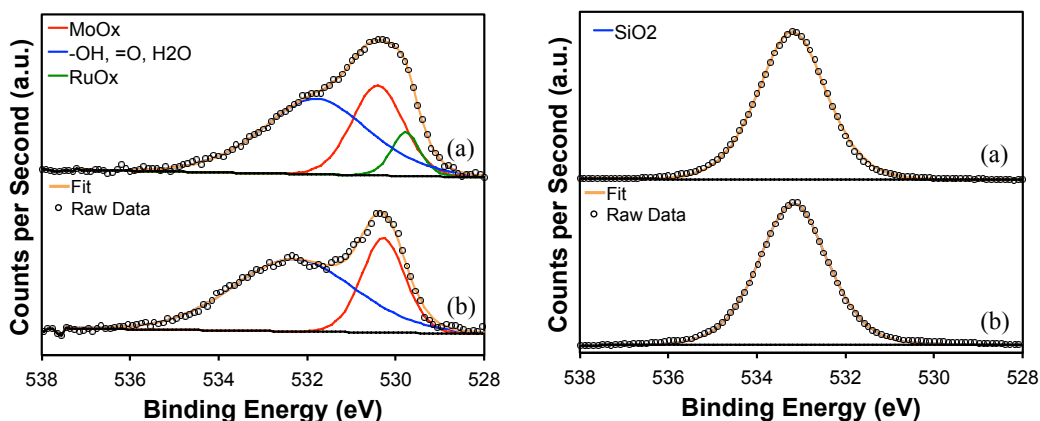
Figure 5.6. Oxygen 1s spectra for Ru/Mo$_2$C (left) and Ru/SiO$_2$ (right) catalysts that were (a) passivated and (b) pretreated in 15% CH$_4$/H$_2$ for 4 hours.
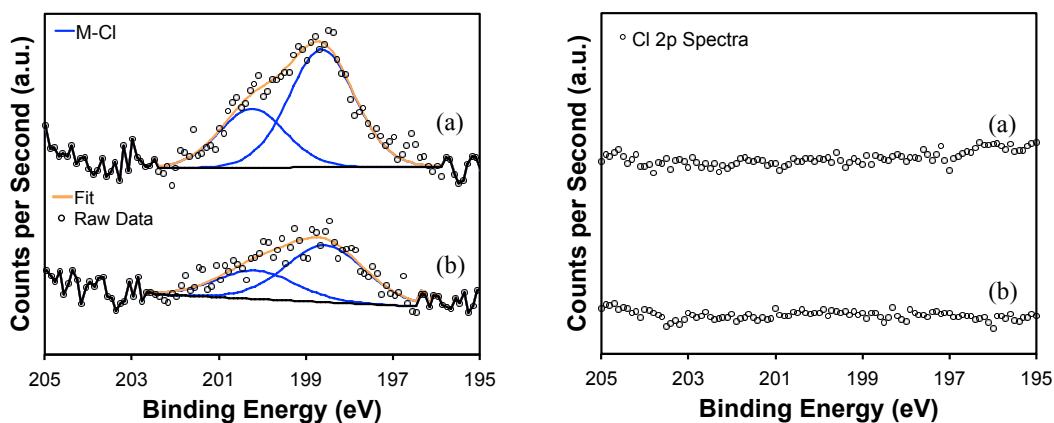
Figure 5.7. Chlorine 2p spectra for Ru/Mo$_2$C (left) and Ru/SiO$_2$ (right) catalysts that were (a) passivated and (b) pretreated in 15% CH$_4$/H$_2$ for 4 hours.

Significant variations in the surface chemistry of the Ru-based catalysts were observed following reduction of the passivated materials in 15% CH$_4$/H$_2$ at 590°C. The Mo species shifted from predominantly oxidized species (40% as MoO$_3$) to a more reduced surface (>70% as Mo$^{\delta+}$ and Mo^{2+}). In the case of the Ru/Mo$_2$C catalyst, the percentage of carbidic carbon increased following reduction. The C/Mo atomic ratio of carbidic carbon to Mo in Mo$_2$C (Mo^{2+}) decreased from 1.97 to 1.09 while the total O/Mo ratio decreased from 3.51 to 1.43. These two results indicate that the surface is transitioning from a predominantly Mo oxide surface to a surface that more closely resembles Mo$_2$C.

Table 5.2. Binding energies and percentages for surface species associated with passivated and pretreated Ru/Mo_2C and Ru/SiO_2 catalysts

Catalyst	Treatment	Mo 3d$_{5/2}$ (eV)[a]			
		Mo^{6+}	Mo^{4+}	Mo$^{\delta+}$	Mo^{2+}
Ru/Mo_2C		232.1 (40%)	230.0 (16%)	228.5 (24%)	228.0 (20%)
Ru/Mo_2C	CH_4/H_2[b]	232.2 (6%)	230.1 (21%)	228.5 (30%)	228.0 (42%)
Ru/SiO_2		--	--	--	--
Ru/SiO_2	CH_4/H_2[b]	--	--	--	--

Catalyst	Treatment	Ru 3d$_{5/2}$ (eV)[a]		
		Ru^{0}	RuO$_2$	RuCl$_3$
Ru/Mo_2C		279.9 (32%)	280.7 (34%)	282.2 (34%)
Ru/Mo_2C	CH_4/H_2[b]	280.1 (81%)	281.0 (10%)	282.4 (9%)
Ru/SiO_2		280.0 (67%)	280.9 (21%)	281.5 (12%)
Ru/SiO_2	CH_4/H_2[b]	280.0 (91%)	--	282.1 (9%)

Catalyst	Treatment	C 1s (eV)[a]			
		Carbidic	Adventitious	C-O	C=O
Ru/Mo_2C		283.4 (12%)	284.8 (66%)	286.1 (7%)	288.8 (15%)
Ru/Mo_2C	CH_4/H_2[b]	283.4 (23%)	284.8 (57%)	286.0 (15%)	288.9 (5%)
Ru/SiO_2		--	284.8 (75%)	286.2 (8%)	288.6 (17%)
Ru/SiO_2	CH_4/H_2[b]	--	284.8 (74%)	286.0 (20%)	288.8 (6%)

Catalyst	Treatment	O 1s (eV)[a]			
		RuO$_x$	MoO$_x$	-OH, =O, H$_2$O	SiO$_2$
Ru/Mo_2C		529.6 (9%)	530.4 (33%)	531.9 (58%)	-
Ru/Mo_2C	CH_4/H_2[b]	--	530.3 (32%)	532.2 (68%)	-
Ru/SiO_2		--	--	--	533.2 (100%)
Ru/SiO_2	CH_4/H_2[b]	--	--	--	533.2 (100%)

Catalyst	Treatment	Cl 2p$_{3/2}$ (eV)[a]
		RuCl$_3$
Ru/Mo_2C		198.7 (100%)
Ru/Mo_2C	CH_4/H_2[b]	198.5 (100%)
Ru/SiO_2		--
Ru/SiO_2	CH_4/H_2[b]	--

[a] The first number listed represents the binding energy of the peak following deconvolution. The number in parentheses represents the atomic percentage of the species relative to other species of the same element.
[b] Pretreatment of the catalysts occurred at 590°C in 200 mL/min 15% CH_4/H_2 for 4 hours with 1.5 hour heating and cooling ramps.

More importantly, reduction resulted in the transition from slightly oxidized Ru to predominantly metallic Ru on both Mo_2C and SiO_2 supports. Roughly 81% and 91% of the Ru was Ru^0 following pretreatment for Ru/Mo_2C and Ru/SiO_2, respectively. These similar results indicate that the Ru oxidation state is not the likely cause for the inactivity.

Chlorine 2p analysis (Figure 5.7, left) on the passivated and pretreated Ru/Mo_2C and Ru/SiO_2 catalysts showed the presence of Cl in the Mo_2C catalysts but not in the SiO_2 catalysts. While the Cl:Mo ratio decreased from 0.17 to 0.06 following pretreatment of Ru/Mo_2C, chlorine still adhered to the surface. Surface chlorine is typically regarded as an inhibitor in FTS. As chloride content increases, CO conversions have been reported to decrease [19,20]. There have also been reports of chlorine inhibition during wet impregnation syntheses using carbides and nitrides. The adsorption of nitrate metal salts onto Mo_2C was rapid while chlorides resulted in negligible adsorption [27]. These results indicate that chlorine may be influencing the performance of the Mo_2C catalysts.

Two conclusions can be drawn from this surface analysis. First, the oxidation state of Ru is relatively consistent between supports, and thus, not the cause of Ru inactivity. Second, chloride is present on the surface of the Ru/Mo_2C catalysts, but not on the Ru/SiO_2 catalysts.

To test the effect of chlorine, a Ru/Mo_2C catalyst was synthesized by dry impregnating Mo_2C with $Ru(acac)_3$. However, $Ru(acac)_3$ is relatively insoluble in water. In order to dissolve $Ru(acac)_3$ at reasonably high concentrations, water was replaced with 1,3-dioxolane (referred to herein as DO) as the dry impregnation solvent. However, 0.9M were the highest concentrations that could be achieved, while 4.5M was required to match the Ru loading of 50% of a monolayer. Therefore, five sequential impregnations

were conducted using the Ru(acac)$_3$/DO solution to obtain the desired Ru weight loading. Mo$_2$C was also similarly dry impregnated with metal-free DO five sequential times to ensure any differences observed during FTS were not due to the solvent used.

X-ray diffraction patterns for the synthesized catalysts are shown in Figure 5.8 (left image). Small Ru diffraction peaks were discernable for only the catalyst produced using Ru(acac)$_3$. The measured Ru loading via ICP was slightly lower for the Ru(acac)$_3$ catalyst likely due to the loss of some of the Ru(acac)$_3$ during the H$_2$ reduction step (red material in Figure 5.8, right image). This is likely due to the volatization of Ru(acac)$_3$ from the catalyst at high temperatures, followed by condensation of the gaseous complex on the walls of the reactor where it exits the furnace insulation.
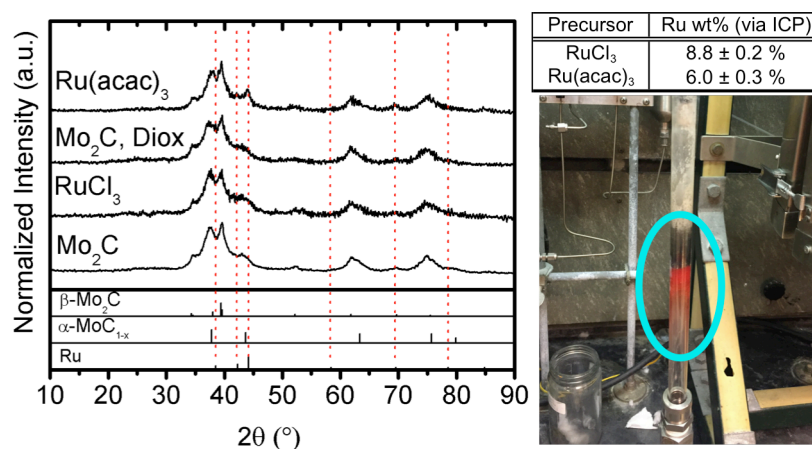
Figure 5.8. (Left) X-ray diffraction patterns for the Mo$_2$C-based catalysts. The nominal surface coverages of the catalysts were 50% of a monolayer for the Ru-promoted catalysts. (Right) Ru weight loadings for the Ru/Mo$_2$C catalysts depending on the precursor used. Image in bottom right shows the loss of Ru(acac)$_3$ from the catalyst bed during reduction (red powder).

CO uptakes and BET surface areas for the catalysts are shown in Table 5.3. As observed previously, Ru addition decreases both the BET surface area and CO uptake capacity of the catalysts. Differences in the extent of reduction in CO uptake may simply be due to differences in the Ru weight loading (Figure 5.8). Treatment of Mo$_2$C with DO

resulted in a ~10% decrease in both surface area and CO uptake, similar to that observed

after H_2O treatment of Mo_2C.

Table 5.3. BET surface areas and CO uptakes for the $RuCl_3$ and $Ru(acac)_3$-based Ru/Mo_2C catalysts as well as bulk and DO-treated Mo_2C

Catalyst	BET Surface Area $(m^2/g)^a$	CO Uptake Capacity $(\mu mol/g_{cat})^b$
Mo_2C	101	410
Ru/Mo_2C, $RuCl_3$	66	239
Mo_2C, DO	91	367
Ru/Mo_2C, $Ru(acac)_3$	74	295

[a] BET surface areas were calculated from a N_2 physisorption isotherm
[b] CO uptake capacity calculated via pulse chemisorption of a 5% CO/He mixture over the catalyst at 35°C following pretreatment in 15% CH_4/H_2 at 590°C for 4 h.

Gravimetric FTS rates and turnover frequencies are shown in Figure 5.9. The activity trend decreases as follows: Mo_2C > DO-treated Mo_2C > Ru/Mo_2C from $Ru(acac)_3$ > Ru/Mo_2C from $RuCl_3$. However, the rates were again indifferent when normalized to CO uptake capacity indicating that Ru remains inactive regardless of the metal precursor used. Instead the activity remains dominated by the Mo_2C surface available for reaction, as probed by CO uptake. Further, the hydrocarbon selectivities show no differences for the four catalysts studied (Figure 5.10). It is evident that for these Ru/Mo_2C systems, the Mo_2C still dominates the activity under the conditions studied.
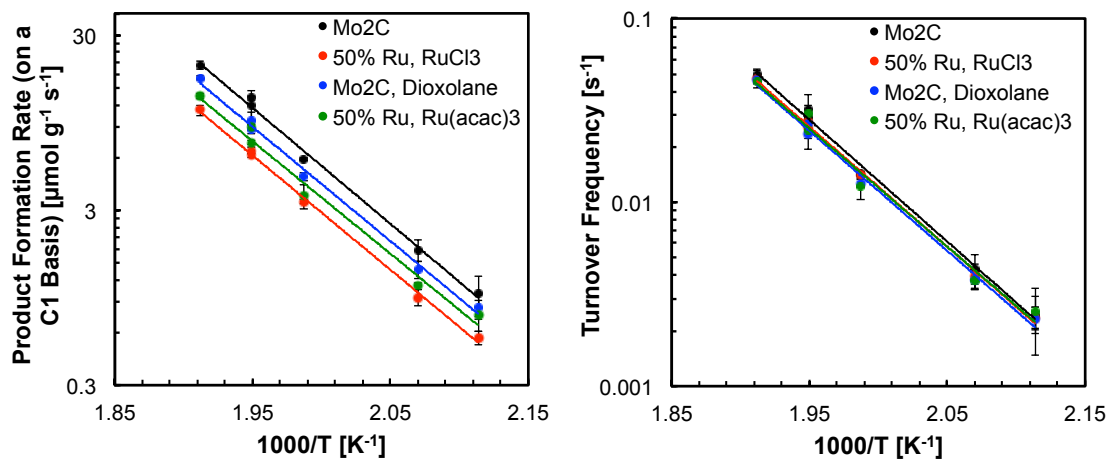
Figure 5.9. Gravimetric rates (left) and turnover frequencies (right) for the Ru-promoted Mo_2C catalysts using $RuCl_3$ or $Ru(acac)_3$.
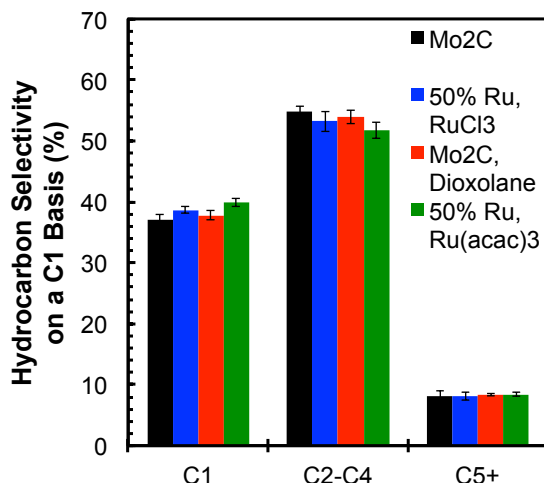
Figure 5.10. Hydrocarbon selectivities for the Ru-promoted Mo_2C catalysts using $RuCl_3$ or $Ru(acac)_3$. Data collected at 240°C.

5.3.3. Effect of Pretreatment Temperature on FTS Performance for Mo_2C-supported Ru and Co Catalysts

While strong metal-support interactions typically enhance catalyst performance, the interactions between Ru and Mo_2C may have the effect of deactivating the Ru. The possibility exists that high temperatures may facilitate a chemical or physical interaction between Ru and Mo_2C. High temperature reductions are used on two occasions in the process of synthesizing and evaluating the Ru/Mo_2C catalysts (Figure 5.11). After dry impregnation, the $RuCl_3/Mo_2C$ is subjected to H_2 at 450°C for 4 hours in an attempt to reduce the metal and remove/decompose the anion from the metal salt. In addition, prior to evaluation for FTS, the passivated catalyst is pretreated in 15% CH_4/H_2 at 590°C for 4 hours to recarburize the Mo_2C and reduce the metal promoter. Both of these reduction steps have the potential to facilitate an interaction between Mo_2C and Ru, resulting in Ru deactivation. To test this hypothesis, experiments were designed to limit the catalyst exposure during reduction and pretreatment to lower temperatures in H_2 by removing the high temperature steps (in green text in Figure 5.11) and replacing them with a single, low temperature pretreatment immediately prior to reactivity testing.

221
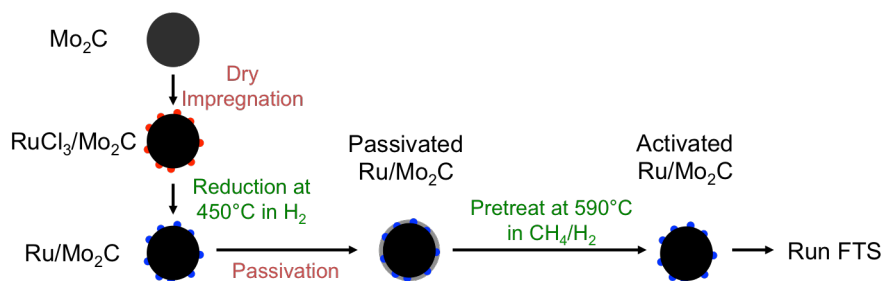
Figure 5.11. Process diagram detailing the steps for synthesizing and evaluating Ru/Mo$_2$C Fischer-Tropsch synthesis catalysts. High temperature reduction steps are highlighted in green text.

RuCl$_3$/Mo$_2$C and RuCl$_3$/SiO$_2$ catalysts were again synthesized by dry impregnating SiO$_2$ or unpassivated Mo$_2$C with RuCl$_3$ at loadings consistent with 50% monolayer coverage. Instead of reducing the catalyst in H$_2$ prior to passivation, each catalyst was only passivated, resulting in a catalyst containing RuCl$_3$ species as opposed to metallic Ru (the resulting catalyst is referred to as RuCl$_3$/Mo$_2$C or RuCl$_3$/SiO$_2$). X-ray diffraction patterns for the SiO$_2$ and Mo$_2$C-supported RuCl$_3$ catalysts are compared to the reduced Ru/Mo$_2$C and Ru/SiO$_2$ catalysts studied previously (Figure 5.12). No noticeable differences are observed for the Mo$_2$C-based catalysts. No peaks associated with Ru are observed for RuCl$_3$/SiO$_2$. The broad peak at ~35° 2θ potentially corresponds to RuCl$_3$,
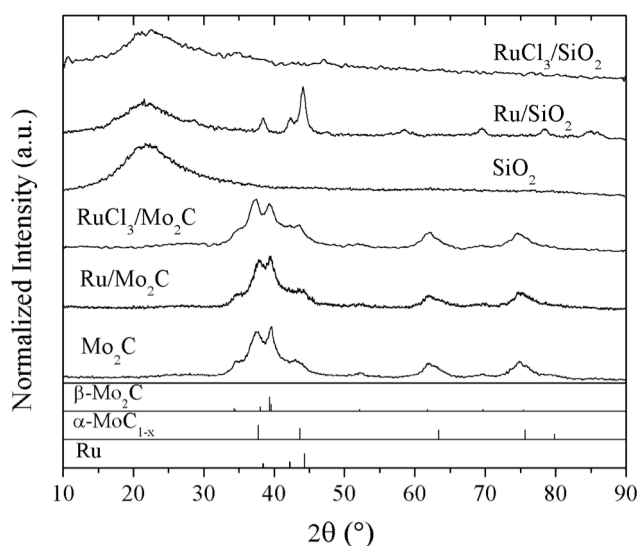
Figure 5.12. X-ray diffraction patterns for the supported RuCl$_3$ and Ru based catalysts.

222

though it is of low intensity. It is likely that the large crystallite size of the Ru species in the Ru/SiO$_2$ catalysts are due to sintering during the high-temperature reduction.

The RuCl$_3$/Mo$_2$C and RuCl$_3$/SiO$_2$ catalysts were then pretreated at more moderate temperatures in order to reduce Ru while limiting the interaction of Ru with Mo$_2$C. To determine a viable reduction temperature, H$_2$-TPRs were conducted on RuCl$_3$/Mo$_2$C and RuCl$_3$/SiO$_2$ (Figure 5.13). RuCl$_3$/SiO$_2$ exhibits one reduction peak around 110°C. Reduction peaks for RuCl$_3$/Mo$_2$C are observed around 90°C and 190°C, perhaps due to reduction of RuCl$_3$ to Ru and the Mo$_2$C passivation layer, respectively. As a result of this analysis, three pretreatment conditions were selected to analyze the effect of reduction temperature on the RuCl$_3$-Mo$_2$C system: (1) H$_2$ at 150°C, (2) H$_2$ at 300°C, and (3) CH$_4$/H$_2$ at 590°C. These conditions represent reduction of the first H$_2$ consumption peak in the RuCl$_3$/Mo$_2$C spectrum, reduction of the first and second H$_2$ consumption peak in the RuCl$_3$/Mo$_2$C spectrum, and the typical pretreatment conditions used for Mo$_2$C, respectively. The last condition will allow for connection to previous work.
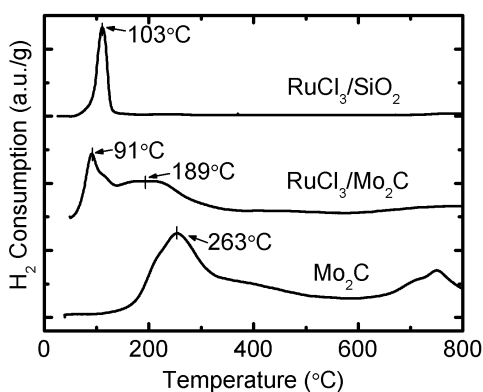
Figure 5.13. Hydrogen temperature-programmed reductions for the RuCl$_3$-based catalysts. Heating rates were set to 20°C/min.

The BET surface areas and CO uptake capacities of the three materials following each of the three pretreatment conditions are shown in Table 5.4. Of note, the BET surface area of the RuCl$_3$/Mo$_2$C catalyst was close to that of bulk Mo$_2$C, in contrast to

that of Ru/Mo$_2$C, which decreased to 68 m^2/g as shown previously (Table 4.4, Section 4.3.2). For all of the Mo$_2$C-based catalysts, CO uptakes increased with increasing reduction temperature. The CO uptake of RuCl$_3$/Mo$_2$C was consistently ~50% the uptake of bare Mo$_2$C for each pretreatment studied. Conversely, the CO uptakes remained approximately constant for the RuCl$_3$/SiO$_2$ catalysts, perhaps with a small decreasing trend with increasing pretreatment temperature.

Table 5.4. BET surface areas and CO uptakes for Mo$_2$C and the RuCl$_3$-based catalysts pretreated at 3 different conditions.

Catalyst	Pretreatment Conditions	BET Surface Area (m^2/g)[1]	CO Uptake Capacity (μmol/g$_{cat}$)[2]
Mo$_2$C	150°C in H$_2$	104	105
	300°C in H$_2$		197
	590°C in CH$_4$/H$_2$		410
RuCl$_3$/Mo$_2$C	150°C in H$_2$	110	46
	300°C in H$_2$		136
	590°C in CH$_4$/H$_2$		221.4
RuCl$_3$/SiO$_2$	150°C in H$_2$	103	59
	300°C in H$_2$		49
	590°C in CH$_4$/H$_2$		47

[1] BET surface areas were calculated from a N$_2$ physisorption isotherm on the materials before any pretreatments
[2] CO uptake capacity was calculated via pulse chemisorption of a 5% CO/He mixture over the catalyst at 35°C following pretreatment in 15% CH$_4$/H$_2$ at 590°C for 4 h.

Gravimetric FTS rates and turnover frequencies are shown for the Mo$_2$C (Figure 5.14), RuCl$_3$/Mo$_2$C (Figure 5.15), and RuCl$_3$/SiO$_2$ (Figure 5.16) catalysts. Low reduction temperatures (150°C) yielded lower gravimetric rates for Mo$_2$C compared to the typical 590°C reduction, though TOFs were equivalent; the difference in gravimetric rates is likely due to varying degrees of surface reduction. These results indicate that, the pretreatment conditions play a role in performance for Mo$_2$C as it relates to gravimetric rates, but not TOF. Conversely, for the RuCl$_3$/SiO$_2$ and RuCl$_3$/Mo$_2$C catalysts, the highest and lowest rates were achieved following pretreatment at 150°C and 590°C, respectively.

RuCl$_3$/SiO$_2$ exhibited relatively minor increases in both gravimetric rate and TOF with decreasing pretreatment temperature. The differences in gravimetric rate were likely due to sintering and loss of Ru surface area. On the other hand, gravimetric rates for RuCl$_3$/Mo$_2$C following the different pretreatments were roughly four times higher
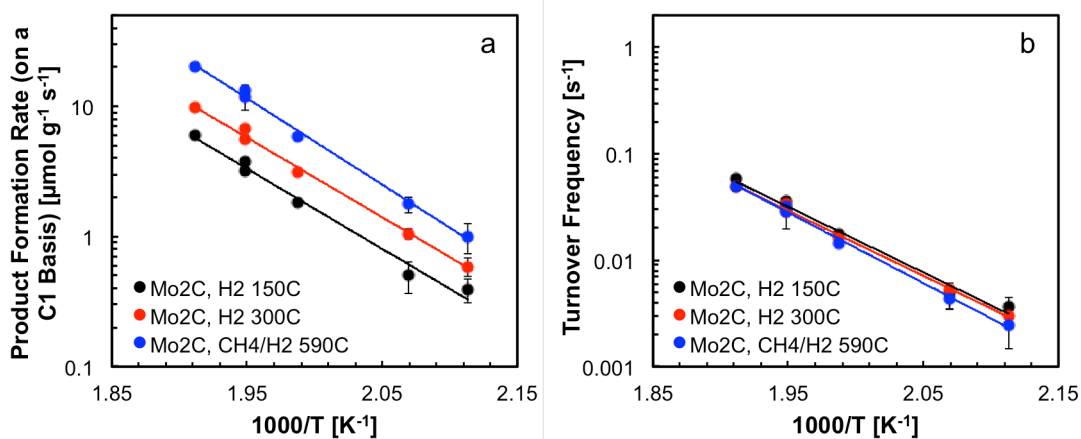
Figure 5.14. (a) Gravimetric and (b) CO-normalized (turnover frequency) FTS rates for Mo$_2$C following the three different pretreatments.
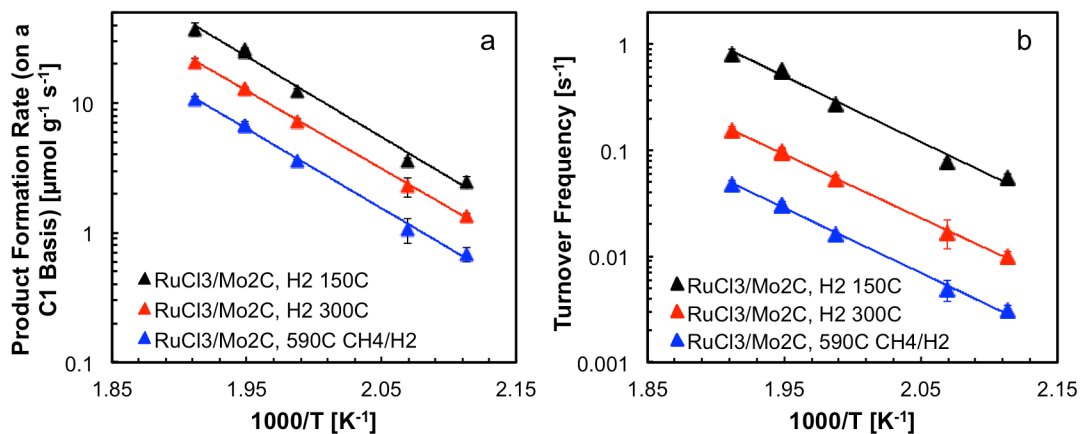
Figure 5.15. (a) Gravimetric and (b) CO-normalized (turnover frequency) FTS rates for RuCl$_3$/Mo$_2$C following the three different pretreatments.
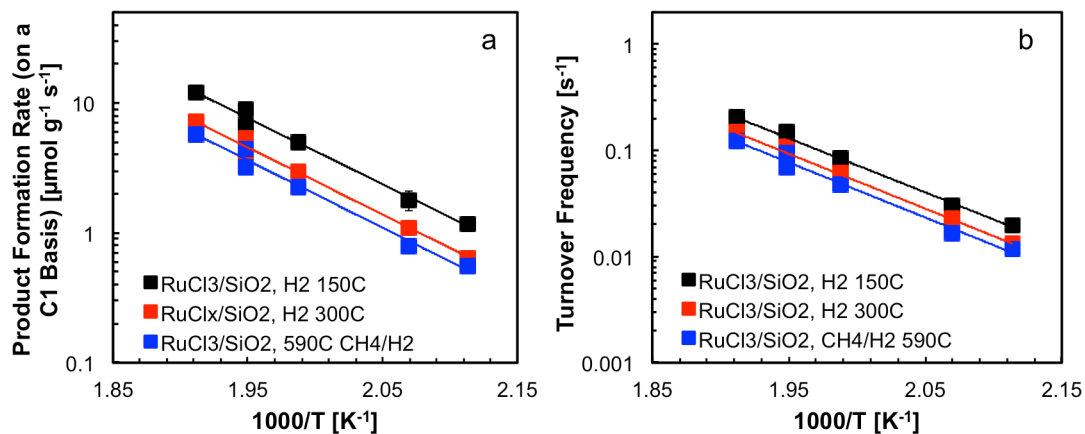
Figure 5.16. (a) Gravimetric and (b) CO-normalized (turnover frequency) FTS rates for RuCl$_3$/SiO$_2$ following the three different pretreatments.

Table 5.5. Gravimetric rates and turnover frequencies for Mo$_2$C, RuCl$_3$/Mo$_2$C, and RuCl$_3$/SiO$_2$ catalysts following 3 pretreatment conditions. Apparent activation energies are also listed for each catalysts and condition.

Catalyst	Pretreatment Conditions	Gravimetric Rate (μmol/g/s)[a]	Turnover Frequency (1/s)[a]	E$_{a, Apparent}$ (kJ/mol)
	150°C in H$_2$	3.74	0.036	118 ± 8
Mo$_2$C	300°C in H$_2$	6.68	0.034	115 ± 2
	590°C in CH$_4$/H$_2$	13.17	0.032	127 ± 5
	150°C in H$_2$	25.11	0.551	119 ± 7
RuCl$_3$/Mo$_2$C	300°C in H$_2$	13.01	0.096	117 ± 4
	590°C in CH$_4$/H$_2$	6.71	0.030	117 ± 4
	150°C in H$_2$	8.92	0.151	98 ± 6
RuCl$_3$/SiO$_2$	300°C in H$_2$	5.35	0.109	99 ± 6
	590°C in CH$_4$/H$_2$	4.42	0.094	99 ± 7

[a] Calculated at 240°C

following 150°C reduction than 590°C reduction. This difference became more pronounced when comparing the TOFs of the catalyst; RuCl$_3$/Mo$_2$C exhibited ~18 times higher TOF following 150°C reduction relative to the 590°C reduction (shown numerically in Table 5.5). The performance of this catalyst following 300°C reduction was in between the results for the two other conditions. Of particular note, the TOF for the RuCl$_3$/Mo$_2$C catalyst following pretreatment at 590°C resembles that of bare Mo$_2$C

following similar pretreatment. The different pretreatments failed to generate significant changes in the activation energies of the catalysts (Table 5.5), indicating that the pretreatment conditions do not alter the energetics of the rate-limiting step. The SiO_2-based catalysts exhibited lower activation energies than the Mo_2C-based catalysts.

The different pretreatments did not appear to have a drastic effect on hydrocarbon selectivity for the catalysts with the exception of $RuCl_3/Mo_2C$ (Figure 5.17). Mo_2C produced less CH_4 and more C_2-C_4 and C_{5+} production as the pretreatment temperature was increased from 150°C to 590°C. Conversely, $RuCl_3/SiO_2$ exhibited the lowest CH_4 and highest C_{2+} production at lower reduction temperatures. Of more interest, $RuCl_3/Mo_2C$ exhibited higher C_{5+} selectivity (by a factor of ~2) following 150°C (18.8%) compared to 590°C (8.7%) reduction. $RuCl_3/Mo_2C$ performed similarly to the Mo_2C following pretreatment in 15% CH_4/H_2 at 590°C, confirming that Ru is inactive in Ru/Mo_2C after high temperature pretreatments, as also observed in earlier experiments. However, the C_{5+} product selectivity gained for $RuCl_3/Mo_2C$ pretreated at 150°C was accompanied by a decrease in only the C_2-C_4 selectivity as the CH_4 selectivity remained similar to that for bulk Mo_2C. These 150°C results indicate a strong deviation from the Anderson-Schultz-Flory distribution. No substantial shifts in total product type selectivity were observed for each catalyst at the three different pretreatment conditions (Figure 5.18). However, across the three catalysts, two general trends were observed. Alcohol selectivity decreased in the following order: $RuCl_3/Mo_2C$ > Mo_2C > Ru/SiO_2. CO_2 selectivity decreased as: Mo_2C > $RuCl_3/Mo_2C$ > $RuCl_3/SiO_2$. While the CO_2 selectivity results might be expected as Ru is not known to be a good water-gas shift catalyst, the

results observed for alcohol selectivity suggest synergy between Ru and Mo_2C and that

new or modified sites have been generated that enhance the production of alcohols.
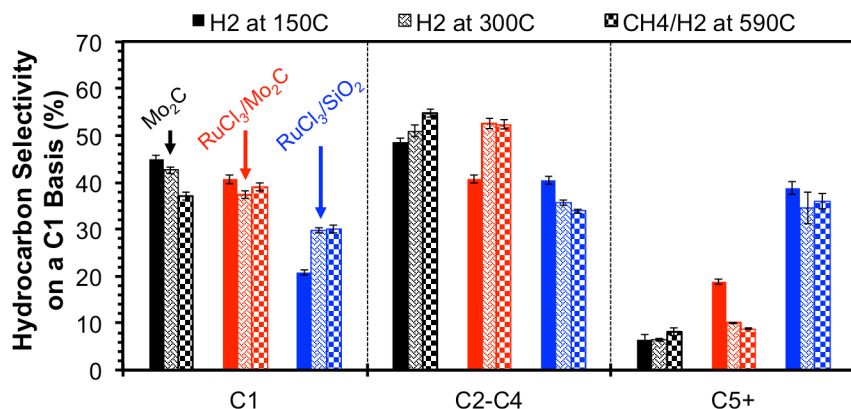
Figure 5.17. FTS hydrocarbon selectivities on a C1 basis for the Mo_2C, $RuCl_3/Mo_2C$, and $RuCl_3/SiO_2$ catalysts following the three pretreatment cases. Hydrocarbon selectivities calculated at 240°C.
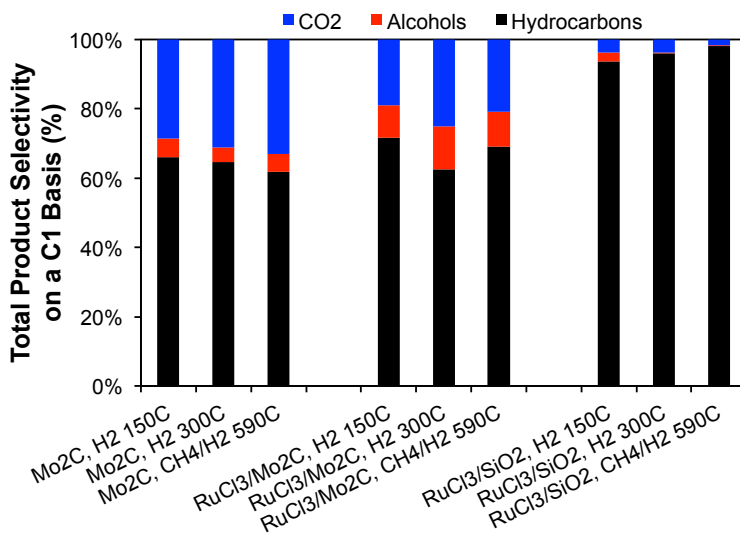
Figure 18. Total FTS product selectivities for the Mo_2C, $RuCl_3/Mo_2C$, and $RuCl_3/SiO_2$ catalysts following the three pretreatment cases. Selectivities calculated at 240°C.

The above results suggest that high temperature reductions instigate the

deactivation of Ru in the Ru/Mo_2C system as the reactivity and selectivity of Ru/Mo_2C

catalysts are highly dependent on reduction pretreatments. By reducing the $RuCl_3/Mo_2C$

catalysts at 150°C reduction in H_2, higher rates and C_{5+} selectivities were observed

relative to those for bare Mo_2C. These results suggest that it may be beneficial to retain

parts of the oxide passivation layer on the Mo_2C surface in order to retain Ru activity. Furthermore, given that the $RuCl_3/Mo_2C$ catalyst exhibited the highest gravimetric and TOF of all catalyst studied, far exceeding the additive performance of Ru and Mo_2C separately, it is possible that a synergistic effect is observed with Ru and Mo_2C. This possibility will be explored in the Discussion section.

Given the similar inactivity observed for Co supported on Mo_2C, this analysis was extended to the Co-Mo_2C system. Similarly, unpassivated Mo_2C was dry impregnated with $Co(NO_3)_2$ and passivated (no reduction) to afford the unreduced $Co(NO_3)_2/Mo_2C$ catalyst. H_2-TPRs were performed on $Co(NO_3)_2/Mo_2C$ and $Co(NO_3)_2/SiO_2$ to inform the pretreatment conditions to be used (Figure 5.19). The $Co(NO_3)_2/Mo_2C$ spectrum exhibited only one H_2 consumption peak, presumably for reduction of both $Co(NO_3)_2$ and the passivation layer. This peak exists at the same reduction temperature as that of the passivation layer for bare Mo_2C. The $Co(NO_3)_2/SiO_2$ spectrum contains a dominant reduction peak at ~190°C with a shoulder at ~220°C. Based on the H_2-TPR , pretreatment conditions were chosen: (1) 200°C in H_2, (2) 300°C in H_2, and (3) 590°C in CH_4/H_2.
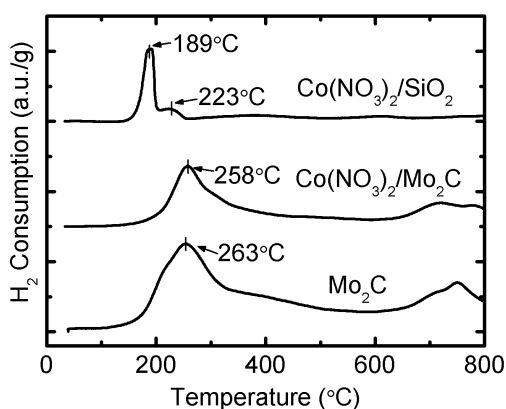
Figure 5.19. Hydrogen temperature-programmed reduction of the $Co(NO_3)_2$-based catalysts. Heating rates were set to 20°C/min.

Fischer-Tropsch synthesis was performed over 3 catalysts (Mo_2C, $Co(NO_3)_2/$ Mo_2C, $Co(NO_3)_2/SiO_2$) following pretreatment at each of the three different conditions.

Gravimetric rates increased for both Mo_2C and $Co(NO_3)_2/SiO_2$ with increasing pretreatment temperature (not shown). It is possible that higher pretreatment temperatures for $Co(NO_3)_2/SiO_2$ led to further reduction of the Co species towards metallic Co. It is well known in the literature that Co is a difficult metal to completely reduce [41], and promoters are commonly added to aid in the reduction [41,42]. While H_2-TPR spectra suggested that $Co(NO_3)_2$ is reduced near 200°C, it is not known whether this reduction forms metallic Co or a Co oxide (i.e. CoO). Further, there were broad peaks in the H_2-TPR at higher temperatures (~400 and 600°C). Co oxides have been reported to reduce around 350-400°C [41].

The $Co(NO_3)_2/Mo_2C$ catalysts that were pretreated at low temperatures (i.e., 200 and 300°C) exhibited improved FTS performance relative to Mo_2C. Pretreatment of both $Co(NO_3)_2/Mo_2C$ and Mo_2C catalysts at 590°C resulted in the same reactivity. A maximum gravimetric rate was obtained following pretreatment at 300°C and gravimetric rates following pretreatment at 200°C and 590°C were similar. This difference between the Co and Ru results was likely due to the temperatures required to reduce the deposited metal in the two systems (~260°C for Co versus ~100°C for Ru). Results from the Ru/Mo_2C studies suggest that high temperatures cause metal-support interactions for Metal-Mo_2C systems. As Co requires higher reduction temperatures to form the active Co FTS phase, there is likely a trade-off between activation of Co via formation of the metallic phase and deactivation of Co via high-temperature interaction with Mo_2C. This trade-off likely results in the observed lower enhancement and the maximum in performance observed at moderate reduction temperatures. Hydrocarbon (Figure 5.20) and total product selectivities (Figure 5.21) were relatively unaffected by pretreatment

conditions for all of the Co catalysts studied. It is evident that lower pretreatment temperatures have a lesser effect on the Co/Mo$_2$C system than in the Ru/Mo$_2$C system.
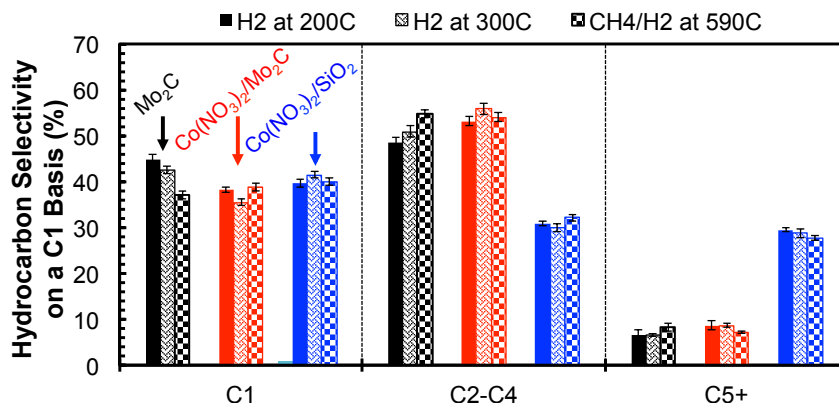
Figure 5.20. FTS hydrocarbon selectivities on a C1 basis for the Co(NO$_3$)$_2$-based catalysts following the three pretreatment cases. Selectivities were calculated at 240°C.
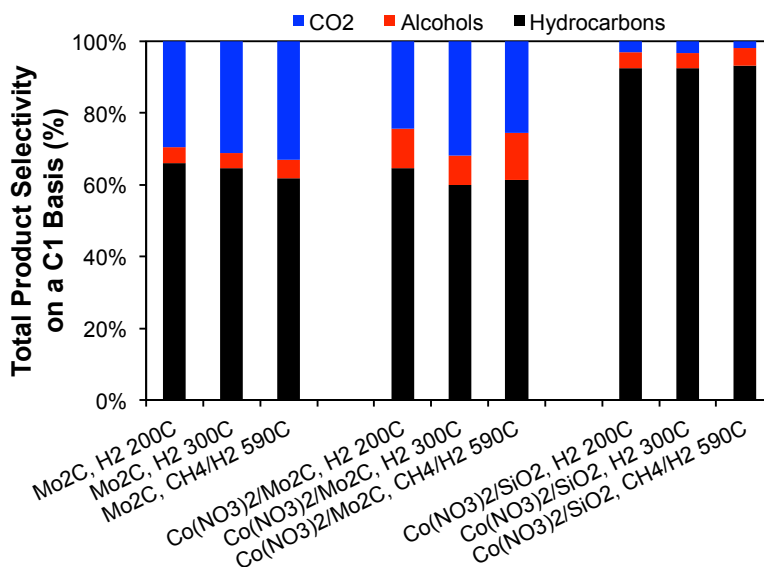
Figure 5.21. Total FTS product selectivities for the Co(NO$_3$)$_2$-based catalysts following the three pretreatment cases. Selectivities calculated at 240°C.

5.4. Discussion

In this chapter, experiments were conducted to further understand the Fischer-Tropsch synthesis performance of Ru/Mo$_2$C and Co/Mo$_2$C catalysts reported previously in Chapter 4. Ru and Co are known to be highly active metals for FTS [2,3], so the inactivity of or lack of enhancement from these metals when supported on Mo$_2$C was

unexpected. Numerous potential deactivation factors were explored for the Ru/Mo_2C system including particle size, pretreatment gas, Ru oxidation state, and the effect of residual chloride. To ensure the formation of larger particles of Ru, the weight loading was increased from ~8 wt% to ~20 wt% Ru (150% of a monolayer). Surprisingly, even at 20 wt% Ru, no enhancement in rate or C_{5+} selectivity was observed. The rates were not different from those for Mo_2C following normalization to the number of CO sites, indicating that the activity of the catalyst was solely due to active sites on the Mo_2C surface, not Ru. X-ray photoelectron spectroscopy of the pretreated Ru/Mo_2C and Ru/SiO_2 catalysts indicated that the Ru was in a similar oxidation state (~90% Ru^0) for both catalysts, but also suggested the presence of residual chlorine on the Mo_2C catalyst, which was absent on the SiO_2 catalyst. However, replacing the $RuCl_3$ precursor with $Ru(acac)_3$ had no impact on the performance of the Ru/Mo_2C catalyst for FTS. These collective results indicate that particle size, Ru oxidation state or chloride poisoning were not the cause of the observed Ru inactivity.

As these factors still failed to explain the inactivity of Ru supported on Mo_2C, the problem was approached from a different perspective. Typical heterogeneous catalysts are synthesized via dry impregnation of an inactive support, such as silica or alumina, followed by oxidation in air to form an oxide species (i.e., Fe_3O_4, RuO_2, or CoO). These syntheses generate a catalyst consisting of a metal oxide (of the active metal) supported on an inactive oxide support [41,43], which is then pretreated immediately prior to use in a reaction in order to reduce the metal oxide to the metallic phase. Pretreatment temperatures are typically selected based on the H_2 temperature-programmed reduction

spectra of the supported metal oxide catalyst, specifically the reduction of the active phase [41,43]. This common practice was extended to the Ru-Mo_2C system.

Synthesized RuCl$_3$/Mo_2C pretreated at low temperatures (150°C) exhibited some Ru-like performance, as its FTS activity and C_{5+} selectivity exceeded those of Mo_2C. Gravimetric rates and C_{5+} selectivities for RuCl$_3$/Mo_2C following 150°C reduction were both two times higher than those following 590°C reduction. The activity and selectivity of RuCl$_3$/Mo_2C following pretreatment at 590°C resembled that of bare Mo_2C. Therefore, as the temperature was increased from 150°C to 590°C, the activity for FTS of Ru supported on Mo_2C declined. Conversely, the RuCl$_3$/SiO_2 catalysts retained activity and selectivity when the pretreatment temperature was increased from 150°C to 590°C.

A few possible deactivation routes for Ru on Mo_2C at high temperatures are illustrated in Figure 5.22. One hypothesis is that Mo_2C or $Mo_xC_yO_z$ species are mobile at high temperature and these species cover or coat the Ru nanoparticles, thereby reducing the exposed Ru surface area to negligible levels. While this is difficult to prove experimentally, some theoretical and experimental support exists for this explanation. Surface free energies can be used to rationalize the covering of Ru by Mo species. It may also be possible for Ru to dissolve into the Mo_2C particles. Ru surface free energies have been reported to be 3.409 [44] and 3.231 J/m^2 [45], while Mo surface free energies have been reported as 2.877 [44] and 2.752 J/m^2 [45]. These values suggest that it is energetically favorable for Mo to cover Ru as the free energy of Mo is less than that of Ru. BET surface areas determined for Mo_2C, RuCl$_3$/Mo_2C, and Ru/Mo_2C (103, 110, and 69 m^2/g, respectively) help to corroborate the mobility of Mo_2C or $Mo_xC_yO_z$. These results indicate that loss of surface area only occurs following reduction at high

233

temperatures (i.e., 450°C). Notably, no loss of surface area was observed between RuCl$_3$/SiO$_2$ and Ru/SiO$_2$.
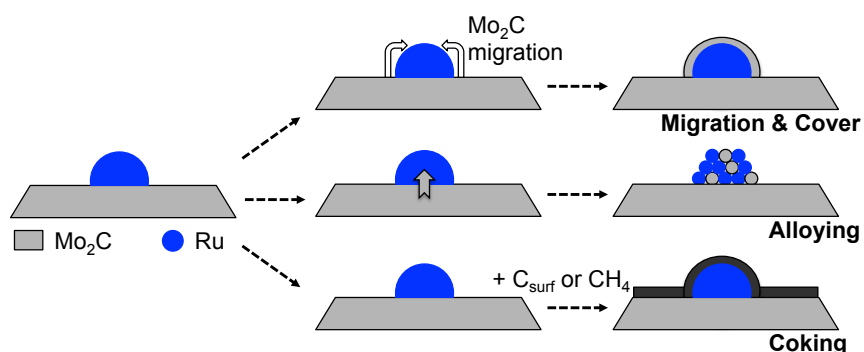
Figure 5.22. Schematic detailing possible deactivation routes for Ru when RuCl$_3$/Mo$_2$C is exposed to high temperature reductions.

The other potential deactivation mechanisms (Figure 5.22) are less likely. Coking/carbon deposition does not appear to be the deactivation mechanism of Ru as Ru/SiO$_2$ pretreated at 590°C in 15% CH$_4$/H$_2$ showed excellent performance for FTS (see Section 4.3.3. Further, while alloying of Mo and Ru is possible [46], the temperatures required to achieve Ru dissolution into Mo are quite high (1450°C) and not reached during typical pretreatment and operating conditions for the FTS reactor [47].

It is also worth commenting on the synergy observed for RuCl$_3$/Mo$_2$C following pretreatment at 150°C in H$_2$, which produced higher C$_{5+}$ selectivity than bare Mo$_2$C. Under a typical Anderson-Schultz-Flory (ASF) distribution, this improvement in C$_{5+}$ should result in a decrease in both CH$_4$ and C$_2$-C$_4$ selectivity [48]. However, the CH$_4$ selectivity remained unchanged, while the C$_2$-C$_4$ dropped significantly. In the absence of synergy between Ru and Mo$_2$C, one would expect an overall decrease in the CH$_4$ production with increases in the C$_2$-C$_4$ and C$_{5+}$ selectivities simply based on the selectivities of Ru and Mo$_2$C separately. However, the unaffected CH$_4$ selectivity, along with the increase in reaction rate observed relative to Mo$_2$C indicates the presence of new

active site(s) for Fischer-Tropsch synthesis associated with this Ru/Mo$_2$C catalyst. To achieve the observed performance, the site(s) would be characterized by both a high FTS rate and high CH$_4$ selectivity in order to offset the expected performance of bare Ru and bare Mo$_2$C. Physically, this site may exist at the interface between Ru and Mo$_2$C or be associated with the Ru and the Mo oxycarbide passivation layer. More studies are required to further understand the origin of the enhanced rate and high CH$_4$ selectivity not in agreement with the ASF model.

Lastly, the Co(NO$_3$)$_2$/Mo$_2$C catalyst failed to exhibit the same response towards lower pretreatment temperatures as the RuCl$_3$/Mo$_2$C catalyst. This difference likely results from the higher temperatures required to fully reduce Co to the zero-valent state, and may also contribute to the deactivation of Co on Mo$_2$C. It is also plausible that the deactivation mechanism of Co on Mo$_2$C is different from that of Ru. The free surface energy of Co has been reported to be 2.709 [44] and 2.775 J/m^2 [45], which is quite close to that for Mo (2.877 and 2.752 J/m^2 [44,45]) so Mo covering Co does not appear likely.

In conclusion, the RuCl$_3$/Mo$_2$C (following reduction at 150°C) exhibited promising reaction rates and product selectivities. Furthermore, the potential presence of synergy between Ru and Mo$_2$C calls for further investigation into the nature of the active sites and the difference between RuCl$_3$/Mo$_2$C and the bare Mo$_2$C or RuCl$_3$/SiO$_2$ catalysts.

5.5. Summary

Evaluation of early transition metals supported on Mo$_2$C for their Fischer-Tropsch synthesis performance showed that Co and Ru supported on Mo$_2$C were surprisingly inactive, exhibiting no promotional effect. SiO$_2$-supported Co and Ru exhibited excellent FTS performance, suggesting the observed inactivity is specific to the Mo$_2$C-based

catalysts. The cause of Ru inactivity was probed by looking at the effects of particle size, pretreatment gas, Ru oxidation state, the presence of chloride in the metal precursor, and reduction temperature. The results suggested that the Ru inactivity is caused by the interaction of Ru and Mo_2C at high temperatures, perhaps by Mo coating the Ru nanoparticles. Following low temperature pretreatments of $RuCl_3/Mo_2C$, rates and C_{5+} selectivities were enhanced to an extent where synergy is probable between Ru and Mo_2C. In addition, $Co(NO_3)_2/Mo_2C$ also exhibited slightly improved performance relative to Mo_2C following low temperature reductions, but the performance enhancement in the case of Co was not as significant as for Ru.

5.6. References

[1]   V.U.S. Rao, G.J. Stiegel, G.J. Cinquegrane, R.D. Srivastava. Fuel Processing Technology, 30 (1992) 83-107.
[2]   G.P. Van Der Laan, A.A.C.M., Beenackers, Catalysis Reviews: Science and Engineering 41 (1999) 255-318.
[3]   M.A. Vannice, J. Catalysis 37 (1975) 449-461
[4]   N.M. Schweitzer, J.A. Schaidle, O.K. Ezekoye, X. Pan, S. Linic, L.T. Thompson, J. Am. Chem. Soc., 133 (2011) 2378-2381.
[5]   A. Griboval-Constant, J. Giraudon, G. Leclercq, L. Leclercq, Appl. Cat. A: General, 260, (2004) 35-45.
[6]   A. Griboval-Constant, J. Giraudon, I. Twagishema, G. Leclercq, M.E. Rivas, J. Alvarez, M.J. Pérez-Zurita, M.R. Goldwasser, J. Molec. Cat. A: Chemical, 259 (2006) 187-196.
[7]   J.A. Schaidle, Ph.D. Dissertation, University of Michigan, 2011.
[8]   Y. Chen, Ph.D. Dissertation, University of Michigan, 2015.
[9]   J.J. Patt, Ph.D. Dissertation, University of Michigan, 2003.
[10]   T.E. King, Ph.D. Dissertation, University of Michigan, 2007.
[11]   M.D. Porosoff, X. Yang, J.A. Boscoboinik, J.G. Chen, Angew. Chem. Int. Ed. 53 (2014) 6705-6709.
[12]   J.M.G. Carballo, J. Yang, A. Holmen, S. García-Rodríguez, J. Catalysis, 284 (2011) 102-108
[13]   X.-Y. Quek, I.A.W. Filot, R. Pestman, R. A. van Santen, Chem. Commun., 50 (2014) 6005-6008.
[14]   D.L. King, J. Catalysis, 51 (1978) 386-397.
[15]   G.L. Bezemer, J.H. Bitter, H.P.C.E. Kuipers, H. Oosterbeek, J.E. Holewijn, X. Xu, F. Kapteijn, A.J. van Dillen, K.P. de Jong, J. Am. Chem. Soc. 128 (2006) 3956

[16] T. Herranz, X. Deng, A. Cabot, J. Guo, M. Salmeron, J. Phys. Chem. B. 113 (2009) 10721-10727.

[17] J.P. den Breejen, P.B. Radstake, G.L. Bezemer, J.H. Bitter, V. Frøseth, A. Holmen, J. Am. Chem. Soc. 131 (2009) 7197-7203

[18] L. Spadaro, F. Arena, M.L. Granados, M. Ojeda, J.L.G. Fierro, F. Frusteri, J. Catalysis 234 (2005) 451-462.

[19] V. Ragaini, R. Carli, C.L. Bianchi, D. Lorenzetti, G. Vergani, Appl. Cat. A: General 139 (1996) 17-29.

[20] E.T. Iyagba, T.E. Hoost, J.U. Nwalor, J.G. Goodwin, Jr. J. Catalysis 123 (1990) 1-11.

[21] S.J. Tauster, S.C. Fung, J. Catalysis 55 (1978) 29-35.

[22] A.A. Khassin, T.M. Yurieva, V.V. Kaichev, V.I. Bukhtiyarov, A.A. Budneva, E.A. Paukshtis, V.N. Parmon, Journal of Molecular Catalysis A: Chemical 175 (2001) 189–204

[23] R.P. Mogorosi, N. Fischer, M. Claeys, E. van Steen, Journal of Catalysis 289 (2012) 140-150.

[24] J.M.G. Carballo, E. Finocchio, S. García, S. Rojas, M. Ojeda, G. Busca, J.L.G. Fierro, Catalysis Science & Technology 1 (2011) 1013-1023.

[25] J. Zhang, J. Chen, Y. Li, Y. Sun, J. Natural Gas Chemistry 11 (2002) 99-108.

[26] H. Jahangiri, J. Bennet, Mahjoubi, P.; Wilson, K.; Gu, S.; Catal. Sci. Technol. 4 (2014) 2210.

[27] J.A. Schaidle, N.M. Schweitzer, O.T. Ajenifujah, L.T. Thompson, J. Catalysis, 289 (2012) 210-217.

[28] A. Patterson. Phys. Rev. 56 (1939) 978-982.

[29] J.A. Schaidle, A.C. Lausche, L.T. Thompson, J. Catalysis, 272 (2010) 235-245.

[30] J.A. Schaidle, J. Blackburn, C.A. Farberow, C. Nash, K.X. Steirer, J. Clark, D.J. Robichaud, D.A. Ruddy. ACS Catal. 6 (2016) 1181-1197.

[31] Reddy, B.M.; Chowdhury, B.; Reddy, E.P.; Fernández, A. Appl. Cat. A: General 213 (2001) 279-288

[32] Delporte, P.; Meunier, F.; Pham-Huu, C.; Vennegues, P.; Ledoux, M.J.; Guille, J. Catalysis Today 23 (1995) 251-267.

[33] P.K. Cheekatamarla, W.J. Thomson, Appl. Cat. A: General 287 (2005) 176-182.

[34] A. Griboval-Constant, J. Giraudon, G. Leclercq, L. Leclercq, Appl. Cat. A: General, 260, (2004) 35-45.

[35] D.J. Morgan, Surf. Interface Anal. 47 (2015) 1072-1079.

[36] C.L. Bianchi, V. Ragaini, M.G. Cattania, Materials Chemistry and Physics 29 (1991) 297-306.

[37] T.P. St. Clair, S.T. Oyama, D.F. Cox, S. Otani, Y. Ishizawa, R.-L. Lo, K.-I. Fukui, Y. Iwasawa, Surface Science 426 (1999) 187-198.

[38] W. Wang, S. Guo, I. Lee, K. Ahmed, J. Zhong, Z. Favors, F. Zaera, M. Ozkan, C.S. Ozkan, Scientific Reports, 4 (2014) 4452

[39] D.S. Jensen, S.S. Kanyal, N. Madaan, M.A. Vail, A.E. Dadson, M.H. Engelhard, M.R.Linford, Surface Science Spectra 20 (2013) 36-42.

[40] J. Okal, M. Zawadzki, L. Kępiński, Krajczyk, W. Tylus, Appl. Catal. A: General 319 (2007) 202-209

[41] G. Jacobs, T. K. Das, Y. Zhang, J. Li, G. Racoillet, B. H. Davis, Appl. Cat. A: General 233 (2002) 263-281.

[42] M. E. Dry, Studies in Surface Science and Catalysis 152 (2004) 533-600.

[43] P. Munnik, N.A. Krans, P.E. de Jongh, K.P. de Jong, ACS Catal. 4 (2014) 3219-3226.

[44] L.Z. Mezey, J. Giber. Jap. J. Appl. Physics 21 (1982) 1569

[45] L. Vitos, A.V. Ruban, H.L. Skriver, J. Kollár. Surf. Sci. 411 (1998) 186-202.

[46] B.X. Liu, B.M. Clemens, R. Gaboriaud, W.L. Johnson, M-A. Nicolet. Appl. Phys. Letters 42 (1983) 624-626.

[47] E. Anderson, W. Hume-Rothery. J. Less Common Metals. 2 (1960) 443-450.

[48] R.B. Anderson, Catalysts for the Fischer-Tropsch Synthesis, Van Nostrand Reinhold, New York, 1956. Vol. 4.

CHAPTER 6

Summary and Future Work

6.1.   Summary and Overall Conclusions

The overall goal of research described in this dissertation was to develop property-reactivity relationships for early transition-metal carbides and nitrides, in particular for reactions relevant to biomass conversion into liquids. Material properties such as hydrogen adsorption sites, redox interactions between the precursors and support, and metal-support interactions, were investigated. Catalytic properties for the selective hydrogenation of crotonaldehyde, water-gas shift reaction, or Fischer-Tropsch synthesis were assessed. This work has advanced the understanding of these catalytic materials by correlating directly performance to intrinsic material properties, such as the hydrogenation selectivity differences observed for surface and subsurface hydrogen as well as the effect of surface redox chemistry on deposited metal dispersion.

The hydrogen sites for the carbides and nitrides of Mo, W, V, Nb, and Ti were initially investigated using thermal desorption spectroscopy following high temperature reduction in H_2. The carbides possessed one hydrogen desorption peak, while hydrogen desorbed from the nitrides producing two distinct peaks. The hydrogen desorption site from the carbides was tentatively attributed to surface C-H bonds based on previous literature [1]. For the nitrides, the two desorption peaks observed were attributed to surface and subsurface hydrogen species, based on results from thermal desorption spectroscopy, density functional theory and inelastic neutron scattering. By varying the

thermal treatments, different distributions of the surface and subsurface hydrogen ($\sim$40% to $\sim$95% subsurface) were obtained for the Mo_2N-H_x materials. The resulting materials were tested for crotonaldehyde hydrogenation in batch reactors. Interestingly, the hydrogenation product selectivity was a function of the site distribution. The relative density of subsurface hydrogens correlated with selectivity for hydrogenation of the carbonyl group only. Furthermore, the results are consistent with surface hydrogen being responsible for the hydrogenation of C=C bonds to form butyraldehyde, while both surface and subsurface hydrogen were capable of hydrogenating the C=O bond. This analysis was extended to include the W_2N-H_x and VN-H_x materials. No trends were observed between the site population and selectivity for these two catalysts, although the formation of (hemi)acetal by-products varied for different catalysts and was ultimately correlated to the density of surface acid sites for the catalysts. Quantity of acid sites decreased for the catalysts in the following order: W_2N > Mo_2N > VN. In addition, the hydrogen sites on the Mo and W carbides and nitrides could be populated via dehydrogenation reactions of model substrates, such as *N*-methylpyrrolidine, although the reaction rates were relatively low.

Second, expanding on previous work by Schaidle et al. [2], the surface redox chemistry during wet impregnation of metals, most notably Pt, onto Mo_2C was experimentally characterized using X-ray absorption spectroscopy. During wet impregnation, $PtCl_6^{2-}$ ions were reduced to zero-valent Pt while Mo was concurrently oxidized on the Mo_2C surface. Reduction of the Pt and oxidation of the Mo were also confirmed using X-ray photoelectron spectroscopy. The implications of this redox chemistry were explored using unpassivated and passivated Mo_2C surfaces as materials

that would undergo facile and inhibited redox, respectively. Platinum adsorption for the unpassivated material was rapid and complete, while adsorption on the passivated material was complex, consisting of an induction period followed by further adsorption. Significant differences were observed between the resulting catalysts in terms of composition and structure. These differences translated to drastic differences in their water-gas shift (WGS) activities. These differences, which are summarized in Table 6.1, illustrate the importance of surface redox chemistry on the catalyst composition, metal dispersion, and reactivity for carbide-supported metal catalysts.

Table 6.1. Summary of the Pt composition, Pt particle size, and WGS gravimetric rates for Mo_2C and Pt supported on passivated or unpassivated Mo_2C.

Catalyst	Pt wt%	Pt Dispersion (Particle Size)	WGS Rates ($\mu mol/g/s$)[1]
Mo_2C	-	-	64 ± 4
Pt/unpassivated Mo_2C	3.7	Good (<250nm)	238 ± 11
Pt/passivated Mo_2C	1.1	Agglomerated (10-20μm)	71 ± 8

[1] Rates correspond to steady state rates collected at 240°C.

Regarding interactions between Mo_2C and Fischer-Tropsch synthesis active metals (Ru, Co, Fe, Ni), enhancements in catalytic performance were observed for a select few metals. In particular, higher rates and turnover frequencies were observed for the Fe/Mo_2C and Ni/Mo_2C than for unpromoted Mo_2C catalysts. Furthermore, enhanced C_{5+} selectivities were observed with Fe/Mo_2C while Ni/Mo_2C produced more CH_4, consistent with the intrinsic activity of these metals as reported in the literature [3,4,5]. However, no enhancement was observed when depositing Co and Ru, two known and highly active FTS metals, onto Mo_2C; conversely, Co and Ru were active when

supported on SiO_2. This result suggests that Co and Ru are deactivated when supported on Mo_2C. Several potential causes for deactivation were evaluated. For example, the low activity of Ru observed could have been due to carbon deposition from the use of 15% CH_4/H_2 during pretreatment, poisoning of Ru by residual chlorine from the $RuCl_3$ precursor, or the formation of very small Ru nanoparticles, which are less active than larger Ru particles for FTS. The results from these studies suggest that the deactivation was linked to high temperature reduction steps during the synthesis/pretreatment of these catalysts. In fact, the best performing Mo_2C-based catalyst (in terms of both activity and selectivity) was for Ru/Mo_2C when pretreated at low temperatures (<150°C). Under these conditions, Ru/Mo_2C exhibited turnover frequencies (CO-normalized rates) ~18 times higher and C_{5+} selectivity more than double those of bare Mo_2C. While the deactivation mechanism at high temperatures has not been defined, it is possible that the mobility of Mo_2C is enhanced at high temperatures and Mo ultimately covers Ru due to differences in surface free energies [6].

6.2. Future Work in Current Research Areas

The research covered in this dissertation establishes a foundation for future investigations of the property-reactivity relationships for early transition-metal carbides and nitrides. The suggested areas for further examination include: (1) identifying the hydrogen sites participating *in situ* during hydrogenation reactions, under both stoichiometric batch and flow conditions, (2) investigating the mechanism for hydrogen addition to crotonaldehyde from subsurface sites in Mo_2N, (3) elucidating metal-support redox chemistry over other carbides and nitrides, and (4) determining the physical cause for the high-temperature deactivation of Ru supported on Mo_2C.

6.2.1. Identifying the hydrogen sites participating *in situ* during hydrogenation reactions

The research presented in Chapter 2 compared the intrinsic reactivity of hydrogen occupying surface sites (κ^1-NH) with those in the interstitial sites (μ^6-MoH) of Mo_2N. However, few definitive conclusions could be drawn about the participation of these sites typical hydrogenation conditions in stoichiometric versus flow reactors. The limited amount of data indicated that surface hydrogen predominated during crotonaldehyde hydrogenation over Mo_2N with the reactor headspace pressurized to 10 bar with H_2 at 70°C. Determining which hydrogen sites are active and catalytic under typical reaction conditions could further explain some of the results reported to-date on these materials and inform selection of process conditions needed to obtain the desired catalyst performance.

In situ spectroscopic techniques could prove beneficial for this purpose. Collaborators at the University of North Texas (Prof. Tom Cundari, Dr. Daniel Pardue) have calculated unique infrared (IR) frequencies for the various Mo_2N-H_x configurations. For example, calculated vibrational frequencies for κ^1-NH and μ^6-MoH were 3364 cm^{-1} and 1201 or 1269 cm^{-1}, respectively. Using Diffuse Reflectance Infrared Fourier Transform Spectroscopy (DRIFTS), it may be possible to identify which, if any, of these Mo_2N-H_x hydrogen species are present during a hydrogenation flow reaction. Additionally, DRIFTS can provide information on the adsorption of reactants and generation of intermediates. This technique has been utilized previously for crotonaldehyde hydrogenation [7] and for carbide and nitride-based catalysts [8,9]. For example, Shou et al. used DRIFTS to investigate the high selectivity of Rb/Mo_2C

catalysts for alcohol synthesis via CO hydrogenation, noting that the shift in selectivity towards alcohols from hydrocarbons was due to the mobility of Rb under reaction conditions to neutralize acid sites [9].

6.2.2. Characterizing the mechanism for hydrogen addition to crotonaldehyde from subsurface sites in Molybdenum Nitride

Results presented in Chapter 2 indicated subsurface hydrogen sites in Mo_2N are active for hydrogenation reactions. In particular, subsurface hydrogens appeared to be nearly 100% selective towards the hydrogenation of C=O versus C=C bonds in crotonaldehyde. Given the physical location of hydrogen in subsurface interstitial sites, the mechanism of this reaction is of great interest. Both computational and experimental approaches could be used to identify a possible mechanism. It would be beneficial to investigate the transition states computationally for both the diffusion path from subsurface sites to the surface, as well as hydrogen addition to crotonaldehyde.

Experimentally, deuterium-labeling would provide valuable information regarding the hydrogenation mechanism. This technique, commonly used in homogeneous catalysis research to understand reaction pathways and isolate reactions involving the solvent from the reactions of interest [10,11], will allow direct observations of the progression of hydrogen from surface or subsurface sites. For example, catalysts containing hydrogen-populated subsurface sites can be used to hydrogenate crotonaldehyde in deuterated ethanol (C_2H_5OD). The products could then be analyzed using GC or nuclear magnetic resonance (NMR) spectroscopy to determine the extent of participation of solvent in the reaction; if deuterium appears in the crotonaldehyde hydrogenation products, it suggests that ethanol may participate in the reaction directly.

The mechanism to form crotyl alcohol can also then be elucidated. Likely, Mo_2N-H_x first hydrogenates crotonaldehyde at C1 to form the alkoxide ion, which can either be further hydrogenated by Mo_2N-H_x or through solvent participation to form crotyl alcohol. The location of deuterium and hydrogen in the product(s) will provide information regarding this sequential addition.

6.2.3. Metal-support spontaneous redox chemistry over other carbides and nitrides

Since most early transition-metal carbides and nitrides are highly reduced, pyrophoric compounds, it is possible that other carbides and nitrides supports exhibit similar redox behavior to that observed during wet impregnation of Pt on Mo_2C. Using similar techniques, other carbides and nitrides, such as W_2C, WC, and Mo_2N, can be evaluated for the presence of redox chemistry. Therefore, it would be useful to examine trends in the redox behavior of carbide and nitride materials relative to their standard reduction potentials as reported by Schaidle et al. [2]. Recall that Schaidle et al. hypothesized that in order to undergo spontaneous metal reduction over Mo_2C, the metal salt must have a standard reduction potential above ~0.3 V. If other carbides or nitrides exhibit a similar standard reduction potential for oxidation to that of Mo_2C, one would expect spontaneous reduction to occur over these supports as well. For example, the standard reduction potentials for the oxidations of metallic Cr, Mo, and W to the trivalent state are known [12].

$$Cr \rightarrow Cr^{3+} + 3\,e^-, \qquad\qquad E^0 = -0.74\,V \qquad (6.1)$$

$$Mo \rightarrow Mo^{3+} + 3\,e^-, \qquad\qquad E^0 = 0.20\,V \qquad (6.2)$$

$$W \rightarrow W^{3+} + 3\,e^-, \qquad\qquad E^0 = 0.10\,V \qquad (6.3)$$

While these are not the half reactions for carbides or nitrides (thermodynamic data typically not available), these standard reduction potentials suggest that carbides and nitrides of these metals should all be able to spontaneously reduce the Pt, Pd, and Cu salts as observed by Schaidle et al [2]. Furthermore, the low standard potentials for Cr suggest that Cr carbides/nitrides may be able to reduce metals such as the $Co(NO_3)_2$ and $Fe(NO_3)_3$ that remained oxidized after interacting with Mo_2C. Differences may also be observed in the adsorption profiles of metals onto other early-transition-metal carbides and nitrides.

6.2.4. Physical cause for the high-temperature deactivation of Ru supported on Mo_2C

Results in Chapter 4 indicate that the relative inactivity of Ru when supported on Mo_2C was due to deactivation caused by deleterious interactions between Ru and Mo_2C, likely accelerated by high temperatures. Understanding the mechanism of Ru deactivation is important since the Ru/Mo_2C catalysts when pretreated at low temperatures were the most promising candidates of the Mo_2C-based materials studied. In fact, the RuCl$_3$/Mo_2C following 150°C reduction in H_2 exhibited the highest FTS turnover frequency of all of the Mo_2C catalysts evaluated, by nearly an order of magnitude; these turnover frequencies are also comparable to, if not higher than, Ru/Al$_2$O$_3$ catalysts [13]. As hypothesized in Chapter 4, one mechanism for Ru deactivation could be the migration of Mo species onto the Ru nanoparticles given the difference in surface free energies [14,15]. Using scanning transmission electron microscopy (STEM), high-resolution images of the RuCl$_3$/Mo_2C catalyst before and after high temperature reduction may provide information about the mobility of Mo_2C or Mo. However, as Mo (Z = 42) and Ru (Z = 44) are close in atomic number, contrast will be

very poor between these elements, limiting the resolution. Line scans using energy dispersive X-ray spectroscopy (EDX) may help provide higher resolution between Mo and Ru. An alternative approach is the use of surface sensitive techniques, such as selective chemisorption and/or IR/Raman spectroscopies. For these techniques to provide useful information, adsorbates must be selected that adsorb on Ru, but not on Mo_2C. If Mo_2C covers Ru after high temperature reductions, adsorbate chemisorption will be observed following low temperature reductions, but not after high temperature reductions.

6.3. Research Thrusts in New Areas

The research described in this dissertation has the potential to inform future efforts to utilize early transition-metal carbide and nitride-based catalysts for the transformation of biomass-derived compounds into fuels or commodity chemicals. Much of the knowledge gained through the studies presented herein can be applied to the use of these materials in different applications than as catalysts for biomass conversion.

In Chapter 2, Mo_2N, W_2N, and to a lesser extent VN were found to absorb hydrogen into subsurface sites. This suggests that the materials can be used in hydrogen membranes and membrane reactors. Recently, carbides and nitrides have been successfully employed as hydrogen permeable membranes. Wolden et al. showed that a Mo_2C/V composite membrane was capable of permeabilities exceeding that of pure Pd, a benchmark material for hydrogen dissolution and diffusion [16]. These Mo_2C/V materials function by dissociating H_2 on the Mo_2C surface, then H atoms diffuse through the Mo_2C and V layers, and recombine on a layer of Mo_2C on the other side of the membrane (Figure 6.1). Given the similarities of this transport process to our systems, Mo_2N may be

an excellent material for these composite membranes; alternatively, pure Mo_2N thin films may also be useful. These catalytic materials may also be valuable in membrane reactors, a useful engineering construct that allow for the complete separation of the two reactants. A well-known example is the H_2 proton exchange membrane (PEM) fuel cell. In this system, H_2 and O_2 are fed into adjacent compartments and, following H_2 dissociation on a catalyst, the protons move across the PEM to the reactor containing O_2, and H_2O evolves. In an analogous manner, a membrane reactor could be developed for the selective hydrogenation of substrates (e.g., crotonaldehyde) utilizing Mo_2N thin films as both the catalyst and membrane. In such a system, H_2 would dissociate on Mo_2N at one side of the reactor, diffuse through Mo_2N to the opposite side and react with crotonaldehyde from subsurface sites with high selectivity. This is one possible engineering solution for improving the throughput of the catalytic system described in Chapter 2.
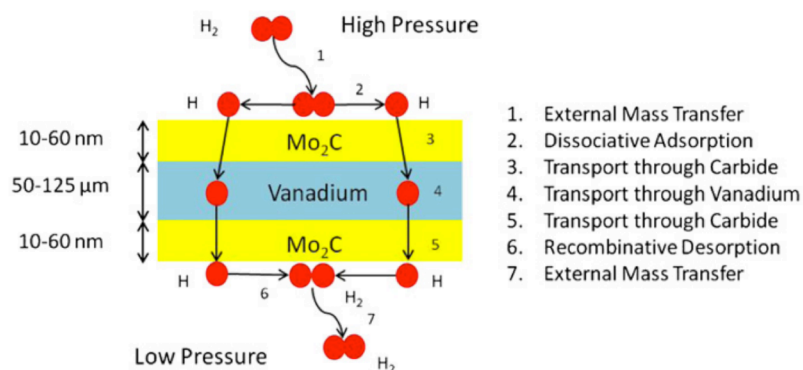

Figure 6.1. Schematic of the Mo_2C/V composite membrane and the mechanism for hydrogen transport through the membrane. Taken from [16].

Based on our experience with deactivation of Ru, the reduction and pretreatment conditions used for carbide- and nitride-supported metal catalysts have a significant influence on their performance. Future work utilizing Mo_2C as a catalyst support should be explored using pretreatment temperatures only high enough to reduce the deposited metal, with little attention given to reduction of the carbide or nitride. This may be

applied to all catalytic applications of carbide/nitride-supported metal catalysts and result

in different catalyst performance than previously reported.

6.4.   References

[1]   A.J. Medford, A. Vojvodic, F. Studt, F. Abild-Pedersen, J.K. Nørskov. J. Catalysis 290 (2012) 108-117.

[2]   J.A. Schaidle, N.M. Schweitzer, O.T. Ajenifujah, L.T. Thompson. J. Catalysis 289 (2012) 210-217.

[3]   D.W. Goodman, R.D. Kelley, T.E. Madey, J.T. Yates, Jr., J. Catalysis 63 (1980) 226-234.

[4]   C.C. Kao, S.C. Tsai, Y.W. Chung, J. Catalysis 73 (1982) 136.

[5]   J.-Y. Park, Y.-J. Lee, P.K. Khanna, K.-W. Jun, J.W. Bae, Y.H. Kim. J. Mol. Catal. A: Chem., 323 (2010) 84-90.

[6]   L.Z. Mezey, J. Giber. Jap. J. Appl. Physics 21 (1982) 1569

[7]   A. Dandekar, M.A. Vannie, J. Catalysis 183 (1999) 344-354.

[8]   S. Yang, C. Li, J. Xu, Q. Xin, J. Phys. Chem. B. 102 (1998) 6986-6993.

[9]   H. Shou, L. Li, D. Ferrari, D.S. Sholl, R.J. Davis, J. Catalysis 299 (2013) 150-161.

[10]   S.H. Kim, S.H. Hong, ACS Catal. 4 (2014) 3630-3636.

[11]   S.R. Klei, J.T. Golden, T. Don Tilley, R.G. Bergman, J. Am. Chem. Soc. 124 (2002) 2092-2093.

[12]   A.J. Bard, R. Parsons, J. Jordan. *Standard Potentials in Aqueous Solution*. Marcel Dekker, Inc. New York, New York, 1985.

[13]   D.L. King, J. Catalysis, 51 (1978) 386-397.

[14]   L.Z. Mezey, J. Giber. Jap. J. Appl. Physics 21 (1982) 1569

[15]   L. Vitos, A.V. Ruban, H.L. Skriver, J. Kollár. Surf. Sci. 411 (1998) 186-202.

[16]   C.A. Wolden, K. Adeyemo, R.H.J. Vervuurt, M. Ostwal, J.D. Way. J. Membrane Science 427 (2013) 150-154.